

Study of the action of antimicrobial peptides by spectroscopic methods : From model membrane to bacterial biofilm

Oona Freudenthal

▶ **To cite this version:**

Oona Freudenthal. Study of the action of antimicrobial peptides by spectroscopic methods : From model membrane to bacterial biofilm. Medicinal Chemistry. Université de Lorraine, 2016. English. NNT : 2016LORR0197 . tel-01585915

HAL Id: tel-01585915
https://hal.univ-lorraine.fr/tel-01585915

Submitted on 26 Sep 2017

HAL is a multi-disciplinary open access archive for the deposit and dissemination of scientific research documents, whether they are published or not. The documents may come from teaching and research institutions in France or abroad, or from public or private research centers.

L'archive ouverte pluridisciplinaire **HAL**, est destinée au dépôt et à la diffusion de documents scientifiques de niveau recherche, publiés ou non, émanant des établissements d'enseignement et de recherche français ou étrangers, des laboratoires publics ou privés.

AVERTISSEMENT

Ce document est le fruit d'un long travail approuvé par le jury de soutenance et mis à disposition de l'ensemble de la communauté universitaire élargie.

Il est soumis à la propriété intellectuelle de l'auteur. Ceci implique une obligation de citation et de référencement lors de l'utilisation de ce document.

D'autre part, toute contrefaçon, plagiat, reproduction illicite encourt une poursuite pénale.

Contact : ddoc-theses-contact@univ-lorraine.fr

LIENS

Code de la Propriété Intellectuelle. articles L 122. 4
Code de la Propriété Intellectuelle. articles L 335.2- L 335.10
http://www.cfcopies.com/V2/leg/leg_droi.php
http://www.culture.gouv.fr/culture/infos-pratiques/droits/protection.htm

Thèse de Doctorat

Etude de l'action de peptides antimicrobiens par méthodes spectroscopiques : De la membrane modèle au biofilm bactérien

Présentée par

Oona FREUDENTHAL

Pour l'obtention du titre de

Docteur en Chimie de l'Université de Lorraine

Soutenue publiquement le 15 décembre 2016

Rapporteurs

Giovanna FRAGNETO – Professeur, Université Joseph Fourier (Grenoble – I), Grenoble

Vincent DUPRES – Maître de conférences, Université de Lille, Institut Pasteur de Lille, Lille

Examinateurs

Andreea PASC – Maître de conférences, Université de Lorraine, SRSMC, Villers-lès-Nancy

Véronique ROSILIO – Professeur, Université Paris Sud, Paris

Invitée

Fabienne QUILES – Chargée de recherche CNRS, LCPME, Villers-lès-Nancy

Superviseurs

Ewa ROGASLKA – Professeur, Université de Lorraine, SRSMC, Vandœuvre-lès-Nancy

Grégory FRANCIUS – Chargé de recherche, CNRS, LCPME, Villers-lès-Nancy

UMR 7565 CNRS SRSMC, UNIVERSITE DE LORRAINE
FACULTE DES SCIENCES – BP239 – 54506 VANDOEUVRE-LES-NANCY CEDEX - FRANCE

Thesis

Study of the action of antimicrobial peptides by spectroscopic methods: From model membrane to bacterial biofilm

Presented by

Oona FREUDENTHAL

To fulfill requirements for the degree of

***Philosophiæ Doctor* (PhD) in Chemistry of University of Lorraine**

Public defense on December 15th 2016

Referees

Giovanna FRAGNETO – Professor, Université Joseph Fourier (Grenoble – I), Grenoble

Vincent DUPRES – Associate Professor, Université de Lille, Institut Pasteur de Lille, Lille

Examinators

Andreea PASC – Associate Professor, Université de Lorraine, SRSMC, Villers-lès-Nancy

Véronique ROSILIO – Professor, Université Paris Sud, Paris

Invited

Fabienne QUILES – Senior Researcher, CNRS, LCPME, Villers-lès-Nancy

Supervisors

Ewa ROGASLKA – Professor, Université de Lorraine, SRSMC, Vandœuvre-lès-Nancy

Grégory FRANCIUS – Senior Researcher, CNRS, LCPME, Villers-lès-Nancy

UMR 7565 CNRS SRSMC, UNIVERSITE DE LORRAINE
FACULTE DES SCIENCES – BP239 – 54506 VANDOEUVRE-LES-NANCY CEDEX - FRANCE

Les grandes personnes aiment les chiffres.
Quand vous leur parlez d'un nouvel ami,
elles ne vous questionnent jamais sur l'essentiel.
Elles ne vous disent jamais: "Quel est le son de sa voix ?
Quels sont les jeux qu'il préfère ?
Est-ce qu'il collectionne les papillons ?"
Elles vous demandent: Quel âge a-t-il ?
Combien a-t-il de frères? Combien gagne son père ?"
alors seulement elles croient le connaître.

-Antoine de Saint-Exupéry, Le Petit Prince

À mon fils

The gift of Truth excels all other gifts.

-Gautama Buddha

To my husband

Acknowledgements

I completed this thesis work at Laboratoire de Chimie Physique et Microbiologie pour l'Environnemment (LCPME) in the team of Chimie des Surfaces et des Interfaces. I would therefore like to thank Pr. Alain Walcarius, the director of the laboratory, as well as Pr. Christian Ruby, the director of the team for letting me stay in their laboratory for the past three years.

I would like to thank Pr. Ewa Rogalska and Dr. Gregory Francius for providing me the opportunity to complete a thesis at Université de Lorraine as well as Institut Jean Barriol for their financial support that made this work possible. I would like to give special acknowledgements to Dr. Fabienne Quilès, who enabled multiple discussions and showed everlasting patience when introducing me to the world of biofilms and infrared spectroscopy. It was a real pleasure to be working with you.

I would also like to express my appreciation to the members of the jury, Giovanna Fragneto, Véronique Rosilio, Vincent Dupres, Andreea Pasc, Fabienne Quilès, Gregory Francius and Ewa Rogalska for examining my work.

In addition, I would like to thank Jalal Bacharouche, Sofiane El Kirat Chatel, Angelina Razafitianamaharavo and Audrey Beaussart for their helpfulness concerning AFM experiments, Camille Troux for her contribution to the bacterial biofilm experiments and Muayad Al-Jaberi for sharing the office with me and for being all ears when needed.

I would like to thank the whole staff of LCPME for being there and for creating such a pleasant working environment.

Last, but defenetely not the least, I would like to express my deepest gratitude towards my family who has been there through thick and thin; to my husband who has encouraged me to find my own path and to my son who has helped me to open my eyes as wide as a child's. Kiitos rakkaimmat!

Résumé

L’émergence des infections impliquant des bactéries résistantes aux traitements par voie antibiotique sont actuellement un défi majeur dans le domaine de la santé d’où la nécessité de faire appel à de nouvelles thérapies. Les peptides antimicrobiens sont considérés comme de bons candidats dans la lutte contre microorganismes multi-résistantes, principalement en raison de leur faible toxicité sur les cellules eucaryotes et de leurs différents modes d'action par rapport aux antibiotiques classiques. En effet, ces derniers sont généralement moins susceptibles de mener aux phénomènes de résistance observés pour les antibiotiques classiques. L'objectif des travaux menés dans ce mémoire était d'étudier l'action des deux agents antimicrobiens différents; i) la colistine, un polypeptide cyclique utilisé pour traiter les infections causées par des bactéries multi-résistantes et ii) la catestatine bovine (bCAT), un peptide linéaire faisant partie de la famille des HDP (Host Defense Peptides), produite par le système endocrinien.

L'activité des peptides sur des membranes phospholipidiques pures et mixtes a été suivie en temps réel par microscopie à force atomique et spectroscopie infrarouge. Les mesures de spectroscopie infrarouge nous ont permis de renforcer l'hypothèse selon laquelle l'activité du peptide était plus intense sur les membranes mixtes que sur les membranes pures. En outre, nos résultats montrent que des changements conformationnels ont lieu quand la bCAT était en contact avec la membrane.

Nous nous sommes également intéressés à l’action des deux peptides sur des membranes constituées principalement d’extraits naturels de lipopolysaccharides et Lipid A bactériens. Nos résultats ont mis en évidence que les deux agents antimicrobiens étaient à l’origine d’une réorganisation de la structure des membranes et dans certains cas, le peptide était à l’origine de la formation des pores de différentes tailles. L'influence de l'élasticité de la membrane a également été étudiée à l’aide de la spectroscopie de force.

Nous avons étudié en parallèle l’activité des deux peptides antimicrobiens sur des biofilms bactériens de *E. coli*. Les résultats obtenus ont montré des changements métaboliques dus à l’exposition à la colistine et qui affectent principalement la production d'acide nucléique, alors que l’exposition à la bCAT semble plutôt modifier la production de polysaccharides. L’étude des propriétés mécaniques du biofilm au cours du traitement antimicrobien a confirmé le mode d’action différent des deux peptides. La colistine présente un effet de rigidification des parois bactériennes alors qu’un effet inverse caractérisé par une fluidification de la paroi bactérienne est observé pour la bCAT. Par ailleurs, la colistine induit une transition morphologique bacille-cocci alors que la bCAT semble être à l’origine d’une déstructuration du septum conduisant à une morphologie plus allongée et filamenteuse des bactéries. L’ensemble de ces observations ont été corrélées aux mesures

réalisées par microscopie à épifluorescence. Enfin, nous avons également mis en évidence que le traitement par la colistine était plutôt de nature bactériostatique puisque nous avons observé un redémarrage de la croissance bactérienne quand en fin de traitement, le biofilm était soumis à un flux de milieu nutritif. Nous avons également relevé que ce n'était pas le cas après le traitement à la bCAT où l'effet du peptide sur le biofilm est plutôt de nature bactériolytique.

Ce travail a montré que deux peptides antimicrobiens différents en termes de structures peut avoir un mode d'action très différent et qu'ils induisent outre les modifications morphologiques et mécaniques et des changements métaboliques. Enfin, nous pouvons souligner qu'il serait intéressant d'exploiter les effets de synergies de cocktail couplant peptides antimicrobiens et antiobiotiques classiques, notamment pour l'élaboration de nouveaux traitements contre les microorganismes multi-résistants.

Abstract

Several multidrug resistant infections are currently a major challenge for the healthcare. Antimicrobial resistance is becoming increasingly concerning and new therapies are constantly needed to be introduced. Antimicrobial peptides (AMPs) are good candidates in the battle against multidrug resistant micro-organisms, mainly due to their reduced toxicity on eukaryotic cells and their different modes of action in comparison to conventional antibiotics. AMPs are non-specific and bacteria are less likely to develop antimicrobial resistance against these peptides. The objective of this work was to study the action of two different antimicrobial agents; i) colistin, a cyclic polypeptide already used in treatment of infections caused by multi-resistant bacteria and ii) bovine catestatine (bCAT), a relatively recently discovered linear HDP (Host Defence Peptide) produced by the endocrine system.

The activity of these peptides on pure and mixed phospholipid membranes (DPPC, DOPC and DPPE) were studied in real time and *in-situ* with atomic force microscopy and infrared spectroscopy. Infrared spectroscopy allowed us to strengthen the hypothesis that the peptide activity was stronger in the case of the mixed membranes in comparison to pure lipid membranes. We also observed changes in catestatine conformation when in contact with certain membrane lipids.

The action of these peptides was equally studied on membranes of natural extractions of different lipopolysaccharides and Lipid A found in bacteria. Our results show that both of the studied peptides caused reorganization of the LPS/Lipid A membranes and in some cases, the peptide formed pores of various sizes onto the membrane. The influence of the peptides on the membrane elasticity was also studied with force spectroscopy.

In addition, the activity of the two antimicrobial peptides were studied on *E. coli* biofilms. Our results show that both of the peptides change the bacterial metabolism, however, whereas colistin had an effect principally on the nucleic acid production of the bacteria, catestatin altered the production of polysaccharides. Our studies on the mechanical properties of the bacterial membrane confirmed the distinct actions of these peptides; colistin had a stiffening effect on the bacterial membranes whereas catestatin acted in an inversed manner by fluidizing the bacterial membranes. However, colistin induced morphological changes on the bacteria, which underwent a rod-to-coccus shape transition, whereas catestatin seemed to be the origin of an altered behavior of the septum formation process causing the bacteria to adopt long and even filamentous shapes. All of these findings correlated with our observations with epifluorescence microscopy. Finally, it was observed that colistin effect was rather bacteriostatic since the biofilm growth continued after colistin

treatment when the biofilm was subjected to a new growth medium. This was not the case for catestatin which rather had a bacteriolytic effect on the biofilm.

This work showed that two antimicrobial peptides with distinct structures can have very different modes of action on multiple levels such as bacterial morphology, mechanics and metabolic activity. Given the very different action of these two peptides, it should be of interest to study the synergies of AMPs and classical antibiotics to find new therapies for fight against multidrug resistant microbes.

Table of Contents

List of figures 11
List of tables 20
List of equations 21
List of abbreviations 22
1. Scientific context 25
1.1 Biological membranes 25
1.1.2. Eukaryotic and prokaryotic cell membrane structures 26
1.1.3. Phospholipids 29
1.1.3.1 Phosphoglycerides 30
1.1.3.2 Physical states of membrane phospholipids 31
1.1.4. Lipopolysaccharides 34
1.2. From a single bacterium to bacterial biofilms 35
1.3. Antimicrobial peptides 38
1.3.1. Polymyxins 40
1.3.2. Bovine Catestatin 41
1.4 Application of lipid membrane and bacterial biofilm models on peptide studies 42
1.4.1 Langmuir monolayers 42
1.4.2 Atomic force microscopy 43
1.4.3 Attenuated total reflection Fourier transform infrared spectroscopy (ATR-FTIR) 45
1.5 Aim of this work 49
2. Materials and methods 50
2.1. Preparation of phospholipid and lipopolysaccharide bilayers 51
2.2. Bacterial culture and formation of bacterial biofilms 52
2.2.1. *E. coli* bacterial strain 52
2.2.2 Determination of minimal inhibitory concentration 53
2.2.3. Bacterial culture 53
2.2.3. Bacterial growth in suspension 54
2.2.1. Formation of bacterial biofilms 55

2.2.4. Fluorescence microscopy and *Bac*Light ™ staining 56
2.3. Langmuir method 58
2.3.1. Compression isotherms 60
2.3.2. Brewster angle microscopy (BAM) 61
2.3.3. Preparation of Langmuir monolayers and compression isotherms 62
2.4. Atomic force microscopy (AFM) 63
2.4.1. Principle and basis of AFM technique 63
2.4.2 Force spectroscopy 67
2.4.3. AFM for phospholipid and LPS bilayer experiments 68
2.4.4. AFM imaging and force spectra of biofilms 69
2.5. Attenuated total reflectance Fourier transform infrared spectroscopy (ATR-FTIR) 70
2.5.1. Principles of ATR-FTIR 70
2.5.2. ATR-FTIR on phospholipid bilayers 75
2.5.3. ATR-FTIR on bacterial biofilms subjected to AMPs 76
3. Antimicrobial peptide action on model membranes 78
3.1 Phospholipid monolayer interaction with a cyclic antimicrobial peptide 78
3.2 Phospholipid bilayer interaction with antimicrobial peptides 80
3.2.1 Morphological and spectral characteristics of phospholipid bilayers 80
3.2.2 Phospholipid bilayer interaction with a cyclic antimicrobial peptide 84
3.2.3 Phospholipid bilayer interaction with a linear antimicrobial peptide 93
3.3 Lipopolysaccharide bilayer interaction with antimicrobial peptides 101
3.3.1 Morphological characteristics of LPS bilayers 101
3.3.2 Lipopolysaccharide bilayer interaction with a cyclic antimicrobial peptide 102
3.3.3 Lipopolysaccharide bilayer interaction with a linear antimicrobial peptide 104
3.4 Comparison of the action of a cyclic and a linear peptide on model membranes 108
4. Antimicrobial peptide action on bacterial biofilms 111
4.1 Bacterial growth in planktonic form 111

4.2 Formation of a bacterial biofilm 117

4.3 Cyclic antimicrobial peptide action on a bacterial biofilm 129

4.4 Linear antimicrobial peptide action on a bacterial biofilm 136

4.5 Comparison of the action of a cyclic and a linear peptide on biofilms 148

5. Conclusions 151
References 154
Annexes 171

List of figures

Figure 1-1. A schematic three-dimensional and cross-sectional view of the fluid mosaic model of a cell membrane as proposed by Singer and Nicholson in 1972 (modified from [5]). Integral proteins floating in the lipid bilayer matrix are randomly distributed in the plain of the membrane. 25

Figure 1-2. A schematic structure of a eukaryotic cell membrane; a phospholipid bilayer with membrane proteins embedded into and on top of the bilayer. Cholesterol and glycolipids are floating within the phospholipids of the membrane [14]. 27

Figure 1-3. A schematic structure of a bacterial cell wall. a) Gram positive bacteria cell wall with the phospholipid plasma membrane under the thick peptidoglycan layer. b) Gram negative bacteria cell wall with distinct inner plasma membrane, periplasmic space with peptidoglycan and an outer lipid membrane [15]. 28

Figure 1-4. A cross section of a Gram negative bacteria cell wall structure showing the different layers and important parts of the constituting membrane molecules (drawn based on [29, 30]). 29

Figure 1-5. A common structure of a phosphoglyceride with two fatty acid chains, a glycerol backbone, a phosphate and a polar alcohol group R (modified from [38]). 30

Figure 1-6. Shapes and corresponding membrane structures adopted by different phospholipids (modified from [31]). 31

Figure 1-7. Different membrane phases of phospholipid bilayers; solid gel-like (s_o), liquid-disordered (l_d) and liquid-ordered (l_o) containing cholesterol (drawn based on [11]). 33

Figure 1-8. Ripples in a l_o/l_d phase coexistence of a (1:1) DMPC/DSPC double bilayer. a) Height mode AFM image at 32.5 °C. b) Deflection mode zoom of a, showing ripples in the l_o phase domain (white arrow) [48]. 33

Figure 1-9. Common structure with different regions and variability of LPS molecules (modified from [53]). 34

Figure 1-10. Scheme illustrating the different forms and structures adopted by bacteria (modified from [57]). 35

Figure 1-11. General structure of a bacteria with its genetic material floating in the cytoplasm bounded by the bacterial cell wall to which several external structures such as pili and flagella are attached. 36

Figure 1-12. Five steps of the development of a bacterial biofilm. Stage 1: Reversible adhesion on the substrate surface; stage 2: Irreversible adhesion and production of extracellular polymeric substance (EPS) matrix; stage 3: Maturation and early development of biofilm architecture; stage 4:

Maturation of biofilm architecture; stage 5: Dispersion of bacterial cells from the biofilm (drawn based on [67, 73, 74]).....38
Figure 1-13. A scheme of the carpet-like mechanism of antimicrobial peptide action on lipid bilayer (drawn based on [87, 89, 93]).....39
Figure 1-14. Pore formation mechanisms of peptides in lipid bilayers. a) Barrel-Stave mechanism b) toroidal pore formation (drawn based on [91]).....40
Figure 1-15. Chemical structure of colistin (polymyxin E) [108].....41
Figure 1-16. a) bCAT chemical structure b) bCAT in a 'random coil' secondary structure.....42
Figure 2-1. External structure of *E2146* with type 1 *fimbriae* (modified from [172]).....53
Figure 2-2. Flow circulation system used to form bacterial biofilms.....55
Figure 2-3. a) Flow cell and Ge crystal used for ATR-FTIR setup, 1: chamber for Ge crystal, height 0.3 cm. b) Flow cell and Ge disc used for AFM setup, 2: chamber for Ge disc, height 0.2 cm.....56
Figure 2-4. Principle of fluorescence microscopy (drawn based on [177]).....57
Figure 2-5. A typical π-A isotherm of a membrane lipid (DPPC) with different monolayer phase transitions indicated (drawn based on [181]).....61
Figure 2-6. A schematic figure of the Langmuir trough and the principle of Brewster angle microscope. a) No monolayer present at the air-water interface and therefore no reflection occurring from the *p*-polarized light beam. b) A monolayer is present at the air-water interface and a reflection of the *p*-polarized light occurs when the beam comes on the surface at a Brewster's angle of incidence (α) (drawn based on [182]).....62
Figure 2-7. The principle of an atomic force microscope (AFM) (drawn based on [174, 189]).....64
Figure 2-8. Different interaction forces between the tip and the sample surface (modified from [174, 189].....65
Figure 2-9. Schematic representation of a force curve obtained by AFM force spectroscopy indicating the different regions of the approach and retraction zones (drawn based on [174]).....67
Figure 2-10. Symmetric (a) and asymmetric (b) stretching vibrations [41].....72
Figure 2-11. Different kinds of bending vibrations, + and – indicating movements on opposite directions out of the plane [41].....72
Figure 2-12. Schematic of ATR-FTIR technique and formation of the evanescence wave (drawn based on [149]).....73
Figure 2-13. Principle of the polarization of light (drawn based on [177]).....75
Figure 3-1. Compression isotherms of phospholipid monolayers spread on water subphase (solid lines) or colistin (50 μM) aqueous solution (dashed lines). a,c) Π-*A* isotherms b,d) Δ*V*-*A* isotherms.

Results obtained with pure DPPC (black), DOPC (blue), DPPE (red), and mixed DPPC/DOPC (orange) and DPPE/DOPC (olive) monolayers. Brewster angle micrographs of mixed DPPC/DOPC (e, f) and DPPE/DOPC (g, h) monolayers spread on pure water subphase (e, g) and on colistin (50 µM) aqueous solution (f, h). The micrographs were taken at Π = 25.0 mNm^{-1}. Temperature 20 °C [108]. 79

Figure 3-2. ATR-FTIR spectra of a) DPPC, b) DOPC and c) mixed DPPC/DOPC SLBs on germanium crystal in TRIS buffer (NaCl 150 mM, $CaCl_2$ 1mM, pH=7.4). Major assignments are indicated. Background: TRIS buffer [108]. 81

Figure 3-3. Time-evolution of the ATR-FTIR spectra of the DPPC (a, c) and DOPC (b, d) phospholipid SLBs on the Ge crystal during 2 h without AMP injection (control experiment) without rinse (a, b) and with rinse (c, d). The background spectra are the SLBs at 0 min. *: water vapour not completely removed [108]. 82

Figure 3-4. Atomic force microscope topographical images of a) DPPC/DOPC SLB and b) DPPE/DOPC immersed in TRIS buffer. 83

Figure 3-5. ATR-FTIR spectra of colistin in aqueous solution [108]. a) 1.1 mM mother solution on diamond b) 150 µM solution on germanium. 84

Figure 3-6. Time-evolution of the ATR-FTIR spectra of the phospholipid SLBs on the Ge crystal in the presence of 150 µM colistin with rinse of the SLB before colistin injection [108]. The background spectra are the SLBs before colistin injection. a) DPPC b) DOPC c) DPPC/DOPC SLB. 86

Figure 3-7. Polarized spectra at polarization angles of 0° and 90° of the CH_2-stretching region of DPPC bilayer before and 2 h after colistin (150 µM) injection. 87

Figure 3-8. Time-evolution of integrated intensity ratios Amide II/νC=O during the action of colistin at 150 µM for DPPC (black squares), DOPC (red discs), and DPPC/DOPC (blue triangles) SLBs [108]. Integration regions: νC=O: 1760-1712 cm^{-1}, Amide II: 1580-1485 cm^{-1}. 88

Figure 3-9. Atomic force microscope topographical images of DPPC/DOPC SLBs immersed in TRIS buffer a) before and b) 40 min after colistin injection (10 µM). No changes in topography of the SLB were observed. 89

Figure 3-10. Atomic force microscope topographical images of DPPC/DOPC SLBs immersed in TRIS buffer before (a, c) and 40 min after (b, d) colistin injection (b: 50 µM, c: 150 µM) [108]. ... 89

Figure 3-11. Representative force-distance curves recorded on DPPC domain (blue), DOPC domain (green) before colistin injection and on DPPC remaining domain (red) and revealed mica (black) 40 min after colistin (150 µM) injection [108]. 90

Figure 3-12. Typical distributions of DPPC/DOPC SLB elasticity before (a, c) and 40 min after colistin injection (b: 50 µM, d: 150 µM) with peak centres indicated. Derjaguin-Muller-Toporov (DMT) modulus images of supported DPPC/DOPC SLB in TRIS buffer e) before and f) 40 min after colistin (150 µM) injection [108]. 91
Figure 3-13. Atomic force microscope topographical images of supported DPPE/DOPC vesicle immersed in TRIS buffer [108] a) before and b) 40 min after colistin (50 µM) injection. 92
Figure 3-14. Typical distributions of DPPE/DOPC vesicle elasticity a) before and b) 40 min after colistin (50 µM) injection with peak centres indicated. Derjaguin-Muller-Toporov (DMT) modulus images of supported DPPE/DOPC SLBs in TRIS buffer c) before and d) 40 min after colistin (50 µM) injection [108]. 92
Figure 3-15. Roughness time-evolution of DPPE (black lines) and DPPC (grey lines) domains within 60 min after colistin (10 µM: hollow symbols and 50µM: filled symbols) injection [108]... 93
Figure 3-16. ATR-FTIR spectra of bCAT in aqueous solution. a) 0.41 mM mother solution on diamond. b) 60 µM solution on germanium. 94
Figure 3-17. Time-evolution of the ATR-FTIR spectra of the phospholipid SLBs on the Ge crystal in the presence of 60 µM bCAT with rinse of the SLB before bCAT injection. The background spectra are the SLBs before bCAT injection. a) DPPC b) DOPC c) DPPC/DOPC SLB. 95
Figure 3-18. a) Change of Amide II band wavelength in DPPC bilayer within time after bCAT injection. b) Time-evolution of integrated intensity ratios Amide II/νC=O during the action of bCAT at 60 µM for DPPC (black squares), DOPC (red discs), and DPPC/DOPC (blue triangles) SLBs. Integration regions: νC=O: 1760-1712 cm^{-1}, Amide II: 1580-1485 cm^{-1}. 96
Figure 3-19. Polarized spectra at polarization angles of 0° and 90° of the CH_2-stretching region of DPPC bilayer before and 2 h after bCAT (60 µM) injection. 98
Figure 3-20. Atomic force microscope topographical images of DPPC/DOPC SLBs immersed in TRIS buffer a) before b) 5 min and c) 60 min after bCAT (60 µM) injection. 99
Figure 3-21. a) Red line: h_1 before bCAT injection, black lines: three distinct heights, h_1, h_2 and h_3, seen at the phase boundaries of the DPPC/DOPC system 5 min after bCAT injection b) Values and standard deviations of the phase boundary heights. Each value obtained from an average of 10 different height profiles. 99
Figure 3-22. Derjaguin-Muller-Toporov (DMT) modulus images (top panel) and elasticity distributions (bottom panel) of supported DPPC/DOPC SLBs in TRIS buffer a) before, b) 5 min and c) 60 min after bCAT (60 µM) injection. 100

Figure 3-23. Atomic force microscope topographical images of Lipid A/LPSt SLBs in air a) before, b) 20 min, c) 40 min and d) 60 min after colistin (150 µM) injection. 102
Figure 3-24. Distributions of Lipid A/LPSt SLB elasticity in TRIS buffer a) before b) 60 min after colistin (150 µM) injection. c) Elasticity change within time. 103
Figure 3-25. Atomic force microscope topographical images of Lipid A/LPS-S SLBs in air a) before, b) 20 min c) 40 min and d) 60 min after colistin (150 µM) injection..... 103
Figure 3-26. Distributions of Lipid A/LPS-S SLB elasticity in TRIS buffer a) before b) 60 min after colistin (150 µM) injection. c) Elasticity change within time. 104
Figure 3-27. Atomic force microscope topographical images of Lipid A/LPSt SLBs in air a) before, b) 20 min c) 40 min and d) 60 min after bCAT (60 µM) injection..... 105
Figure 3-28. Distributions of Lipid A/LPSt SLB elasticity in TRIS buffer a) before, b) 0 min, c) 20 min and d) 60 min after bCAT (60 µM) injection. e) Elasticity within time..... 106
Figure 3-29. Atomic force microscope topographical images of Lipid A/LPS-S SLBs in air a) before, b) 20 min c) 40 min and d) 60 min after bCAT (60 µM) injection. 107
Figure 3-30. Distributions of Lipid A/LPS-S SLB elasticity in TRIS buffer a) before b) 60 min after bCAT (60 µM) injection. c) Elasticity change within time. 107
Figure 3-31. Hypothesized mechanism of action of the two AMPs on DPPC/DOPC bilayers. a) colistin as a function of concentration at 60 min after peptide injection b) bCAT (60 µM) as a function of time after bCAT injection..... 109
Figure 4-1. Two growth curves of the *E2146* S0Ec suspension with different growth phases (1-4) indicated. 1: Lag phase, 2: Exponential growth phase, 2b: end of exponential growth phase/beginning of stationary phase, 3: stationary phase, 4: advanced stationary phase/death phase. Initial OD_{600} for red and green graphs 0.49 and 0.46 respectively. 111
Figure 4-2. Two growth curves of the *E2146* S1Ec suspension with different growth phases (1-4) indicated. Initial OD_{600} for red and green lines 0.05 and 0.06 respectively..... 113
Figure 4-3. ATR-FTIR spectra of *E2146* bacterial suspensions on a diamond crystal; S0Ec at 0 h (black) and 2.5 h (red), S1Ec at 4 h (green) and 24 h (blue). Different spectral zones indicated; 1: Amide II, 2: AmIII-NA, 3: PS total. Spectra normalized with respect to Amide II band. 113
Figure 4-4. Epifluorescence images of the *Bac*Light™ stained *E2146* suspensions a) culture at 2 h (initial OD_{600}=0.55) b) S0Ec at 0 h (initial OD_{600}=0.46) c) S0Ec at 2.5 h (initial OD_{600}=0.49) d) S1Ec at 3 h (initial OD_{600}=0.05). 116
Figure 4-5. a) Evolution of ATR-FTIR spectra during the growth of a *E2146* biofilm aged 2.5 h. Bacterial adhesion with 30 min static and 2 h open circulation (50 mL/h) inoculation of bacterial

suspension. Spectra presented from bottom to up every 10 min. Background spectrum recorded immediately after filling the flow cell with bacterial suspension. b) Epifluorescence image of the non-stained side (entry) side of a *E2146* biofilm aged 2.5 h, initial OD_{600}=0.46, average coverage ratio of 43.3 ± 21.6 %, exposure time 100 ms. 118
Figure 4-6. ATR-FTIR spectra of adhered sessile bacteria in a biofilm aged 2.5 h (dashed line) on Ge crystal at the end of the bacterial inoculation (at 2.5 h) and planktonic bacteria in S0Ec suspension at 2.5 h (solid line) on diamond ATR. Spectra normalized with respect to Amide II band. 119
Figure 4-7. a) Evolution of ATR-FTIR spectra of a *E2146* biofilm aged 26.5 h during 24 h open circulation (50 mL/h) of LB/10. Background spectrum recorded immediately after filling the flow cell with fresh LB/10 solution. b) Evolution of the integrated intensities of the main ATR-FTIR bands of *E2146* biofilm aged 26.5 h as a function of time; zone 1: inoculation of 2.5 h (30 min static), zone 2: 24 h open circulation of LB/10. Integration limits: ν*OH*: 3580-3400, Amide II: 1591-1484, Amide III-NA: 1279-1182, PS total: 1199-950, total: 1591-950. 120
Figure 4-8. ATR-FTIR spectra of adhered sessile bacteria in a 26.5 h-old biofilm (dashed line) on Ge crystal at the end of the open LB/10 circulation (4 h) and planktonic bacteria in S1Ec suspension at 4 h (solid line) on diamond ATR. Spectra normalized with respect to Amide II band. 122
Figure 4-9. Epifluorescence image of non-stained (entry) side of a *E2146* biofilm aged 26.5 h, initial OD_{600}=0.51, average coverage ratio of 38.7 ± 18.7 %, exposure time 100 ms. 122
Figure 4-10. a) Evolution of ATR-FTIR spectra of a 5.5 h-old *E2146* biofilm during its 3 h open circulation (50 mL/h) of LB/10. Spectra presented every 30 min from bottom to top. Background spectrum recorded immediately after filling the flow cell with fresh LB/10 solution. b) Evolution of the integrated intensities of the main ATR-FTIR bands of a *E2146* biofilm aged 5.5 h as a function of time; zone 1: inoculation of 2.5 h (30 min static), zone 2: 3 h open circulation of LB/10. Integration limits: ν*OH*: 3580-3400, Amide II: 1591-1484, Amide III-NA: 1279-1182, PS total: 1199-950, total: 1591-950. 123
Figure 4-11. Epifluorescence images of a *E2146* biofilm aged 5.5 h. a) non-stained (entry) side, initial OD_{600}=0.46, average coverage ratio of 44.7 ± 15.7 %, exposure time 100 ms. b) *Bac*Light ™ stained (exit) side, initial OD_{600}=0.46, average coverage ratio of 40.5 ± 11.4 %, exposure time 100 ms. 124
Figure 4-12. a-c) AFM images at different lateral sizes (a: 20 µm, b: 10 µm and c: 5 µm) showing the morphology of a *E2146* biofilm aged 5.5 h without peptide treatment. Top panel: height images, middle panel: deflection images and bottom panel: height profiles corresponding to the lateral cross

sections indicated by the white dashed lines. d) Statistical distribution of the Young modulus of a *E2146* biofilm aged 5.5 h. e) Representative force-indentation curve (open circle) with theoretical model (solid red line) recorded from the untreated *E2146* biofilm aged 5.5 h. 125
Figure 4-13. The chosen biofilm setup for peptide studies. A Reference biofilm aged 5.5 h was chosen, which was then subjected to 24 h closed circulation of either pure LB/10 (control) or LB/10 containing peptide (biofilm aged 29.5 h). Bacteriolytic/bacteriostatic effect of peptide was checked by an open circulation of LB/10 (17 h) directly after peptide circulation (biofilm aged 46.5 h). ... 126
Figure 4-14. a) Evolution of ATR-FTIR spectra of a *E2146* biofilm aged 29.5 h (control) during 24 h closed circulation (50 mL/h) of LB/10. Spectra presented at 0.5, 1.5, 2.5, 3.5, 4.5, 6.5, 10.5, 14.5, 20.5, and 24 h from bottom to top. Background spectrum recorded immediately after filling the flow cell with fresh LB/10 solution. Red arrows show typical bands assigned for glycogen. b) Evolution of the integrated intensities of the main ATR-FTIR bands of a *E2146* biofilm aged 29.5 h as a function of time; zone 1: inoculation of 2.5 h (30 min static), zone 2: 3 h open circulation of LB/10, zone 3: 24 h closed circulation of 40 mL of LB/10. Integration limits: νOH: 3580-3400, Amide II: 1591-1484, Amide III-NA: 1279-1182, PS total: 1199-950, total: 1591-950. 127
Figure 4-15. Epifluorescence image of a *E2146* control biofilm aged 29.5 h a) non-stained (entry) side, OD_{600}=0.45, average coverage ratio of 71.2 ± 19.1 %, exposure time 100 ms b) Backlight™ stained (exit) side, average coverage ratio of 49.9 ± 17.3 %, exposure time 100 ms. 128
Figure 4-16. a) Evolution of ATR-FTIR spectra of a *E2146* biofilm aged 29.5 h during 24 h closed circulation (50 mL/h) of colistin (0.87 µM) LB/10. Background spectrum recorded immediately after filling the flow cell with fresh colistin (0.87 µM) LB/10 solution. b) Evolution of ATR-FTIR spectra of a *E2146* biofilm aged 46.5 h during 17 h open circulation of LB/10. c) Evolution of the integrated intensities of the main ATR-FTIR bands of *E2146* biofilm aged 46.5 h as a function of time; zone 1: inoculation of 2.5 h (30 min static), zone 2: 3 h open circulation of LB/10, zone 3: 24 h closed circulation of colistin (0.87 µM) LB/10, zone 4: 17 h open circulation of LB/10. Integration limits: νOH: 3580-3400, Amide II: 1591-1484, Amide III-NA: 1279-1182, PS total: 1199-950, total: 1591-950. 130
Figure 4-17. Epifluorescence images of a *E2146* biofilm aged 29.5 h with 24 h colistin (0.87 µM) LB/10 closed circulation, initial OD_{600}=0.33 a) non-stained side (entry side), average coverage ratio of 48.9 ± 11.9 %, exposure time 7000 ms. b) *Bac*Light ™ stained side (exit) side, average coverage ratio of 66.8 ± 16.4 %, exposure time 278 ms. 131
Figure 4-18. A *E2146* biofilm aged 29.5 h after colistin 0.87 µM treatment. AFM images at different lateral sizes (a: 20 µm, b: 10 µm and c: 5 µm, zoom of (a) indicated with the red square, d:

1 µm, zoom of (c) indicated with the blue square) showing the morphology of the biofilm; Top panel: height images, middle panel: deflection images and bottom panel: height profiles corresponding to the lateral cross sections indicated by the white dashed lines.....133
Figure 4-19. *E2146* biofilm aged 29.5 h with 24 h colistin (0.87 µM) treatment. a) Statistical distribution of the Young modulus. b) Representative force-indentation curve (open circle) with theoretical model (red line).....134
Figure 4-20. Epifluorescence images of a *E2146* biofilm aged 46.5 h with 24 h colistin (0.87 µM) LB/10 closed circulation and 17 h pure LB/10 open circulation, initial OD_{600}=0.41 a) non-stained (entry) side, average coverage ratio of 66.7 ± 8.1 %, exposure time 500 ms. b) *Bac*Light ™ stained (exit) side, initial OD_{600}=0.41, average coverage ratio of 77.8 ± 10.4 %, exposure time 570 ms...135
Figure 4-21. a) Evolution of ATR-FTIR spectra of a *E2146* biofilm aged 29.5 h during 24 h closed circulation (50 mL/h) of bCAT (30 µM) LB/10. Background spectrum taken immediately after filling the flow cell with fresh bCAT (30 µM) LB/10 solution. b) Evolution of ATR-FTIR spectra of a *E2146* biofilm aged 46.5 h during 17 h open circulation of LB/10. c) Evolution of the integrated intensities of the main ATR-FTIR bands of *E2146* biofilm aged 46.5 h as a function of time; zone 1: bacterial inoculation of 2.5 h (30 min static), zone 2: 3 h open circulation of LB/10, zone 3: 24 h closed circulation of bCAT (30 µM) LB/10, zone 4: 17 h open circulation of LB/10. Integration limits: *ν*OH: 3580-3400, Amide II: 1591-1484, Amide III-NA: 1279-1182, PS total: 1199-950, total: 1591-950.....137
Figure 4-22. Epifluorescence images of a *E2146* biofilm aged 29.5 h with 24 h bCAT (30 µM) LB/10 closed circulation, OD_{600}=0.33 a) non-stained (entry) side, average coverage ratio of 40.4 ± 11.9 %, exposure time 3000 ms. b) *Bac*Light ™ stained (exit) side, average coverage ratio of 61.0 ± 8.1 %, exposure time 243 ms.....139
Figure 4-23. A *E2146* biofilm aged 29.5 h with 24h bCAT (30 µM) treatment. AFM images at different lateral sizes (a: 20 µm, b: 10 µm, c: 5 µm and d: 1 µm zoom of red square) showing the biofilm morphology. Top panel: height images, middle panel: deflection images and bottom panel: height profiles corresponding to the lateral cross sections indicated by the white dashed lines. 140
Figure 4-24. A *E2146* biofilm aged 29.5 h with 24h bCAT (30 µM) treatment. a) Statistical distribution of the Young modulus a) Representative force-indentation curve (open circle) with theoretical model (red line).....141
Figure 4-25. Epifluorescence images of a *E2146* biofilm aged 29.5 h with 24 h bCAT (30 µM) LB/10 closed circulation and pure LB/10 open circulation, initial OD_{600} = 0.38 a-b) non-stained

(entry) side, average coverage ratio of 25.6 ± 16.1 %, exposure time 250 ms. c) *Bac*Light ™ stained (exit) side, average coverage ratio of 34.9 ± 16.9 %, exposure time 250 ms. 142

Figure 4-26. a) Evolution of ATR-FTIR spectra of a *E2146* biofilm aged 29.5 h during 24 h closed circulation (50 mL/h) of bCAT (60 µM) LB/10, initial OD_{600} = 0.46. Background spectrum taken immediately after filling the flow cell with fresh bCAT (60 µM) LB/10 solution. b) Evolution of ATR-FTIR spectra of a *E2146* biofilm aged 46.5 h during 17 h open circulation of LB/10. c) Evolution of the accumulated integrated intensities of the main ATR-FTIR bands of a *E2146* biofilm aged 46.5 h as a function of time; zone 1: bacterial inoculation of 2.5 h (30 min static), zone 2: 3 h open circulation of LB/10, zone 3: 24 h closed circulation of bCAT (60 µM) LB/10, zone 4: 17 h open circulation of LB/10. Integration limits: νOH: 3580-3400, Amide II: 1591-1484, Amide III-NA: 1279-1182, PS total: 1199-950, total: 1591-950. 143

Figure 4-27. Epifluorescence images of a *E2146* biofilm aged 29.5 h with 24 h bCAT (60 µM) LB/10 closed circulation, initial OD_{600}=0.49 a) non-stained (entry) side, average coverage ratio of 36.5 ± 7.3 %, exposure time 3000 ms. b) *Bac*Light ™ stained (exit) side, average coverage ratio of 25.5 ± 9.8 %, exposure time 50 ms. 145

Figure 4-28. A *E2146* biofilm aged 29.5 h with 24h bCAT (60 µM) treatment. AFM images at different lateral sizes (a: 20 µm, b: 10 µm and c: 5 µm, zoom of b indicated with a red square) showing the biofilm morphology. Top panel: height images, middle panel: deflection images and bottom panel: height profiles corresponding to the lateral cross sections indicated by the white dashed lines. d) Statistical distribution of the Young modulus e) Representative force-indentation curve (open circle) with theoretical model (red line). 146

Figure 4-29. Epifluorescence images of a *E2146* biofilm aged 29.5 h with 24 h bCAT (60 µM) LB/10 closed circulation and pure LB/10 open circulation, initial OD_{600} = 0.45 a) non-stained (entry) side, average coverage ratio of 1.0 ± 0.8 %, exposure time 500 ms. b) *Bac*Light ™ stained (exit) side 147

Figure 4-30. Hypothesized mechanism of action of the two AMPs at minimal inhibitory concentration on *E. coli* biofilms. a) colistin (0.87 µM) action as a function of time b) bCAT (60 µM) action as a function of time). 150

List of tables

Table 1-1. Major infrared absorption bands of a membrane lipids [41, 149, 155]. 47

Table 1-2. The major IR absorption bands assigned for *pseudomonas* strain [160, 164]. 48

Table 2-1. Chemicals used in this study with their suppliers and storage form and temperature indicated. 50

Table 2-2. Maximal excitation and emission wavelengths of the different fluorochromes used to visualize *E2146* biofilms with epifluorescence microscopy (λ: wavelength, ex: excitation, em: emission) [174]. 58

Table 2-3. Different degrees of freedom of polyatomic molecules [41]. 71

Table 2-4. Evolution of the depth of penetration (d_p, in µm) of the evanescent wave as a function of the wavenumber of the incoming IR radiation at the surface of two commonly used ATR crystals [198]. 74

Table 3-1. Compression isotherm parameters at collapse of phospholipid monolayers on pure water subphase and subphase containing 50 µM colistin [108]. 79

Table 3-2. Suggested secondary structures based on wavenumbers for bCAT in the presence of different phospholipid bilayers (based on [215]). 97

Table 4-1. Principal attributions of ATR-FTIR absorption bands of *E2146* S0Ec suspension in exponential phase on diamond crystal. ν_s: symmetric stretch, ν_a: antisymmetric stretch, δ: deformation. 115

Table 4-2. Average sizes of *E2146* bacteria in different suspensions calculated from 10 randomly chosen individual bacteria. 117

Table 4-3. Average sizes of bacteria in biofilms of various ages obtained by epifluorescence microscope. Length and width calculated from 30 randomly taken individual bacteria. 129

Table 4-4. Sizes of 29.5 h-old *E2146* biofilm bacteria obtained by epifluorescence microscopy with different treatments; directly after 24 h LB/10 or peptide treatment and after 17 h LB/10 open circulation post peptide treatment. 149

Table 4-5. Sizes and Young modulus values of *E2146* biofilm bacteria with different AMP treatments obtained by AFM. *Values calculated on the average of 10 randomly taken individual bacteria. **Young modulus average of three individual force maps. 150

List of equations

Equation 1. Molecular area ($\hat{A}_M$) of a monolayer molecule. 59
Equation 2. Surface pressure (π). 59
Equation 3. Total force (F) acting on the Wilhelmy plate. 59
Equation 4. Surface pressure π as obtained by Wilhelmy plate method. 60
Equation 5. The compressibility of a monolayer. 61
Equation 6. Compressibility modulus. 61
Equation 7. Hooke's law 66
Equation 8. Sneddon model used for calculating the Young modulus *E* from the force-indendation curves obtained by AFM. 69
Equation 9. Bohr equation relating the energy of a photon to its wavelength 71
Equation 10. Beer-Lambert law relating sample absorbance, pathlength and concentration. 72
Equation 11. Critical angle at which total reflection of a light beam occurs at the interface of two materials having a refractive index ratio equal to or below one. 73
Equation 12. Depth of penetration of the evanescent wave penetrating the sample in close contact with the ATR crystal. 73
Equation 13. Dichroic ratio calculated from parallel and perpendicularly polarized light. 75
Equation 14. Bacterial generation time. 112

List of abbreviations

AFM	Atomic Force Microscopy
Amp	Ampicillin
AMP	Antimicrobial peptide
ATR-FTIR	Attenuated Total Reflection Fourier Transform Infrared Spectroscopy
BAM	Brewster Angle Microscopy
bCAT	Bovine catestatin
Cm	Chloramphenicol
COL	Colistin (Polymyxin E)
CTL	Cateslytin
DNA	Deoxyribonucleic acid
DMPC	1,2-Dimyristoyl-*sn*-glycero-3-phosphocholine
DOPC	1,2-Dioleoyl-*sn*-glycero-3-phosphocholine
DPPC	1,2-Dipalmitoyl-*sn*-glycero-3-phosphocholine
DPPE	1,2-Dipalmitoyl-*sn*-glycero-3-phosphoethanolamine
DSPC	1,2-Distearoyl-*sn*-glycero-3-phosphocholine
E. coli	*Escherichia coli*
EPS	Extracellular polymeric substances
FVI	Force-volume image
Ge	Germanium
Hep	L-glycero- D-manno-heptose
Kdo	3-Deoxy- D-manno-octulsonic acid
Km	Kanamycine
Leu	Leucine

LPS	Lipopolysaccharide
LPS-Re	Rough lipopolysaccharide
LPS-S	Smooth lipopolysaccharide
LPSt	Total extract of lipopolysaccharide
MIC	Minimum Inhibitory Concentration
NA	Nucleic Acid
PC	Phosphocholine
PE	Phosphatidylethanolamine
PEI	Polyethylenimine
PG	Phosphatidylglycerol
PGA	β-1,6-poly-N-acetylglucosamine
Phe	Phenylalanine
PI	Propidium iodidide
PL	Phospholipid
PS	Phosphatidylserine
SLB	Supported Lipid Bilayer
SPM	Scanning Probe Microscopy
TFA	Trifluoroacetic acid
TRIS	Tris(hydroxymethyl)aminomethane
Zeo	Zeocin

1. Scientific context

1.1 Biological membranes

The study of biological membranes has become increasingly important in the past years and is an essential key to the understanding of cell function as well as most biological processes. The plasma membrane is a border of life; it separates the living cell from its environment and encounters the cytosol, keeping it separate from the extracellular matrix. The plasma membrane has a selective permeability which enables it to let some substances easier through the cell than others [1]. Transmembrane movement is possible due to a common general structure of all biological membranes; the membranes consist of a thin film of lipid and protein molecules that are held together by non-covalent interactions [2]. The knowledge on the specific structure of cell membranes is a result of years of combined, multidisciplinary studies in the fields of chemistry, biology and physics.

In 1935 Hugh Davson and James Danielli suggested a sandwich model of the cell membrane, in which a phospholipid bilayer lies between hydrophilic proteins [3]. This model became largely accepted and even the first electron microscope studies in 1950s supported the sandwich model. However, the sandwich model had its limitations, and it was overruled by the currently accepted model; the fluid mosaic model proposed by Jonathan Singer and Garth Nicholson in 1972 (figure 1-1) [4]. In the fluid mosaic model the plasma membrane has a fluid structure with various proteins embedded in or attached to a double layer of phospholipids.

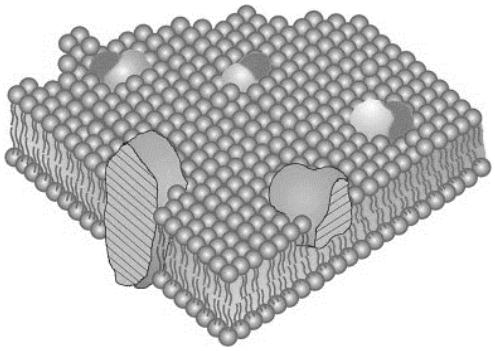


Figure 1-1. A schematic three-dimensional and cross-sectional view of the fluid mosaic model of a cell membrane as proposed by Singer and Nicholson in 1972 (modified from [5]). Integral proteins floating in the lipid bilayer matrix are randomly distributed in the plain of the membrane.

Indeed, phospholipids are the most plentiful membrane lipids among glycolipids and cholesterol. Lecithin was the first discovered phospholipid, found from egg yolk by Théodore-Nicolas Gobley in 1846 [6], well before Gorter and Grendel suggested in 1925 that cell membranes are composed of phospholipid bilayers [7]. Phospholipids have a hydrophobic and a hydrophilic region, making them amphiphilic in nature and allowing them to form spontaneously various different structures, among them the double layers. Gorter and Grendel's work was based on the studies of fatty acids conducted by Irving Langmuir in 1917 [8]. Langmuir revealed the formation of monolayers when fatty acids were spread at air-water interfaces. Langmuir's methods for studying lipid monolayer systems are still in use within the scientific community, showing that membrane models have been constructed on an excellent basis, as they have continuously inspired further experiments and shaped the future research. On top of the monolayer systems suggested by Langmuir, other membrane models have been developed, notably supported lipid bilayers (SLBs) that are used to understand specific interactions between membrane lipids and exogenous agents.

1.1.2. Eukaryotic and prokaryotic cell membrane structures

All organisms that consist of cells having a nucleus and other organelles enclosed by membranes, are called eukaryotes. Prokaryotes on the other hand are single-celled organisms which do not have a nucleus or any other internal organelle surrounded by a membrane. These two types of cells are very different from each other, also by the cell membrane surrounding them.

Cell membranes consist of large amounts (50% of their dry mass) of various different lipids; phospholipids, glycolipids and in the case of eukaryotic cells, cholesterol [9]. Phospholipids are a major class of membrane lipids and their variations can be found in different quantities among species. Eukaryotic cells have one phospholipid bilayer as their cell membrane (figure 1-2). Phospholipids are active participants of the cell membrane functions and influence the properties of proteins associated with the membrane. Phospholipids however, do not possess innate catalytic activities, making it a challenge to investigate the precise roles that phospholipids have in cell functions and identify the underlying reasons for the vast phospholipid diversity [10].

Phospholipids are insoluble in water and they possess a unique characteristic of being able to form bilayers without additional energy input due to their specific amphiphilic structure. Phospholipids are organized in the bilayer in such a way that the polar head groups of the molecules are facing the surrounding aqueous media and the hydrophobic carbohydrate tails are facing each other to form the core of the membrane; giving the bilayer an overall thickness of about 5 nm [2]. This

hydrophobic core restrains the exchange of hydrophilic compounds, such as water and ions through the cell membrane. The phospholipids mostly found in eukaryotic cells are phosphatidylcholine (PC), phosphatidylethanolamine (PE) and phosphatidylserine (PS) [11], the latter being negatively charged and mainly in the inner leaflet of the phospholipid double layer [12]. Phosphatidylcholine on the other hand, is the most plentiful of them all, representing over 50% (molar) of all the membrane lipids [13].

Besides lipids, the second half of the mass of most cellular membranes is accounted by proteins floating in the phospholipid bilayer (figure 1-2). The contribution in cell function of these membrane proteins are numerous; they take part in the selective transportation of substances, such as nutrients, waste and ions in and out of the cell, and their role in energy and signal transduction as well as cell-cell recognition is vital for the organism.

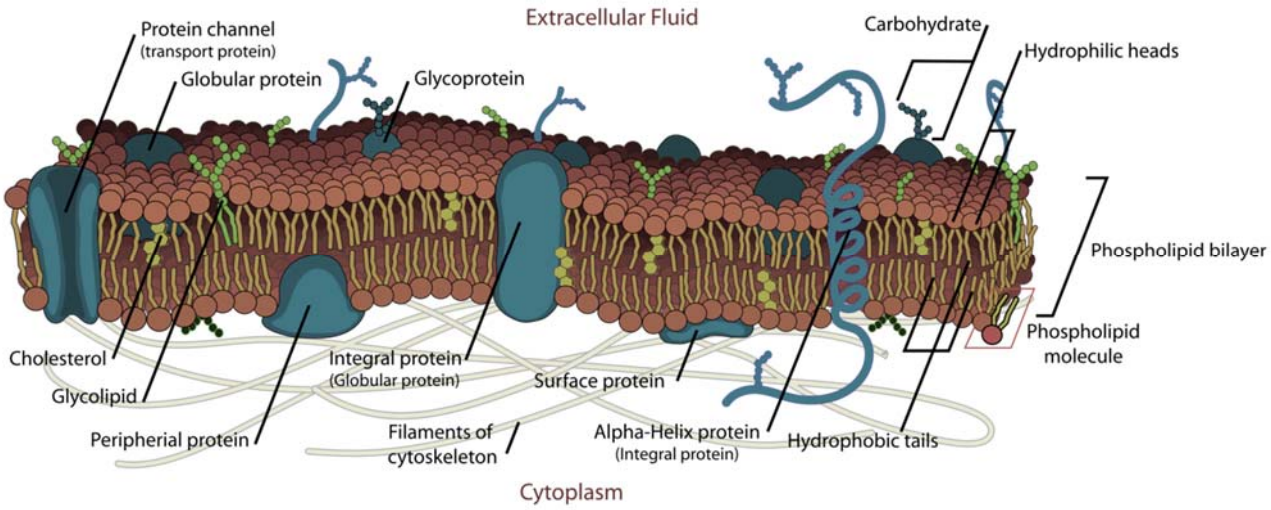


Figure 1-2. A schematic structure of a eukaryotic cell membrane; a phospholipid bilayer with membrane proteins embedded into and on top of the bilayer. Cholesterol and glycolipids are floating within the phospholipids of the membrane [14].

Bacteria are prokaryotes and bacterial cells differ from eukaryotic cells of mammals not only by cell functions, but also by the membrane separating the cell from its environment. Bacterial membrane has a more complex structure than that of eukaryotic cells. In addition to the plasma membrane, bacterial cells are covered by a cell wall. Based on the composition of this wall, bacteria can be classified into two categories; Gram-negative and Gram-positive bacteria. Gram-positive bacteria have cell walls with large amount of peptidoglycan on top of a plasma membrane (figure 1-

3a), whereas Gram-negative bacteria have peptidoglycan in a periplasmic space and an additional lipid bilayer on top of the peptidoglycan sheet (figure 1-3b).

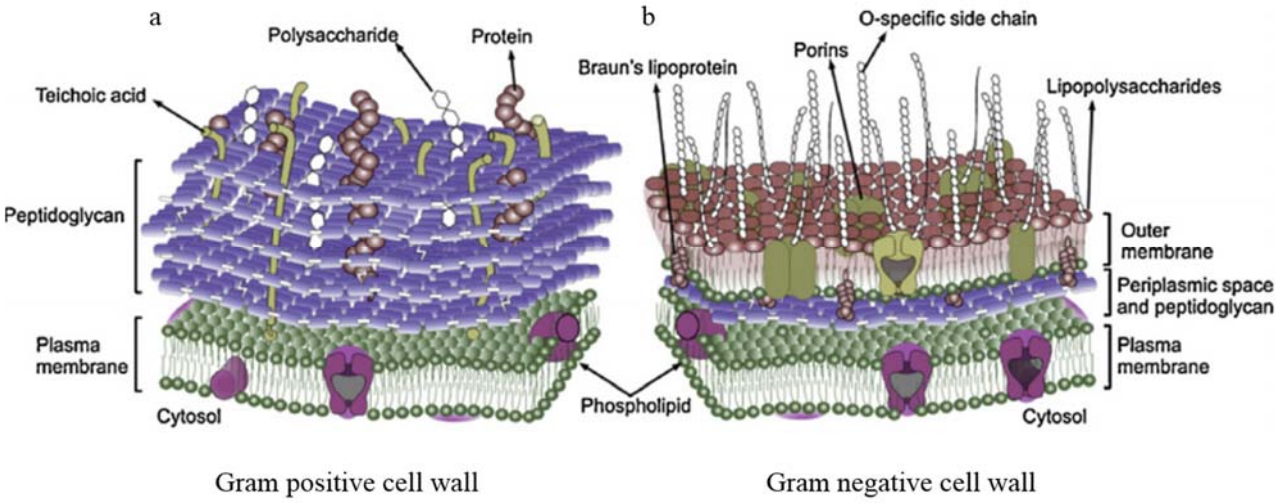


Figure 1-3. A schematic structure of a bacterial cell wall. **a)** Gram positive bacteria cell wall with the phospholipid plasma membrane under the thick peptidoglycan layer. **b)** Gram negative bacteria cell wall with distinct inner plasma membrane, periplasmic space with peptidoglycan and an outer lipid membrane [15].

In this study we will concentrate on Gram-negative bacteria and therefore the membrane structure of Gram-negative bacteria is presented in more detail (figure 1-4).

Despite the fact that the outer lipid-protein bilayer is not the outermost layer of Gram-negative bacteria (more external layers such as capsules, S-layers and sheaths are present), it is usually referred to as the outer layer of the bacterial cell wall [16]. This outer membrane is composed of phospholipids, membrane proteins and lipopolysaccharides (LPS) and it separates the periplasm of the bacterial cell from the extracellular space. Although the lipid bilayer does not possess a good permeability for hydrophilic solutes, it is still in charge of the transportation of nutrition and wastes. This functionality is enabled by β-barrel proteins called porins present in the membrane (figure 1-4) [17-19].

Lipopolysaccharides, covering 75% of the outer leaflet of the outer membrane of most Gram-negative bacteria [20, 21], consist of an endotoxin lipid A to which a core oligosaccharide and further an O-antigen is attached. The outer membrane plays an important role in the defense mechanism of Gram-negative bacteria against toxic components and LPS molecules are claimed to play a role in the resistance of Gram-negative bacteria against various antibiotics [22, 23]. They are

also known as endotoxins due to their ability to provoke the activation of the immune response [24, 25]. On the contrary to phospholipid bilayers, the LPS layer has a more rigid and highly ordered structure, explaining the low permeability of Gram-negative bacteria membrane towards various hydrophobic compounds [21, 26]. The inner leaflet of the outer membrane as well as the cytoplasmic membrane of the Gram-negative bacteria are mainly composed of phospholipids, phosphatidylethanolamine (PE) playing the largest role (70-80%) in addition to phosphatidylglycerol (PG) and cardiolipin [18, 27]. Gram negative bacteria containing high amounts of unsaturated fatty acids, contain phosphatidylcholine (PC) [28].

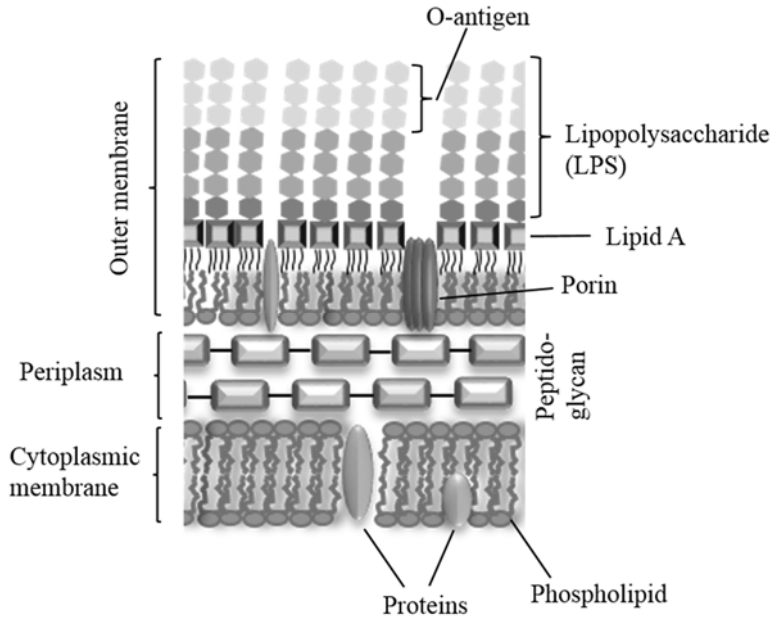


Figure 1-4. A cross section of a Gram negative bacteria cell wall structure showing the different layers and important parts of the constituting membrane molecules (drawn based on [29, 30]).

1.1.3. Phospholipids

In a typical eukaryotic cell, the lipid bilayer thickness is about 5 nm and the bilayer has an uninterrupted surface area of hundreds of square microns. This area includes hundreds of different types of lipids and over 10^8 individual molecules [31], including phospholipids. The majority of phospholipid synthesis occurs in the membranes of the endoplasmic reticulum in mammalian cells [11, 32]. Phospholipids consist of a polar head group and two hydrophobic hydrocarbon tails, which typically are fatty acids containing 14 to 24 carbon atoms [33]. The fatty acids can either be unsaturated, meaning that one or multiple double bonds exist between the carbons of the

hydrocarbon chain, or saturated with only single bond present. The differences in carbon chain length and saturation of the carbon chain affect the physico-chemical properties of phospholipids. Depending on their overall structure, phospholipids are classified either as phosphoglycerides or as sphingolipids, the latter having a sphingosine backbone instead of glycerol [34]. Phosphoglycerides are a principle class of phospholipids and will therefore be presented here in more detail.

1.1.3.1 Phosphoglycerides

Phosphoglycerides are constructed from three main parts: a glycerol molecule linked to two fatty acid chains, often one of them being saturated and the other being unsaturated, esterified to two of the three hydroxyl groups of the glycerol, the third hydroxyl group being esterified to a phosphate [9, 35]. The phosphate acts as an acylating agent and a polar alcohol; either inositol or serine is introduced to form a phosphate ester. Phosphatidylserine (PS), a compound obtained by the addition of serine to the phosphate group, can then further be decarboxylated and transferred into phosphatidylethanolamine (PE) [36], the precursor of phosphatidylcholine (PC). The choline head of phosphatidylcholine is highly polar and is obtained by three methylations of the nitrogen atom of the ethanolamine [37]. Thus the polar head group of a phosphoglyceride is usually an alcohol; either inositol, serine, ethanolamine or choline (figure 1-5).

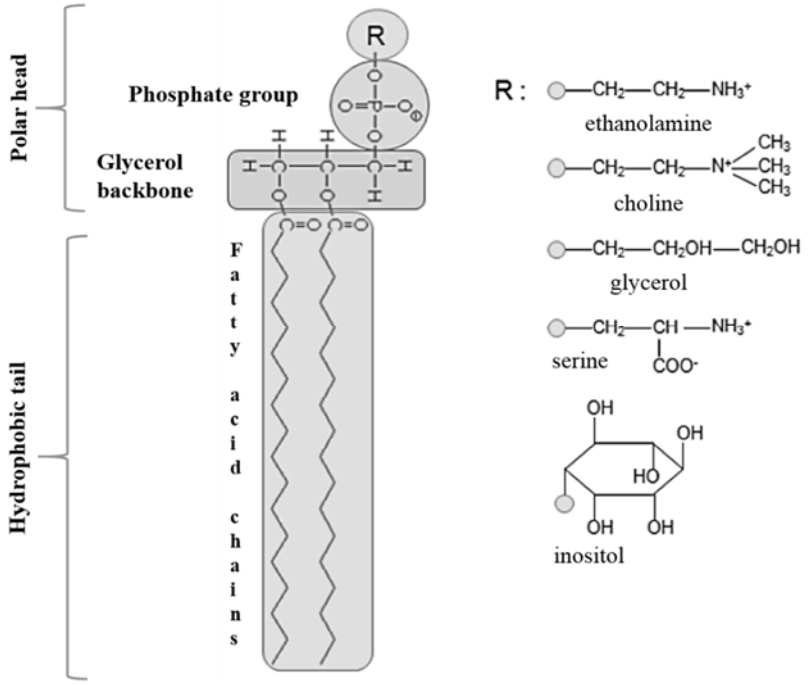


Figure 1-5. A common structure of a phosphoglyceride with two fatty acid chains, a glycerol backbone, a phosphate and a polar alcohol group R (modified from [38]).

Due to these hydrophilic head groups that form favorable electrostatic interactions with water molecules, phospholipids are able to aggregate into different energetically advantageous structures such as micelles, vesicles and bilayers, in which the hydrocarbon chains are sheltered from water and attracted to each other by Van der Waals forces. Each distinct head group contribute to the overall default shape of the phospholipid, such as the cylindrical molecular geometry of PC, and therefore different phospholipids have tendencies to form various different membrane structures [11, 31]. The different phospholipid shapes and their corresponding membrane structures are shown in figure 1-6. Certain lipid molecules, such as PEs, possess an overall conical shape and have therefore a tendency to form structures with negative curvatures [31]. PC and PE both have a dipole moment across their head groups which are able to orientate by the electrochemical potential of the membrane. However, the head group of PE is smaller than that of PC, resulting PE to prefer inverted non-bilayer curvature structures [27, 28]. Concerning vesicle formation and other specific structures, PC has more desirable physical properties in solution and is therefore the usual choice of preference for *in vitro* studies. The curvature of phospholipid leaflets can be altered by changing the lipid composition of the leaflet.

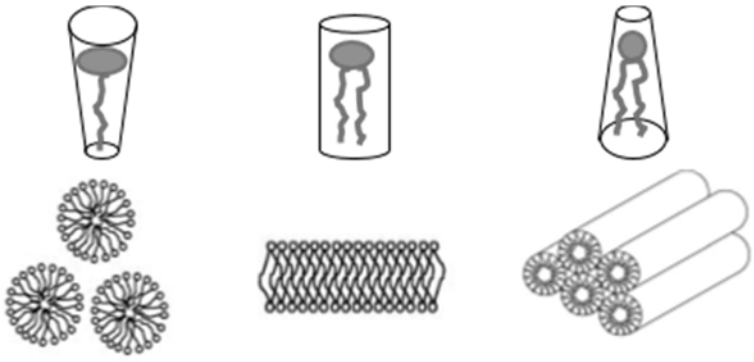


Figure 1-6. Shapes and corresponding membrane structures adopted by different phospholipids (modified from [31]).

1.1.3.2 Physical states of membrane phospholipids

Biological membranes are dynamic structures and an important characteristic of the phospholipid bilayer is its ability to maintain movement within the membrane. Lipid bilayers can exist in distinct phases regarding to the physical states of their constituting lipids. These states are dependent on various physico-chemical parameters such as the pH, the temperature and the nature of the lipid itself. Phase transition, also known as the order-disorder transition, is a temperature-dependent

change of state of the acyl moieties of membrane phospholipids from a solid (gel-like, s_o) to a fluid phase, and can be seen as a sharp transition between the gel and fluid phase for purified phospholipids [39, 40]. At temperatures below the phase transition, the fatty acyl chains of the phospholipids are in a tightly packed hexagonal array, and the order parameter (S) of a segment of the acyl chain is high but the translational diffusion coefficient (D_T) is slow (10^{-3} μm^2 s^{-1}) [11]. At this phase, the chains are in an all-*trans*-conformation [41]. Once the phase transition has taken place, the chains are in fluid phase and contain *gauche* conformers, the array is more random and the D_T is faster (1 μm^2 s^{-1}). The temperature at the midpoint of the transition (T_t) as well as the temperature range between the beginning and completion of the transition (Δt) are both dependent on the fatty acyl content as well as the polar head group composition of the phospholipid. Certain rules do apply for the relation between fatty acid composition and transition properties and some of them are listed below [40]:

I) The T_t of lipids containing saturated fatty acids is higher than those containing *cis* monosaturated fatty acids.

II) The T_t of lipids with a homologous fatty acid substitution is directly dependent on chain length.

III) Lipids that contain *trans* unsaturated fatty acids possess a higher T_t than those with homologous *cis* unsaturated derivatives.

The clear separation of the fluid and the gel phase has been well described by model membranes, however, it only exists in biological membranes of exceptional cases [42]. Most glycerophospholipid membranes have unsaturated hydrocarbon chains leading these biomembranes often to be rich in lipid fluid phases [11]. Above the T_t, the fluid phase can either be a liquid-ordered (l_o) or liquid-disordered (l_d) phase. The l_d phase lipids have a large mobility rotationally as well as laterally, leading the order parameter S to be low, whereas the lipids in the l_o phase are densely packed and highly ordered with a reduced mobility, possessing a high order parameter, yet fast translational diffusion coefficient [11, 39]. The lipids of the l_o phase therefore have intermediate properties of the gel and the l_d phase lipids. A phase separation between the different fluid phases of model membranes containing binary mixtures of lipids with saturated hydrocarbon chains and cholesterol has been reported by many authors [43-45]. It has been described that this phase separation increases with increasing amount of cholesterol in the membrane [42]. Different membrane phases of phospholipid bilayers are presented in figure 1-7.

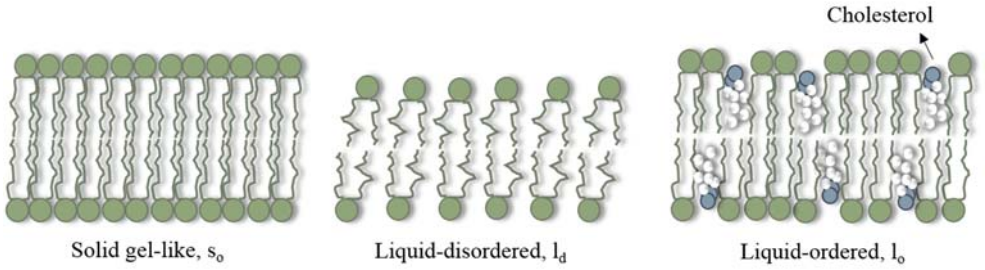


Figure 1-7. Different membrane phases of phospholipid bilayers; solid gel-like (s_o), liquid-disordered (l_d) and liquid-ordered (l_o) containing cholesterol (drawn based on [11]).

In addition to the gel and fluid phases, certain lipids such as the PCs are able to form an intermediate phase between the temperature range of the two conventional phases mentioned [46]. This phase, the ripple phase (P_β), is characterized by periodic ripples of 10-30 nm, formed by local spontaneous curvatures in the bilayer structure [46, 47].

These different physical states of membrane lipids are important to understand the phenomenon of phase separation that naturally occurs in biological membranes and are also the basis of multiple techniques used to characterize model membranes of phospholipids, such as the atomic force microscopy imaging. Leidy *et al.* [48] have imaged different lipid phases with AFM and a part of their work is illustrated in Figure 1-8, showing clear ripple phases at a l_o/l_d phase coexistence of (1:1) 1,2-dimyristoyl-*sn*-glycero-3-phosphocholine (DMPC) and 1,2-distearoyl-*sn*-glycero-3-phosphocholine (DSPC) double bilayers.

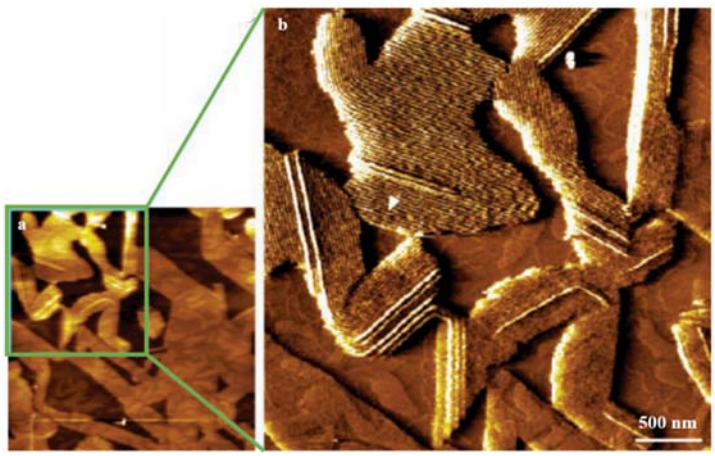


Figure 1-8. Ripples in a l_o/l_d phase coexistence of a (1:1) DMPC/DSPC double bilayer. **a)** Height mode AFM image at 32.5 °C. **b)** Deflection mode zoom of a, showing ripples in the l_o phase domain (white arrow) [48].

1.1.4. Lipopolysaccharides

Lipopolysaccharides (LPS) are amphiphilic molecules found from the outer leaflet of Gram-negative bacteria outer membrane. The LPS molecule consists of three covalently linked parts. The membrane-most part is a diglucosamine phosphate with 5 to 6 attached fatty acyl chains, called lipid A, which anchors the LPS into the outer membrane of the bacteria. The second moiety, a core oligosaccharide, can be further distinguished into inner and outer parts. The inner part is composed of sugars, 3-deoxy-D-manno-octulsonic acid (Kdo) and L-glycero-D-manno-heptose (Hep) whereas sugars such as hexoses and hexoamines are the main components of the outer core region. The third, a polysaccharide known as O-antigen, is followed by this non-repeating core oligosaccharide [49-51]. The O-antigen is a polysaccharide with repeating oligosaccharide units of 3-6 sugars, mainly tri to –pentasaccharides, stretching outward of the bacterial cell surface [52]. The O-antigen part varies tremendously within and between bacterial species; *Escherichia coli* (*E. coli)* for instance is found to have 173 different types of O-antigens on its outer membrane [52]. Figure 1-9 illustrates the common structure and variability of LPS molecules.

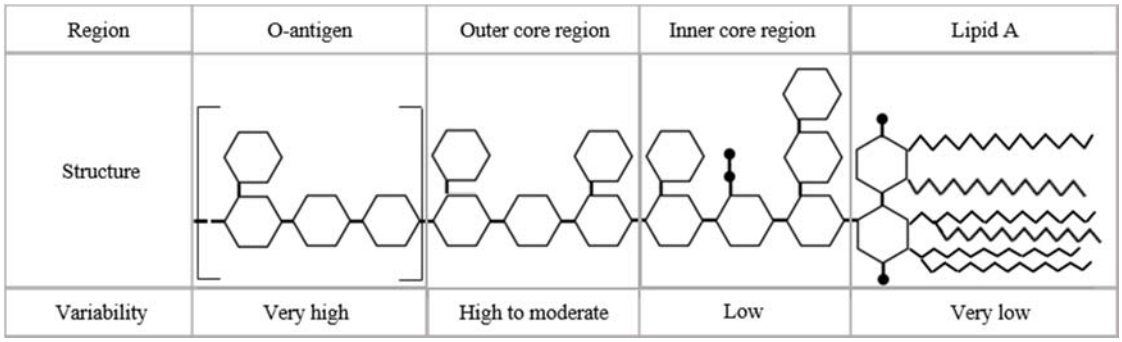


Figure 1-9. Common structure with different regions and variability of LPS molecules (modified from [53]).

LPS molecules having an O-antigen at the very end of their structure are referred to as smooth type (LPS-S) whereas LPS molecules lacking this O-antigen region are named as rough type LPS (LPS-Re). Such names are derived from the morphology differences of bacterial colonies expressing these molecules; colonies lacking the O-antigen region in their bacterial cell membrane are morphologically rougher than colonies of bacteria with LPS containing the O-antigen [54].

The importance of LPS properties and structure can be featured by the fact that the LPS containing repeated O-antigens in smooth *Salmonella typhimurium* provide the bacteria with a more efficient

barrier towards membrane disrupting molecules than for instance the LPS found in rough *E. coli* [55].

1.2. From a single bacterium to bacterial biofilms

Bacteria are classified by levels, divided into families, which are subdivided into genera and species. Bacteria vary from one to another by their shape, size and structure, despite the rigid cell wall that helps bacteria to keep their shape. Among the large variety of shapes and structures exhibited by bacteria are spherical (coccus), rod-shaped (bacillus) and spiral (vibrio), which can be grouped as clusters (staphylo), chains (strepto) or pairs (diplo). The diversity of bacterial form and structure are shown in figure 1-10. The form of a bacterium is an important physiological character in bacterial adaptation and bacteria modify actively their shapes along their life cycle [56].

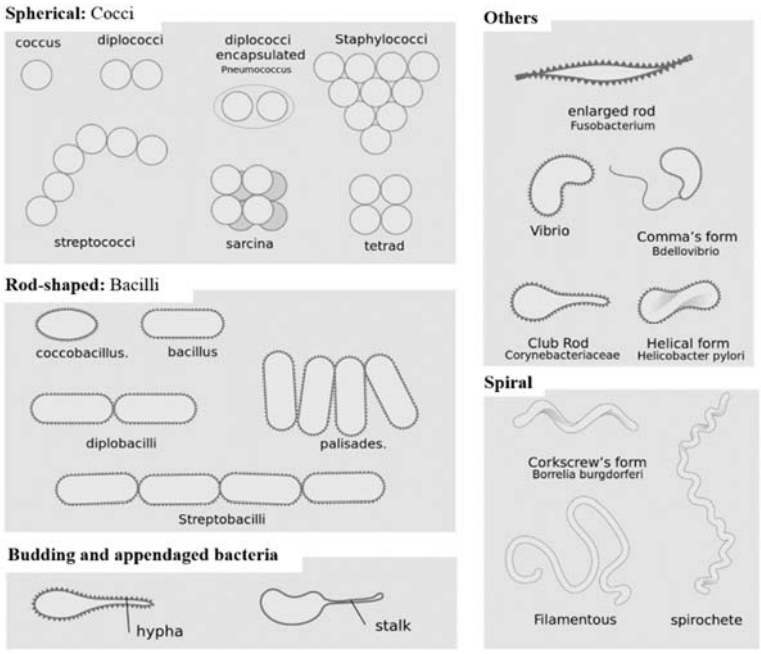


Figure 1-10. Scheme illustrating the different forms and structures adopted by bacteria (modified from [57]).

Generally, a bacterium consists of a wall, a cytoplasm, a single chromosome and various organelles, such as ribosomes and plasmids (figure 1-11). Some structures such as pili and flagella extend from the bacteria surface. Pili, consisting of hundreds of pilins, help the bacteria in the exchange of genetic material, are known as virulence factors and identified as adhesive organelles [58]. Fimbriae

are short pili that aid the attachment of the bacteria onto a surface and are therefore crucial in biofilm formation. Flagella that are identified as locomotion organelles [59], help the bacteria to swim. Moreover, certain bacteria have an additional protection covering their cell wall; a jelly-like capsule composed of polysaccharides. The capsules are known to play an important role in protecting bacteria against dehydration, phagocytosis [60], antimicrobial peptides (AMPs) [61] and other microorganisms. The capsule is also a major virulence factor among the most pathogenic bacteria, such as certain strains of *E. coli* and *Streptococcus pneumoniae*.

In nature, single cell organisms are likely to form sessile communities adhered on solid surfaces. These kinds of surface associated communities enable microbes to idle in a favorable microenvironment

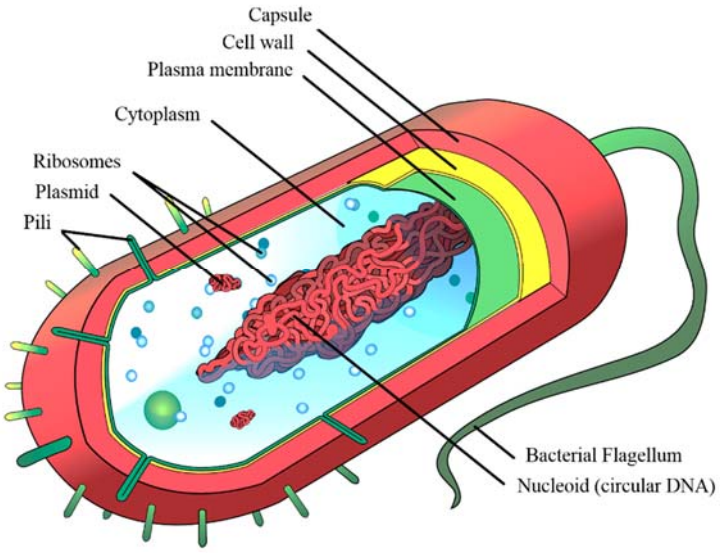


Figure 1-11. General structure of a bacteria with its genetic material floating in the cytoplasm bounded by the bacterial cell wall to which several external structures such as pili and flagella are attached.

rather than being in planktonic, freely floating conditions [62]. This friendly microenvironment consists of self-produced extracellular matrix in which the bacteria are embedded [63]. There are several reasons why micro-organisms prefer to reside on solid surfaces; the surface could provide a source of nutrients for the microbes, the current of liquids serve fresh nutrients and oxygen continuously and the removal of waste material is up scaled due to flow of water [64].

In the seventeenth century, a Dutch scientist, Antonie van Leeuwenhoek, was the first to describe what was later known as a “biofilm”, by examining the plaque on his teeth, naming it the

“animalcule”. However, the concept of biofilms was developed only years afterwards, when Claude Zobell realized in 1943 that organic content has a tendency to concentrate on solid surfaces by adsorption, and preferentially grow attached on these surfaces [65]. It was in 1978 when Costerton *et al.* described and defined the term “biofilm” [66], which Donlan *et al.* updated in 2002 as follows; “—biofilm is a microbially derived sessile community characterized by cells that are irreversibly attached to a substratum or interface or to each other, embedded in a matrix of extracellular polymeric substances that they have produced, and exhibit an altered phenotype with respect to growth rate and gene transcription” [67]. An extensive amount of research has ever since been conducted with bacterial biofilms; it has been revealed that sessile bacteria represent 99.9% of the bacterial population in aqueous media and that bacteria within a biofilm hold very different properties than bacteria in planktonic cultures [66, 67]. One of the differences in the properties of planktonic and biofilm bacteria is their resistance towards antimicrobial agents. Bacterial biofilms can indeed be even 10-1000 times more resistant to antimicrobial agents than their planktonic counterparts [68]. Several possible explanations for such an increased resistance has been suggested; 1. A slow or completely failed penetration of the antibiotic beyond the surface of the biofilm, 2. Development of antimicrobial resistance in several bacteria of the biofilm and 3. Antagonized antimicrobial action due to altered micro environment in which nutrient depletion and/or waste product accumulation can cause the bacteria to be in a non-growing state [69]. It has also been suggested that the reduced susceptibility toward antimicrobial agents of a biofilm could be influenced by the altered cellular growth rate and the repression or induction of gene expression within the micro-organisms in a sessile form [63].

Bacteria, fungi and algae, are able to create biofilms on almost any type of surfaces in aqueous conditions [67, 70-72]. Herein, we concentrate on homogenous biofilms formed by a single species of bacteria and describe the formation of such biofilms.

Bacterial biofilm formation can be seen as a five step process. The first step of this process is the reversible attachment of planktonic bacteria onto a surface. When this attachment becomes irreversible due to production of extracellular polymeric substances (EPS) by the organism, a proliferation and accumulation of bacteria on the surface occur [73]. At this stage the bacteria can no longer be removed from the surface by gentle rinsing. The microbes start forming organized film structures that become more and more mature [72]. Finally, the bacteria disperse from these colonies to form further biofilm colonies elsewhere on the surface [74]. The five step biofilm formation process is described in figure 1-12.

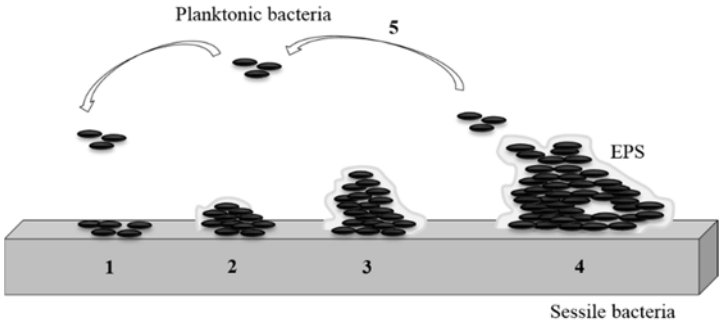


Figure 1-12. Five steps of the development of a bacterial biofilm. **Stage 1**: Reversible adhesion on the substrate surface; **stage 2:** Irreversible adhesion and production of extracellular polymeric substance (EPS) matrix; **stage 3:** Maturation and early development of biofilm architecture; **stage 4:** Maturation of biofilm architecture; **stage 5:** Dispersion of bacterial cells from the biofilm (drawn based on [67, 73, 74]).

1.3. Antimicrobial peptides

Micro-organisms battle endlessly against harmful microbes. The important increase of drug-resistant bacteria and the lack of new antibiotics to combat them have presented a serious challenge to antimicrobial therapies [75-79]. Reported toxicity of certain antimicrobial agents on mammalian cells is a cause that decelerates the antimicrobial drug approval. The emergence and the development of new antimicrobial molecules such as AMPs are considered as an alternative to conventional antibiotics since they are not specific, and they are less susceptible to give rise to bacterial resistance [80]. AMPs have been found to perform effectively in synergy together with conventional antibiotics against multidrug-resistant bacteria [81]. AMPs are components of the immune system providing protection against such pathogens. AMPs have been present in organisms throughout evolution and AMPs of natural origin, effective against various different microbes such as bacteria, fungi as well as enveloped viruses, have been extracted from multiple biological sources including mammals, amphibians and plants [82]. AMPs including cecropins and magainins were first found in frogs and insects in 1980s and ever since 1200 of them have been isolated [83]. AMPs exist in vast amounts of different structures and amino acid sequences and so their classification can be difficult. Yet two large groups can be identified; AMPs with a linear structure, forming α-helical amphipathic conformations and those with cyclic peptide structures [84]. However, AMPs do possess many similarities, among them the fact that their target of action is often the lipid bilayer of the cell membrane. Additionally, many AMPs have a positive net charge, explaining their tendency to specifically target the globally negatively charged bacterial membranes [85]. The ability of

AMPs to penetrate cell membranes rely on several distinguished methods such as the self-promoted uptake model [86]. A widely used model referred to as Shai-Matsuzaki-Huang model, explains the initial interactions taking place between membrane lipids and antimicrobial peptides [87, 88]. It is believed that the peptide is in an unstructured state in solution prior to interaction with the phospholipid membrane, but changes its three-dimensional structure, such as α-helix or β-sheet, once in interaction with the membrane lipids [89]. The positively charged peptide integrates into the outermost layer of the phospholipid membrane and as a consequence, the outer leaflet becomes thinner [90], initiating the peptide to form channels through the phospholipid double layer. The channel formation taking place after the initialization steps can either occur by a mechanism called "carpet" mechanism, toroidal pore formation or by a mechanism called the Barrel-Stave model [87, 91, 92].

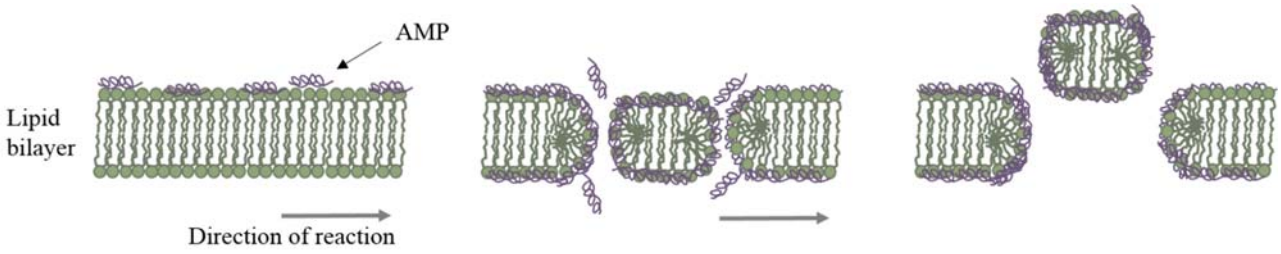


Figure 1-13. A scheme of the carpet-like mechanism of antimicrobial peptide action on lipid bilayer (drawn based on [87, 89, 93]).

In the carpet model (figure 1-13), eventually leading to toroidal pore formation [86], the peptides are to a lesser extend in interaction with the hydrophobic core of the membrane lipids, where as in the Barrel-Stave model the hydrophobic surfaces of the peptide interact with the core of the lipid membrane (figure 1-14a). In toroidal pore formation (figure 1-14b) the peptides are always associated with head groups of the phospholipids even while situated perpendicularly within the lipid bilayer [87, 91]. This causes the lipid bilayer to bend from the outer leaflet towards the inner one so that the pore becomes boarded by the peptide and the lipid head groups.

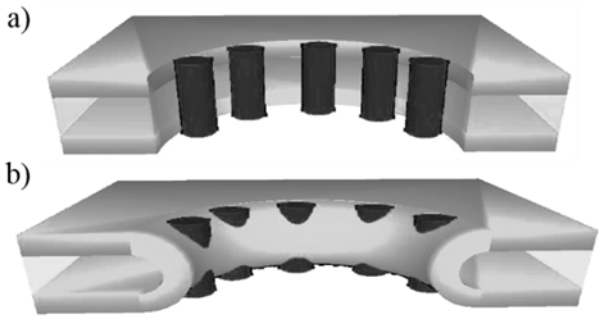


Figure 1-14. Pore formation mechanisms of peptides in lipid bilayers. **a)** Barrel-Stave mechanism **b)** toroidal pore formation (drawn based on [91]).

Here we describe two antimicrobial agents, a cyclic peptide, colistin (polymyxin E) and a linear one, catestatin, as denoted CAT.

1.3.1. Polymyxins

Polymyxin B and polymyxin E are secondary metabolite nonribosomal cyclic lipopeptides that are produced by the soil bacterium *Basillus polymyxa*. They share the same primary sequence with five positive charges due to L-α,γ-diaminobutyric acid. The only difference between these two polymyxines is at position 6, which is occupied by D-Phe in polymyxine B and D-Leu in polymyxin E [94]. Colistin (polymyxin E, figure 1-15) is known for its antibacterial effects. Although discovered in 1949, the use of colistin has been limited due to concerns of its nephro- and neurotoxicity [95, 96]. However, polymyxins are especially renowned for their potential against multi-resistant Gram-negative bacteria such as *Pseudomonas aeruginosa*, *Acinetobacter baumannii* and *Klebsiella pneumoniae*, in which the antimicrobial action of polymyxins is directed against the external leaflet of the cell membrane [97-101]. More specifically, the mechanism of action of polymyxins is suggested to be targeted to the lipopolysaccharides (LPS) of the external bilayer, causing deformities in the outer cell membrane of the pathogen [102]. Due to the peptide cationic moiety also present in colistin molecule, polymyxins interact with negatively charged components of the pathogen cell membrane. These electrostatic interactions are an important contribution to the polymyxin mechanism of action [103]. Colistin being studied to a smaller extend on a molecular scale, it has however been shown for polymyxin B that this peptide interacts with the LPS and lipid A parts as well as with negatively charged phospholipids of the bacterial cell membrane [104-107]. The suggested mechanism of polymyxin antimicrobial action is relying on the self-promoted uptake model, in which a polycationic peptide binds to the Mg^{2+} binding site of the LPS molecule,

displacing the Mg^{2+} ion and leading to the disturbance of the stabilizing effect of the Mg^{2+}. This stabilizing effect of the Mg^{2+} on the LPS is due to cross-bridging in the outer membrane. It has been shown that a fluorescent derivative of polymyxin B, dansyl-polymyxin has multiple different binding sites in the LPS molecule (in its negatively charged parts) and one of these is the Mg^{2+} binding site [104]. Although studies have been conducted with polymyxin B, the exact mechanism of action of polymyxin E on a molecular level remains rather unclear and the causes of the reported toxicity of colistin on eukaryotic cells should be further studied. Therefore the interactions of colistin with eukaryotic cell phospholipids is of interest.

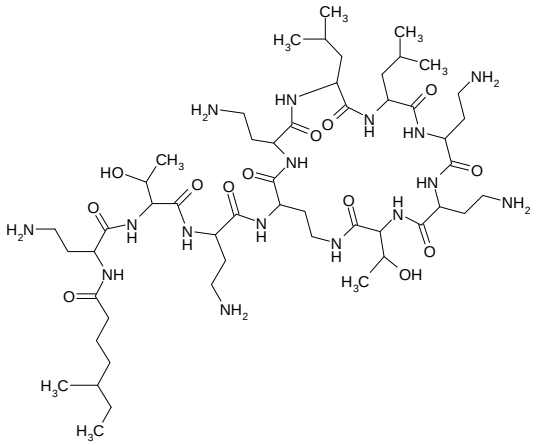


Figure 1-15. Chemical structure of colistin (polymyxin E) [108].

1.3.2. Bovine Catestatin

Chromogranin A (CgA) is an acidic protein (48 kDa) expressed by the endocrine system, first identified in the adrenal medulla [109]. After its expression, CgA is subjected to proteolytic cleavages resulting in various biologically active peptides [110]. One of these cleavages, catestatin, is a linear 21 amino acid peptide with a net charge of +5, which has fairly recently shown antimicrobial activity for instance on human skin [111, 112]. The amino acid sequence of bovine catestatin (bCAT, figure 1-16) is as follows: RSMRLSFRARGYGFRGPGLQL (see annex 2 for amino acid letter codes and pK_a values). The first 15 amino acids of the bCAT peptide sequence are active against bacteria [113]. The positive charges in this sequence are not placed at regular intervals, implying that even in the proximity of an anionic membrane, the peptide would not form amphipatic structures [114]. Supposedly, the peptide does not cause destruction of the membrane, but instead increases membrane permeability by inducing phase separation and phase boundary defects through which it finds its passage across the membrane [113]. Nevertheless, the

antimicrobial activity of this peptide being recently discovered, we chose to study this natural, linear AMP to compare it with a more conventional cyclic colistin.

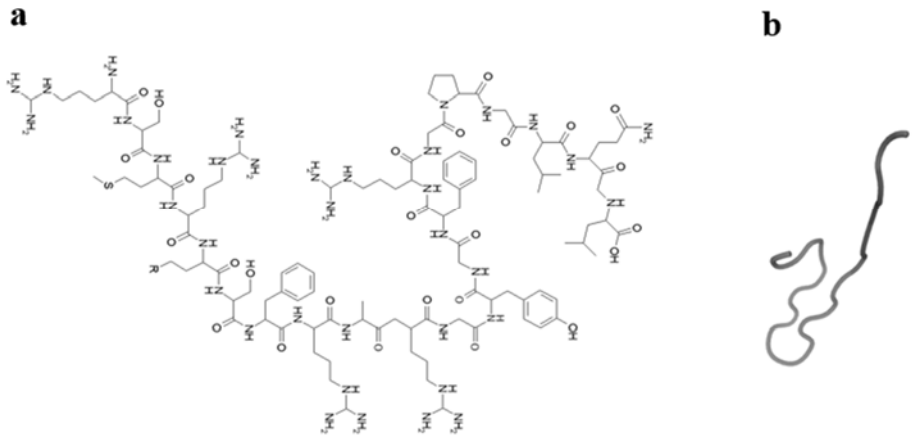


Figure 1-16. a) bCAT chemical structure **b)** bCAT in a 'random coil' secondary structure.

1.4 Application of lipid membrane and bacterial biofilm models on peptide studies

A major challenge when studying biological systems at the nanoscale, is the manipulation, correct arrangement and careful investigation of the biomimetic structures on a molecular level. This generally requires fabrication and organization of the biological molecules in two- or three dimensional spaces, leading to the need of special techniques and methods to obtain such structures. Herein we describe some techniques and applications used to study biological systems, from the nanoscale investigation of lipid model membranes to the physico-chemical characterization of more complex biological structures, biofilms.

1.4.1 Langmuir monolayers

The first scientific paper on oil films was written in 1774 by B. Franklin and it was only in 1878 when J. Gibbs described the thermodynamic analysis of adsoption. A couple of decades later, in 1891, Agnes Pockels demonstrated how to manipulate oil films by using barriers, but finally in 1917 the theoretical and still accepted concepts of insoluble monolayers saw the light after work conducted by Irwing Langmuir [115]. The work conducted by Langmuir brought him a Nobel Prize of chemistry in 1932. Monolayers of phospholipids were used in the first experiments in history to mimic biological membranes. A phospholipid monolayer spread at the air-water interface can be

considered to resemble half of a biomembrane and therefore it can be used as a simplified model of biological membranes [116]. Lipid monolayers at air-water interface are an advantageous method as their nature, surface density and packing of the monolayer material as well as the composition, pH and temperature of the subphase can be defined in a controlled manner [117, 118]. Indeed, many scientists still use this method to examine simple, one leaflet models of phospholipid membranes, their physico-chemical characteristics as well as their interactions with exogenous compounds. Langmuir monolayers of phospholipids deposited at the air-water interface have in particular been descriptive as models for examining the organization and interactions of AMPs on membranes [119]. The physical and morphological analyses of membrane-peptide interactions have been conducted by various techniques including thermodynamic methods by pressure-area isotherms [103, 120, 121] and electric surface potential [120], as well as with microscopic techniques such as Brewster angle microscopy [122, 123] and fluorescence microscopy [122, 124], revealing lipid domain structures at a μm scale. By these means, it is possible to obtain quantitative information on the impact of the peptide on the structure and stability as well as penetration kinetics and affinity onto the phospholipid monolayer. As an example, Volinsky *et al.* studied the surface pressure-area isotherms as well as the interactions of different antimicrobial peptides including alamethicin, gramicidin and valinomycin, with phospholipid monolayers, [119]. Their studies on phospholipid monolayers were completed with morphological examination of the membranes with the aid of BAM. When BAM is used on top of a Langmuir trough, it allows the visualization of monolayer organization, segregation and anisotropy. In the studies of Volinsky *et al.* BAM provided images of formed peptide aggregates and showed their distribution within DMPC phospholipid films, supporting the results obtained by surface pressure measurements [119]. For instance valinomycin was found to be most likely phase-separated in the DMPC monolayer, whereas gramicidin was confirmed to be immiscible within the phospholipid film [119].

1.4.2 Atomic force microscopy

The first Atomic Force Microscope (AFM) was developed by Gerd Binnig, Calvin Quate and Christopher Gerber in 1986 [125]. Their work was based on a previous technology, Scanning Tunneling Microscope (STM) that had been invented in 1981 by Binnig *et al.* [126], who later received a Nobel Prize in Physics for their invention. Being high in resolution and a sensitive imaging technique at an atomic scale, STM showed potential and interest particularly for biological samples as it could be used in conditions closely resembling those of biological systems. However,

the technique was not optimal for such applications due to the poor conductivity of most biological samples [127]. AFM having no limitations in the conductivity of the specimen, answered the needs required by imaging of biological samples at an atomic or near atomic scale. The first AFMs were operating with contact mode [125, 128], which unfortunately again caused difficulties for biological samples that are often soft and weakly attached to their support, easily being damaged by the AFM probe scanning the sample surface. Determined to overcome the challenges faced with biological samples, scientists continued the development of high resolution systems for imaging and in 1987 Martin *et al.* [129] introduced an AFM which used a non-contact mode. In this system the AFM cantilever oscillated near to its resonant frequency just 1-10 nm above the sample surface, maintaining a constant separation during scanning [129]. In 1994 Lee *et al.* [130] used for the first time the force spectroscopy technique of AFM in a biological application, measuring forces between two complementary strands of deoxyribonucleic acid (DNA). As of today, AFM is a largely used and accepted imaging and force spectroscopy technique in the field of biology and biologically inspired systems and AFM imaging speeds have developed rapidly within the last decade [131, 132].

AFM can be used to detect topographic changes of a sample within the nanometer scale and therefore one suitable application for this technique is the studies performed on lipid bilayers, their structure and changes in morphology for instance due to exogenous compounds. Due to the different phases in which DPPC (T_t = 41°C) and DOPC (T_t = -17°C) exist at room temperature, these two lipids form bilayers that are extensively studied and to which detailed protocols for AFM experiments have been reported [133]. A large variety of antimicrobial peptides and their interactions with model lipid bilayers have been studied with AFM together with different complementary techniques. Shaw *et al.* reported concentration dependent indolicidin activity on various phospholipid bilayer compositions using *in situ* AFM imaging [134], whereas Domenech *et al.* found a relation between oritavancin action and lipid bilayer composition on the permeability and membrane lipid organization via similar methods [135]. Francius *et al*. used real time AFM imaging to study the effects of geometry, charge and hydrophobicity of different surfactins on their activity on DPPC/DOPC bilayers [136]. Tong *et al.* reported their work which they conducted on supported LPS bilayers on bare mica and mica coated with polyethylenimine (PEI) and showed that bilayer structures can be obtained also with LPS molecules [137]. They found a better LPS bilayer coverage for the PEI coated mica surface than for a bare mica surface [137]. AFM is not only useful for real-time visualization of phenomena happening within lipid bilayers, but can also provide interesting information on bilayer nanomechanics via force spectroscopy [138-140].

The application of AFM as a tool to examine biofilm formation has recently shown increasing interest [70]. AFM has been proven to be effective also in the close examination of single bacteria as well as bacterial biofilm properties such as surface roughness, elasticity and bacteria size, and changes in these properties due to the influence of several antibacterial agents have been investigated with different bacteria [63, 141, 142]. Meincken *et al.* were first to visually demonstrate the effect of two antimicrobial peptides, magainin 2 and PGLa, on the cell envelopes of living *E. coli* cells [141]. However, some constraints in the AFM imaging of bacterial cells do exist, mainly due to the dehydration step that is needed in order to get high resolution images of the bacteria samples [142, 143]. The dehydration of the bacteria could affect the bacterial properties [144] and has to be taken into serious consideration when analyzing obtained data.

Force spectroscopy provides valuable information about the elastic properties of cell surfaces, described by a physical quantity named as Young modulus [145]. According to literature, the typical values of the Young modulus obtained for living bacteria cells have been in the order of magnitude of mega pascals [146, 147]. Mularski *et al.* investigated the effect of a melittin derivative (P14K) on the stiffness of *Klebsiella pneumoniae* cell wall, and found that the peptide caused an initial increase in the Young's modulus, finally leading to a decrease of the cell wall stiffness, suggesting drastic changes in the cell morphology [142]. Similar results have been obtained by da Silva Jr. *et al.* [148], who showed a loss in the stiffness of membrane elasticity of *E. coli* in the presence of an antimicrobial peptide, PGLa. Furthermore, Quilès *et al.* investigated the effects of different concentrations of dermaseptin S4 on the morphology and nanomechanical properties of a *Pseudomonas fluorescens* biofilm by using AFM imaging and force spectra [63].

1.4.3 Attenuated total reflection Fourier transform infrared spectroscopy (ATR-FTIR)

Infrared (IR) spectroscopy is a non-destructive and non-invasive technique used to gain information on the molecular composition as well as the structure and interactions within a sample, including lipid bilayers and bacterial biofilms. The technique is based on the measuring of vibrational energy levels associated with different chemical bonds within the specimen, with each sample having a unique spectral fingerprint. Because the depth of penetration (d_p) of the evanescent wave produced in attenuated total reflection (ATR) spectroscopy is only in the order of a few hundred nanometers, even thin samples such as lipid membranes and bacterial biofilms are thick enough to absorb the electromagnetic radiation of the evanescent wave and therefore the ATR mode of Fourier transform infrared (FTIR) spectroscopy is a highly surface-sensitive technique [149]. When combined with

polarized light, ATR-FTIR spectroscopy also enables the determination of molecular orientation of the sample molecules with respect to the normal of the sample surface, such as the tilt angle of the hydrocarbon chains of phospholipids [150]. Furthermore, the absorption of molecules in the bulk solution, such as water, is reduced in the ATR mode of FTIR spectroscopy [149]. This being said, ATR-FTIR is a very suitable technique for the studies of different interfacial phenomena, notably the interactions between biological systems and peptides, without the need to introduce disturbing external probes into the setup [150].

As a relatively inexpensive technique, FTIR spectroscopy has been used to reveal multiple structural properties of lipid membranes, including their conformation, orientation, phase transition and separation [149, 151]. In addition, ATR-FTIR spectroscopy permits the orientation of the sample directly on the ATR crystal and the sample can be kept in aqueous conditions throughout the experiment [152]. ATR-FTIR technique allows the detection of methylene stretching region of the infrared spectrum at 2800-3000 cm^{-1}, which is a good indicator of the lipid hydrocarbon chain conformational disorder, as the *gauche* conformer hydrocarbon chains of lipids in l_d phase absorb IR radiation at higher frequencies than those of the lipids in the s_o phase having their hydrocarbon chains in all-*trans*-conformation [153]. This enables the monitoring of lipid phase transitions, whether due to temperature change or due to exogenous compounds such as peptides. Furthermore, polarized FTIR spectroscopy can be used to reveal the orientation of lipid molecules on solid substrates as the absorption of the IR radiation depends on the angle between the transition moment of a given vibration and the polarization of the incident radiation [152]. This molecular orientation can be determined by the measurement of a dichroic ratio R, calculated from the absorption coefficients of parallel and perpendicularly polarized light [154]. The stretching vibrations of carbonyl groups (C=O) of phospholipid ester bonds at 1750-1700 cm^{-1} are also sensible to various changes such as hydrogen bonding, and are therefore of interest [155]. In addition to the data obtained from the methylene and C=O stretching regions of the IR spectrum, the IR spectral region of the phospholipid polar head and its functional groups, especially the phosphate vibrational bands at 1300-1000 cm^{-1} can be studied. Brandenburg *et al.* examined the order parameters and phase behavior of ordered multilayers of phospholipids, and showed that the functional groups of the polar head regions contribute to the s_o-l_d phase transition of the hydrocarbon chains [156]. As of phospholipid-peptide interactions, Correa *et al.* analyzed changes in the head group region of hydrated DMPC under the influence of two positively charged synthetic peptides, Gm1 and ΔGm1, and for both cases found a shift of the asymmetric C-O-PO_2 band at 1036 cm^{-1} towards higher wavelengths, indicating sterical changes in the head group region [157].

Furthermore, Frey *et al.* used ATR-IR spectroscopy to determine the order parameter of melittin attached to fully hydrated single supported planar bilayers and reported that orientation of the peptide was parallel to the plane of the bilayer [158]. Among these mentioned IR absorption bands, other characteristic phospholipid IR bands and their wavelengths are shown in Table 1-1.

It has been observed since over 50 years ago, that different bacteria show different IR spectra, making IR spectroscopy applicable also in the field of microbiology [159]. ATR-FTIR is a suitable and non-invasive technique for the characterization and real-time dynamic follow-up of bacterial biofilm formation in aqueous *in situ* conditions, and it has been especially used to study the first stages of a biofilm formation and the accumulation of biomass on the ATR crystal [159, 160]. Delille *et al.* [161] investigated the accumulation of biomass onto an ATR crystal by monitoring the spectral evolution of IR bands assigned for proteins (amide I, II and III bands), nucleic acids (1240 and 1085 cm^{-1}) and polysaccharides (1150-900 cm^{-1}), within time. The major IR absorption bands assigned for *Pseudomonas* strain of bacteria are shown in table 1-2.

Table 1-1. Major infrared absorption bands of a membrane lipids [41, 149, 155].

Wavenumber (cm^{-1})	Assignment
2956-2957	CH_3 stretching, asymmetric
2918-2926	CH_2 stretching, asymmetric
2870-2871	CH_3 stretching, symmetric
2850-2854	CH_2 stretching, symmetric
1730-1734	C=O stretching, esters
1463-1473	CH_2 scissoring
1456-1460	CH_2 bending, asymmetric
1378-1380	CH_3 bending, symmetric
1228-1233	PO_2^- stretching, asymmetric
1170-1171	CO-O-C stretching, asymmetric
1085-1082	PO_2^- stretching, symmetric

Quilès *et al.* [160] however, studied the FTIR fingerprints of *P. fluorescens* and found that IR spectra could be used to detect significant metabolism changes within bacterial biofilms as a function of the changing environment. ATR-FTIR has been combined together with microscopic techniques to relate the chemical modifications observed by spectroscopic methods to structural modifications of the biofilm and Suci *et al.* [162] found, in their experimental conditions, a correlation between the Amide II band intensity and bacterial density on the crystal. Antimicrobial agents have also been investigated on bacterial biofilms with the aid of ATR-FTIR. In a previous study of theirs, Suci *et al.* [163] used ATR-FTIR to examine the penetration of ciprofloxacin into a *P. aeruginosa* biofilm and Quilès *et al.* [63] used the technique to study the influence of a dermaseptin S4 derivative on the early stages of *P. fluorescens* biofilm formation *in situ* and real time.

Table 1-2. The major IR absorption bands assigned for *pseudomonas* strain [160, 164].

Wavenumber (cm^{-1})	Vibration	Attribution
3300-3150	H-bonded OH groups, NH_2 stretching	adenine, quinine, cytosine
2960-2850	νC-H	fatty acids
1693-1627	νC=O, δN-H (Amide I), δH_2O	Proteins, water
1568-1531	δN-H, νC-N (Amide II)	Proteins
1467-1455	δCH_2, $\delta_a CH_3$	Lipids
1317; 1281	τCH_2, ρCH_2, νC-H, δN-H (Amide III)	Fatty acid chains, proteins
1238	$\nu_a PO_2$-	Phospholipids, LPS, nucleic acids
1200-900	νC-O, νC-C, δC-O-H, νC-O-C	Polysaccharides
1086	$\nu_s PO_2$-	Phospholipids, LPS, nucleic acids
1058	ν_sC-O-C, ν_sP-O-C,	Polysaccharides

1.5 Aim of this work

Since the last century, model membranes have been widely studied in order to better understand the structures and different phenomena happening at the interfaces of biological boundaries. However, biological membranes are much more complex systems than the model membranes examined in the literature, in which the membrane components are often restricted to only three or four lipids, whereas biological membranes are constituted of thousands [13], with membrane proteins embedded in the phospholipid bilayer leaflets. Such a simplification is crucial for the analysis of contribution of specific membrane structures, but it causes restrictions to the understanding of how these structures are influenced by the presence of each other. In addition, these model membranes do not have the complex network of a cytoskeleton which participates in multiple functions of the cell membrane.

In particular, monolayers presenting only a single leaflet of the phospholipid bilayer, are less suitable for transmembrane process studies, however they are convenient for mimicking processes at the surfaces of membranes [117]. Although bilayers are presenting a more complex membrane structure than monolayers, they can be influenced by the structure curvature of their constituting lipids as well as the support on which the SLBs are laying on [120]. On one hand, the solid support holding the SLBs could be assimilated as a “cytoskeleton”, on the other hand it would not provide the dynamic processes associated with the cytoskeleton of a cell.

Nevertheless, membrane models have provided valuable insight to specific lipid behavior and structure and are continuously used to explain lipid-peptide interactions.

As model lipid membranes have been under interest whilst explaining the mechanisms of action of AMPs, our approach is to use the above mentioned techniques in the characterization of model membranes, with the aim to better understand the underlying interactions between membranes and AMPs. However, keeping in mind the limitations of model membranes, we expanded the study to also concern living organisms. Therefore the methods and results obtained on peptide action on various lipid and LPS membranes are first described in this manuscript, followed by a study on the peptide action on bacterial biofilms. We have chosen to study two very different types of AMPs, colistin which is known to have neurotoxic side effects on mammalian cells although found decades ago, and a new generation AMP, bCAT, which has only recently been discovered. bCAT is potentially a good candidate for antimicrobial treatments as it is of natural origin in eukaryotes and therefore non-toxic for eukaryotic cells.

2. Materials and methods

All the chemicals used in this manuscript are gathered in table 2-1 with their suppliers, form of storage and storage temperature indicated.

Table 2-1. Chemicals used in this study with their suppliers and storage form and temperature indicated.

Chemical	Supplier	Form of storage	Storage temperature (°C)
1,2-Dioleoyl-sn-glycero-3-phosphocholine, DOPC, 99%	Sigma-Aldrich	$CHCl_3$ or TRIS solution	4
1,2-Dipalmitoyl-sn-glycero-3-phosphocholine, DPPC, 99%	Sigma-Aldrich	$CHCl_3$ or TRIS solution	4
1,2-Dipalmitoyl-sn-glycero-3-phosphoethanolamine, DPPE, 97%	Sigma-Aldrich	$CHCl_3$ or TRIS solution	4
Anhydrous calcium chloride, $CaCl_2$	Sigma-Aldrich	Powder	21
***Bac*Light™, 7012**	Life technologies	Diluded in H_2O	-20
Ampicillin	Sigma-Aldrich	100 g/L in 50 % EtOH	-20
Buffered Glycerol Saline,	ThermoFisher	-	21
Catestatine bovine, bCAT	ProteoGenix	H_2O or TRIS solution	-20
Chloroform, HPLC grade, 99.9%	Prolabo	-	21
Colistin sulfate	Sigma-Aldrich	H_2O or TRIS solution	-20
Deionized water	Millipore Corp., Milli-Q	-	21
Ethanol, 99.5%,	VWR International	-	21
Glycerol for molecular biology, 99%	Sigma-Aldrich	-	21
Kanamycin, ≥95%	Sigma-Aldrich	25 g/L in H_2O	-20
Lipid A	Avanti Polar Lipids	TRIS solution	4
LPSt, LPS extract from *Salmonella enterica* serotype Minnesota	Sigma-Aldrich	TRIS solution	4
LPS-S, LPS from *Salmonella abortus equi* S-form	Enzo Lifesciences	Diluded in H_2O	4
Lysogeny Broth, LB	Fluka	25 g/L (LB), 2.5 g/L (LB/10) in H_2O, pH 7.0	21
Mixed agar/LB powder	Sigma-Aldrich	35 g/L in H_2O, pH 7.0	21
NaCl	Sigma-Aldrich	Powder	21

Non-pyrogenic sterile water	B. Braun	-	21
Phosphate-buffered saline, PBS	Sigma-Aldrich	Diluded in H_2O	21
Polyethylenimine, PEI	Sigma-Aldrich	Diluded in H_2O, 0.1%	4
Trimethylamine, > 98.5%	Sigma-Aldrich	-	4
Tris(hydroxymethyl)amino-methane, Tris, 99.9%	Sigma-Aldrich	Diluded in H_2O	21

2.1. Preparation of phospholipid and lipopolysaccharide bilayers

There are several methods of preparing supported lipid bilayers. One of them is the vesicle fusion by which a droplet of suspension of unilamellar phospholipid vesicles is deposited on a solid substrate, such as the mica surface [165]. The vesicles spontaneously form bilayers after the adsorption on the solid substrate. Excessive vesicles are washed away and a symmetric phospholipid bilayer is obtained. Bilayer formation from vesicles require a sequence of events in which the formed vesicles are firstly adsorbed onto the solid substrate, ruptured and finally spread on the surface. For the two last steps to take place, the density of adsorbed particles must be high [166]. Due to electrostatic repulsive forces, it is challenging to prepare bilayers of negatively charged phospholipids by vesicle fusion without the use of divalent cations. Another method for preparing SLBs is the Langmuir-Blodgett (L-B) method developed by Katherine Blodgett (1935). In this method a monolayer is spread at the air-water interface in a Langmuir trough and a solid substrate is pulled through the monolayer from the subphase into air. The second layer can be obtained by dipping the solid substrate through the monolayer back into the subphase. Due to certain reported difficulties in the L-B technique of bilayer formation, such as the stripping of the first layer when dipping of the second occurs, the vesicle formation is a more common way for bilayer preparation [166] and also used for the bilayer studies of this manuscript.

For our bilayer studies, unilamellar liposomes of DPPC, DPPE and DOPC were prepared: the lipids were dissolved in chloroform and deposited on the wall of a rotating round bottom flask under a stream of nitrogen gas. The flasks were then kept under vacuum for 3 h to avoid traces of chloroform, and finally filled with 10 mL of TRIS-Ca buffer (10 mM Tris, 150 mM NaCl, 1 mM anhydrous $CaCl_2$, pH 7.4) to obtain a lipid suspension with a concentration of 1 mM. A sonication of 3 × 2 min was performed to detach the lipid aggregates from the edges of the flask into the buffer and to form the vesicles. The vesicle suspensions were then filtered through a syringe filter (200 nm) and stored at 4 °C until use (storage did not exceed 15 days). Lipid A solution (1 g/L) was prepared by dissolving lipid A powder (Avanti Polar Lipids, Alabaster, USA) into TRIS-Ca buffer containing 0.2 % trimethylamine and vortexing for 2 min. LPSt and LPS-S solutions (1 g/L) were

obtained by dissolving LPSt or LPS-S into TRIS-Ca buffer. Supported DPPC, DOPC, DPPC/DOPC (1:1, v/v), DPPE/DOPC (1:1, v/v), LipidA/LPSt (1:1, mol:mol) and LipidA/LPS-S (1:1, mol:mol) bilayers were then obtained by the vesicle fusion method [139]. The prepared suspensions of vesicles were let to spontaneously deposit onto the surface (65 °C pre-heated well-cleaved mica in an AFM closed fluid cell, or Ge crystal enclosed in a batch infrared cell) by incubating the vesicle solutions at 65 °C for 45 min. Lipid A/LPS vesicles were deposited on PEI coated mica (immersed in PEI solution for 12 h). Preheated (65 °C) TRIS buffer was then added into the cell, and the cell was gradually let to cool down to room temperature (21 °C) after which it was rinsed with TRIS buffer and used immediately for experiments.

2.2. Bacterial culture and formation of bacterial biofilms

2.2.1. *E. coli* bacterial strain

Escherichia coli (*E. coli)* is a small rod-shaped Gram negative bacteria of the *Enterobacteriaceae* family, first described by Theodor Escherich in 1885 [167]. *E. coli* is a facultative anaerobic bacteria naturally found in the intestines of vertebrae and these non-pathogenic strains are referred to as commensals [168]. Some strains of *E. coli* however are pathogenic, killing over 2 million humans each year due to intestinal and extraintestinal infections [169]. *E. coli* have long been in the fame of laboratory purposes as a lot of information of this bacterial species has already been reported [170]. *E. coli* grow well in nutrient media in laboratory conditions and one of its standard strains is the K12 strain, which has a well-known genome sequence [169-171]. The *E2146* strain used in this work was provided graciously by Professor Jean-Marc Ghigo from Institut Pasteur in Paris.

The *E. coli* used for the biofilms in this work is the *E2146* strain which has been modified from the K12 strain by Institut Pasteur in Paris, France. Due to the *gfpmut3* gene transfected into the genome of *E2146*, the strain is able to express green fluorescent protein (GFP) enabling the observation of the bacteria by epifluorescence microscopy without the need to use external staining. The *E2146* strain is resistant to ampicillin (Amp), kanamycine (Km), zeocin (Zeo) and chloramphenicol (Cm). *E2146* does express solely Type I *fimbriae*, anchored at the outer membrane of the bacteria, playing an important part in the biofilm formation [172]. The type 1 *fimbriae* consist of a fimbrilin protein that is anchored at the outer membrane of the bacteria and of a FimH adhesin protein situated at the end of the fimbrilin (figure 2-1). The type 1 *fimbriae* have a reported total length of 1-10 µm [172].

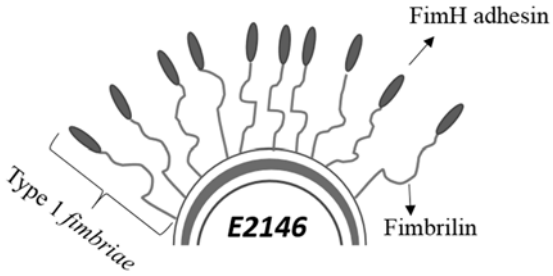


Figure 2-1. External structure of *E2146* with type 1 *fimbriae* (modified from [172])

2.2.2 Determination of minimal inhibitory concentration

The minimal inhibitory concentrations (MIC) of colistin and bCAT for the *E2146* strain were determined by broth microdilution. An overnight preculture of the *E2146* bacterial strain was diluted (OD_{600} = 0,001). 90 µL of the diluted culture was plated in 96-well plates in the presence of of bCAT or colistin at different concentrations. After 24 h of incubation, the micro-organism growth was assessed by optical density OD_{600} using a Multiskan™ EX microplate spectrophotometer (Thermo Fisher Scientific). The MIC, defined as the lowest concentration of drug able to inhibit 100 % of the inoculum, was determined from a modified Gompertz function as described elsewhere [173]. The MICs for bCAT and colistin were reported to be 60 µM and 0.87 µM respectively, obtained by University of Strasbourg.

2.2.3. Bacterial culture

The *E2146* strain used in this work was stocked in the laboratory at -80 °C in a stock buffer composed of 920 µL of bacterial culture and 390 µL of glycerol/water (50:50, v/v). The growth medium used for the bacterial cultures was Lysogeny Broth (LB) with a composition of tryptone 10 g/L, yeast extract 5 g/L and NaCl 10 g/L. All the growth media solutions as well as the glass ware were sterilized by autoclave at 121 °C for 15 min. The bacterial working culture as well as the pre-culture were both realized under the presence of Amp and Km. For the bacterial working and pre-culture, the concentrations of Amp and Km were 100 µg/mL and 50 µg/mL respectively. The bacterial working culture was prepared by harvesting frozen bacteria with a toothpick into an Eppendorf containing 50 µL of LB. This solution was then deposited on the agar/LB on a Petri dish and spread equally across the surface. The Petri dish was then let to incubate for 24 h at 37 °C after

which the developed bacterial working culture was conserved at 4 °C and used within the next 2 weeks for bacterial pre-cultures.

The pre-cultures were prepared in 20 mL of LB solution containing the antibiotics as described above, by scratching a colony of the bacterial working culture into the LB solution and letting the obtained culture to incubate in a water bath at 37 ± 1 °C for 16 h under stirring (160 rpm). The optical density at 600 nm (OD_{600}) of 1 mL of the obtained bacterial suspension was measured in disposable plastic cuvette with a WPA S1000 Spectrawave visible spectrophotometer (Biochrom Ltd.), fresh LB medium as reference, to monitor bacterial growth. An adequate amount of the pre-culture suspension was then added into 200 mL of LB to prepare the bacterial work culture with an initial optical density of 0.05 ± 0.01. This bacterial culture suspension was then let to incubate at 37 ± 1 °C in water bath under stirring (160 rpm) until the end of the exponential growth phase when OD_{600} reached 0.5-0.6 (after 2 h of incubation). The bacterial culture was then harvested by centrifugation (10 min, 5000 g, 4 °C) and the supernatant was carefully eliminated to collect the pellet. The bacteria in the pellet were then re-suspended in 200 mL of LB/10 in a glass flask containing a sterile magnetic stirrer and the OD_{600} of this final bacterial working culture suspension (S0Ec) was measured. This S0Ec suspension was then used to form the biofilms.

2.2.3. Bacterial growth in suspension

To verify the growth of the bacteria in the S0Ec suspension under conditions close to those of biofilm formation, the S0Ec suspension was placed in room temperature (21 ± 1 °C) under magnetic stirring (160 rpm) in a 500 mL bottle and the OD_{600} of the suspension was measured after 2.5 h, after which an adequate amount of the S0Ec suspension was placed into 200 mL of LB/10 in order to obtain a OD_{600} equal to 0.05. This new suspension was called S1Ec and it was placed under magnetic stirring (160 rpm). The S1Ec suspension corresponded to the change of the growth media in biofilm formation (described below). Growth curves of both of these suspensions (S0Ec and S1Ec) were recorded by taking 1 mL of the suspension in question every 15 min during 4 h to measure its OD_{600}. The suspension was then let to incubate for 20 h and from 20 h to 24 h 1 mL of the suspension was taken every 60 min. FTIR-ATR spectra with diamond crystal was recorded on chosen samples. This follow-up of the bacterial growth was realized two times for both of the suspensions. Epifluorescence microscopy was used to visualize the planktonic bacteria in S0Ec and S1Ec suspensions at 2.5 h and 3 h respectively.

2.2.1. Formation of bacterial biofilms

All of the biofilms were formed on germanium (Ge) surface. Ge was chosen as a good support for several reasons; it is transparent in IR spectra (5500-780 cm^{-1}), it has a high refractive index necessary in ATR mode, it is non-cytotoxic and stable in a large spectrum of different pH values [174]. Each biofilm described in this manuscript have been formed at least twice in an independent manner. The flow system used for growing the biofilms is described in figure 2-2.

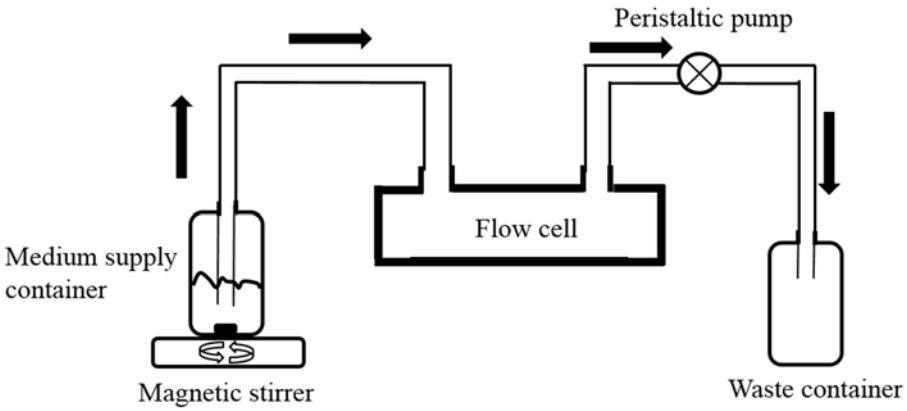


Figure 2-2. Flow circulation system used to form bacterial biofilms.

It consisted of the inoculation flask containing the bacterial suspension placed on a magnetic stirrer surface, a flow cell, a peristaltic pump (Minipuls3 Gilson, Middleton, USA) and a waste reservoir all of which were connected by silicon tubing with inside diameter of either 5 mm (VWR, Fontenay-sous-Bois, France) for ATR-FTIR experiments or 3 mm (Versilic, Limonest, France) for AFM experiments. All of the silicon tubes used in the set-up were sterilized in autoclave at 121 °C for 15 min. The peristaltic pump of the system was adjusted to flow liquids at a rate of 50 mL/h.

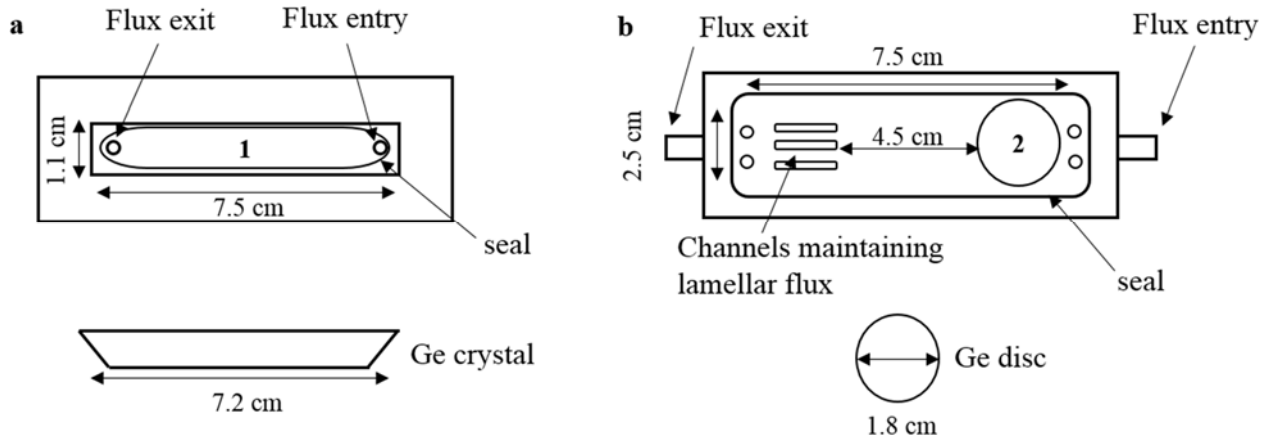


Figure 2-3. a) Flow cell and Ge crystal used for ATR-FTIR setup, 1: chamber for Ge crystal, height 0.3 cm. **b)** Flow cell and Ge disc used for AFM setup, 2: chamber for Ge disc, height 0.2 cm.

Figure 2-3 illustrates the different flow cells used for the two experimental setups. For ATR-FTIR setup (figure 2-3a) a commercial flow cell (SPECAC, Kent, United Kingdom) was used with a trapezoidal ATR Ge crystal (1.0 cm × 7.2 cm). Considering the dimensions and shape of the cell, a lamellar flux of liquids can be assumed. For the AFM setup, a homemade flow cell with dimensions permitting a lamellar and a homogenous flow was used (figure 2-3b) with a circular Ge disc (d = 1.8 cm) attached inside the cell. The AFM flow cell consisted of a poly(methyl methacrylate) base plate that was milled out to form a shallow flow chamber and had an inlet and exit for liquid. Using a gasket, a glass microscope plate was clamped on the top of the base to seal the flow cell.

Ethanol (70 %) and non-pyrogenic sterile water were circulated through the open circulation system prior to *E2146* inoculation for 5 h and 18 h respectively.

2.2.4. Fluorescence microscopy and *Bac*Light ™ staining

Fluorescence microscopy is an optical microscopy technique that has a low detection limit for specifically labeled components. Bright-field light microscopes have also been used for specific labelling, however the greatness of fluorescence microscopy relies under the fact that after fluorescence markers have evolved, the relatively low concentrations of a fluorescent stain needed for marking cells enables the visualization of dynamic cell processes as the vital functions of the cells remain unaffected [175]. This allows the observation of specific cellular components in as native organization and state as possible, without problems of cell death. In an epifluorescence microscope, light is emitted from a light source, such as mercury or xenon lamp. Specific

wavelengths are then transmitted through an excitation filter. The used excitation filter depends on the fluorochrome in question. This light then reaches a dichroic mirror that reflects short-wavelength light to the sample through an objective. The light is absorbed by the fluorochrome of the sample, which then emits longer-wavelength light which is transmitted by the dichroic mirror and separated from the weaker emitted fluorescence by an emission filter (figure 2-4) [176].

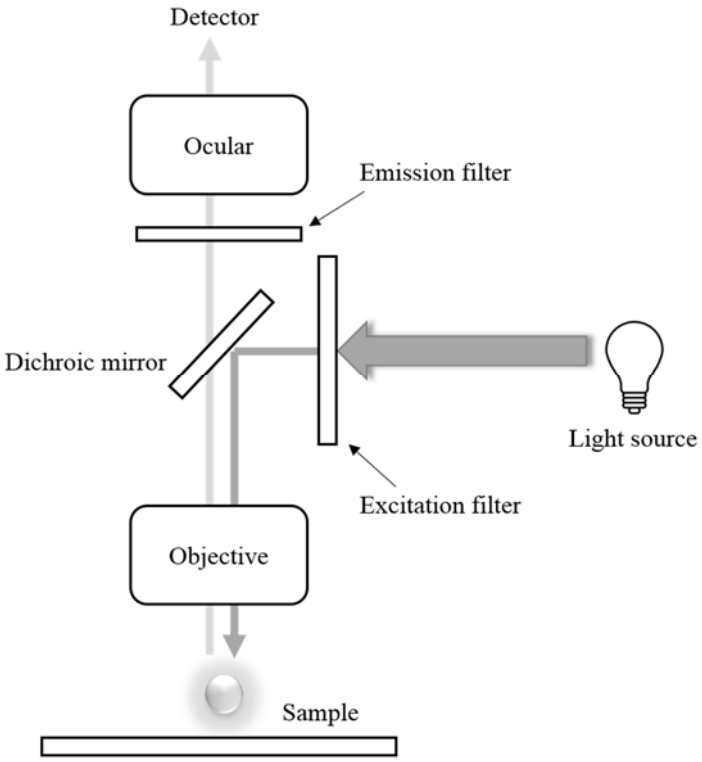


Figure 2-4. Principle of fluorescence microscopy (drawn based on [177]).

In order to observe the bacterial biofilms with epifluorescence microscopy, the Ge crystal was removed from the flow cell aseptically under a microbiological safety cabinet and the biofilm on the Ge crystal was rinsed with 10 mL of non-pyrogenic sterile water to eliminate any non-adhered bacteria. A perpendicular cross sectional scratch was made to the midpoint of the Ge crystal surface in order to divide the surface into two parts: the non-stained "entry" side and the "exit" side to which 100 µL of the readily prepared *Bac*Light™ marking solution (0.15 µL of 0.085 % NaCl solution containing 0.17 mM Syto9® and 1 mM PI is diluted with 1 mL of non-pyrogenic sterile water) was added and let to stay in contact with the biofilm for 20 min in dark, after which the biofilm was rinsed with non-pyrogenic sterile water and gently dried with a Kimwipe® (Kimberly-Clark, Nanterre, France) to remove excess water. One drop of buffered glycerin solution was then

added to the non-stained side of the crystal and one drop of *Bac*Light™ mounting oil provided with the kit was added on the *Bac*Light™ side of the crystal. Two fine glass lamellae were then deposited onto the biofilm and both, non-stained and *Bac*Light™ marked sides of the Ge crystal were visualized by using an Olympus BX51 epifluorescence microscope with oil immersion and a 100 × objective (UPlan FLN), equipped with an Olympus XC50 camera.

The *Bac*Light™ is a bacterial viability test that was used to observe the permeability of bacterial membranes and estimate the average bacterial surface coverage. *Bac*Light™ is based on the use of two fluorochromes, a green-fluorescent nucleic acid stain, Syto9®, and a red-fluorescent nucleic acid stain, propidium iodidide (PI). Due to the small size of Syto9®, it is able to penetrate into all cells, however, the larger size of PI limits PI only to penetrate into cells with damaged cell membranes. PI having a higher affinity towards nucleic acids than Syto9®, in the case when both of these markers are present inside a cell, the nucleic acids will be marked with PI and the cells will fluorescent in red. Table 2-1 presents the maximal emission wavelengths of the different fluorochromes used at maximal excitation wavelengths.

Table 2-2. Maximal excitation and emission wavelengths of the different fluorochromes used to visualize *E2146* biofilms with epifluorescence microscopy (λ: wavelength, ex: excitation, em: emission) [174].

Fluorochrome	**λ_{ex} maximal (nm)**	**λ_{em} maximal (nm)**
Syto9®	480	500
PI	490	635
GFP	395	509

2.3. Langmuir method

Molecules that have an amphiphilic nature consist of a hydrophobic and a hydrophilic part, such as the phospholipids seen in chapter 1. When an amphiphilic molecule comes in contact with water, it accumulates at the air-water interface causing the surface tension (γ) of water to decrease. Amphiphilic substances can be spread on a subphase (usually water) surface to form an insoluble monolayer at the air-water interface, called a Langmuir (L) film [8]. In order to form a monolayer on the surface of a subphase, the amphiphilic molecules are dissolved in a volatile solvent such as chloroform, hexane or toluene. Good solvents have certain preferential characteristics: they dissolve an adequate amount of the monolayer material, but do not react chemically with it, they must not

dissolve in the subphase and must evaporate in a reasonable amount of time without leaving traces at the air-water interface [178, 179]. Once the monolayer solution is spread on the surface with the aid of a microliter syringe, the solvent evaporates and only the monolayer material is left, forming a Langmuir film at the air-water interface.

Isotherms of monolayers are obtained with equipment called a Langmuir trough [180]. The trough itself is shallow with hydrophobic edges preventing any leakage of the subphase and hydrophilic barriers preventing any leakage of the monolayer material.

The area occupied by one molecule ($\hat{A}_M$) of the monolayer material can be calculated when the total area occupied by the monolayer (*A*) and the number of molecules of the monolayer material (N_M) is known (equation 1) [180].

$$\hat{A}_M = \boldsymbol{A/N_M} \qquad \text{Equation 1}$$

When the barriers are compressed on the surface of the trough, sweeping the monolayer at the interface, the $\hat{A}_M$ is reduced and the difference between surface tension of that of clean water (γ_w, 72.5 $mN.m^{-1}$ at 20 °C) and of water with monolayer present (γ_m) increases (equation 2) [180]. This difference is known as surface pressure (π) and it can be monitored by a process known as Wilhelmy plate method.

$$\pi = \Delta\gamma = \gamma_w - \gamma_m \qquad \text{Equation 2}$$

The Wilhelmy plate is a thin plate, usually made of platinum, hanging from a scale above the surface, immersed into the subphase. The Wilhelmy plate monitors the change of the surface pressure according to equations 3-4. The total force (F) acting on the Wilhelmy plate has a downward direction and consists of the weight of the plate, buoyancy and surface tension force (equation 3) [38].

$$F = \rho_p twHg - \rho_l twhg + 2\gamma(t+1)cos\theta \qquad \text{Equation 3}$$

where ρ_p and ρ_l are the plate and subphase densities respectively, t and w are the thickness and width of the plate, H is the total height of the plate, g is gravity (equal to 9.81 N/kg), h is the height of the immersed part of the plate, θ is the contact angle between the subphase and the plate and γ is the surface tension.

When the plate is completely wetted by the subphase, the contact angle θ between the subphase and the plate is $\Theta = 0°$ and therefore $\cos\Theta = 1$. The surface pressure can then be written as shown in equation 4 [38].

$$\pi = \Delta\gamma = \frac{\Delta F}{2(t+1)} \qquad \text{Equation 4}$$

2.3.1. Compression isotherms

A compression isotherm of a monolayer can be obtained by compressing a constant number of moles of the monolayer with the hydrophilic barriers at a constant temperature and atmospheric pressure. The surface pressure increases according to the nature of the monolayer of amphiphilic molecules. Compression isotherms can be used to observe phase transitions of the monolayer material in question. When $\hat{A}_M$ is high, the molecules are sparsely distributed at the air-water interphase and only very few are interacting with each other. This is called the gas phase, in which the surface pressure is zero or very close to zero. When the barriers are compressed sufficiently, the surface pressure starts increasing and a phase transition first from gas (G) to a liquid expanded (LE) and finally to liquid condensed (LC) phase is observed. In the liquid phase the molecules are slightly more packed together. If the barriers are compressed even further, the liquid phase turns into a solid phase and the surface pressure increases dramatically. In this phase, the molecules are very closely packed together and the monolayer is said to be in a solid-like (S) phase. A typical compression isotherm of a membrane lipid (DPPC) is shown in figure 2-5.

At a certain point it is not possible to increase the surface pressure further – the $\hat{A}_M$ has reached its minimum (A_{coll}), the forces acting on the film are high and the film collapses. At this point the molecules are forced out of the monolayer, forming micelles and layers on top of each other and dissolving into the subphase, causing the surface pressure to drop.

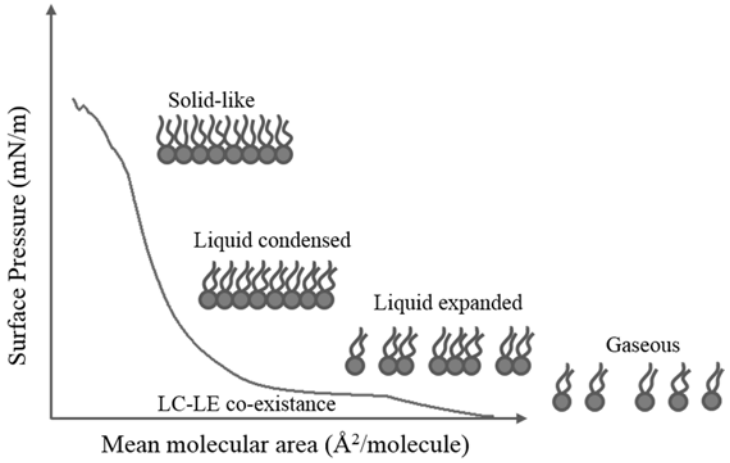


Figure 2-5. A typical π-A isotherm of a membrane lipid (DPPC) with different monolayer phase transitions indicated (drawn based on [181]).

The point of collapse depends on variety of factors, including the history of the film, temperature, rate of compression and the monolayer material itself. The compressibility (C_s) of the film characterizes its rigidity and is given in equation 5 [182].

$$C_s = -\frac{1}{A} \cdot \left(\frac{dA}{d\pi}\right) \qquad \text{Equation 5}$$

The inverse of the compressibility, the compressibility modulus, C_s^{-1}, is usually calculated from the point of collapse of the isotherm and is written as follows (equation 6) [108]:

$$C_s^{-1} = -A\left(\frac{\partial \Pi}{\partial A}\right) \qquad \text{Equation 6}$$

2.3.2. Brewster angle microscopy (BAM)

Monolayers at air-water interface can be further analyzed with Brewster angle microscopy (BAM) and electric surface potential meter [183, 184]. BAM is a microscopic technique relying on the reflectivity differences of water and monolayer surfaces. P-polarized light at a Brewster's angle of incidence (α) results in a minimum reflectivity from water surface and thus when monolayer is present, the optical properties of the interface are altered, resulting in increased reflectivity of the

regions covered by the monolayer (figure 2-6). This allows a visual investigation of the monolayer structure, such as domain growth [122, 185]. Electric surface potential is used to study the difference in electrical potential above and below a monolayer at the air-water interface and is measured by observing the potential difference between a vibrating plate placed above the monolayer and a counter electrode immersed in the subphase [186].

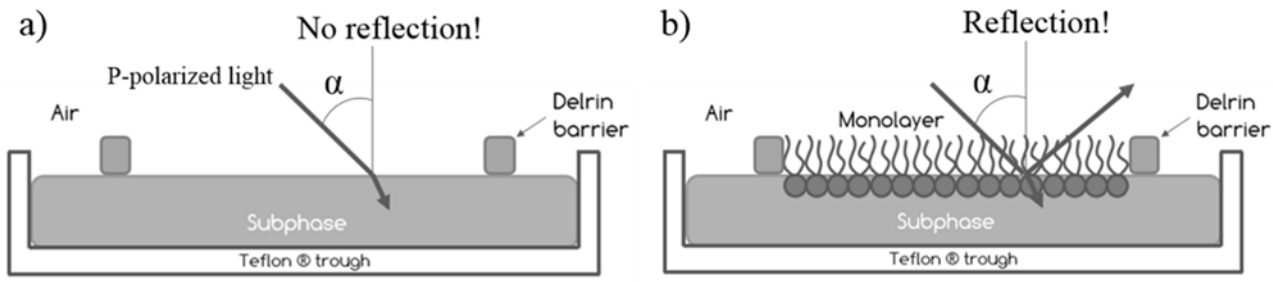


Figure 2-6. A schematic figure of the Langmuir trough and the principle of Brewster angle microscope. **a)** No monolayer present at the air-water interface and therefore no reflection occurring from the *p*-polarized light beam. **b)** A monolayer is present at the air-water interface and a reflection of the *p*-polarized light occurs when the beam comes on the surface at a Brewster's angle of incidence (α) (drawn based on [182]).

2.3.3. Preparation of Langmuir monolayers and compression isotherms

For Langmuir film studies, DPPC, DPPE, DOPC and equimolar mixtures of DPPC/DOPC and DPPE/DOPC phospholipids were dissolved in chloroform at a concentration of 1 mM. The solutions were further stored at 4 °C before use. The surface pressure (π) and electric surface potential (ΔV) measurements were carried out with a KSV 2000 Langmuir balance (KSV Instruments, Ltd., Helsinki, Finland). Compression isotherms were determined for pure lipid monolayers as well as their various equimolar (1:1) mixtures with a Teflon® trough [6.5 cm (l) x 58 cm (w) x 1.0 cm (d)] holding two hydrophilic Delrin® barriers for symmetric compression. The system was equipped with an electrobalance holding a platinum Wilhelmy plate (perimeter 3.94 cm) as a surface pressure sensor and a surface potential measuring head with a vibrating electrode (KSV SPOT1). A stainless steel plate immersed 4 mm below the surface was used as a counter electrode. The apparatus was kept in a Plexiglas cabinet and temperature was kept constant at 20 ± 0.1 °C. Prior to each experiment, the trough and the barriers were washed by cotton soaked in chloroform and ethanol and then rinsed with Milli-Q water. The platinum plate was cleaned between each run by rinsing with Milli-Q water and ethanol, and finally heated to a red-hot glow in

a propane flame to eliminate any organic contaminants. All solvents used for cleaning the trough and the barriers were of analytical grade. Any residual surface-active impurities were removed from subphase surface by sweeping and suction. The stability of the surface potential signal was checked before each experiment after cleaning the subphase surface. After the ΔV signal had stabilized and the surface pressure fluctuation was less than 0.2 $mN.m^{-1}$ during compression stage, monolayers were spread from calibrated solutions using microsyringe (Hamilton Co., USA). After an equilibration time of 10 min, the films were compressed at the rate of 10 $mm.min^{-1}$ by two symmetrically advancing barriers (5$mm.min^{-1}$ per barrier). A computer and KSV software were used to control the experiments. Each compression isotherm was performed at least three times. Changes in the mechanical properties of the monolayers were studied through the values of compressibility modulus [187] and the collapse parameters, π_{coll}, A_{coll} and ΔV_{coll} were determined directly from the compression isotherms.

During compression, the morphology of the films was imaged with a computer-interfaced Brewster angle microscope (KSV Optrel BAM 300, Helsinki, Finland) using *p*-polarized light from a class IIIb 10-mW laser at 632.8 nm, the lateral resolution of the instrument being 1 μm.

2.4. Atomic force microscopy (AFM)

Atomic force microscope (AFM) is a scanning probe microscope (SPM) that is used to form three dimensional images of surfaces with the aid of a physical probe with nano-scale dimensions. The surface of the sample is scanned while the interaction forces with the sharp cantilever tip are recorded. Apart from topography of the surface, AFM can be used to measure close-range interactions between the sample and the tip. AFM has been increasingly used in biological and medical applications in the 21st century and one of its major advantages indeed is its usability in aqueous and physiological conditions in real time [188].

2.4.1. Principle and basis of AFM technique

AFM is an interesting tool as it is able to provide images at atomic resolution with nanometer scale resolution height information. A typical AFM probe has multiple cantilevers each having their own tip made of silicon or silicon nitride, with a specific shape, usually triangular or rectangular. The probe scans the surface of the sample and the high precision movements of the sample positioning in x, y and z directions are adjusted by a piezoelectric scanner. This scanner controls the relative

position of the probe and the sample surface and is located at the sample stage under the sample. A laser is directed on top of the AFM cantilever and a position sensitive photodetector is used to collect the laser beam reflected on top of the cantilever to record tip deflection while moving the sample surface. The top of the cantilever usually has a gold coating to improve reflection of the laser beam. The deflection signal is used to measure the forces resulting from the interactions between the AFM tip and the sample surface. Figure 2-7 illustrates the principle of AFM operation.

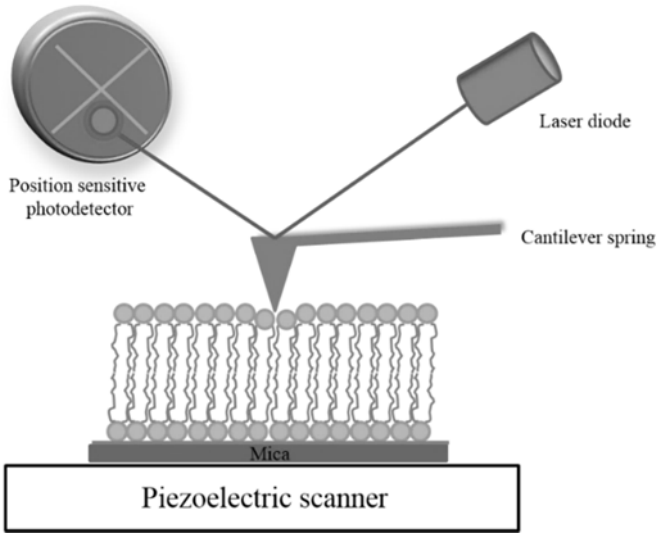


Figure 2-7. The principle of an atomic force microscope (AFM) (drawn based on [174, 189]).

When the AFM tip approaches the sample surface, it undergoes various different forces such as ionic repulsion, van der Waals forces, electrostatic and magnetic forces that act on the tip depending on the separation distance and physico-chemical nature of the tip and the sample. These forces are either attractive or repulsive and result in the deflection of the tip cantilever. At long separation distance the tip and the sample are not in contact and the forces acting between are attractive Van der Waals forces (shown as non-contact zone on figure 2-8) [190].

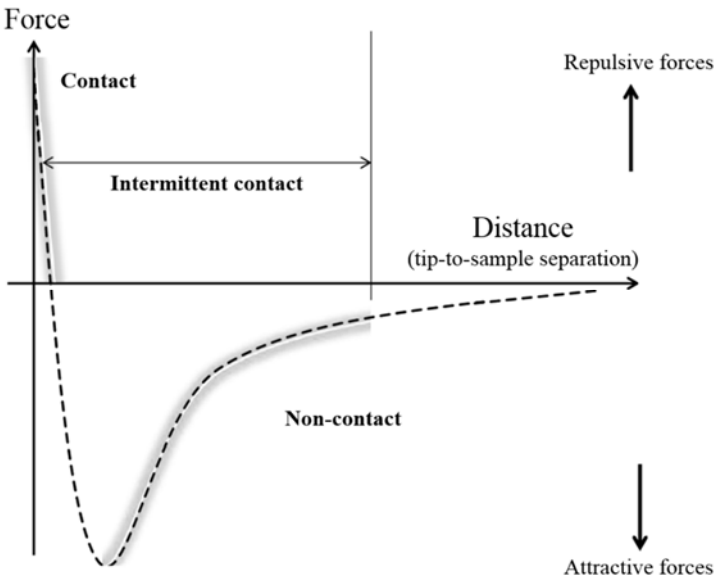


Figure 2-8. Different interaction forces between the tip and the sample surface (modified from [174, 189].

The cantilever deflects downwards. At short separation distance as the cantilever is brought closer to the surface, the tip makes contact with the sample and a repulsive force caused by electrostatic interactions between the sample and the tip increasingly takes over and causes the cantilever to deflect away from the surface (shown as contact zone on figure 2-8). These deflections lead to a change of the position of the laser spot reflected to a position sensitive photodetector with four sectors, and therefore changes the laser intensity received by each of these sectors. This light signal is then converted into an electric signal and sent to the piezoelectric scanner and thus a feedback loop to conserve either the height of the tip above the surface or the interaction forces between the tip and the surface can be created. The displacements of the piezoelectric scanner can then be used to construct a topographical height image of the sample surface. The resolution of the AFM image depends on the number of pixels of the image and the dimensions of the AFM tip (radius of curvature). The more pixels there are in an image, the more acquisition time the image recording requires. Generally an image resolution of 256 × 256 or 512 × 512 is sufficient in obtaining good quality images. The smaller the radius of curvature of the AFM tip, the better the precision of the sample topography is [191]. The radius of curvature of an AFM tip is typically from 1 to 20 nm.

Depending on the level of contact between the sample and the tip, AFM can be operated in three different modes; contact mode, intermittent contact mode (Tapping^{TM} mode) and non-contact mode. In contact mode the tip and the sample are maintained in contact with each other and repulsive

forces act on the tip and the cantilever is deflected with distance (d) proportionally to the force (F) according to Hooke's law (equation 7) [174].

$$F = -k_C d \qquad \text{Equation 7}$$

where k_C is the spring constant of the cantilever. The contact mode can either be used by keeping the applied force (and therefore also the set-point value of the photodetector) constant in which case the measured tip-sample distance (z) changes due to the feedback loop, or by maintaining the z value constant and measuring the cantilever deflection. The contact mode provides images with high resolution and is the most frequently used of the three modes, however, it is not optimal for biological samples as the applied force can potentially damage fragile biological specimen and the tip can easily get contaminated by the sample.

The intermittent contact mode (Tapping™ mode) is based on the oscillation of the tip at its resonance frequency (5-300 kHz) at defined amplitude. This causes the tip to periodically interact with the sample. When the tip comes into contact with the sample, the forces acting between the tip and the sample cause the pre-defined amplitude of the tip oscillation to change. Thus reduction of the oscillation amplitude is used as a feedback control signal [192]. The oscillation amplitude is directly proportional to the average separation distance [193]. Topographical height images can thus be obtained. In this mode the contact is only intermittent and therefore the frictional forces between the tip and the sample can be neglected and the damages to the sample are minimized [193]. However, the acquisition time of an image with the intermittent contact mode is longer than the one with the contact mode.

In the non-contact mode the tip does not come into contact with the sample but oscillates around its resonance frequency at 1-10 nm above the sample surface, scanning the attractive forces between the tip and the surface. The oscillation amplitude is changed due to these forces. The non-contact mode does not cause any contamination of the tip by the sample, but the scanning time is very slow and the lateral resolution is weak.

2.4.2 Force spectroscopy

A part from imaging, AFM can be used to measure mechanic forces between the AFM tip and the sample, such as the lipid bilayer or cell membrane, revealing structure-function relationships of single molecules at a pico Newton (pN) scale [194]. These forces are obtained from the cantilever deflection according to Hooke's law (equation 7) and are presented as force-distance curves (figure 2-9) showing the intensities of the forces acting between the tip and the sample as the tip approaches or retracts towards and from the sample surface.

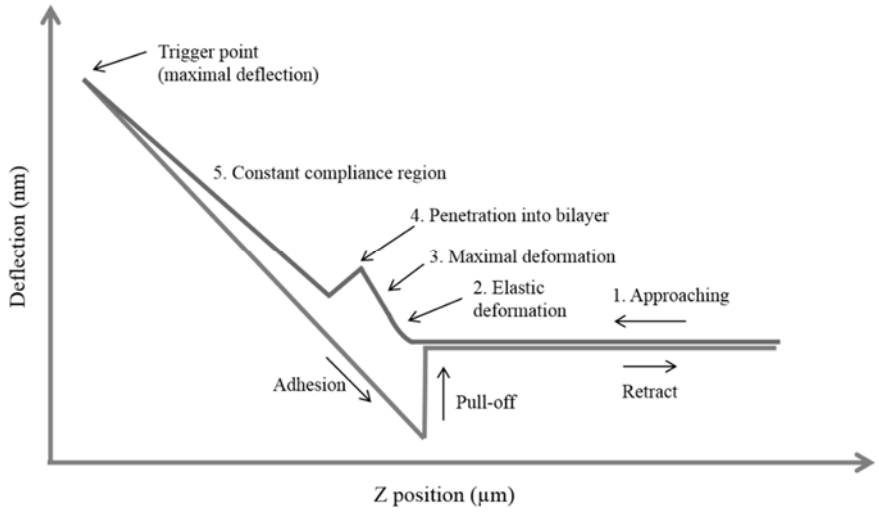


Figure 2-9. Schematic representation of a force curve obtained by AFM force spectroscopy indicating the different regions of the approach and retraction zones (drawn based on [174]).

When the tip approaches the sample surface (phase 1 in figure 2-9), it is far from the surface, at its equilibrium, and no interaction between the tip and the sample occurs. This is where the baseline of the force-distance curve (F = 0) is defined. Information on the long range interactions such as electrostatic effects at few micrometres above the surface can be obtained when the tip approaches the sample. These long-range interactions would cause a negative peak in the approach zone of the force-distance curve, finally leading to the detection of short-range forces, such as the Van der Waals forces, which are seen as a linear deflection of the tip (snap-in) shown as regions 2-5 in figure 2-9. At region 2 the tip is in contact with the bilayer sample, causing it to deform elastically, finally coming to the maximal deformation of the bilayer and, at region 4, penetrating into the membrane. At region 5 the tip continues to push the sample until the maximal force indicated by the user is reached and the tip is retracted from the sample, seen as a retraction curve, showing a region

of adhesion and finally a point of rupture at which the tip and the sample are separated. The force difference between the pull-off and the baseline is referred to as the rupture force (f_u). The approach zone of the force-distance curve, notably the elastic deformation region (region 2 of figure 2-9) allows the determination of the sample elasticity and rigidity such as the Young modulus or the stiffness, by different physical models. The larger the curvature of the contact point region is, the bigger is the sample deformation. The physical models of contact mechanics used for the determination of the sample elasticity include the Hertzian (sphere-on-flat) and Sneddon (cone-on-flat) theories, in which adhesion forces between the tip and the sample are neglected, and Derjaguin-Muller-Toporov (DMT) theory that takes the attractive interactions outside the contact area into account. The DMT model is readily integrated in the NanoScope Analysis software (Bruker, Palaiseau, France) but to gain more precision in elasticity calculations and in particularly in the case of the biofilms, we used the Sneddon model integrated in our automated algorithm [196].

2.4.3. AFM for phospholipid and LPS bilayer experiments

In order to study the topography and elasticity of phospholipid and lipopolysaccharide bilayers, different lipid systems were used: DPPC/DOPC, DPPE/DOPC, lipidA/LPSt and lipidA/LPS-S. The bilayers were formed onto Muscovite mica slides (25 × 25 mm, Electron Microscopy Sciences, Hatfield, PA, USA). AFM images of the immersed bilayers were recorded with a Bruker Dimension FastScan (Bruker Nano, Palaiseau, France) and analyzed with NanoScope Analysis software (Bruker Nano, Palaiseau, France). Topographic images (size 5 µm × 5 µm for DPPC/DOPC and LipidA/LPS, 15 µm × 15 µm for DPPE/DOPC, 512 × 512 pixels, scan rate 1 Hz) and force maps using Peakforce Tapping mode™ (frequency 1 Hz) were recorded before and during 1 h after colistin (final concentrations of 10, 50, and 150 µM) or bCAT (60 µM, ProteoGenix, Schiltigheim, France) injection. AFM-tips were conical gold coated tips with spring constants of 0.350 $N.m^{-1}$ and were purchased from Bruker (NPG-10, Bruker AXS, Palaiseau, France). AFM measurements of PLs were performed in two steps. At first, imaging was performed with a setpoint of 0.25 nN (without mechanical information). Secondly, at the same location, the amplitude of the setpoint was 3 nN for acquiring the force curves. The spring constants (k_c) of the cantilevers were determined with thermal calibration method. Each experiment presented here is representative of at least three independently conducted measurements. A first order flattening filter was applied on the height images and section analysis was used to obtain the corresponding cross sections of each image. The roughness of the different PL domains within the samples were estimated by five random average

root mean square (R_q) values for areas of 128 × 128 nm^2 for DPPC/DOPC bilayers and 541 × 541 nm^2 for DPPE/DOPC bilayers.

In addition, imaging of Lipid A/LPS bilayers were done in air. The Lipid A/LPS bilayers were prepared in previously described manner. After preparation, samples were let to incubate either with 150 µM colistin or 60 µM bCAT for 0, 20, 40 or 60 min. The bilayers were then rinsed with phosphate-buffered saline (PBS) solution and dried under a gentle stream of nitrogen (0.2 bar for 2 min). AFM imaging was performed with a MFP3D-BIO instrument (Asylum Research Technology, Atomic Force F & E GmbH, Mannheim, Germany). Silicon nitride cantilevers of conical shape with spring constants of 0.07 $N.m^{-1}$ (MLCT-AU, Bruker-nano AXS, Palaiseau, France) were used for imaging in air at room temperature (21 °C).

2.4.4. AFM imaging and force spectra of biofilms

In order to study the topographical and elastic properties of *E2146* biofilms under the influence of antimicrobial peptides, the biofilm aged 5.5 h was chosen as a reference biofilm (blank). This biofilm was subjected to closed circulation of 24 h of either LB/10 solution with 0.87 µM colistin or with 60 or 30 µM bCAT, after which the biofilm samples were rinsed with non-pyrogen sterile water and deciphered in liquid condition with AFM MFP3D-BIO instrument by force spectra (force-volume images of 1024 pixels, scan rate of 1 Hz) using Silicon nitride cantilevers of conical shape with spring constants of 0.200-0.250 $N.m^{-1}$, purchased from Atomic Force (OMCL-TR400PSA-3, Olympus, Japan). Nanomechanical properties of the biofilms were measured by recording at least 3 Force-Volume Images (FVI) at different location over the biofilm, each consisting of a grid of 32-by-32 force curves performed with an approach rate of 2 μms^{-1}. The bacterial Young modulus *E* was calculated by analyzing the force-indentation curves according to the Sneddon model (equation 8) [195] with a MatLab algorithm previously described by Polyakov *et al.* [196].

$$F = \frac{2ETan(\sigma)}{\pi(1-\nu^2)}\delta^2 \qquad \text{Equation 8}$$

where δ is the indentation depth, ν the Poisson coefficient, and σ the semi-top angle of the tip. The average values of Young modulus given in this work were calculate from at least 3072 force curves.

The biofilms were then carefully dried under a gentle stream of nitrogen and used for AFM imaging with the MFP3D-BIO instrument. Topographic images of sizes 20 µm × 20 µm, 10 µm × 10 µm and 5 µm × 5, with 512 × 512 pixels and a scan rate of 1 Hz were obtained by contact mode AFM using conical gold coated tips with spring constants of 0.200-0.250 $N.m^{-1}$ (NPG purchased from Bruker nano, Palaiseau, France).

2.5. Attenuated total reflectance Fourier transform infrared spectroscopy (ATR-FTIR)

Vibrational spectroscopy is based on the interactions of electromagnetic radiation and surrounding matter. Various spectroscopic methods, such as ultraviolet, infrared and nuclear magnetic resonance are used in experimental chemistry. All of these techniques are based on the absorption of energy by different molecules in different regions of the electromagnetic spectrum. Spectroscopic techniques can be used to examine almost any kind of matter such as liquids, gases, powders, films, fibers and pastes.

2.5.1. Principles of ATR-FTIR

Infrared spectroscopy is a well-developed and widely used spectroscopic technique that enables the identification of chemical compounds and monitoring changes occurring during a chemical reaction. With the exception of an extremely low temperature at zero Kelvin, all molecules are in motion in one way or another; they move from one place to another (translation), they rotate in space and they vibrate. Infrared spectroscopy is based on these vibrations taking place at the atomic level of a molecule. By passing infrared radiation through a sample, it is possible to determine the fraction of the incident radiation absorbed at a particular energy. The sample molecule changes from its original energy level to another, causing an energy difference of ΔE. As a molecule can only absorb radiation having the same frequency than one of its fundamental modes of vibration, the peaks of the absorption spectrum correspond to the frequency ν (in wavenumbers cm^{-1}) of the electromagnetic radiation at which a part of the sample molecule vibrate. The likelihood of a photon to be absorbed by a certain molecule is governed by the change in the induced dipole moment that occurs during molecular vibration, essential for the molecule to show any infrared activity. The energy of a photon is related to its wavelength by Bohr equation (equation 9) [41].

$$\Delta E = h\nu = hc/\lambda \qquad \text{Equation 9}$$

where h is the Planck constant (h = 6.626 × 10^{-34} J s) and c is the speed of light in vacuum (c = 3 × 10^{8} m.s^{-1}). Vibrations are stretching (the bond length changes) and bending (the bond angle changes) movements of bonds between atoms within a molecule and a molecule with only two atoms has only one possible vibration corresponding to the stretching and bending movement between the two constituting atoms. It is said that a diatomic molecule has one degree of vibrational freedom. Molecules with N amount of atoms have 3N degrees of freedom from which three of them correspond to the translation of the entire molecule in a three dimensional space. Triatomic molecules can either be linear (like CO_2) or non-linear (such as H_2O).

Table 2-3. Different degrees of freedom of polyatomic molecules [41].

Type of degrees of freedom	**Linear**	**Non-linear**
Translational	3	3
Rotational	2	3
Vibrational	3N-5	3N-6
Total	**3*N***	**3*N***

Linear molecules with more than two atoms have three movements of the molecule around its center of gravity, corresponding to three degrees of rotational freedom, whereas non-linear triatomic molecules have only two [41]. Therefore there are 3N-5 degrees of freedom for linear molecules and 3N-6 degrees of freedom for non-linear molecules (table 2-3). Stretching vibrations can either be symmetric or asymmetric depending on the in and out movement of the two bonds of the constituting atoms along the bond axis (figure 2-10).

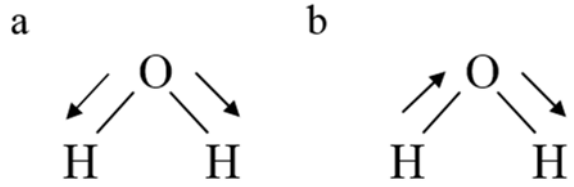


Figure 2-10. Symmetric **(a)** and asymmetric **(b)** stretching vibrations [41].

Similarly, different types of bending vibrations (figure 2-11) exist, among these are scissoring, rocking, wagging and twisting.

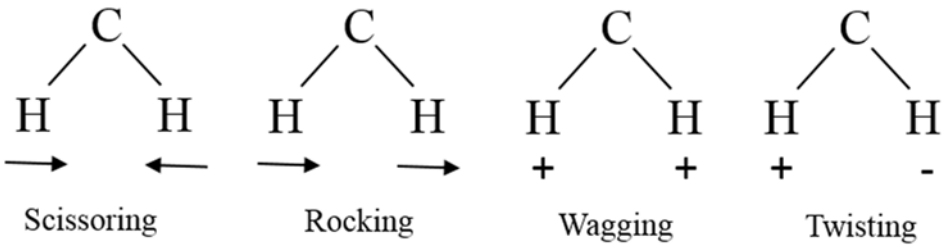


Figure 2-11. Different kinds of bending vibrations, + and – indicating movements on opposite directions out of the plane [41].

Beer-Lambert law (equation 10) is used in the transmission mode of IR spectroscopy. Beer-Lambert law relates the sample thickness to the amount of light transmitted by the sample. The absorbance (*A*) of a solution at a wavelength λ is directly proportional to the thickness (*l*) and the concentration (*c*) of the sample and the Beer-Lambert law can be written as follows [41]:

$$A(\lambda) = log \frac{I_\lambda^0}{I_\lambda} = \varepsilon_\lambda cl \qquad \text{Equation 10}$$

ᵑ where I_λ^0 and I_λ are the intensities of the initial light beam and the absorbed beam respectively and where I_λ^0 and I_λ are the intensities of the initial light beam and the absorbed beam respectively and ε_λ is the molar absorptivity coefficient. Because of the strong absorption properties of water, the recording of spectra in aqueous solutions is a challenge. The absorption of water is reduced in ATR spectroscopy, making the ATR mode a great solution to overcome the challenge faced for the absorbance of molecules in an aqueous bulk. The principle of attenuated total reflectance infrared

(ATR-IR) spectroscopy (figure 2-12) relies on total reflection of an IR beam at an interface of the sample and an IR transparent material with a high refractive index, when the angle of incidence at the interface is greater than the critical angle θ_c.

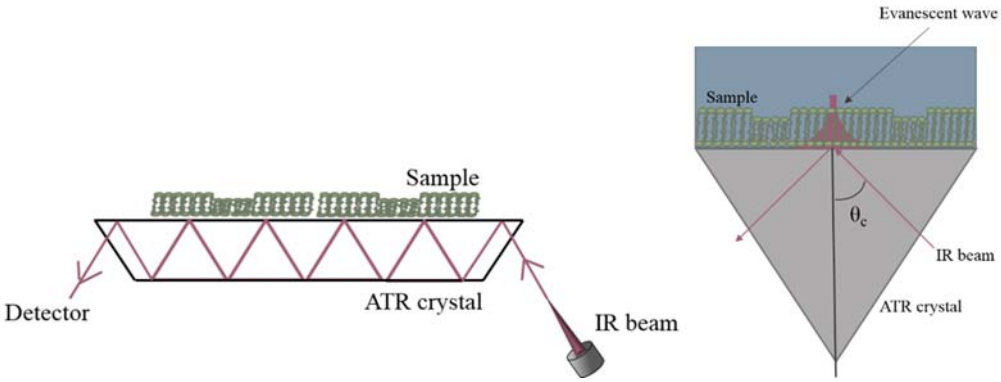


Figure 2-12. Schematic of ATR-FTIR technique and formation of the evanescence wave (drawn based on [149]).

The sinus of the critical angle is equal to the ratio of the refractive index of the sample (n_2) and of the ATR crystal (n_1) according to equation 11 [150].

$$\theta_c = sin^{-1}(\frac{n_2}{n_1}) \qquad \text{Equation 11}$$

A fraction of a wavelength of the beam penetrates beyond the reflecting ATR crystal and the beam loses energy at the wavelength at which the sample material selectively absorbs. These progressive transversal and longitudinal waves penetrating the sample are called evanescent waves (figure 2-12). The electromagnetic field of this evanescent wave decays exponentially within the sample and the depth of penetration of the evanescent wave, d_p, defined as the distance at which the evanescent wave drops e^{-1} times its initial intensity on the surface of the crystal, is dependent on the wavelength of the incoming IR radiation as well as on the refractive indexes of the ATR crystal and the sample according to equation 12 [152, 161].

$$d_p = \frac{\lambda}{2\pi n_1 (sin^2\theta - (\frac{n_2}{n_1})^2)^{1/2}} \qquad \text{Equation 12}$$

The IR beam undergoes 6 reflections inside the Ge crystal used in this study (figure 2-12). When the relation of the depth of penetration is applied to certain chosen wavelengths of the IR beam and when the refractive indexes of two commonly used ATR crystal materials, Ge and diamond, are known to be 4.0 and 2.4 respectively, the depth of penetration of the evanescent wave can be calculated at these wavelengths according to equation 12, knowing that the refractive index of a biofilm or a supported lipid layer can be considered as 1.5 [197, 198] and the angle of incidence is 45°. The corresponding values of d_p at 3000, 1550 and 1100 cm^{-1} are listed in table 2-3.

Table 2-4. Evolution of the depth of penetration (d_p, in µm) of the evanescent wave as a function of the wavenumber of the incoming IR radiation at the surface of two commonly used ATR crystals [198].

Crystal material/wavelength	**2900 cm^{-1}**	**1550 cm^{-1}**	**1100 cm^{-1}**
Ge	0.22	0.42	0.59
Diamond	0.67	1.29	1.82

Therefore, taking into consideration the penetration depth values indicated in table 2-4, the evanescent wave is capable to penetrate the entire lipid bilayer sample (thickness of 5 nm). However for bacterial biofilms, the detection range of the evanescent wave extends only to the immediate contact zone of the bacteria and the ATR crystal at longer wavelengths, up to the first bacterial layer (thickness of ~600 nm) at shorter wavelengths.

As light is a transverse electromagnetic wave, its electric and magnetic fields oscillate along directions that are perpendicular to the direction of propagation, unlike longitudinal soundwaves that oscillate in the direction of propagation. Usually natural light sources emit non-polarized light, meaning that the directions of the wave oscillations are random. Light however can be linearly polarized to one direction and in such a case, the direction of polarization is defined as the direction of the oscillation of the electric field (*E*) as shown in figure 2-13. Such polarizing equipment is also available for IR spectroscopy applications.

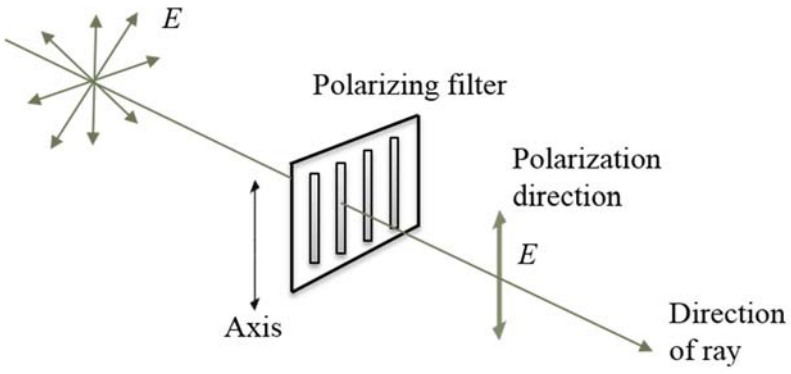


Figure 2-13. Principle of the polarization of light (drawn based on [177]).

When light is polarized parallel and perpendicular to the plain of incidence in an IR spectroscopy setup, the ratio of the absorption (*A*) of these two can be used to calculate the dichroic ratio, R (equation 13) [199, 200].

$$R = \frac{A_{\parallel}}{A_{\perp}} \qquad \text{Equation 13}$$

2.5.2. ATR-FTIR on phospholipid bilayers

ATR-FTIR spectra of phospholipid bilayers were recorded between 4000 and 750 cm^{-1} on a Vector 22 spectrometer (Bruker, Karlsruhe, Germany) equipped with a KBr beam splitter and a deuterated triglycine sulphate (DTGS) thermal detector. The resolution of the single beam spectra was 4 cm^{-1}. All interferograms were Fourier processed using the Mertz phase correction mode and a Blackman-Harris three-term apodization function. No ATR correction was performed. ATR spectra are shown with an absorbance scale corresponding to $\log(R_{reference}/R_{sample})$, where R is the internal reflectance of the device. FTIR measurements were performed at 21 ± 1°C in an air-conditioned room. Recording of spectra, data storage and data processing were performed using the Bruker OPUS 5.0 software. A nine-reflection diamond ATR accessory (DurasamplIR ™, SensIR Technologies) was used for acquiring the spectrum (200 scans) of the mother solutions of colistin and bCAT. The incidence angle is 45° and the refraction index of the crystal is 2.4. For experiments involving the PL bilayers, a SPECAC home-modified ATR-FTIR batch cell enclosing a trapezoidal Ge crystal (72 mm × 10 mm × 6 mm, refraction index: 4.0) with an incidence angle of 45° yielding six internal reflections on the upper face in contact with the sample was used. The penetration depths are

calculated at 0.22 and 0.42 µm at 2900 and 1550 cm^{-1}, respectively. ATR-FTIR experiments were performed with DPPC, DOPC, and DPPC/DOPC phospholipid bilayers. Each experiment presented here is representative of two independently conducted measurements. Background spectra without polarization (200 scans) and with 0° and 90° polarizations (400 scans) of TRIS buffer and TRIS-Ca buffer (1:1, v/v) were recorded prior to the formation of the bilayer on the germanium surface. An Edmund Industrial Optics Polarizer (Barrington, USA) was used. Spectrum of 1 mM lipid solution was also recorded (200 scans). Spectra of the formed bilayer were then obtained without polarization (200 scans) and with polarizations (400 scans). Spectral time-evolution was either performed with or without colistin (final concentrations of 50 µM and 150 µM) or bCAT (60 µM). The spectral evolution was monitored for 2 h (200 scans, spectra recorded every 4 min). Again polarized spectra (400 scans) were recorded after the 2 h follow up and compared to the polarized spectra taken at 0 min. Dichroic ratio was calculated according to equation 13. The water vapor was subtracted and the baseline was corrected (points at: 3585, 3025, 2750, 1800, and 900 cm^{-1}), before integrating the chosen peak intensities ($\nu_a CH_2$: 2945-2880 cm^{-1}, $\nu C{=}O$: 1760-1712 cm^{-1}, Amide II: 1580-1485 cm^{-1}).

2.5.3. ATR-FTIR on bacterial biofilms subjected to AMPs

In order to study the effect of antimicrobial peptides on bacterial biofilm, the biofilms were formed as previously described. The biofilm aged 5.5 h was chosen as a reference biofilm. This biofilm was subjected to closed circulation of 24 h of either pure LB/10 solution, LB/10 solution with 0.87 µM colistin sulfate or with LB/10 solution with 60 or 30 µM bCAT, during which ATR-FTIR spectra was recorded every 15 min with a Tensor 27 (Bruker, Palaiseau, France) IR spectrometer. The spectra were recorded between 4000 and 800 cm^{-1} with the same setup as described for PL SLBs (chapter 2.5.2). Appropriate spectra were used to remove spectral background; a sample-reference spectrum was acquired immediately prior to the step in question for biofilm monitoring. Water vapor was subtracted and the baseline was corrected (points at: 3580, 2750, 1800, and 900 cm^{-1}), before integrating the chosen peak intensities (νOH: 3580-3400, Amide II: 1591-1484, Amide III-Nucleic acids (NA): 1279-1182, polysaccharides (PS) total: 1199-950, total: 1591-950). After peptide circulation of 24 h, the sample was either removed from the flow cell to be examined by epifluorescence microscopy or it was used to study whether the influence of the peptide was bacteriostatic or bacteriolytic. In the latter case all of the silicon tubes were changed again for new

sterilized ones and the biofilm was subjected to open LB/10 circulation of 17 h during which ATR-FTIR spectra was recorded every 15 min.

3. Antimicrobial peptide action on model membranes

3.1 Phospholipid monolayer interaction with a cyclic antimicrobial peptide

To investigate the interaction of colistin with phospholipid (PL) model membranes, pure DPPC, DPPE, DOPC and their mixtures (DPPC/DOPC and DPPE/DOPC) were used to spread monolayers at 21 ± 0.1 ˚C on pure water subphase and subphase containing 50 µM of colistin sulphate salt. The Π-A and ΔV-A compression isotherms of pure PL monolayers as well as their mixtures on pure water and in 50 µM colistin subphase are shown in figures 3-1a-d. For pure PL monolayers (DPPC, DPPE, DOPC) on water subphase, the results were in agreement with those already reported [116, 201-204]. DPPC isotherm showed a typical liquid expanded (LE) to a more liquid condensed (LC) phase transition plateau at around 5 mN.m^{-1} (black line, figure 3-1a), which was not observed for the other PLs used. It can be observed, that for all the studied PLs as well as for their mixtures, the Π-A isotherms containing colistin in the subphase were shifted to higher molecular areas compared to isotherms of films on pure water subphase. The characteristic parameters of the isotherms are collected in table 3-1. Monolayer compressibility can be associated to permeability characteristics of biological membranes [205]. Therefore the C_s^{-1} values were calculated from the obtained Π-A isotherms and they indicated that the DPPC, DPPE, DOPC, DPPC/DOPC and DPPE/DOPC films were in liquid (condensed) or solid phase [187] regardless to the presence of colistin in the subphase. The C_s^{-1} values decrease in the presence of colistin in the subphase, indicating that the peptide induced expansion of the monolayers. This decrease of the C_s^{-1} values was observed for all but the pure DOPC monolayer. The liquefaction was exceptionally remarkable for DPPE. To visualize the influence of subphase composition on the film properties, the collapse parameters of the isotherms, Π_{coll}, A_{coll} and ΔV_{coll} were obtained directly from the compression isotherms (table 3-1). For the DPPC, DOPC, DPPE as well as DPPC/DOPC monolayers the Π_{coll} values changed to a lower extent, indicating that the peptide did not have such a great destabilizing effect on the monolayer. This result is similar to previous studies by A. Clausell *et al*. in which *E. coli* total lipid extract monolayers were studied under the influence of Polymyxin B [206]. However, a significant decrease in the Π_{coll} of DPPE/DOPC was observed, indicating that colistin had a destabilizing and liquefying effect on the DPPE/DOPC monolayer. The Π_{coll} are correlating with ΔV_{coll} values obtained with the surface potential meter. The ΔV_{coll} values indeed were decreasing in the case of the DPPE/DOPC monolayer. The A_{coll} values increased in the presence of colistin for all of the studied monolayers. This increase suggests a different, more tilted orientation of the hydrocarbon chains of the PL molecules relative to the

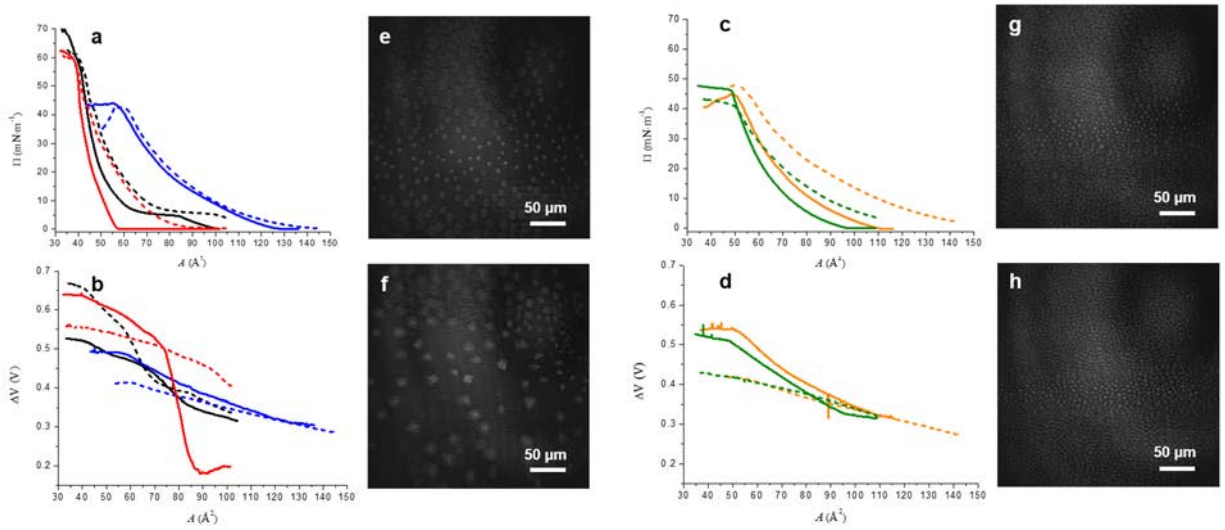


Figure 3-1. Compression isotherms of phospholipid monolayers spread on water subphase (solid lines) or colistin (50 µM) aqueous solution (dashed lines). **a,c)** Π-*A* isotherms **b,d)** Δ*V*-*A* isotherms. Results obtained with pure DPPC (black), DOPC (blue), DPPE (red), and mixed DPPC/DOPC (orange) and DPPE/DOPC (olive) monolayers. Brewster angle micrographs of mixed DPPC/DOPC **(e, f)** and DPPE/DOPC **(g, h)** monolayers spread on pure water subphase **(e, g)** and on colistin (50 µM) aqueous solution **(f, h)**. The micrographs were taken at Π = 25.0 mNm^{-1}. Temperature 20 °C [108].

normal of the water surface when colistin was present, indicating that colistin could penetrate into the monolayer, increasing the surface area. Interestingly, when looking at the collapse areas, colistin seemed to have a greater impact on the mixed (DPPC/DOPC and DPPE/DOPC) monolayers than on the pure PL films. This could suggest that the peptide had a more extensive tendency to penetrate into a mixed than into a pure PL monolayer.

Table 3-1. Compression isotherm parameters at collapse of phospholipid monolayers on pure water subphase and subphase containing 50 µM colistin [108].

	H_2O				**Colistin (50 µM)**			
Monolayers	C_s^{-1} (mNm^{-1})	Π_{coll} (mNm^{-1})	A_{coll} ($Å^2$)	ΔV_{coll} (V)	C_s^{-1} (mNm^{-1})	Π_{coll} (mNm^{-1})	A_{coll} ($Å^2$)	ΔV_{coll} (V)
DPPC	270.0	50.0	42.2	0.647	225.8	50.9	43.6	0.512
DPPE	567.7	47.3	40.4	0.635	185.9	49.7	41.2	0.556
DOPC	103.3	38.5	61.4	0.475	105.6	37.6	64.5	0.405
DPPC/DOPC	104.7	37.0	55.4	0.519	80.9	38.3	61.2	0.403
DPPE/DOPC	148.7	42.9	49.8	0.504	77.5	35.8	53.9	0.413

The obtained BAM images (figures 3-1e-h) showed that indeed colistin did modify the morphology of some monolayers studied. In accordance with the Π-A isotherms, the BAM images suggested that the LE-LC phase transition was shifted to higher surface pressures in the DPPC/DOPC film when colistin was present. The corresponding BAM images were obtained at a surface pressure of 25 $mN.m^{-1}$ in which DPPC/DOPC monolayer in pure water was at 63.3 $Å^2$/molecule whereas the equivalent monolayer in colistin subphase was at 76.7 $Å^2$/molecule. The corresponding values for the DPPE/DOPC monolayer were 58.6 and 64.3 $Å^2$/molecule. When comparing figures 3-1e and 3-1f, it can be observed that the DPPC/DOPC monolayer domains were more sparsely located when colistin was present in the subphase. For DPPE/DOPC monolayer a phase transition from LE to LC phase was not observed with isotherm studies nor in BAM images, neither did the BAM images show any distinction in monolayer morphology between the two experimental conditions (figures 3-1g-h). Nevertheless, it was observed that the PL composition of the monolayer modulates the interaction with colistin. The isotherms provided us with knowledge on the physico-chemical states of the PL monolayers, but a further examination of the PL-colistin interaction was obtained by formation of bilayers of the chosen PLs and studying them with AFM and ATR-FTIR (described in chapter 3.2).

3.2 Phospholipid bilayer interaction with antimicrobial peptides

3.2.1 Morphological and spectral characteristics of phospholipid bilayers

Supported lipid bilayers (SLB) were formed by the vesicle fusion method either on Ge or mica for ATR-FTIR and AFM experiments, respectively. DPPE was reluctant to create a bilayer on either of the substrates, and especially on germanium, so the FTIR experiments concerned only DOPC, DPPC and DPPC/DOPC SLBs. The spectra of the pure SLBs are presented in figure 3-2, and the main assignments are indicated in accordance with the literature [149]. Negative water bands around 3400 and 1640 cm^{-1} were observed. Water molecules on the crystal surface were replaced by PL molecules. In the C-H stretching (νCH) region, the spectra of DPPC showed the characteristic antisymmetric and symmetric $νCH_2$ bands of organized chains in the gel phase at 2918 cm^{-1} and 2850 cm^{-1}, respectively. For pure DOPC SLB the characteristic νCH bands were found to be the following: (C=C)-H stretch at 3003 cm^{-1}, $ν_aCH_2$ at 2923 cm^{-1} and $ν_sCH_2$ at 2853 cm^{-1}, the two latter being specific of the fluid phase DOPC. In the mixed DPPC/DOPC SLB, the bands of both PLs were present, strongly suggesting that as for AFM experiments, both PLs occurred in the SLB.

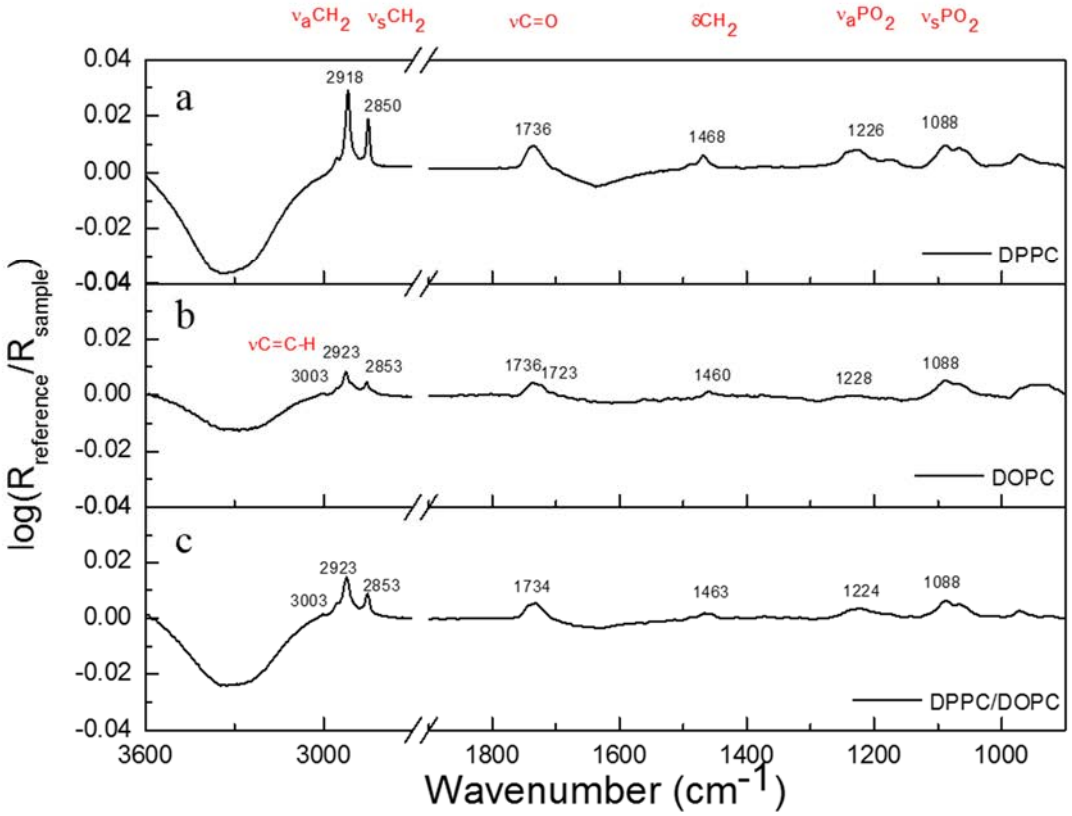


Figure 3-2. ATR-FTIR spectra of **a)** DPPC, **b)** DOPC and **c)** mixed DPPC/DOPC SLBs on germanium crystal in TRIS buffer (NaCl 150 mM, $CaCl_2$ 1mM, pH=7.4). Major assignments are indicated. Background: TRIS buffer [108].

The C=O stretching vibrations were observed at 1736 cm^{-1} for the DPPC SLB, and 1736 and 1723 cm^{-1} for the DOPC SLB. Additionally, vibrations from the polar head groups of the PLs occurred at lower wavenumbers and did not change significantly from one PL to the other. Notably, the PO_2 symmetric stretchings absorbed at 1088 cm^{-1} for both PLs. The spectra of mixed DPPC/DOPC SLBs were fitted by Lorentzian bands in the C-H stretching region (3025-2800 cm^{-1}) to estimate the lipid composition of the mixed bilayer. It was found that the mixed DPPC/DOPC SLBs were composed on average of 75% of DOPC and 25% of DPPC (estimation obtained from 4 independently made mixed SLBs), which did not represent the initial solution composition of 50/50. To find out the efficiency of each PL to form a SLB, a spectrum of each 1 mM lipid solution was recorded prior to the formation of the SLB and the integrated intensities of the νCH bands, IIνCH(PLsolution), were compared to the integrated intensities of the νCH bands of the SLB, IIνCH(SLB). Ratios IIνCH(PLsolution)/IIνCH(SLB) were very different in the cases of the two different PLs. The calculated ratios were 1.55 and 2.81, for DPPC and DOPC, respectively,

suggesting that the formation of the DOPC SLB was more efficient. In most experiments involving SLBs, a rinse is performed before subsequent kinetic studies [136, 207]. This consideration was not taken into account in other studies involving infrared analysis of SLBs [150]. As a blank experiment, the time-evolution of the SLB spectra were monitored during 2 h. Whereas the DOPC SLB spectra showed no time-evolution of the PL vibrational bands (figure 3-3b), the DPPC and the mixed SLBs showed an increase of bands assigned to DPPC (notably the CH and PO_2 stretching bands in regions 3000-2800 and 1100-1000 cm^{-1}, respectively, figure 3-3a). This data suggested that for the SLB formation of DPPC, which is in the gel state at 21°C, the vesicle fusion was not complete. Vesicles stayed in solution, and they progressively approached the Ge crystal and became more concentrated in the reach of the evanescent wave. To check this hypothesis, a thorough but gentle rinse of the freshly made SLB was performed to remove possible vesicles in solution. After verification of the remaining of the bilayer by recording of an ATR-FTIR spectrum, the time-evolution of the infrared spectra of the rinsed bilayer was performed. No evolution of the assigned bands was observed neither for DPPC nor for DOPC (figures 3-3c and d).

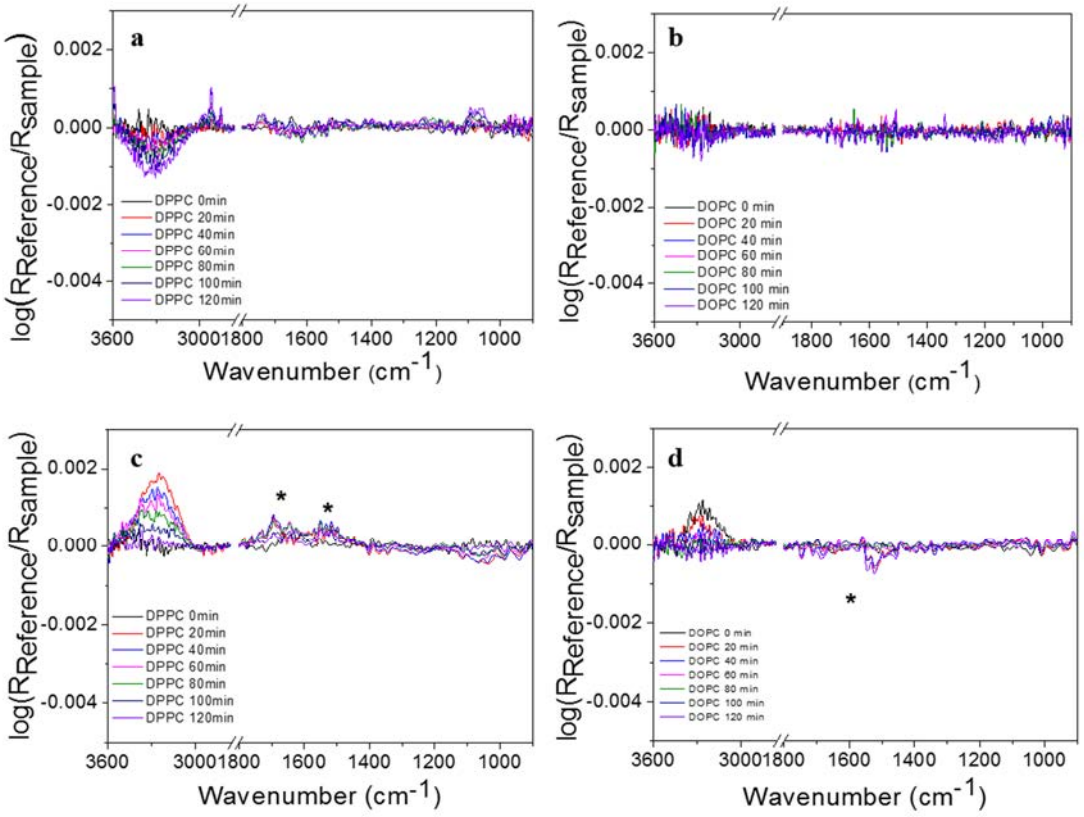


Figure 3-3. Time-evolution of the ATR-FTIR spectra of the DPPC **(a, c)** and DOPC **(b, d)** phospholipid SLBs on the Ge crystal during 2 h without AMP injection (control experiment) without rinse **(a, b)** and with rinse **(c, d)**. The background spectra are the SLBs at 0 min. *: water vapour not completely removed [108].

These results were very important for the following of the study because only the interaction of the AMPs with the SLB was under our interest. Yet these results were informative since the evolution of SLB formation studied by IR spectroscopy has not been extensively described in the literature.

The morphology of the DPPC/DOPC SLBs (figure 3-4a) investigated by AFM was in accordance with observations reported in the literature [208]. DPPC, in gel phase, consisted of several domains of few microns diameter (bright domains in the images) surrounded by the DOPC in fluid phase (dark background in the images). Differences in terms of DPPC domain size and coverage ratios were already observed and described [54]. The differences of morphology of the domains can be attributed to slight variations in the cooling conditions from 65 °C to room temperature. The height difference between these two phases was about 1.2 nm due to the different lengths of the two PLs (see cross sections in figure 3-4a). Conversely to DPPC/DOPC SLB, for which the DPPC gel phase domains were surrounded by the DOPC fluid phase, a different behavior was observed for the DPPE/DOPC samples for which the topographical image is shown in figure 3-4b. Indeed, no micro-domains were observed. Instead, DPPE vesicles of about 11 nm thick (see cross section in figure 3-4b), and a DOPC SLB of about 5 nm thick (deduced from non-covered zones on the mica substrate, data not shown) occurred. Vesicles of DPPE were deposited onto the DOPC bilayer. This difference in terms of morphology can be explained by the fact that PE phospholipids are less stable in the form of a bilayer and rather generate curvature structures at pH values less than 9 [209, 210].

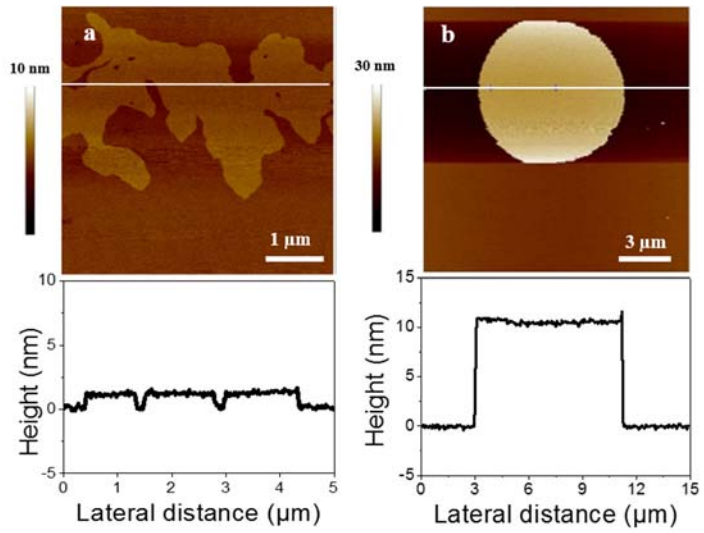


Figure 3-4. Atomic force microscope topographical images of **a)** DPPC/DOPC SLB and **b)** DPPE/DOPC immersed in TRIS buffer.

3.2.2 Phospholipid bilayer interaction with a cyclic antimicrobial peptide

A diamond ATR-FTIR spectrum of pure colistin at 1.1 mM in TRIS buffer was recorded (figure 3-5 a). The characteristic Amide I and II bands of colistin were observed at 1646 and 1538 cm^{-1}, respectively. The band at 1099 cm^{-1} was assigned to the sulphate counter ion in the commercial product (antisymmetric stretching). An equivalent spectrum of colistin at 150 µM was also recorded on germanium ATR-FTIR (figure 3-5b) and Amide I and II bands were observed at 1646 and 1538 cm^{-1} respectively, the sulphate stretching band being absent. This result reflected the high potential for adsorption of proteins on surfaces [211] even at the micromolar level of concentration.

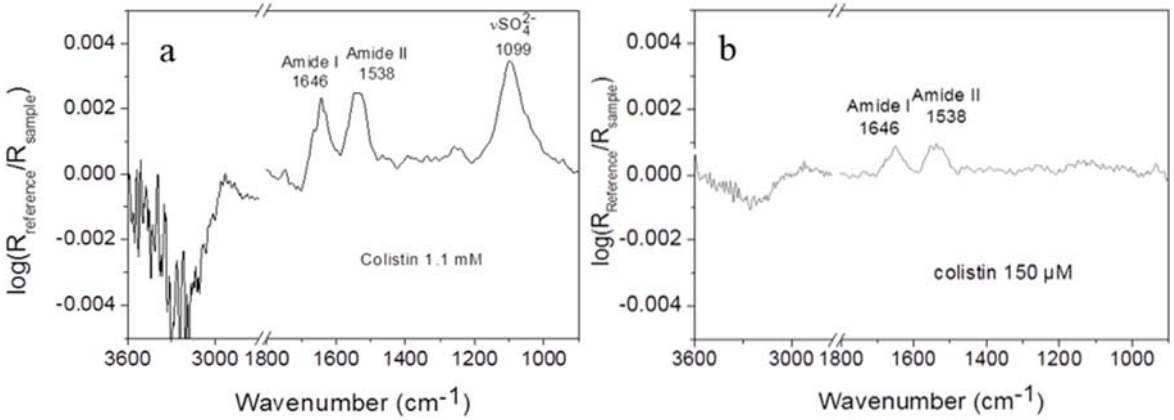


Figure 3-5. ATR-FTIR spectra of colistin in aqueous solution [108]. **a)** 1.1 mM mother solution on diamond **b)** 150 µM solution on germanium.

Spectral evolution was monitored for 2 h for DPPC, DOPC and mixed DPPC/DOPC SLBs with colistin final concentrations of 50 µM and 150 µM. For the colistin concentration of 50 µM, the vibrational fingerprints were close to the level of the spectral noise and they were not interpretable with accuracy. Therefore, only the results with colistin at the concentration of 150 µM are presented. Figure 3-6 shows the time-evolution spectra for the three SLBs submitted to colistin at 150 µM. For each series, the background was the spectrum of the SLB before the injection of colistin, allowing the observation of the spectral evolution within time only due to colistin injection. For the DPPC SLB, Amide bands at 1647, and 1535 cm^{-1} increased at the same time than bands at 2956, 2925, and 2878 cm^{-1} immediately after colistin injection (figure 3-6a). The features of the three latter bands fitted also well with the one usually observed for proteins [212]. The Amide II band wavenumber was slightly lower with respect to the one in pure colistin solution. After 1 h of colistin injection, weak bands occurred at 1081 (PO_2 symmetric stretching) and 1053 cm^{-1} (C-O-P-

O-C stretching), and after 1.5 h the C=O stretching band of DPPC [149] also occurred in the spectrum. For the DOPC and DPPC/DOPC SLBs, only Amide bands increased during the time of the experiment (figures 3-6b and 3-6c). Their wavenumbers were only slightly changed with respect to those recorded for pure colistin, (1649 and 1538 cm^{-1}). All this data suggested that the interaction of colistin with the SLBs was weak. Only in the case of the DPPC bilayer, an interaction with the polar head was suggested by the shifting of the phosphate vibrations. The dichroic ratios were calculated from the integrated intensities of the CH_2 antisymmetric stretchings. The values were 1.00, 1.06, and 1.06 for DPPC, DOPC, and DPPC/DOPC SLBs, respectively (mean values from 4 spectra) before the colistin injection.

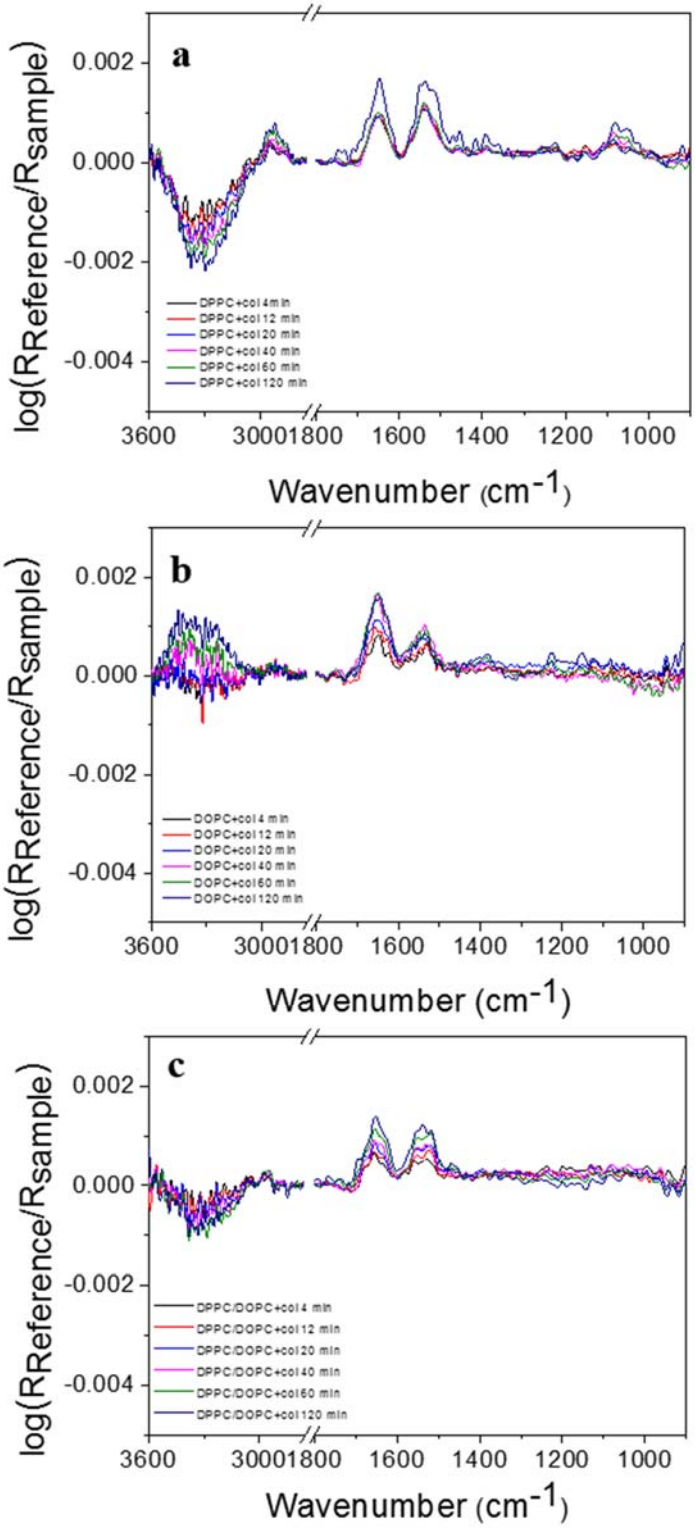


Figure 3-6. Time-evolution of the ATR-FTIR spectra of the phospholipid SLBs on the Ge crystal in the presence of 150 μM colistin with rinse of the SLB before colistin injection [108]. The background spectra are the SLBs before colistin injection. **a)** DPPC **b)** DOPC **c)** DPPC/DOPC SLB.

The calculated values after 2 h of colistin action were 1.06, 1.09, and 1.04, respectively. As an example, polarized spectra (at 0° and 90°) of the CH_2-stretching region of DPPC bilayer before and 2 h after colistin (150 µM) injection is shown in figure 3-7. These variations were considered too low to be significant, and no significant structural change in the SLB following the colistin addition can be evidenced according to findings obtained by ATR-FTIR.

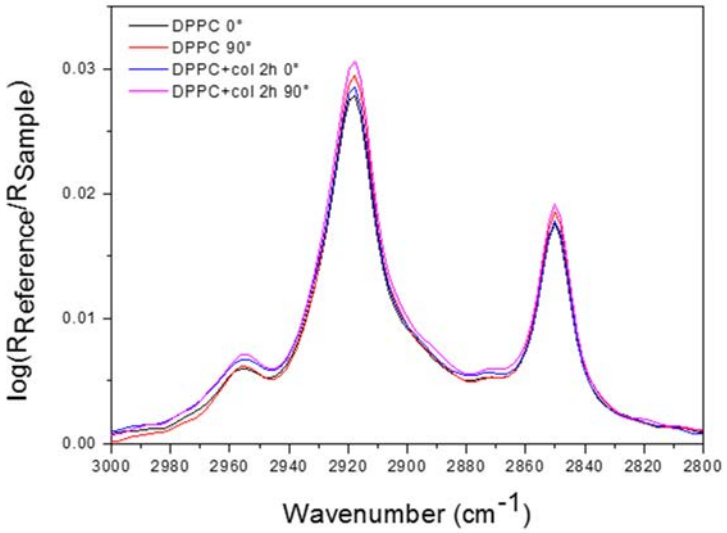


Figure 3-7. Polarized spectra at polarization angles of 0° and 90° of the CH_2-stretching region of DPPC bilayer before and 2 h after colistin (150 µM) injection.

As the PL coverage of the Ge crystal was not known, the Amide II/νC=O integrated intensity ratios were calculated as a function of time and are presented in figure 3-8. The ratios increased exponentially for all the experiments, however, it was 2.5 fold higher for the mixed SLB, suggesting that for the mixed bilayer, colistin was in higher concentration in the field of the evanescent wave. This supports our findings in the case of the monolayers; according to the A_{coll} values obtained for monolayers with various different lipids and their mixed compositions, colistin seemed to have a larger impact for the mixed ones, indicating that the peptide could penetrate the PL membrane more easily when an interface of different PLs was present.

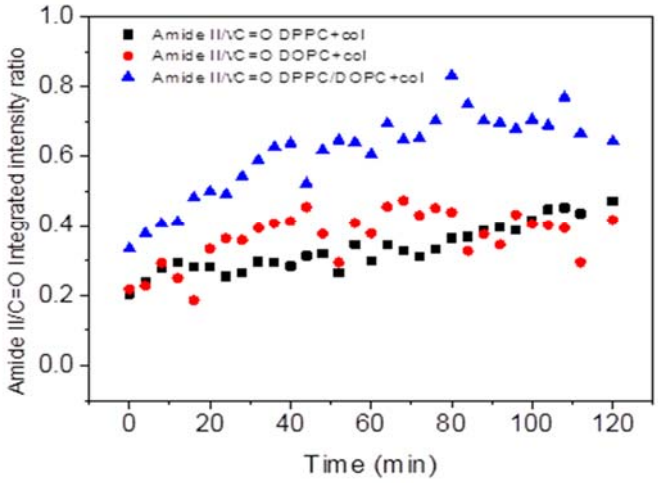


Figure 3-8. Time-evolution of integrated intensity ratios Amide II/νC=O during the action of colistin at 150 µM for DPPC (black squares), DOPC (red discs), and DPPC/DOPC (blue triangles) SLBs [108]. Integration regions: νC=O: 1760-1712 cm^{-1}, Amide II: 1580-1485 cm^{-1}.

The action of colistin on both PL models was evaluated by morphological and mechanical analyses at concentrations of 10 and 50 µM for DPPC/DOPC and DPPE/DOPC, and additionally of 150 µM for DPPC/DOPC. At 10 µM, no significant topographical nor mechanical changes were observed for either system. The topographical results for 10 µM colistin concentration with DPPC/DOPC SLB are reported in figure 3-9. The analyses of DPPC/DOPC SLBs subjected to colistin evidenced a concentration-dependent action. Morphological investigation of DPPC/DOPC SLBs subjected to colistin at 50 and 150 µM for 40 min are reported in figure 3-10. AFM images showed that the SLB topography was altered very moderately on the level of DPPC domains at 50 µM (figures 3-10a-b). For the highest concentration of 150 µM, we observed that the SLB morphology was dramatically impacted (figures 3-10c-d). Indeed, the cross section analysis revealed height differences of about 5 nm after 40 min of colistin action instead of 1.2 nm. DPPC domains were eroded (see arrows in figure 3-10d) and the DOPC background was removed from immediate contact with the mica surface. The modifications in the bilayer were largely edge driven but occurred also in the middle of the DPPC domains (for DOPC data not shown).

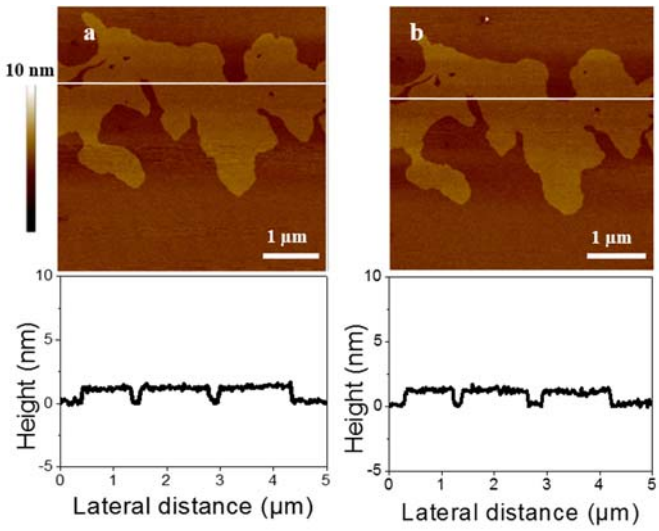


Figure 3-9. Atomic force microscope topographical images of DPPC/DOPC SLBs immersed in TRIS buffer **a)** before and **b)** 40 min after colistin injection (10 μM). No changes in topography of the SLB were observed.

One could consider the interface of the two PL phases to be more fragile and susceptible for the effects of the peptide, due to the less organized packing of these two phases [213]. Such erosion phenomenon has been already reported for surfactants and antimicrobial peptide action onto DPPC/DOPC membrane [208, 214].

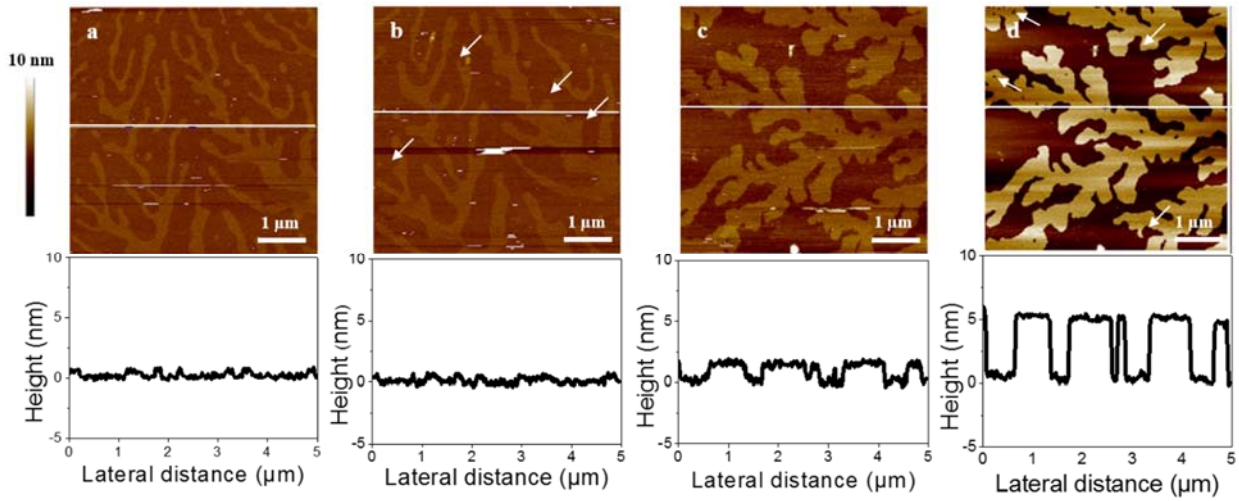


Figure 3-10. Atomic force microscope topographical images of DPPC/DOPC SLBs immersed in TRIS buffer before **(a, c)** and 40 min after **(b, d)** colistin injection (b: 50 μM, c: 150 μM) [108].

Representative force-distance curves of different lipid domains of the DPPC/DOPC system are shown in figure 3-11**.** The mechanical properties of the DPPC/DOPC SLB before and after the action of colistin at 50 and 150 μM concentrations are presented in figure 3-12.

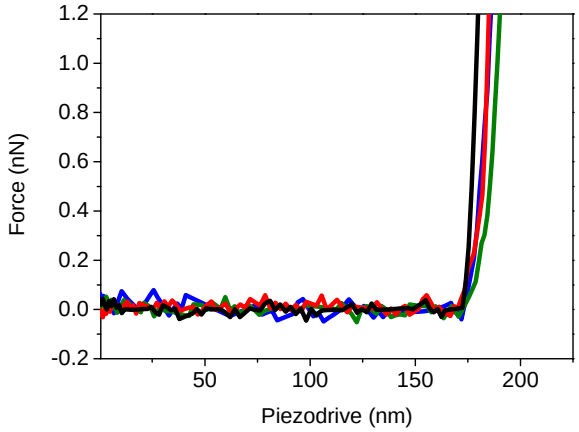


Figure 3-11. Representative force-distance curves recorded on DPPC domain (blue), DOPC domain (green) before colistin injection and on DPPC remaining domain (red) and revealed mica (black) 40 min after colistin (150 µM) injection [108].

Before the injection of colistin, the statistical analysis of the elasticity showed a bimodal distribution for the DPPC/DOPC SLB (figures 3-12a and 3-12c). The highest values of the elasticity can be attributed to the gel phase composed of DPPC while the lower can be attributed to the fluid phase of DOPC. These two phases were also distinguishable in the DMT map of figure 3-12e. The frequency of each elasticity distribution (DPPC and DOPC) depends on their coverage ratio in the region of observation. Indeed, the statistical distribution reported in figure 3-12a corresponds to a surface covered by 85% of DPPC and 11% of DOPC. This distribution differed in the other experiment (figure 3-12c) where 71% of the mica surface was covered by DPPC and 26% by DOPC (in an image of 5 µm). Despite these differences of coverage and gel phase domain distribution and surface areas, the mechanical properties of the different DPPC/DOPC SLBs remained very similar.

At the lower peptide concentrations of 10 (data not shown) and 50 µM (figure 3-12b), no modifications of the elasticity distribution were observed. This result indicated that colistin was not concentrated enough to destabilize or alter both DPPC and DOPC phases of the SLB. However, pronounced topographical and mechanical modifications were observed at colistin concentration of 150 µM (figures 3-12d and 3-12f). The careful inspection of elasticity maps and distributions of DPPC/DOPC SLB after 40 min of colistin action revealed an important modification of the elasticity distribution.

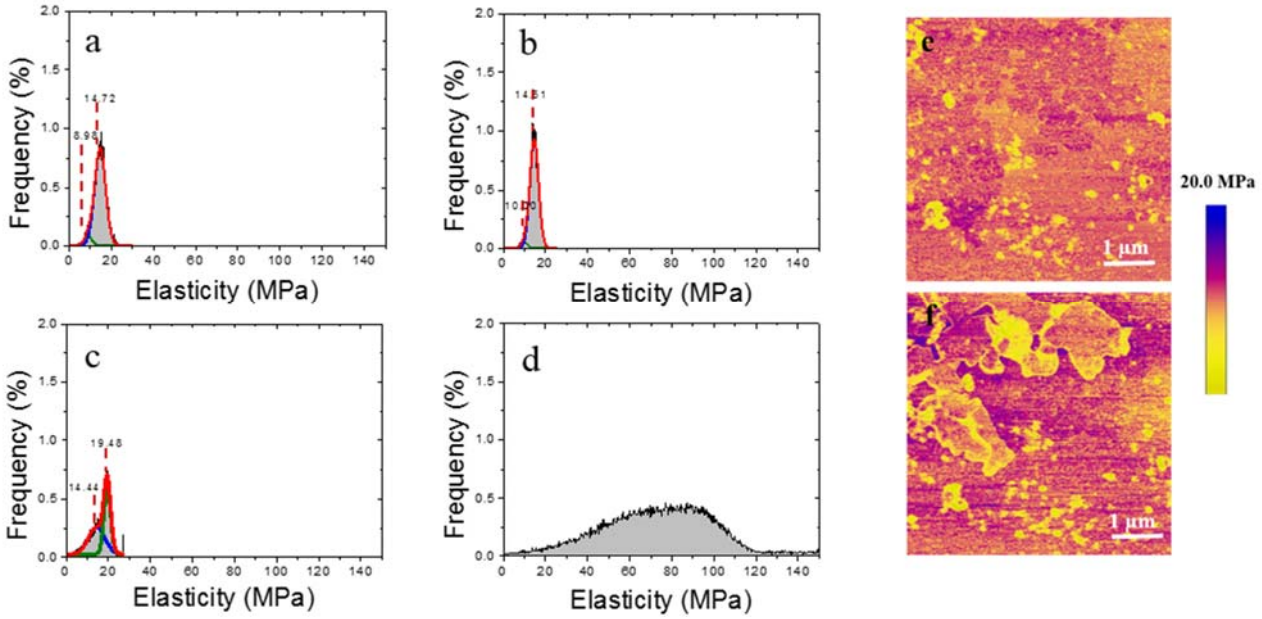


Figure 3-12. Typical distributions of DPPC/DOPC SLB elasticity before **(a, c)** and 40 min after colistin injection (**b**: 50 µM, **d**: 150 µM) with peak centres indicated. Derjaguin-Muller-Toporov (DMT) modulus images of supported DPPC/DOPC SLB in TRIS buffer **e)** before and **f)** 40 min after colistin (150 µM) injection [108].

Here, the Gaussian distribution was lost and became broad and potato-shaped, ranging from 0 up to 120 MPa. This drastic modification can be explained by a remove of DOPC from the surface, and only the elasticity of DPPC and mica were quantified. Furthermore, the erosion of the DPPC domains reported in figure 3-10d suggested an alteration of their mechanical properties, *i,e*. a decrease of the elasticity. Such phenomenon can also explain the low elasticity values (between 0 and 20 MPa) while the high elasticity values can be related to the elasticity of the mica substrate.

For DPPE/DOPC lipid system shown in figure 3-13 as topographical images before (a) and 40 min after (b) colistin injection, no significant modifications of the morphology due to colistin was observed. The height profile and morphology of the DPPE/DOPC system remained the same after 40 min under the action of colistin at 50 µM. However, the statistic distributions of the elastic moduli reported in figure 3-14a-b and the elasticity (figures 3-14c-d) revealed a slight decrease of the SLB stiffness from about 5.57 to 4.00 MPa, and 7.84 to 5.94 MPa for DOPC and DPPE, respectively. This slight decrease occurred on both DPPE and DOPC phases without any morphological impact. This result suggested that colistin at 50 µM concentration could probably get into the DPPE/DOPC system, and thus decreased the surface energy and reduced the membrane stiffness, but was not enough to disorganize the whole structure by pore formation. In other words, the affinity or activity of colistin to DPPE/DOPC SLBs remained low even at 50 µM.

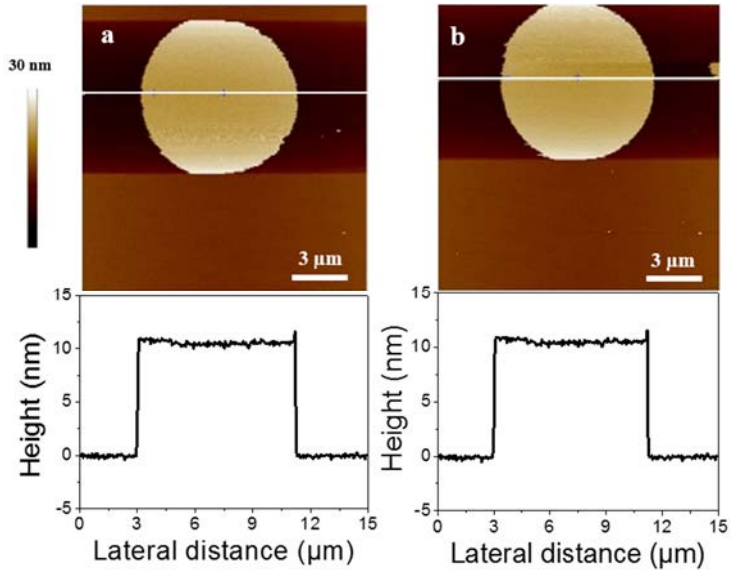


Figure 3-13. Atomic force microscope topographical images of supported DPPE/DOPC vesicle immersed in TRIS buffer [108] **a)** before and **b)** 40 min after colistin (50 µM) injection.

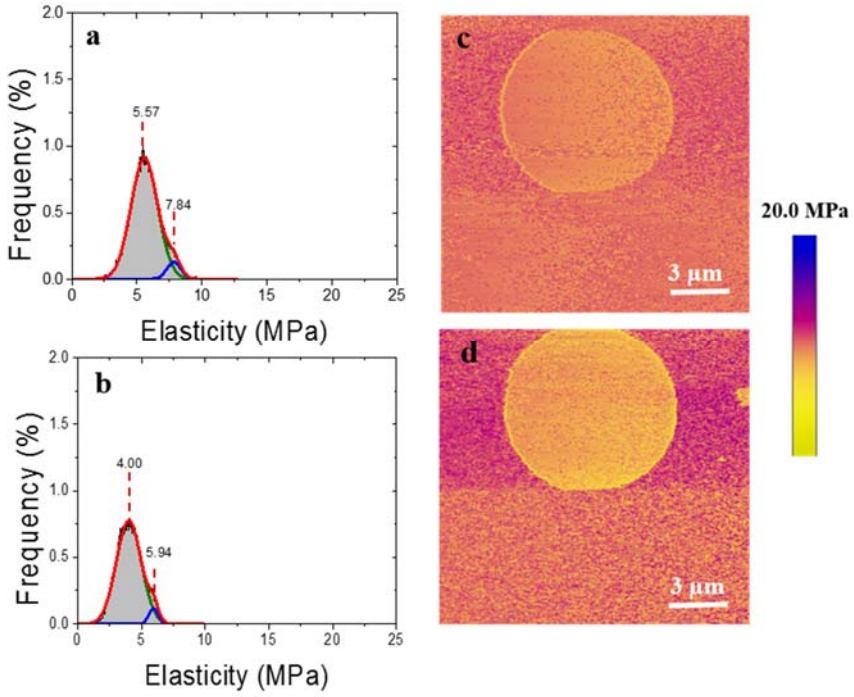


Figure 3-14. Typical distributions of DPPE/DOPC vesicle elasticity **a)** before and **b)** 40 min after colistin (50 µM) injection with peak centres indicated. Derjaguin-Muller-Toporov (DMT) modulus images of supported DPPE/DOPC SLBs in TRIS buffer **c)** before and **d)** 40 min after colistin (50 µM) injection [108].

The roughness of the different domains of the SLBs were calculated by five random average root mean square (R_q) values on areas of 128 × 128 nm^2 for DPPC/DOPC and 541 × 541 nm^2 for

DPPE/DOPC. The roughness of DPPC domains did not change significantly under the influence of the peptide (figure 3-15). However, the peptide had a slight decreasing influence on the DPPE roughness at a concentration of 50 µM.

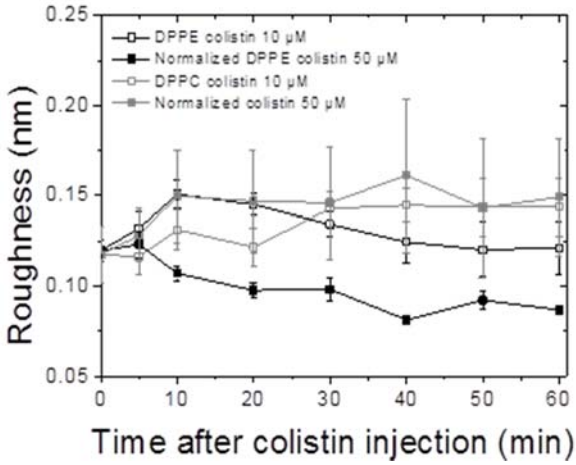


Figure 3-15. Roughness time-evolution of DPPE (black lines) and DPPC (grey lines) domains within 60 min after colistin (10 µM: hollow symbols and 50µM: filled symbols) injection [108].

It can be emphasized that colistin action on the gel phases of DPPC and DPPE lead to a decrease of membrane elasticity in both cases and morphological damages only on DPPC. This result correlates with the results obtained by monolayer studies, in which the peptide did have a destabilizing effect on both of the mixed (DPPC/DOPC and DPPE/DOPC) monolayers, but detectable morphological changes occurred only in the DPPC containing mixed monolayer.

3.2.3 Phospholipid bilayer interaction with a linear antimicrobial peptide

A diamond ATR-FTIR spectrum of pure bCAT at 0.41 mM in TRIS buffer was recorded (figure 3-16a). The characteristic Amide I and II bands of bCAT on diamond were observed at 1646 and 1541 cm^{-1}, respectively. An equivalent spectrum of bCAT at 60 µM was also recorded on germanium ATR-FTIR (figure 3-16b) and Amide I and II bands were observed at 1647 and 1543 cm^{-1} respectively. These wavenumber of the Amide I and II bands obtained on diamond and on Ge crystal suggest that bCAT adopts a random secondary structure in the solution [215]. This is supported by observations of other authors who have reported secondary structures on catestatin in aqueous media and found them to adopt mainly random coils and β-sheets [113, 216, 217]. The peaks seen in the bCAT diamond spectra at 1203 cm^{-1} and 1149 cm^{-1} are contributions of

trifluoroacetic acid (TFA), used in the solid phase synthesis process of the peptide to cleave the peptide from a solid surface [218]. TFA remains as an impurity in the final product. However, at the 60 µM concentration used for the peptide spectra on Ge surface, these peaks were not seen.

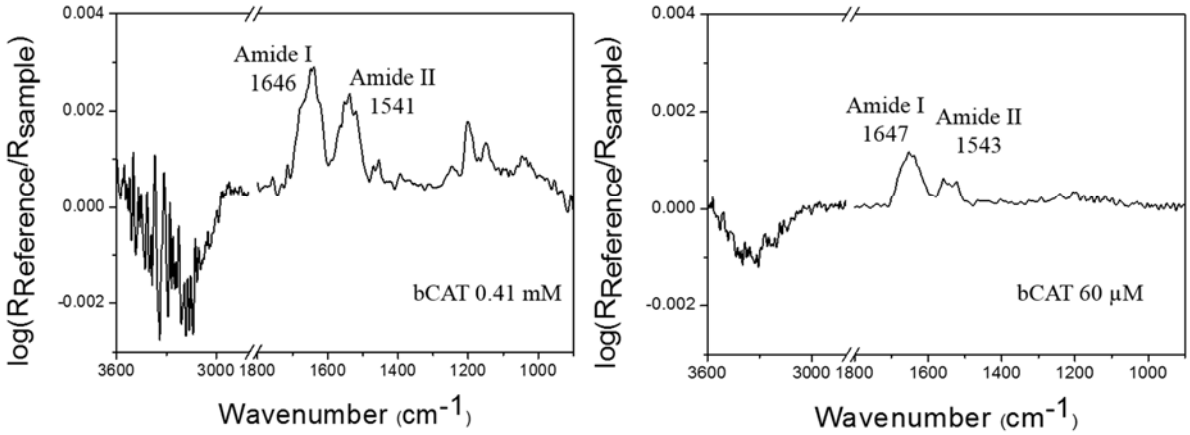


Figure 3-16. ATR-FTIR spectra of bCAT in aqueous solution. **a)** 0.41 mM mother solution on diamond. **b)** 60 µM solution on germanium.

Spectral evolution was monitored for 2 h after bCAT addition for DPPC, DOPC and mixed DPPC/DOPC SLBs with bCAT final concentration of 60 µM. For each series, the background was the spectrum of the SLB before the injection of bCAT, allowing the observation of the spectral evolution within time only due to bCAT injection. As in the case of colistin, the Amide I and II bands increased immediately after bCAT injection (figure 3-17), though for the mixed DPPC/DOPC bilayer the increase was slower at the beginning of the experiment than for the two pure lipid bilayers (figure 3-17c). Because of possible disturbance rising from water bending in the Amide I region, care needs to be taken when analysing the Amide I band. In the case of DPPC SLB, the Amide I band wavenumber shifted to higher wavenumbers (1654 cm^{-1}), with respect to the one in pure bCAT solution (1646 cm^{-1}). This could indicate a change in the bCAT secondary structure from a random coil to an α-helix [41, 215] when the DPPC bilayer is present (table 3-2).

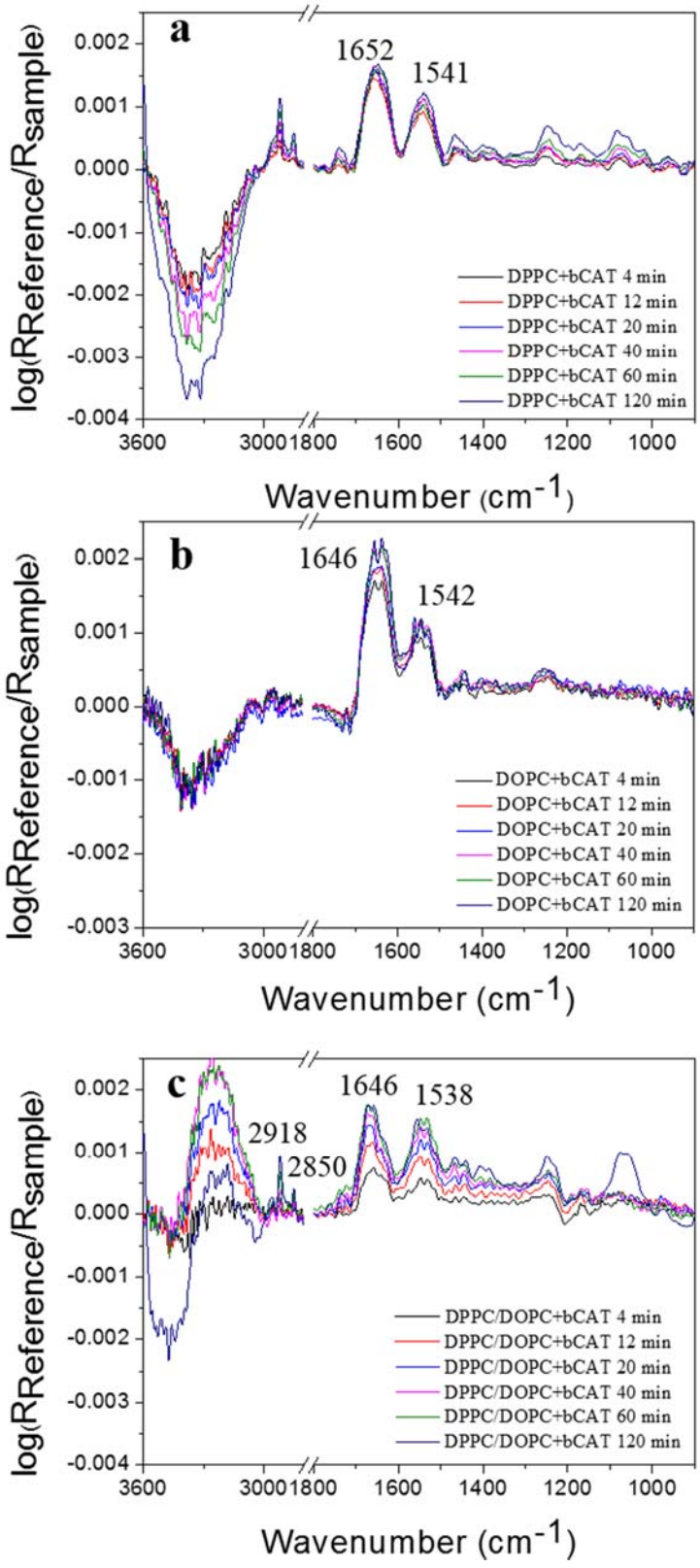


Figure 3-17. Time-evolution of the ATR-FTIR spectra of the phospholipid SLBs on the Ge crystal in the presence of 60 µM bCAT with rinse of the SLB before bCAT injection. The background spectra are the SLBs before bCAT injection. **a)** DPPC **b)** DOPC **c)** DPPC/DOPC SLB.

Also the Amide II wavenumber (1554 cm^{-1}) in the presence of DPPC was higher in the beginning of the experiment, with respect to the Amide II wavenumber of pure bCAT solution (1544 cm^{-1}), but decreased over time closer to the wavenumber of pure bCAT solution (figure 3-18a). Interestingly the characteristic antisymmetric and symmetric νCH_2 bands of DPPC at 2918 and 2850 cm^{-1} increased from the very beginning of bCAT injection. This was not seen on the rinsed DPPC SLB with colistin.

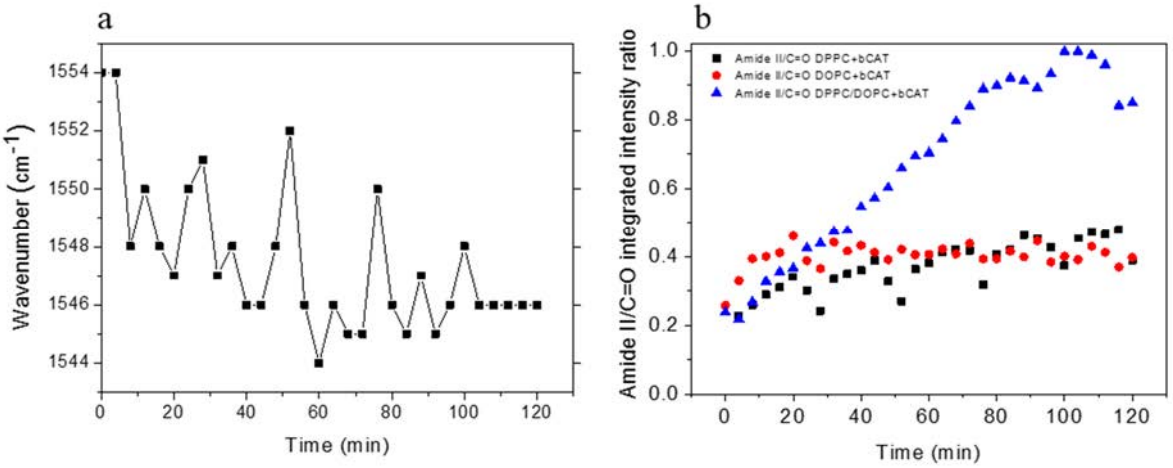


Figure 3-18. a) Change of Amide II band wavelength in DPPC bilayer within time after bCAT injection. **b)** Time-evolution of integrated intensity ratios Amide II/νC=O during the action of bCAT at 60 µM for DPPC (black squares), DOPC (red discs), and DPPC/DOPC (blue triangles) SLBs. Integration regions: νC=O: 1760-1712 cm^{-1}, Amide II: 1580-1485 cm^{-1}.

The growth of the intensities of νCH_2 bands suggests that the DPPC bilayer came into a closer contact with the ATR crystal due to the action of bCAT. This phenomenon was supported by the fact that the integrated intensities of νOH vibration around 3400 cm^{-1} became more and more negative, indicating that water was replaced by PLs at a close proximity of the crystal. Weak bands at 1088 cm^{-1} ($\nu_a PO_2$-) occurred in the spectrum around 10 min after the injection of bCAT and the νC=O at 1736 cm^{-1} was detectable around 20 min after injection. The growth of intensity and shift of the wavelengths of the asymmetric phosphate vibration at 1088 cm^{-1}, of the DPPC SLB were also produced by bCAT, due to which the $\nu_a PO_2$- band shifted to a lower wavelength within time, down to 1084 cm^{-1} 120 min after bCAT injection. An increase in intensity and shift of the $\nu_s PO_2$- band at 1226 cm^{-1} to 1223 cm^{-1} was also observed. These changes in the phosphate vibration could indicate specific interactions taking place between the peptide and the lipid phosphate group. In the case of DOPC SLB, the Amide I and II band wavenumbers were slightly changed, 1646 cm^{-1} and 1552 cm^{-1}

respectively, with respect to the one recorded for pure bCAT. The wavenumbers however stayed rather constant throughout the experiment. This could suggest that the random coil bCAT does not change its secondary structure when a fluid phase lipid is present (table 3-2). In this regard, the spectra of mixed DPPC/DOPC SLB seemed to adopt the properties of the two separate lipid cases, with Amide I and II bands showing at 1651 cm^{-1} and 1540 cm^{-1} respectively, suggesting that in the presence of the mixed bilayer, the peptide could be found in a random coil and α-helix conformation simultaneously (table 3-2). These findings are supported by other authors who have reported a percentage of 30% for α-helix secondary structures of a similar peptide, cateslytin, in the presence of DMPC, with a lipid:peptide molar ratio of 150 [113]. According to the νCH_2 bands (at 2923 and 2853 cm-1) of the DPPC/DOPC bilayer before bCAT injection, DOPC seemed to be more abundant in the bilayer (data not shown). However, after the bCAT addition, the increasing νCH_2 bands were found at 2918 and 2850 cm^{-1}, suggesting that the gel phase DPPC was the primary component of the bilayer to act under the peptide action.

Table 3-2. Suggested secondary structures based on wavenumbers for bCAT in the presence of different phospholipid bilayers (based on [215]).

Sample	**Amide I wavenumber** (cm^{-1})	**Suggested bCAT structure**
DPPC	1654	α-helix
DOPC	1646	random coil
DPPC/DOPC	1651	random coil/α-helix
bCAT (in solution)	1642	random coil

The Amide II/$\nu C{=}O$ integrated intensity ratios were calculated as a function of time for all the SLBs and are presented in figure 3-18b. The ratios increased for all the experiments, however, the growth was significantly (2.6 fold) higher for the mixed SLB, suggesting that for the mixed bilayer, also in the case of bCAT, the peptide was in higher concentration in the field of the evanescent wave. When looking at the Amide II band integrated intensities of the four different samples (bCAT alone, DPPC, DOPC and DPPC/DOPC), the increase in the band areas were very similar in the cases of pure bCAT solution and DOPC SLB, however, for DPPC and DPPC/DOPC SLBs the Amide II band area increase was much more significant and within time, reached even 6 fold the original area at 0 min after bCAT injection (data not shown). This indicates a higher affinity of bCAT towards the two latter SLBs. The dichroic ratios were calculated from the integrated intensities of the CH_2 antisymmetric stretchings also for the bilayers with bCAT and the values

were found to be 0.94, 1.06, 1.00 for DPPC, DOPC and DPPC/DOPC SLBs respectively (mean values from 4 spectra) before the bCAT injection. The calculated values after 2 h of bCAT action were 0.98, 1.00 and 0.97 respectively. As an example, polarized spectra (at 0° and 90°) of the CH_2-stretching region of DPPC bilayer before and 2 h after bCAT (60 µM) injection is shown in figure 3-19. These variations were considered too low to be significant, and no significant structural change in the SLB following the bCAT addition can be evidenced.

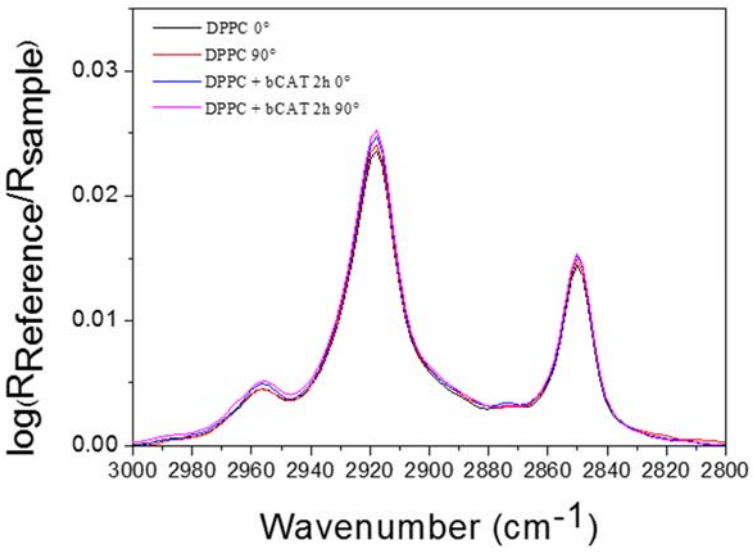


Figure 3-19. Polarized spectra at polarization angles of 0° and 90° of the CH_2-stretching region of DPPC bilayer before and 2 h after bCAT (60 µM) injection.

The action of bCAT on DPPC/DOPC PL model was evaluated by morphological and mechanical analyses at 60 µM bCAT concentration in TRIS buffer. The topographical results before and within time after bCAT injection are reported in figure 3-20.

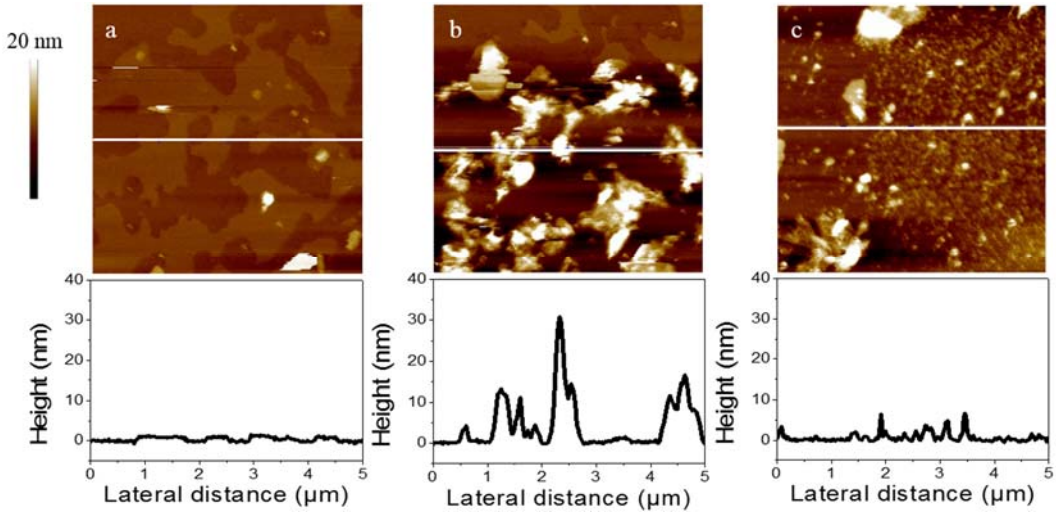
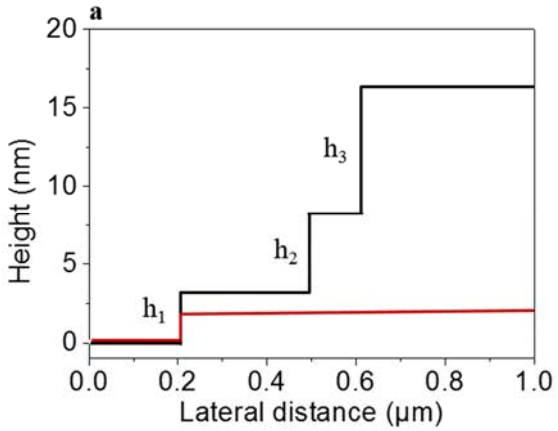


Figure 3-20. Atomic force microscope topographical images of DPPC/DOPC SLBs immersed in TRIS buffer **a)** before **b)** 5 min and **c)** 60 min after bCAT (60 μM) injection.

AFM images taken of the DPPC/DOPC SLB before bCAT injection show a single height difference of 1.24 ± 0.18 nm (figure 3-20a) corresponding the height difference between the two PL domains. AFM images showed that the SLB topography was immediately altered especially in the middle of the DPPC domains 5 min after the injection of bCAT (figure 3-20b) and three distinct heights could be detected at the proximity of the phase boundaries. Their heights are shown in figure 3-21.



b

	h_1 (nm)	h_2 (nm)	h_3 (nm)
Before injection	1.24 ± 0.18	-	-
5 min after injection	3.34 ± 0.98	2.36 ± 0.76	7.56 ± 2.15

Figure 3-21. a) Red line: h_1 before bCAT injection, black lines: three distinct heights, h_1, h_2 and h_3, seen at the phase boundaries of the DPPC/DOPC system 5 min after bCAT injection **b)** Values and standard deviations of the phase boundary heights. Each value obtained from an average of 10 different height profiles.

Supposedly these height differences could represent multiple layers, or aggregates, of the bCAT molecule first attacking the DPPC lipid phase. The detected defects continued to dramatically change within 60 min after injection (figure 3-20c). The cross section analysis revealed total height

differences going up to 35 nm at times between 5 and 30 min after injection, with intermediate steps of heights around 10 nm (data not shown). At 10 min after bCAT injection the h_1 height (3.34 ± 0.98 nm) disappeared, indicating a disappearance of the phase boundaries of the two lipid domain phases due to bCAT. At around 40 min after bCAT injection, the sample settled and stabilized to its final structure, as shown in figure 3-20c, with height differences varying from 1-7 nm, probably rising from the height differences of the two different lipids and the peptide incorporated in between the PL molecules.

Before the injection of bCAT, the statistical analysis of the elasticity showed a bimodal distribution for the DPPC/DOPC SLB (figure 3-22a, bottom panel) with peak centres at 12.6 and 15.1 MPa. As mentioned, the highest value of the elasticity can be attributed to the gel phase composed of DPPC while the lower can be attributed to the fluid phase of DOPC. These two phases are also distinguishable in the DMT map of figure 3-22a, top panel. The inspection of elasticity maps and distributions of DPPC/DOPC SLB after the injection of bCAT (60 µM) reveals that at 5 min after injection the elastic distribution slightly broadens, the peak values coming to 9.30 and 14.6 MPa (figure 3-22b, bottom panel). This change is also seen in the DMT maps of figures 3-22a and 3-22b (top panel) in which the DPPC domains show to lose stiffness whilst the DOPC parts have become stiffer. However, after 5 min the total stiffness of the sample starts to increase (data not shown) and continues to do so until 60 min after injection, with elastic distribution peak values of 22.1 and 32.2 MPa (figure 3-22c). The Gaussian distribution of the total DPPC/DOPC SLB elasticity became broader within time after bCAT addition.

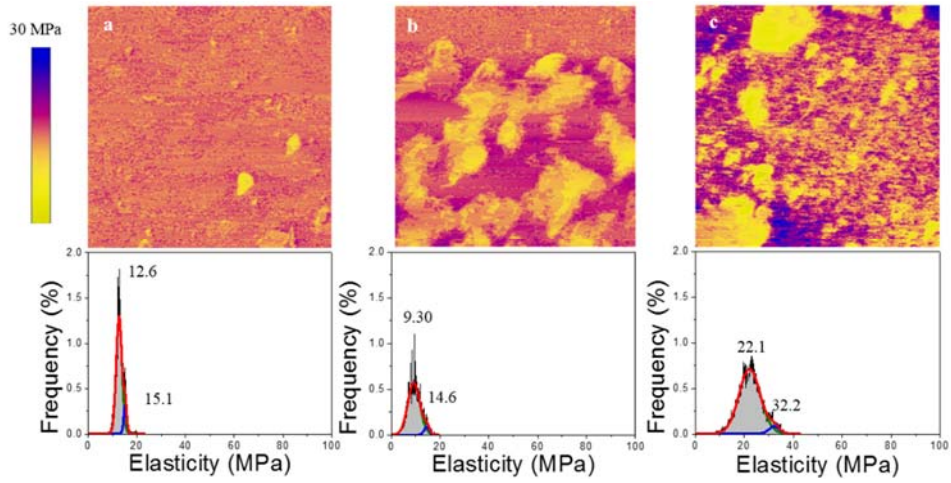


Figure 3-22. Derjaguin-Muller-Toporov (DMT) modulus images (top panel) and elasticity distributions (bottom panel) of supported DPPC/DOPC SLBs in TRIS buffer **a)** before, **b)** 5 min and **c)** 60 min after bCAT (60 µM) injection.

Looking at the AFM and ATR-FTIR data, it seemed that bCAT accumulated on the DPPC domains of the mixed DPPC/DOPC bilayer and interacted specifically with the gel lipid phase. This is supported by the fact that multiple spectral changes was seen specifically concerning the DPPC SLB and the DPPC domains of the mixed DPPC/DOPC SLB, such as the increase of the νCH_2 and $\nu_s PO_2$ stretching band intensities, and notably the change in the secondary structure of the peptide from random coil to α-helix. The topographical AFM images also show the peptide to attack more aggressively on the DPPC domains of the mixed bilayer. It could be hypothesised that the rigid, highly ordered gel phase lipid molecules were in an optimal orientation for the peptide to interact with the polar heads of the PLs. The peptide could incorporate itself between the DPPC molecules, change its secondary structure, thicken and disorganise the DPPC domain, resulting in an alteration of the elastic and topographical properties of the membrane. Increase in membrane rigidity due to the action of a similar peptide, cateslytin, has been previously reported [113]. Even though these increased membrane rigidities have been reported for a mixture of zwitterionic and negatively charged phospholipids in the case of cateslytin, attention should be paid on the results obtained here with purely zwitterionic membranes and bCAT. In particular to the fact that even though the peptide does not form (at least in amounts detectable with ATR-FTIR) β-sheet structures in close contact with zwitterionic PLs, the α-helix structure of bCAT could be the cause for changes in the membrane physico-chemical properties.

3.3 Lipopolysaccharide bilayer interaction with antimicrobial peptides

3.3.1 Morphological characteristics of LPS bilayers

SLBs of LPS were formed by vesicle fusion method, then incubated or not with an AMP, rinsed with deionized water and dried under a gentle stream of nitrogen. The morphology of the LPS SLBs (figures 3-23a, 3-25a, 3-27a and 3-29a) investigated by AFM was in accordance with observations reported in the literature on similar compounds [137, 219]. The Lipid A/LPSt bilayer consisted of Lipid A domains (white arrows on figure 3-23a) and LPS domains of various heights (5-15 nm), with the shorter LPS resulting in a height difference of 2 nm with the Lipid A bilayer. This height difference corresponds to the height of the core of an LPS molecule [219]. The Lipid A/LPS-S bilayer formed, instead of clear domains, rather a network of an alternating Lipid A and LPS-S bilayer on the mica surface, with height differences of around 3 nm (figures 3-25a and 3-29a). This height could correspond to the height of the LPS core and O-antigen portion found in the LPS-S form.

3.3.2 Lipopolysaccharide bilayer interaction with a cyclic antimicrobial peptide

After the bilayer formation with vesicle fusion method, Lipid A/LPSt and Lipid A/LPS-S bilayers were let to incubate with colistin (150 µM) for either 0, 20, 40 or 60 min after which the sample was rinsed with deionized water and dried under a gentle stream of nitrogen to obtain AFM images in air. These images are shown in figures 3-23 and 3-25 for Lipid A/LPSt and A/LPS-S respectively. The elastic properties of the Lipid A/LPS SLBs were studied in aqueous conditions in real time. The effect of colistin on the Lipid A/LPSt bilayer could already be seen after an incubation time of 20 min (figure 3-23b). The previously seen structure of Lipid A domains had started to disappear and lipid aggregates started to form with height differences up to 30 nm. The phenomenon continued and in the images of 40 min after colistin injection (figure 3-23c), even less Lipid A domains are seen. In the images of 60 min after colistin injection, new rearranged and larger domains can be seen with distinct domain heights of around 5 and 15 nm (figure 3-23c). The peptide had caused a complete rearrangement in the Lipid A/LPSt bilayer in which originally the Lipid A domains were clearly distinguished.

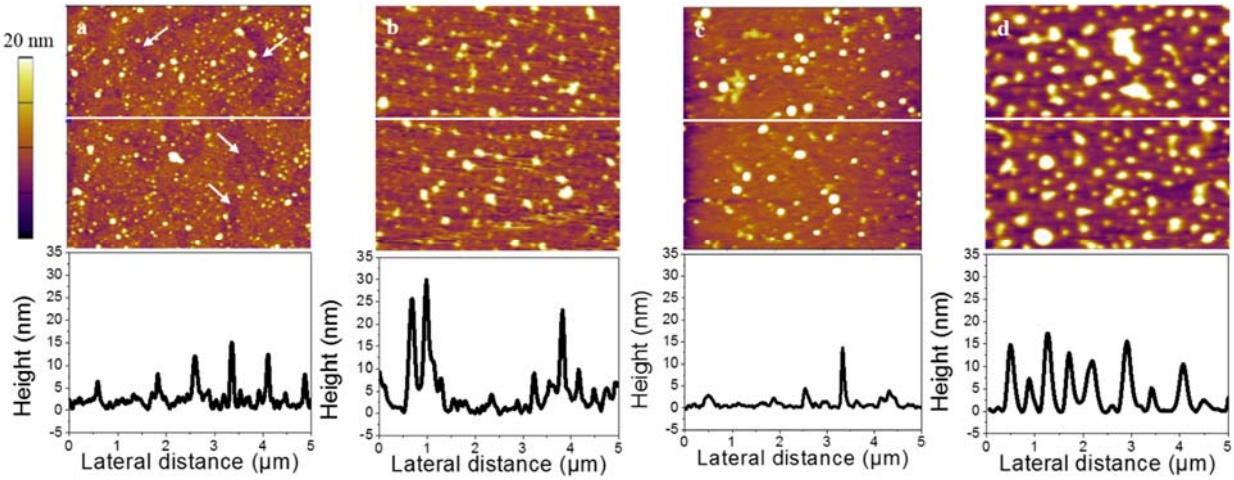


Figure 3-23. Atomic force microscope topographical images of Lipid A/LPSt SLBs in air **a)** before, **b)** 20 min, **c)** 40 min and **d)** 60 min after colistin (150 µM) injection.

The elasticity of the Lipid A/LPSt membrane (figure 3-24) showed a slight gradual increase with time after colistin injection. The initial distribution of the SLB elasticity showed two distinguished peak positions at 60 and 70 MPa (Gaussian fit), whereas the elastic distribution 60 min after colistin injection (figure 3-24b) showed a Gaussian distribution with peak centres at 79 and 90 MPa. On top of the morphological changes due to colistin, the peptide also seemed to have an increasing effect

on the Lipid A/LPSt bilayer stiffness. This could mean that colistin introduced itself between the lipid molecules and caused the membrane to become more rigid.

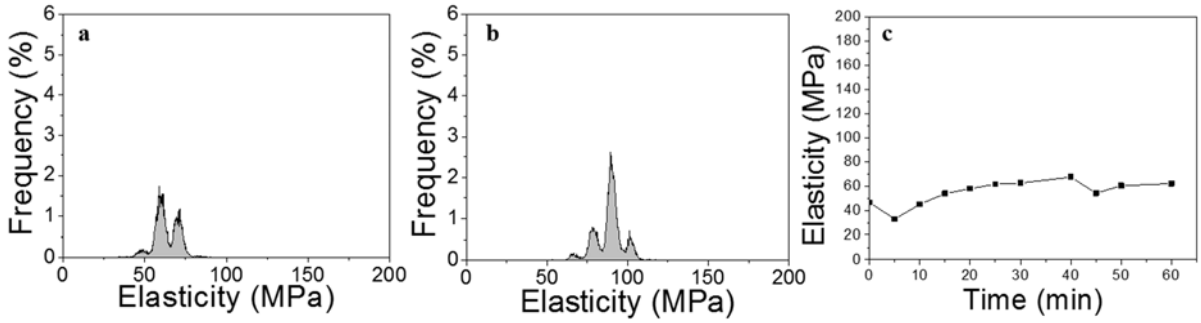


Figure 3-24. Distributions of Lipid A/LPSt SLB elasticity in TRIS buffer **a)** before **b)** 60 min after colistin (150 µM) injection. **c)** Elasticity change within time.

The effect of colistin on the Lipid A/LPS-S bilayer was slower and fewer changes in the structure after an incubation time of 20 min could be seen than for the Lipid A/LPSt sample (figure 3-25b). A slight phase separation could already be seen after 20 min with larger domains being formed. At 40 min after colistin injection (figure 3-25c) most of Lipid A domains had been removed from the surface with only LPS aggregates and domains left, with heights typical to LPS molecules (6-8 nm). However at 60 min after the peptide injection (figure 3-25d), the lipids had rearranged and recovered the mica, the LPS aggregates had disappeared and height differences of 4-8 nm were detected, indicating that Lipid A was again present at the substrate surface.

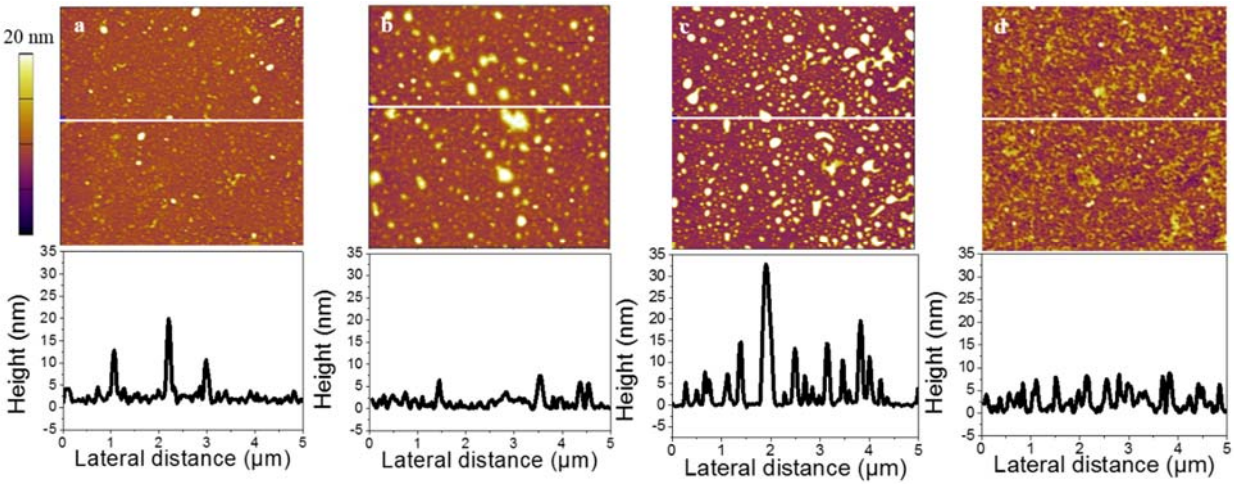


Figure 3-25. Atomic force microscope topographical images of Lipid A/LPS-S SLBs in air **a)** before, **b)** 20 min **c)** 40 min and **d)** 60 min after colistin (150 µM) injection.

The elasticity of the Lipid A/LPS-S membrane (figure 3-26) showed a dramatic decrease immediately at 5 min after colistin injection (data not shown). The initial distribution of the SLB elasticity (figure 3-26a) showed two distinguished peak positions at 67 and 73 MPa (Gaussian fit), whereas the elastic distribution at 60 min after colistin injection (figure 3-26b) showed a bimodal Gaussian distribution with peak centres at 6 and 12 MPa indicating that the peptide had a decreasing effect on the Lipid A/LPS-S bilayer rigidity.

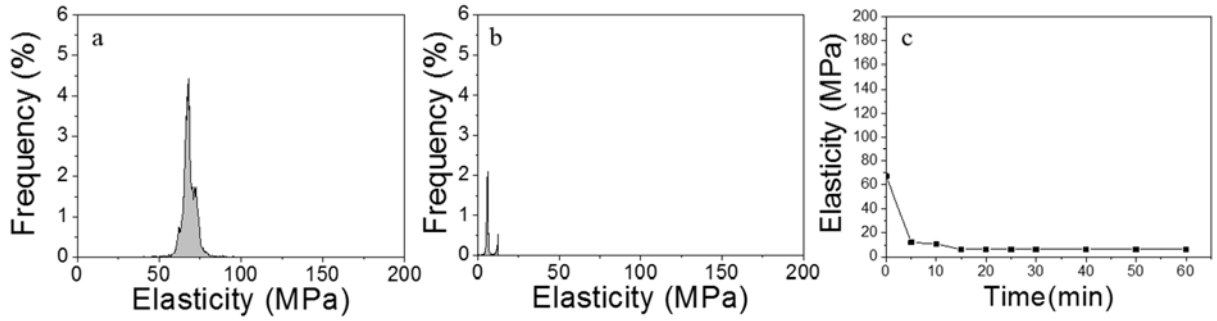


Figure 3-26. Distributions of Lipid A/LPS-S SLB elasticity in TRIS buffer **a)** before **b)** 60 min after colistin (150 µM) injection. **c)** Elasticity change within time.

3.3.3 Lipopolysaccharide bilayer interaction with a linear antimicrobial peptide

After the bilayer formation, Lipid A/LPSt and Lipid A/LPS-S bilayers were let to incubate with bCAT (60 µM) for either 0, 20, 40 or 60 min after which the sample was rinsed with deionized water and dried under a gentle stream of nitrogen. AFM images of the samples were then recorded and these images are shown in figures 3-27 and 3-29 for Lipid A/LPSt and A/LPS-S respectively. Elasticities of the LPS SLBs under the influence of bCAT were studied in aqueous conditions in real-time. The effect of bCAT on the Lipid A/LPSt bilayer was already detected after an incubation time of 20 min (figure 3-27b). Circular structures of bCAT formed on the bilayer, forming pores with height differences of around 20 nm. 40 min after the injection of bCAT, the peptide had become more concentrated on the sample surface, first positioning itself horizontally on the membrane and finally forming pores of various sizes (lateral diameters of up to 5 µm) with height differences ranging up to 150 nm (figure 3-27c).

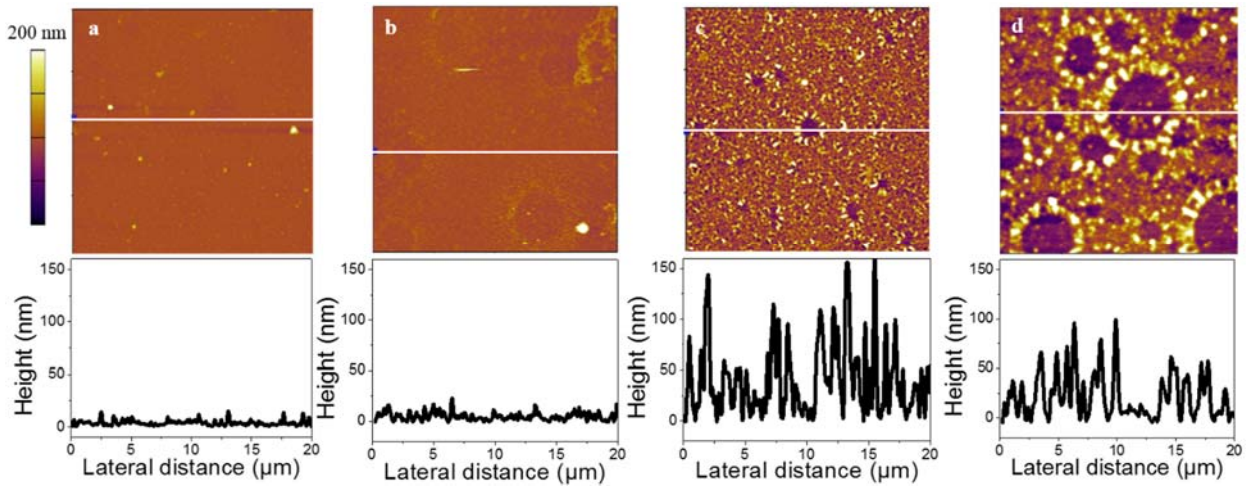


Figure 3-27. Atomic force microscope topographical images of Lipid A/LPSt SLBs in air **a)** before, **b)** 20 min **c)** 40 min and **d)** 60 min after bCAT (60 µM) injection.

The membrane became more porous within time and at 60 min after injection the membrane had a very spongy structure (figure 3-27d), however, the height differences had reduced from 150 to around 100 nm. These images strongly suggest that bCAT could form pores on the membrane, interacting with the Lipid A/LPS moieties of the membrane. Especially in the case when less resistant rough LPS was present. Although a bCAT induced a spongy structure in the Lipid A/LPSt bilayer, the stiffness of the bilayer increased gradually during time after bCAT injection (figure 3-28). After 10 min of bCAT addition (figure 3-28b), the elastic distribution showed peak centers at 123 and 127 MPa and 60 min after the injection a single Gaussian peak at 600 MPa was seen (figure 3-28d), with a much broader shape than in the initial elasticity distribution. This indicated that bCAT incorporated between the lipid molecules and made the membrane more rigid, yet permeable due to the formed pores.

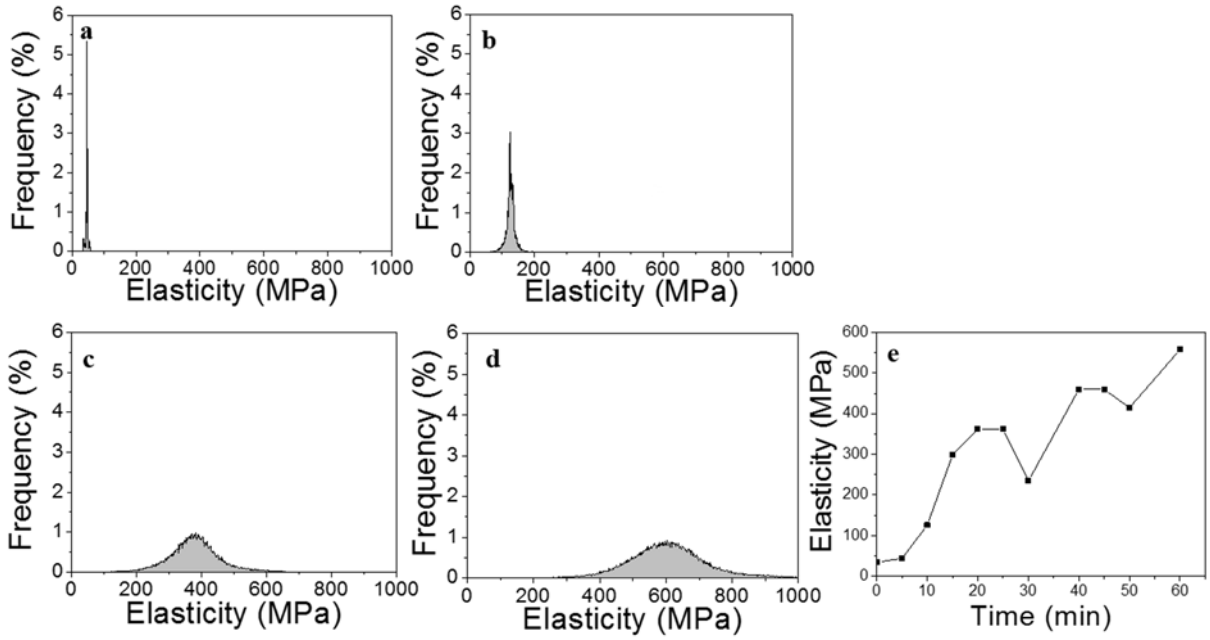


Figure 3-28. Distributions of Lipid A/LPSt SLB elasticity in TRIS buffer **a)** before, **b)** 0 min, **c)** 20 min and **d)** 60 min after bCAT (60 µM) injection. **e)** Elasticity within time.

The effect of bCAT on the Lipid A/LPS-S bilayer (figure 3-29) was very similar to that of colistin, although already at 20 min after bCAT injection (figure 3-29b), the lipid A domains had eroded and only the LPS with height difference of around 8 nm were present. After 40 min (figure 3-29c), the remaining lipids had completely rearranged into small domains equally distributed along the mica surface, still with a height of ~8 nm. Finally, 60 min after bCAT injection (figure 3-29d), the height differences started to decrease again and the lipid domain sizes became smaller (3-5 nm), indicating that the initially eroded Lipid A had been reorganized together with the LPS-S domains. As in the case of colistin, the Lipid A/LPS-S bilayer elasticity distribution (figure 3-30) decreased gradually within time after bCAT injection, initially having a bimodial distribution similar to the one described previously for Lipid A/LPS-S, but 60 min after bCAT action the peak centres of the bimodal Gaussian distribution were found at 11 and 12 MPa. The action of bCAT resulted in a decrease of the rigidity of the bilayer.

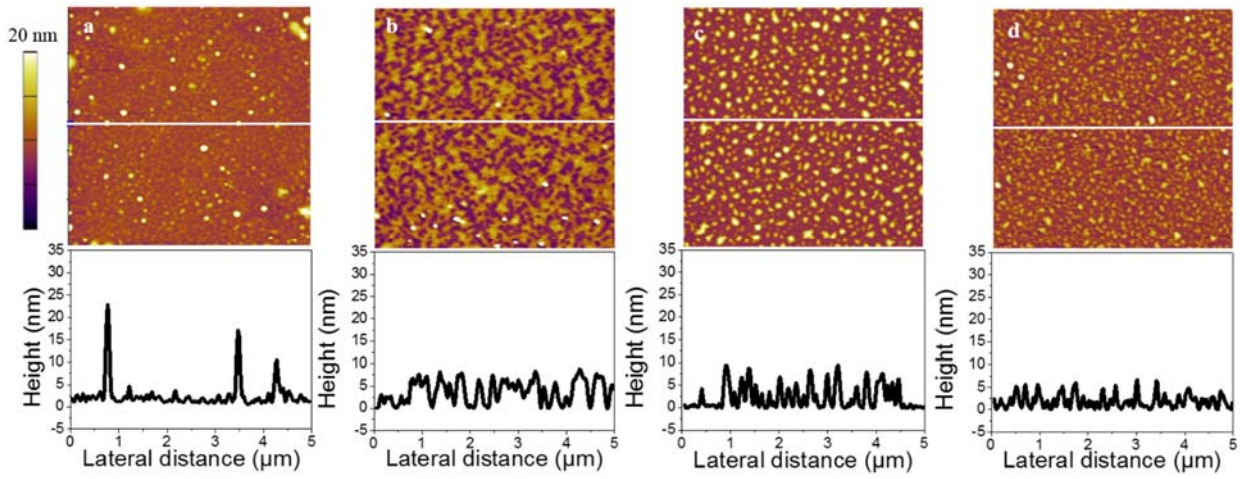


Figure 3-29. Atomic force microscope topographical images of Lipid A/LPS-S SLBs in air **a)** before, **b)** 20 min **c)** 40 min and **d)** 60 min after bCAT (60 μM) injection.

Interestingly, the action of the two different peptides both seemed to be very similar on the Lipid A/LPS membranes, depending on the LPS content of the membrane. It could be concluded that the effect of AMPs on Lipid A/LPS bilayers was most drastic for the Lipid A/LPSt bilayer with bCAT, since large holes appeared in the membrane and the membrane elasticity was greatly altered, with a stiffness of 10 times higher than the initial stiffness of the bilayer. Especially in the case of Lipid A/LPS-S membranes, the experiments showed that both of the peptides would rather target the Lipid A domains than the domains containing LPS. In both of the peptide studies including LPS-S, the Lipid A/LPS-S membrane showed an ability to reorganize and recover the mica surface, which was not seen for the Lipid A/LPSt samples. This could be in accordance with the fact that the O-antigen moiety of the LPS molecules plays a crucial role in the defence mechanisms of bacteria.

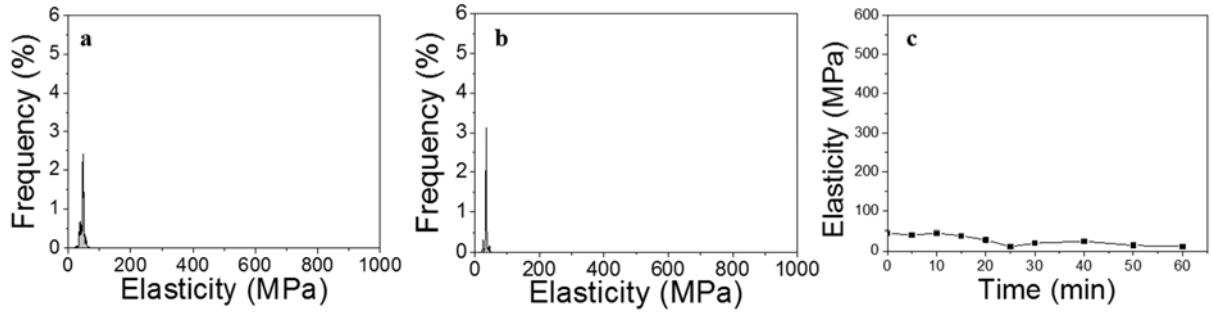


Figure 3-30. Distributions of Lipid A/LPS-S SLB elasticity in TRIS buffer **a)** before **b)** 60 min after bCAT (60 μM) injection. **c)** Elasticity change within time.

3.4 Comparison of the action of a cyclic and a linear peptide on model membranes

In the previous chapters we have demonstrated how phospholipid monolayers and bilayers as well as LPS bilayers with various different compositions were subjected to two distinct antimicrobial agents with different concentrations; colistin being a cyclic polycationic peptide produced by *Basillus polymyxa* and catestatin being a linear antimicrobial peptide produced by eukaryotic cells. The model PL membranes subjected to colistin included DPPC, DOPC, DPPE as well as mixed DPPC/DOPC and DPPE/DOPC mono- and bilayers. Langmuir isotherms of PL monolayers showed a liquefaction of the samples under the presence of colistin and supported the findings in the changes of the elastic properties studied by AFM force spectra on the mixed PL bilayers. The changes in A_{coll} values of the mixed PL monolayers was more important than those found in pure PL monolayers, suggesting that colistin could be more likely to penetrate into a mixed PL membrane. This was supported by the spectral evolution recorded by ATR-FTIR on PL bilayers; the Amide II/νC-O ratio integrated intensities of mixed DPPC/DOPC was more important than those of pure PL bilayers. Severe morphology changes of the bilayers could only be seen at the very high concentration of colistin, and in this case, the action was mainly directed against the fluid lipid phase (DOPC) of the system. The PL bilayers subjected to bCAT included DPPC, DOPC and a mixed DPPC/DOPC. As seen in the case of colistin, the Amide II/νC-O ratio integrated intensities obtained by ATR-FTIR of mixed DPPC/DOPC with bCAT was more important than those of pure PL bilayers. Despite the high concentrations of AMPs used (10, 50 and 150 µM for colistin and 60 µM for bCAT), the spectral evolution evidenced that the interactions of the bilayers and the AMPs were non-specific, except for the DPPC bilayer for which changes in the phosphate group vibrational bands were detected. However, based on the changes in the wavenumbers of the Amide I band of the linear bCAT peptide as a function of different PL bilayers present, this peptide could adopt various secondary structures when in contact with different lipids. Based on the morphology changes detected by AFM imaging and on the ATR-FTIR spectra, the influence of bCAT also seemed to be more directed on the gel phase DPPC, unlike in the case of colistin which, based on morphological images, rather attacked the fluid phase DOPC part of the lipid system. However, some changes of DPPC bilayer were seen when in contact with colistin, these changes mostly directed to the polar head groups of the PL molecules according to the ATR-FTIR findings. Figure 3-31 illustrates a hypothesized mechanism of action of the two AMPs on DPPC/DOPC bilayers. Colistin could cause phase boundary defects (red arrows in figure 3-31a middle panel) at 50 µM concentration, at which it primarily interacts with the polar head groups of the DPPC. However at

150 μM concentration (figure 3-31a bottom panel) colistin could trap DOPC into aggregates and detach the fluid phase lipid from the surface.

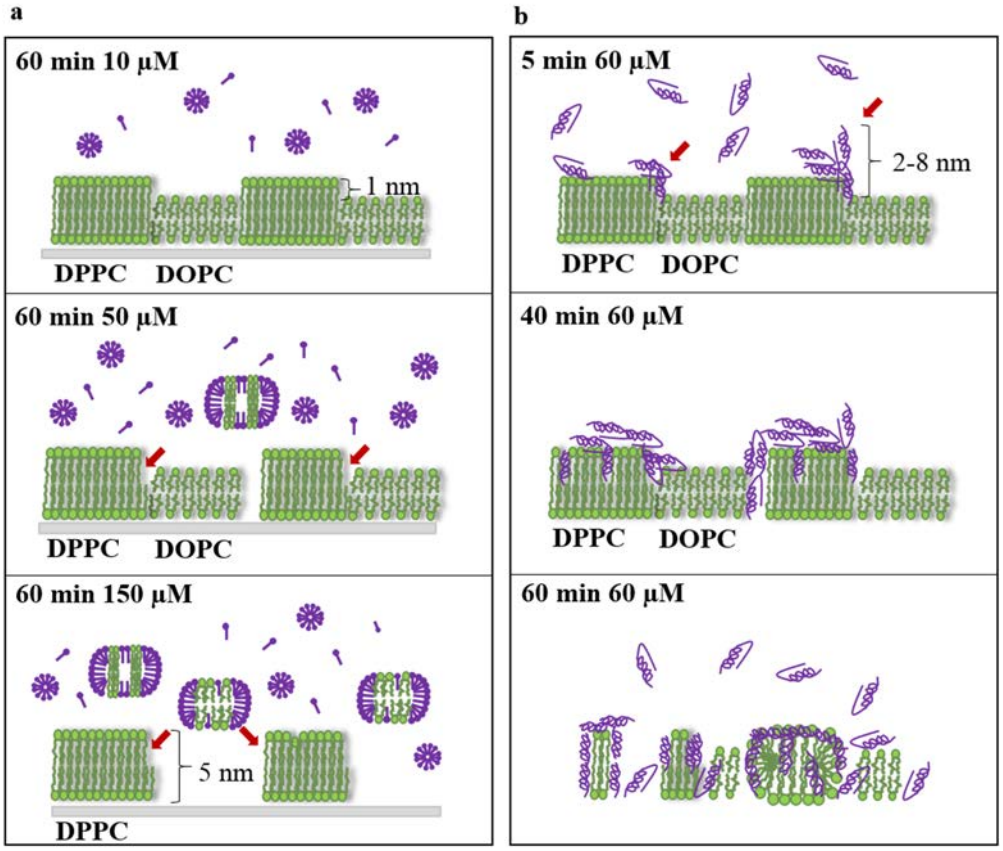


Figure 3-31. Hypothesized mechanism of action of the two AMPs on DPPC/DOPC bilayers. **a)** colistin as a function of concentration at 60 min after peptide injection **b)** bCAT (60 μM) as a function of time after bCAT injection.

bCAT could first accumulate on the phase boundaries of the two lipid domains (figure 3-31b top panel), primarily interacting with the entire DPPC molecules and changing its conformation in the presence of this PL (figure 3-31b middle panel), finally disorganizing the complete membrane structure (figure 3-31b bottom panel).

Concerning the interaction of these two antimicrobial agents with LPS molecules, two different lipid systems were used and examined trough AFM imaging and force spectra; equimolar mixtures containing Lipid A/LPSt and Lipid A/LPS-S. The initial elastic properties of these two systems were very similar; however the action of the peptides on both systems differed from each other. In the case of both of the peptides, the rigidity of the LPSt bilayers increased, whereas the stiffness of the LPS-S membrane decreased. Interestingly the peptide action reduced the stiffness of the Lipid

A/LPS-S bilayer in both peptide cases, which is when only smooth, O-antigen containing LPS was present. This difference between the actions of the peptides in the case of the two LPS molecules with different O-antigen chain lengths could be related to the differences in the packing of the molecules within the bilayer, caused by the different chain lengths. It is also possible that the presence of the long O-antigen chain perturbs the binding of the peptides into the core of the LPS molecules and the resulting differences are seen in the two distinct behaviors of the membrane elasticities with two different LPS compositions. It is known that colistin recognizes LPS molecules with a two-step mode including a fast initial association followed by a less rapid insertion, a mechanism that has also been suggested for other antimicrobial peptides [220]. Based on the morphological images, both of the peptides induced the Lipid A/LPS membranes to restructure, with the exception of the Lipid A/LPSt bilayer in the case of bCAT on which bCAT positioned on the surface of the membrane and started to from pores that grew in size with time. The morphological differences that followed the injection of bCAT into the Lipid A/LPSt bilayer suggest that the linear, positively charged bCAT could first bind to the core of the LPS by electrostatic interactions and then accumulate at the hydrophobic lipidic core of the LPS molecule to form pores seen in image 3-26. However, all of these hypotheses on LPS bilayers need to be investigated in the future, with a broader spectrum of different techniques. Nevertheless, based on these results, at the level of the LPS molecules, it is possible that these two peptides initiate their action in a similar or close to similar manner.

4. Antimicrobial peptide action on bacterial biofilms

4.1 Bacterial growth in planktonic form

As the biofilms of the *E2146* strain of *E. coli* had not been previously studied in the laboratory, it was necessary to develop a culture protocol in order to obtain reproducible results and to describe the characteristics of the resulting biofilm. Therefore growth curves of planktonic *E2146* bacteria in S0Ec suspension were realized by taking a sample of 1 mL of the bacterial suspension (SEc0) every 15 min for 4 h and measuring the OD_{600} of the samples during 24 h incubation at 21 ± 1 °C. The resulting growth curves are shown in figure 4-1.

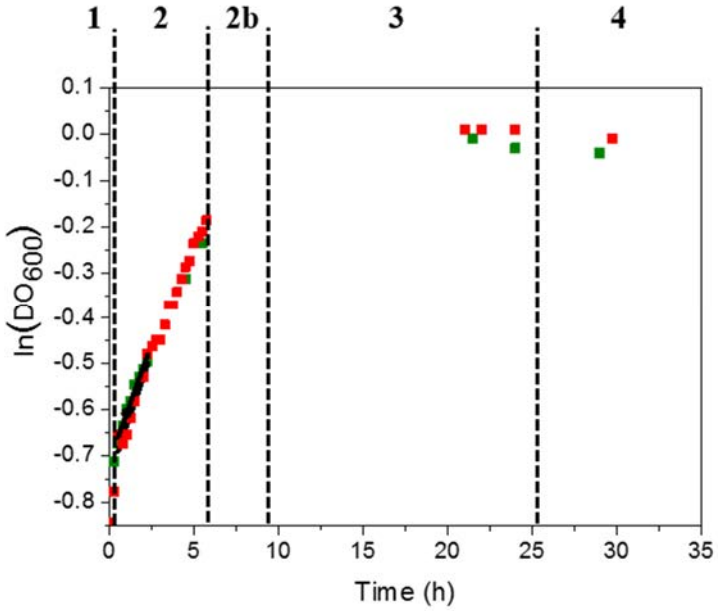


Figure 4-1. Two growth curves of the *E2146* S0Ec suspension with different growth phases (1-4) indicated. **1:** Lag phase, **2:** Exponential growth phase, **2b:** end of exponential growth phase/beginning of stationary phase, **3:** stationary phase, **4:** advanced stationary phase/death phase. Initial OD_{600} for red and green graphs 0.49 and 0.46 respectively.

In a closed environment, bacterial growth typically exposes four distinct stages described by a growth curve: 1) lag phase representing the time period required by the microbes to adapt to their new environment. Due to the lower nutrient content of the LB/10 suspension used as well as low temperature (21°C) of the experimental condition, the growth curves presented for the *E2146* bacteria in suspension in figure 4-1 do not show a lag phase. However an acceleration time of around 15 min was observed, and followed by 2) log (exponential) phase representing the time

period of optimal growth where the growth rate (μ) increases progressively. The growth rate corresponds to the slope of the growth curve in the exponential phase (figure 4-1, solid black line) and can be used to calculate a generation time (G), defined as the time interval required for the bacterial population to double (equation 14) [221]. For the *E2146* growth curve the exponential phase lasted for 300 min (figure 4-1). At the end of the exponential phase (2b) seen at 5 h, the micro-organisms approach the upper limit of the continuous growth and enter a 3) stationary phase. Finally when waste products started to accumulate and nutrition supplies exhaust, 4) the death (decline) phase occured [222], seen as a decline of the growth curve at 24 h, starting from the last dashed line in figure 4-1). At this stage, the bacteria are lyzed due to the action of secondary metabolites and pH changes in the growth medium.

$$G = \frac{\ln(2)}{\mu} \qquad \text{Equation 14}$$

For the growth curves of *E2146* SEc0 presented in figure 4-1, the μ values were 0.0017 and 0.0018 generations/min for the green and red curves respectively, and the corresponding generation times were calculated according to equation 14. Generation times of 408 and 385 min were obtained for the green and blue curves respectively, and an average growth rate of 0.00175 min^{-1}. Sezonov *et al*. have found a generation time of 20 min for an *E. coli* K12 *MG1655* strain in LB solution [223] and previously a generation time of 27 min for the *E2146* strain in LB medium has been calculated in our laboratory at 37 °C. The nutritive solution used in this present study was 10 times more diluted and the temperature was 16 °C lower than in the studies of Sezonov *et al*. This being said, a generation time difference of at least one order of magnitude can be expected. Indeed the generation time found for the *E2146* strain in LB/10 medium and 21 °C was around 20 times slower than in the case of *E. coli* suspension in LB nutritive media with a temperature of 37°C. The time at the middle of the exponential phase of the growth curve at 2.5 h was chosen as an inoculation time for the biofilm formation process, after which a nutrient media change took place.

Similarly, a growth curve was obtained for the S1Ec1 *E2146* bacterial suspension (figure 4-2). This growth curve was destined to correspond to the change of the nutrient media in the biofilm formation processes.

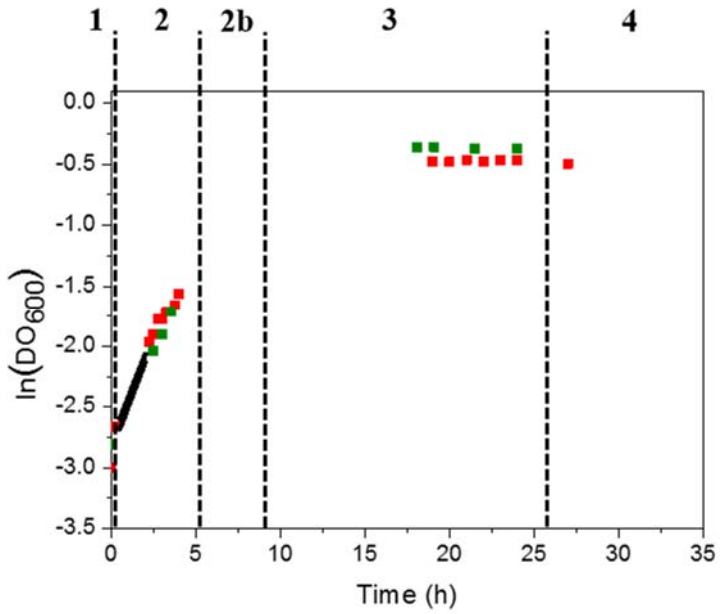


Figure 4-2. Two growth curves of the *E2146* S1Ec suspension with different growth phases (1-4) indicated. Initial OD_{600} for red and green lines 0.05 and 0.06 respectively.

The μ values were 0.0061 and 0.0059 generations/min for the green and red curves respectively, and the corresponding generation times were calculated to be 114 and 117 respectively. These kinetic parameters being more optimal with respect to the ones obtained for the SEc0 suspension show that the bacteria had adapted to the change of the nutritive media.

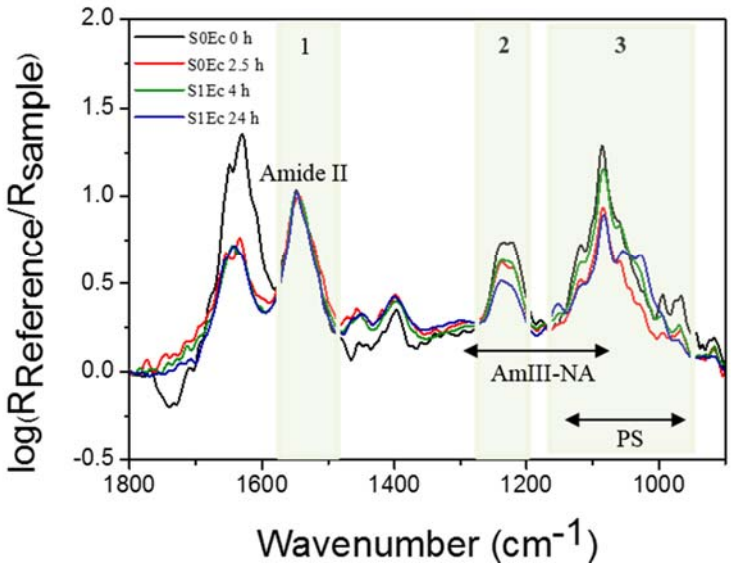


Figure 4-3. ATR-FTIR spectra of *E2146* bacterial suspensions on a diamond crystal; S0Ec at 0 h (black) and 2.5 h (red), S1Ec at 4 h (green) and 24 h (blue). Different spectral zones indicated; 1: Amide II, 2: AmIII-NA, 3: PS total. Spectra normalized with respect to Amide II band.

In order to study the metabolic variations of the *E2146* pellets as a function of different growth phases, FTIR-ATR spectra was recorded of both, the S0Ec and S1Ec samples. The spectra of S0Ec suspension at its exponential phase at 2.5 h and the spectra of S1Ec suspension at its exponential phase at 4 h, normalized with respect to Amide II band are shown in figure 4-3. The principle attributions of ATR-FTIR absorption bands of *E2146* S0Ec suspension in exponential phase on diamond crystal are listed in table 4-1. The region at 1800-900 cm^{-1}, *i.e.* the fingerprint region, shown in figure 4-3 is associated to the characteristics of the bacteria and contain several distinct and interesting bands of the biomolecules of the microbes. These include the Amide I and II bands at 1642 and 1547 cm^{-1} respectively, the Amide II band being associated to the proteins produced by the bacteria (zone 1 in figure 4-3). The region at 1340-1190 cm^{-1} (zone 2 in figure 4-3, hereafter called AmIII-NA) describes the antisymmetric stretching of the phosphate groups of nucleic acids and phospholipids as well as the Amide III band of proteins. Finally, a large massif is observed in region 1185-950 cm^{-1} (zone 3 in figure 4-3, hereafter called PS total), which is attributed to the stretching vibrations and deformations of polysaccharides as well as to the symmetric stretching of the phosphate groups of phospholipids and nucleic acids. The Amide II bands at 1547 cm^{-1} had very similar profiles for all of the samples illustrated in figure 4-3. Similarities of peak profiles could also be found from the region of the Amide III-NA and, in the samples at exponential growth phases, from the PS total. It is however noteworthy that the relative intensities of the Amide III-NA (1237 cm^{-1}) and PS total (1086 cm^{-1}) bands were at their maximal at the beginning of the exponential phase of the S0Ec suspension (black spectrum) and decreased at 2.5 h (red spectrum). The decrease in the relative intensity of the Amide III-NA band with respect to that of Amide II band indicates that the spectral contribution of the PO_2^- of the nucleic acids and phospholipids became less important than those of proteins and suggest a maximal nucleic acid synthesis taking place at the beginning of the exponential phase of the S0Ec suspension (black spectrum), at which the cells divide very actively [160]. In the S1Ec suspension at 4 h (green spectrum), the relative intensity of the PS total band again increased, but the relative intensity of the Amide III-NA remained at the same level than in the S0Ec suspension at 2.5 h. The nucleic acid production had thus remained similar; however the bacteria were producing more polysaccharides, especially glycogen which can be detected as a shift of the maximum of the massif, at the symmetric PO_2^- vibration, from 1086 cm^{-1} to 1084 cm^{-1} and as additional bands rising at 1059 cm^{-1} and 1043 cm^{-1}. These characteristics of glycogen production are already observed at 4 h. Glycogen is an intracellular reserve polymer and bacteria use glycogen biosynthesis to store carbon and energy reserves in the risk of possible starvation conditions [224].

Table 4-1. Principal attributions of ATR-FTIR absorption bands of *E2146* S0Ec suspension in exponential phase on diamond crystal. ν_s: symmetric stretch, ν_a: antisymmetric stretch, δ: deformation.

Wavenumber (cm^{-1})	Vibration	Attribution
~3400	νO-H [225, 226]	Water, proteins, polysaccharides
3288	νN-H	Amide A of proteins [225]
2971-2852	ν_aC-H_n, ν_sC-H_n (n=2, 3)	Fatty acids [225, 226]
1747	ν >C=O [226, 227]	Lipid esters [160]
1642	Amide I: 80% νC=O, 10% νC-N, 10% δN-H [160, 164, 225, 226]	Proteins [225]
1547	Amide II: 60% δN-H, 40% νC-N [160, 164, 225, 226]	Proteins [225]
1457	δCH_n (n=2, 3) [225, 226]	Lipids [160]
1397	ν_sC=O of CO_2^- [225, 226]	Proteins, lipids
~1300	Amide III : 30 % νC-N, 30% δN-H, 10% νC=O, 10 % δO=C-N [160, 225]	Proteins [225]
1236-1221	ν_aP=O of $>PO_2^-$ [225, 226]	Phosphodiesters [225], nucleic acids, phospholipids, lipopolysaccharides [160]
1154	νC-O-H, νC-O [160]	Polysaccharides [160, 225], proteins
1086	ν_sP=O of $> PO_2^-$ [225]	Phosphodiesters, phospholipids, nucleic acids, polysaccharides [160]
1059	νC-O-C, νP-O-C (R-O-P-O-R') [160]	Polysaccharides

This glycogen production was not seen in the S0Ec suspension. Finally, at 24 h in S1Ec (blue spectrum) suspension when the bacteria were in the advanced stationary phase, the relative intensity of the Amide III-NA had decreased indicating slowing of nucleic acid production, and bands

characteristic to glycogen at 1153, 1055, 1043 and 1028 cm^{-1} are clearly detected. These bands have completely changed the profile of the PS total spectral massif.

In order to observe the *E2146* membrane permeability in the biofilms, the suitability of the *Bac*Light ™ kit together with the GFP fluorescing *E2146* bacteria had to be verified. Figure 4-4 illustrates *Bac*Light ™ stained planktonic *E2146* bacteria at various stages and times. Samples of S0Ec suspension harvested at 0 min showed that 30-50% of the bacteria had damaged cell membranes (figure 4-4b), most likely due to centrifugation taking place in the previous step. The appearance of red fluorescing cells also confirmed the proper functioning of the staining kit on the bacterial strain in question. However, when observing the S0Ec suspension at 2.5 h and S1Ec suspension at 3 h (figures 4-4c and d respectively) with epifluorescence microscopy, it was seen that most of the *Bac*Light ™ stained bacteria fluoresced in green, indicating that their cell membranes were intact. As a result, it was concluded that the bacteria could recover from the centrifugation and the centrifugation caused only temporary damage to the cell membranes. Thus the *Bac*Light ™ kit was considered to be suitable for the biofilm experiments.

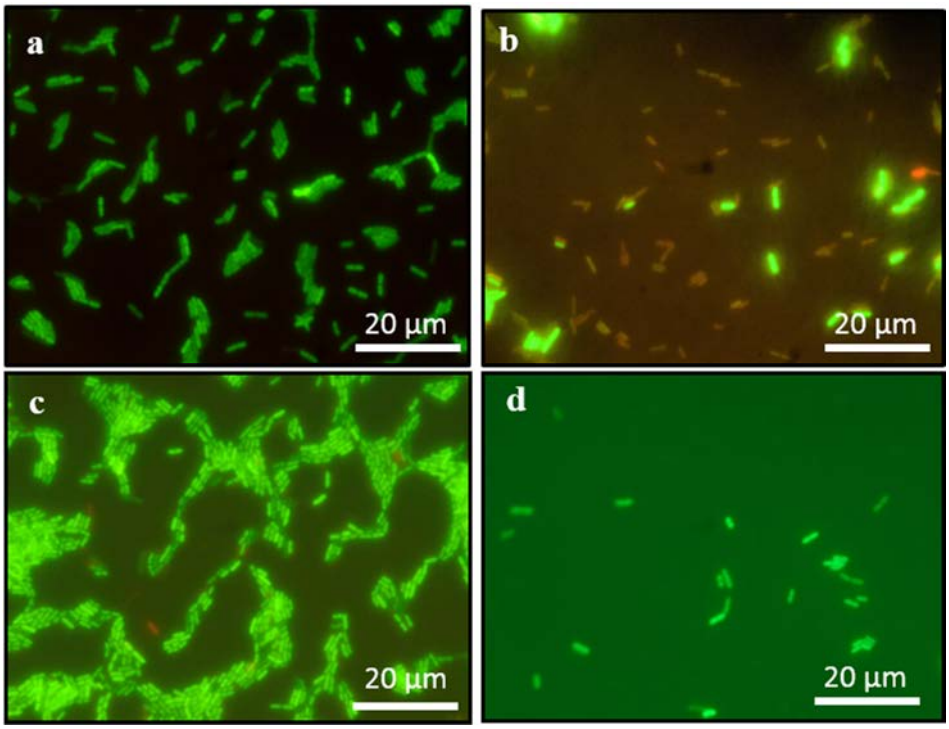


Figure 4-4. Epifluorescence images of the *Bac*Light™ stained *E2146* suspensions **a)** culture at 2 h (initial OD_{600}=0.55) **b)** S0Ec at 0 h (initial OD_{600}=0.46) **c)** S0Ec at 2.5 h (initial OD_{600}=0.49) **d)** S1Ec at 3 h (initial OD_{600}=0.05).

The dimensions of the *E2146* bacteria in the bacterial culture suspension as well as in S0Ec (at 2.5 h) and S1Ec (at 3 h) suspensions were measured from the epifluorescence images by taking the averages of 10 individual randomly chosen bacteria. The length and width of the bacteria in the corresponding suspensions are indicated in table 4-2. The bacteria in the culture and in the S0Ec suspension presented very similar characteristics with average lengths of 2.4 µm in both cases and widths of 0.92 and 0.85 µm, respectively. Meanwhile the bacteria in the S1Ec suspension were slightly shorter in length suggesting that the bacteria had already adapted their morphology to the less nutritive LB/10 solution. As seen in the results obtained by ATR-FTIR, the bacteria were possibly rather producing storages of glycogen instead of growing in size in the LB/10 medium.

Table 4-2. Average sizes of *E2146* bacteria in different suspensions calculated from 10 randomly chosen individual bacteria.

Suspension	Length (µm)	Width (µm)
Culture	2.4 ± 0.75	0.92 ± 0.10
S0Ec	2.4 ± 0.64	0.85 ± 0.11
S1Ec	2.09 ± 0.35	0.94 ± 0.11

4.2 Formation of a bacterial biofilm

In order to study the effects of different antimicrobial peptides on the *E2146* biofilm, it was essential to establish a reference biofilm. The characteristics of this biofilm had to be determined prior to the addition of an AMP treatment step. An ideal biofilm would one with a single layer of bacteria, however, the biofilm should provide IR bands intense enough to be accurately interpreted without significant artifacts. To set up a biofilm formation protocol for *E2146*, we first searched for an optimal biofilm formation time by using ATR-FTIR spectroscopy as a detection aid. In each of these experiments the first 30 min of the biofilm formation were static in order to let the bacteria deposit on the Ge surface. During these 30 static minutes an ATR-FTIR spectrum was recorded every 10 min with the S0Ec suspension freshly pumped into the ATR-FTIR cell as reference spectrum. We then let the biofilm formation continue in one of the three ways described below.

- **Biofilm aged 2.5 h:** The S0Ec suspension was let circulate in an open circulation system for 2 h and ATR-FTIR spectra were recorded every 10 min with the spectrum of the freshly filled flow cell as a reference spectrum.
- **Biofilm aged 5.5 h:** The S0Ec suspension was let to circulate in an open circulation system for 2 h, after which the silicon tubes at the entry side of the system were changed and LB/10 was

let circulate in an open circulation through the system for 3 h to promote biofilm development. An ATR-FTIR spectrum was recorded every 10 min with the spectrum of the 2.5 h-old biofilm as a reference spectrum. The S1Ec suspension corresponds to this part of the biofilm formation.

- **Biofilm aged 26.5 h:** The S0Ec suspension was let circulate in an open circulation system for 2 h, after which the silicon tubes at the entry side of the system were changed and LB/10 was let circulate in an open circulation through the system for 24 h to promote biofilm development. ATR-FTIR spectra were recorded every 15 min with the spectrum of the biofilm aged 2.5 h as a reference spectrum.

A young biofilm aged 2.5 h was initiated by inoculation of bacterial suspension first statically for 30 min, then in open circulation (50 mL/h) for 2 h on Ge crystal in a flow cell. ATR-FTIR spectra were recorded every 10 min during the inoculation. The resulting spectra and an epifluorescence image of the young biofilm are shown in figure 4-5. The spectral profile of the biofilm did not change with respect to that obtained for *E2146* bacteria in S0Ec suspension. The spectral profile (figure 4-5a) showed an increase in intensities of the spectral regions attributed to the *E2146* bacteria within time; the regions typical to proteins, polysaccharides, lipids and nucleic acids. This suggests the adhesion and a gradual colonization of the bacteria on the Ge crystal, confirmed by the increasing integrated intensities of the main bands (data not shown), with the exception of the νOH integrated intensity that had a tendency to decrease. This is due to the bacterial biomass, less concentrated with water, which accumulated on the Ge surface.

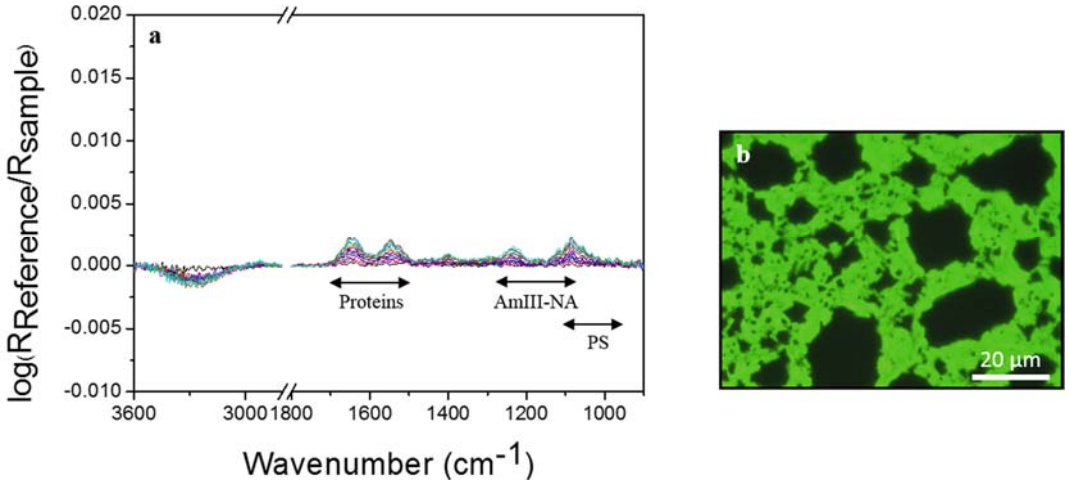


Figure 4-5. a) Evolution of ATR-FTIR spectra during the growth of a *E2146* biofilm aged 2.5 h. Bacterial adhesion with 30 min static and 2 h open circulation (50 mL/h) inoculation of bacterial suspension. Spectra presented from bottom to up every 10 min. Background spectrum recorded immediately after filling the flow cell with bacterial suspension. **b)** Epifluorescence image of the non-stained side (entry) side of a *E2146* biofilm aged 2.5 h, initial OD_{600}=0.46, average coverage ratio of 43.3 ± 21.6 %, exposure time 100 ms.

Figure 4-6 shows the ATR-FTIR spectra of adhered sessile bacteria in a biofilm aged 2.5 h (dashed line) on Ge crystal at the end of the bacterial inoculation at 2.5 h and planktonic bacteria in S0Ec suspension at 2.5 h (solid line) on diamond ATR in the region of 1800-900 cm^{-1}. The spectra are normalized with respect to the Amide II band. The Amide II/PS integrated intensities ratio at 2.5 h was calculated to be 0.55 and 0.69 for the biofilm and the S0Ec suspension respectively. The level of nucleic acids and polysaccharides was therefore higher with respect to the level of protein in both samples, but highest in the case of the biofilm. The metabolism of the bacteria in the biofilm was more active than that of the planktonic and the bacteria in the biofilm produced more nucleic acids, polysaccharides or both compared to their planktonic counterparts.

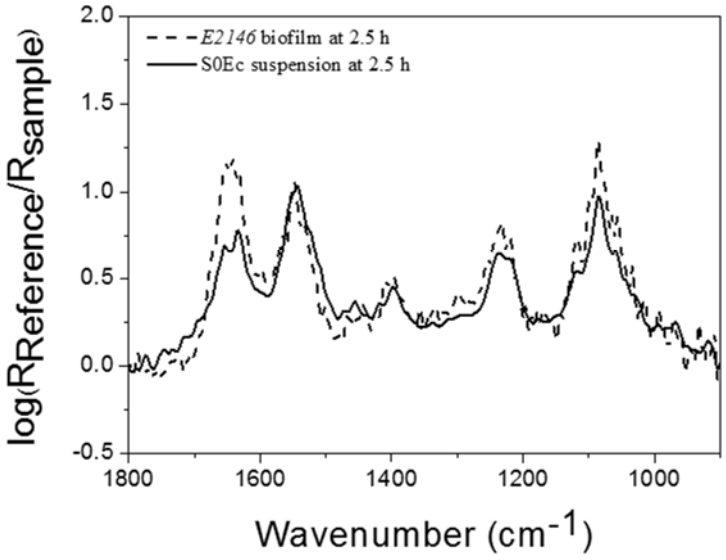


Figure 4-6. ATR-FTIR spectra of adhered sessile bacteria in a biofilm aged 2.5 h (dashed line) on Ge crystal at the end of the bacterial inoculation (at 2.5 h) and planktonic bacteria in S0Ec suspension at 2.5 h (solid line) on diamond ATR. Spectra normalized with respect to Amide II band.

The epifluorescence images of the non-stained biofilm (figure 4-5c) recorded at the end of the circulation showed that a monolayer of bacteria had formed on the Ge surface. The coverage ratios were calculated from a minimum of 20 randomly chosen epifluorescence images from the entire Ge surface. The average coverage of the biofilm aged 2.5 h was found to be 43.3 ± 21.6 %. The relatively high standard deviation of the coverage ratio indicates a heterogenous surface coverage, in which certain areas of the crystal were highly covered by the bacteria and other areas exhibited a sparsely located bacterial population. The bacteria sizes were calculated from at least 30 randomly

taken individual bacteria from the non-stained biofilm on the ATR crystal. The average bacterial length in the biofilm aged 2.5 h was 3.2 ± 0.6 µm and average width 1.1 ± 0.1 µm. The length and width of the bacteria in the biofilm aged 2.5 h was therefore 1.3 fold of that of bacteria in the S0Ec suspension at 2.5 h (corresponding to the biofilm aged 2.5 h). The size of the bacteria had increased when adhered on a solid surface.

A biofilm aged 26.5 h was formed by inoculation of bacterial suspension first statically for 30 min, then in open circulation (50 mL/h) for 2 h on Ge crystal in a flow cell. ATR-FTIR spectra were recorded every 10 min during the inoculation. The growth medium was then changed into fresh LB/10 solution and the silicon tubes used in the circulation of the bacterial solution were changed into sterile ones. Fresh LB/10 solution was then let to circulate in open circulation (50 mL/h) for 24 h. ATR-FTIR spectra were recorded every 10 min during LB/10 open circulation. The resulting spectra of the 24 h LB/10 circulation and the integrated intensities of the main IR bands during the 2.5 h inoculation of the bacterial suspension and 24 h LB/10 circulation are shown in figure 4-7.

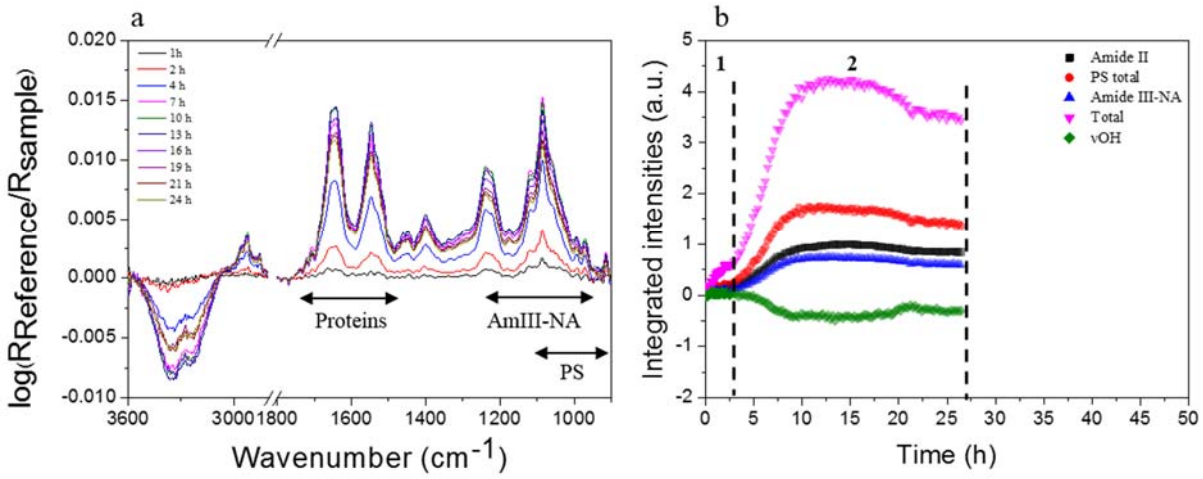


Figure 4-7. a) Evolution of ATR-FTIR spectra of a *E2146* biofilm aged 26.5 h during 24 h open circulation (50 mL/h) of LB/10. Background spectrum recorded immediately after filling the flow cell with fresh LB/10 solution. **b)** Evolution of the integrated intensities of the main ATR-FTIR bands of *E2146* biofilm aged 26.5 h as a function of time; **zone 1:** inoculation of 2.5 h (30 min static), **zone 2:** 24 h open circulation of LB/10. Integration limits: νOH: 3580-3400, Amide II: 1591-1484, Amide III-NA: 1279-1182, PS total: 1199-950, total: 1591-950.

The spectra (figure 4-7a) showed an increase in intensities of the spectral regions attributed to the *E2146* bacteria within time; the regions typical to proteins, polysaccharides, lipids and nucleic acids. The band wavelengths of the biofilm did not change in comparison to those obtained for

E2146 bacteria in S0Ec suspension. The increase in the intensities (also seen as the integrated intensities in figure 4-7b) of these spectral regions continued throughout the time period of the 2.5 h inoculation of the bacterial suspension and 4 h after the start of the fresh LB/10 circulation. The bacteria were multiplying on the Ge crystal. This growth was especially remarkable for the region attributed to polysaccharides (PS) and nucleic acids (NA). The increase in IR band intensities can be associated to the biofilm development; the bacteria divided and colonized the Ge surface, producing PS substances. After 6.5 h of total circulation, the increase of the intensities of all bands became slower until it finally reached a pseudo plateau at around 8 h. The spectral profile of all the bands remained very similar throughout the experiment. The profile of the PS region did not change significantly, on the contrary to the spectral profile in the case of the bacterial suspensions (S0Ec and S1Ec). This was due to the fact that in the case of the biofilm, the circulation of LB/10 happened in an open manner and thus fresh nutrients were continuously available for the bacteria throughout the experiment. Thus the bacteria did not have the urge to prepare stocks of carbon and energy. However, the bacteria in suspension, were living in a closed environment leading to the exhaustion of nutrients and accumulation of bacterial waste material. After 21 h of total circulation, the integrated intensities of the typical bands assigned to the *E2146* bacteria started to decline. The quantity of bacteria started to decrease and dead bacteria in contact with the crystal detached from the Ge surface and got carried away by the open circulating flux.

Figure 4-8 illustrates the ATR-FTIR spectra of adhered sessile bacteria in a 26.5 h-old biofilm on Ge crystal at 4 h after LB/10 open circulation and planktonic bacteria in S1Ec suspension at 4 h, normalized with respect to the Amide II band. The Amide II/PS ratio at 4 h was calculated to be 0.47 and 0.59 for the biofilm and the S1Ec suspension respectively. The level of nucleic acids and polysaccharides was therefore higher with respect to the level of proteins in both samples, but highest in the case of the biofilm. However, the difference between the two samples at 4 h was smaller than that of the biofilm aged 2.5 h and S0Ec suspension at 2.5 h. It can be observed that glycogen production occurred in the planktonic bacteria already at this stage (glycogen bands at 1152 and 1049 cm^{-1} had appeared) whereas no glycogen production was observed for the biofilm.

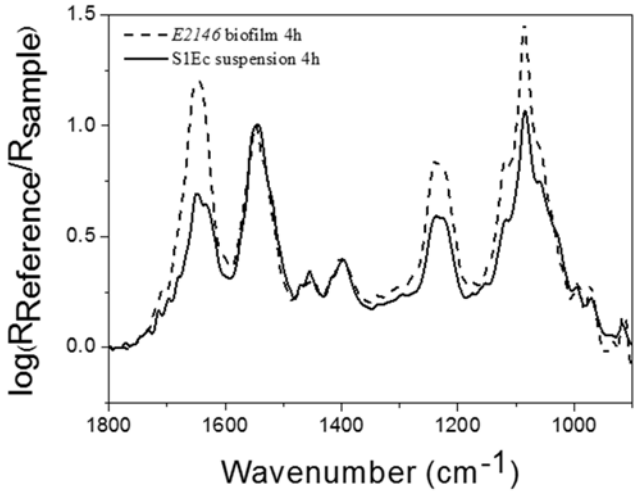


Figure 4-8. ATR-FTIR spectra of adhered sessile bacteria in a 26.5 h-old biofilm (dashed line) on Ge crystal at the end of the open LB/10 circulation (4 h) and planktonic bacteria in S1Ec suspension at 4 h (solid line) on diamond ATR. Spectra normalized with respect to Amide II band.

After 24 h of LB/10 open circulation, the biofilm was examined under epifluorescence microscope (figure 4-9). It was observed that parts of the Ge surface were covered by a monolayer of bacteria, whereas in other parts, multiple bacterial layers were seen. The average coverage was calculated to be 38.7 ± 18.7 %. Despite the difference in the biofilm age, the coverage of the 26.5 h-old biofilm was not higher than that of the biofilm aged 2.5 h. Based on the ATR-FTIR and epifluorescence studies of the biofilm aged 26.5 h, it was observed that to reach a biofilm coverage of around 40 %, 3 h of LB/10 circulation after 2.5 h of bacterial inoculation should be sufficient.

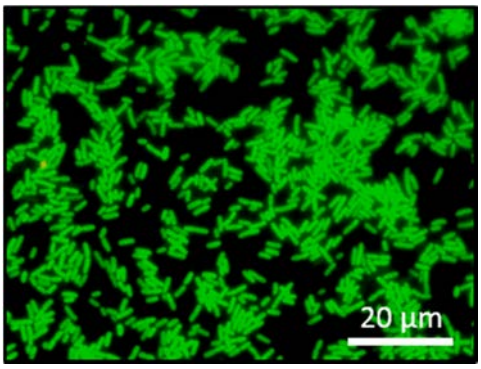


Figure 4-9. Epifluorescence image of non-stained (entry) side of a *E2146* biofilm aged 26.5 h, initial OD_{600}=0.51, average coverage ratio of 38.7 ± 18.7 %, exposure time 100 ms.

Finally when the 26.5 h-old biofilm had enabled the establishment of the lifecycle of a *E2146* biofilm, a biofilm aged 5.5 h was chosen under studies. Based on the integrated intensities of the 26.5 h-old biofilm shown in figure 4-7b, the biofilm seemed to be actively multiplying on the Ge crystal at a total circulation time of 5.5 h. The 5.5 h-old biofilm was formed by inoculation of the bacterial suspension first statically for 30 min, then in open circulation (50 mL/h) for 2 h on a Ge crystal in a flow cell. ATR-FTIR spectra were recorded every 10 min during the inoculation. The growth medium was then changed into fresh LB/10 solution which was then let to circulate in open circulation (50 mL/h) for 3 h. ATR-FTIR spectra were recorded every 10 min during LB/10 open circulation. The resulting spectra of the 3 h LB/10 circulation and the integrated intensities of the main IR bands during the 2.5 h bacterial inoculation and 3 h LB/10 open circulation are shown in figure 4-10.

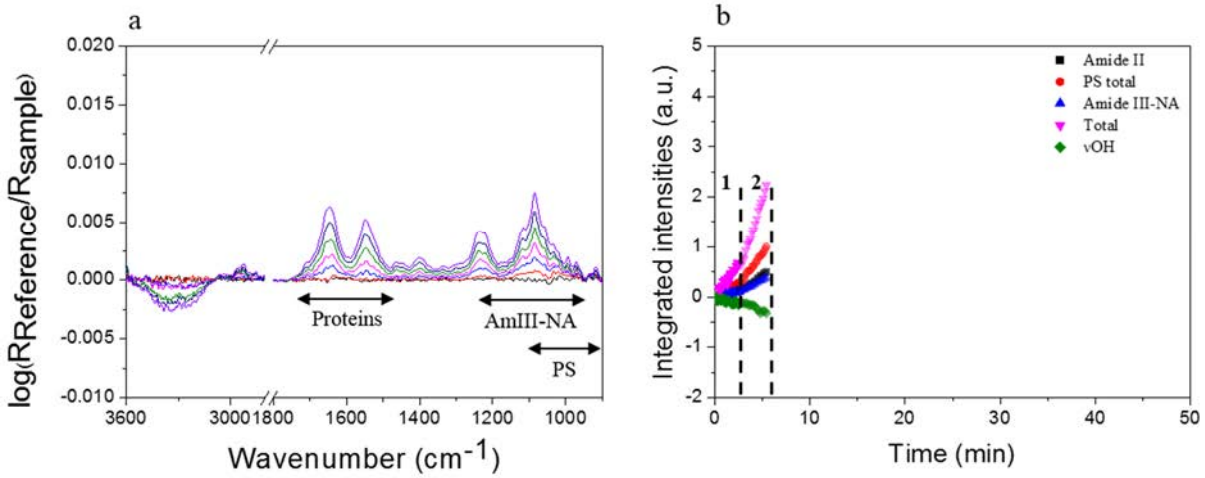


Figure 4-10. a) Evolution of ATR-FTIR spectra of a 5.5 h-old *E2146* biofilm during its 3 h open circulation (50 mL/h) of LB/10. Spectra presented every 30 min from bottom to top. Background spectrum recorded immediately after filling the flow cell with fresh LB/10 solution. **b)** Evolution of the integrated intensities of the main ATR-FTIR bands of a *E2146* biofilm aged 5.5 h as a function of time; **zone 1:** inoculation of 2.5 h (30 min static), **zone 2:** 3 h open circulation of LB/10. Integration limits: νOH: 3580-3400, Amide II: 1591-1484, Amide III-NA: 1279-1182, PS total: 1199-950, total: 1591-950.

As expected, the spectral fingerprints of the typical bands assigned to *E2146* increased in intensity within time, which can also be seen as an increase in the integrated intensities in figure 4-10b. At the end of the experiment, the bacteria in the biofilm were at the middle of their exponential growth.

The biofilm was observed with epifluorescence microscopy by reserving one half of the crystal for *Bac*Light ™ marking and other half for non-stained bacteria as previously described. Representative epifluorescence images of the 5.5 h-old biofilm are shown in figure 4-11. The average coverage

ratios and their standard deviations were calculated from 20 randomly chosen images on each, the non-stained and *Bac*Light ™ stained sides of the crystal and were 44.7 ± 15.7 % and 40.5 ± 11.4 % respectively, with an exposure time of 100 ms on both sides. *Bac*Light ™ enables the visualization of injured bacteria membranes as they are fluorescing in red and provide a clear contrast with green fluorescing, healthier bacteria [228]. In the case of the 5.5 h-old biofilm, only very few (10 %) bacteria fluoresced in red, indicating that most of the bacteria (90 %) in the biofilm had their membranes intact. The average length of the bacteria in the biofilm aged 5.5 h was 2.9 ± 0.9 µm with a width of 0.9 ± 0.1 µm. The bacteria on the 5.5 h-old biofilm were therefore around 1.4 fold in length than those in the corresponding suspension (S1Ec).

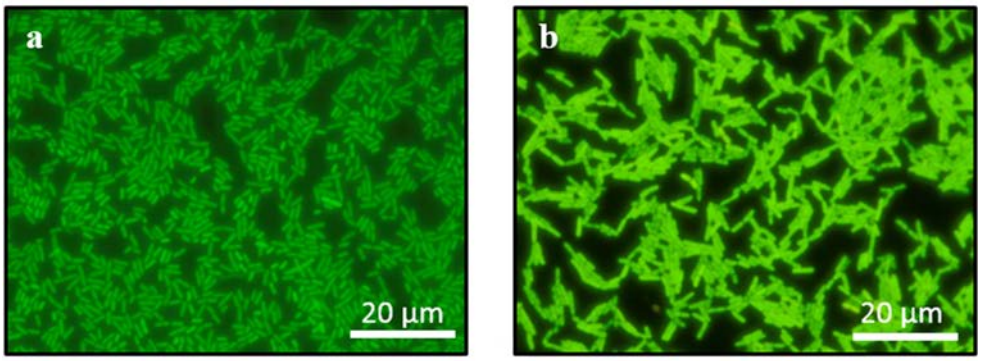


Figure 4-11. Epifluorescence images of a *E2146* biofilm aged 5.5 h. **a)** non-stained (entry) side, initial OD_{600}=0.46, average coverage ratio of 44.7 ± 15.7 %, exposure time 100 ms. **b**) *Bac*Light ™ stained (exit) side, initial OD_{600}=0.46, average coverage ratio of 40.5 ± 11.4 %, exposure time 100 ms.

The 5.5 h-old biofilm was also formed on a disc shaped Ge surface for AFM studies as previously described. The nanomechanical properties of the biofilm were first investigated in aqueous conditions and the Young modulus of the biofilm was calculated from the resulting force-distance curves. The biofilm was then dried under a gentle stream of nitrogen and was imaged in air. The AFM results of the biofilm aged 5.5 h can be observed in figure 4-12. Figure 4-12a-c present the morphology of the biofilm at three different scales (20 × 20, 10 × 10 and 5 × 5 µm). These images revealed that the Ge substrate was almost totally covered by the rod-shaped bacteria. The sizes of the bacteria were measured from the average of 10 randomly chosen bacteria. The average length of the bacteria obtained from the AFM images was calculated to be 2.3 ± 0.6 µm and the width 0.8 ± 0.1 µm (table 4-5). The height and the deflection images of figure 4-12 revealed that the bacteria exhibited a relatively rough cell wall. The root mean square roughness was calculated from several

areas of 200 × 200 nm on the bacteria surfaces and was 59 ± 14 nm. The height profiles given at the bottom panel of figure 4-12a-c show depth differences of 300-700 nm with local multilayers of bacteria, and a bacterial diameter of 303 ± 44 nm (table 4-5). The sizes of the bacteria vary slightly from those obtained by epifluorescence microcopy, as the AFM images were obtained from a dried biofilm instead of a hydrated one. Such values are generally measured when bacteria lose their intracellular water. In hydrated medium the average diameter of *E. coli* cells is around 600-800 nm. Here, the slight drying reduced the thickness of the bacteria by a factor of 3. The differences in height profiles along the cross section reported in figure 4-12a-c revealed that the biofilm was composed of mono- and bilayers of bacteria. Such indications are in line with the high coverage of the germanium surface by the biofilm. The Young modulus distribution of the 5.5 h-old *E2146* biofilm showed a pseudo Gaussian behavior and is illustrated in figure 4-12d. The Young modulus values are in accordance with those previously reported on single cells of the same strain [172], with an average value of 135 ± 89 kPa. A typical force-indentation curve is shown in figure 4-12e with raw AFM data (open circles) and with the theoretical fit according to equation 8 (solid red line).

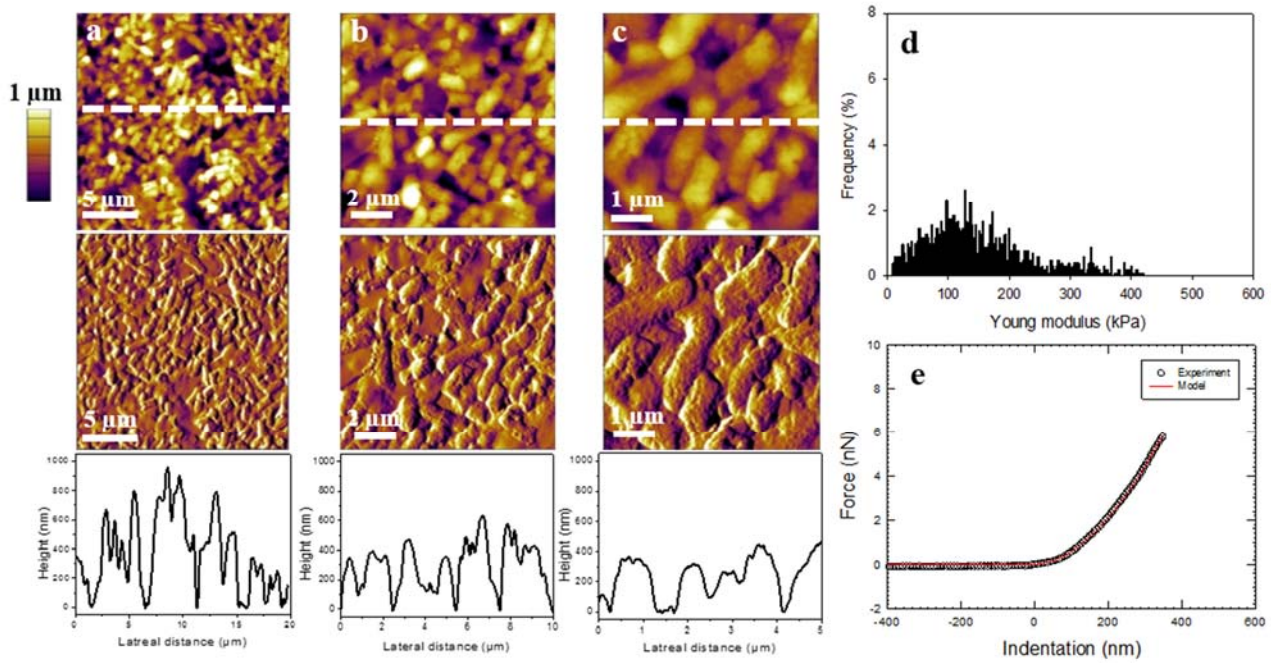


Figure 4-12. a-c) AFM images at different lateral sizes (a: 20 µm, b: 10 µm and c: 5 µm) showing the morphology of a *E2146* biofilm aged 5.5 h without peptide treatment. Top panel: height images, middle panel: deflection images and bottom panel: height profiles corresponding to the lateral cross sections indicated by the white dashed lines. **d)** Statistical distribution of the Young modulus of a *E2146* biofilm aged 5.5 h. **e)** Representative force-indentation curve (open circle) with theoretical model (solid red line) recorded from the untreated *E2146* biofilm aged 5.5 h.

The 5.5 h aged biofilm now being well characterized with various methods, was chosen as a reference biofilm for the AMP studies. The final protocol used to obtain information on the activity of the two peptides, bCAT and colistin, is illustrated in figure 4-13. A reference biofilm aged 5.5 h was first formed either on a Ge ATR crystal or on a Ge circular disc for ATR-FTIR and AFM experiments respectively, with 2.5 h inoculation of bacteria and 3 h of fresh LB/10 in open circulation, 24 h of closed circulation either in pure LB/10 solution (control, biofilm aged 29.5 h) or in LB/10 solution with 0.87 µM colistin, 30 or 60 µM bCAT. The biofilm was then either taken under studies with AFM or epifluorescence microscopy, or all the silicon tubes were changed and fresh LB/10 solution was continued in an open circulation for 17 h (biofilm aged 46.5 h) to study whether the effect of the AMP was bacteriostatic or bacteriolytic.

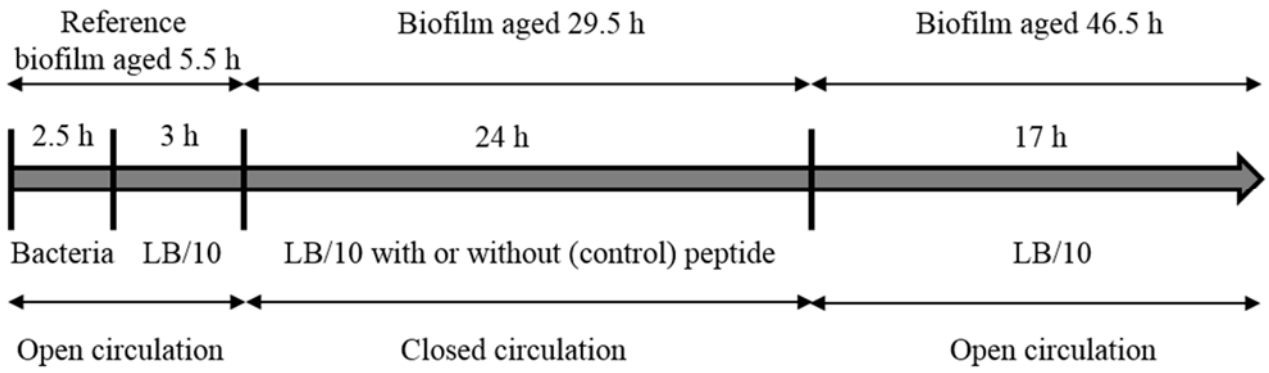


Figure 4-13. The chosen biofilm setup for peptide studies. A Reference biofilm aged 5.5 h was chosen, which was then subjected to 24 h closed circulation of either pure LB/10 (control) or LB/10 containing peptide (biofilm aged 29.5 h). Bacteriolytic/bacteriostatic effect of peptide was checked by an open circulation of LB/10 (17 h) directly after peptide circulation (biofilm aged 46.5 h).

Finally, because a closed circulation was adapted for the flow of the AMP, a control biofilm aged 29.5 h was established as a control to study its evolution without any AMP. This biofilm was formed by a bacterial inoculation of 2.5 h as previously described, after which fresh LB/10 was circulated in an open circulation for 3 h and finally 40 mL of new LB/10 solution was circulated for 24 h in a closed circulation. Figure 4-14 shows the spectral fingerprints and integrated intensities of the main IR bands assigned to the components of the 29.5 h-old control biofilm.

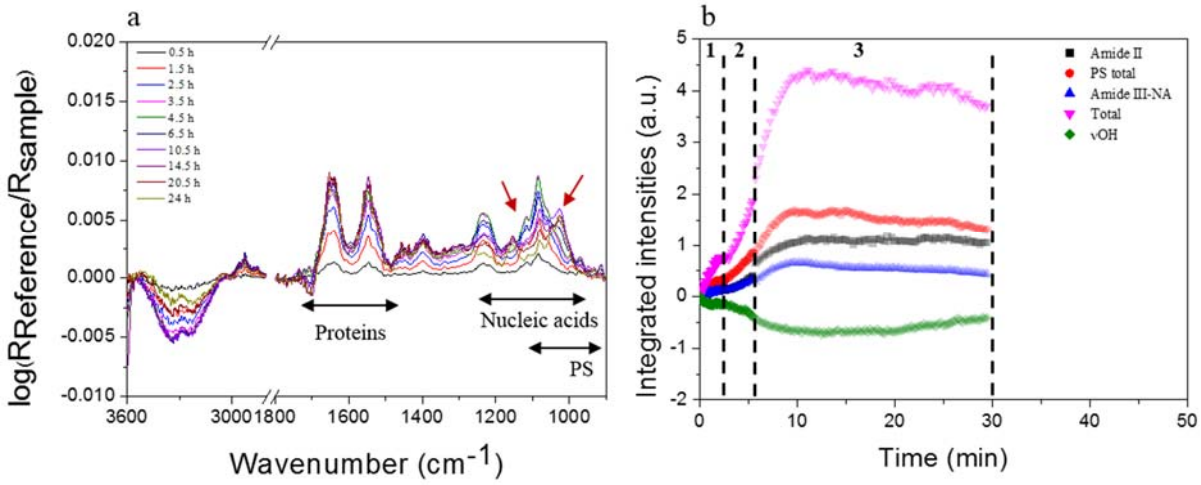


Figure 4-14. a) Evolution of ATR-FTIR spectra of a *E2146* biofilm aged 29.5 h (control) during 24 h closed circulation (50 mL/h) of LB/10. Spectra presented at 0.5, 1.5, 2.5, 3.5, 4.5, 6.5, 10.5, 14.5, 20.5, and 24 h from bottom to top. Background spectrum recorded immediately after filling the flow cell with fresh LB/10 solution. Red arrows show typical bands assigned for glycogen. **b)** Evolution of the integrated intensities of the main ATR-FTIR bands of a *E2146* biofilm aged 29.5 h as a function of time; **zone 1:** inoculation of 2.5 h (30 min static), **zone 2:** 3 h open circulation of LB/10, **zone 3:** 24 h closed circulation of 40 mL of LB/10. Integration limits: *ν*OH: 3580-3400, Amide II: 1591-1484, Amide III-NA: 1279-1182, PS total: 1199-950, total: 1591-950.

The most significant difference of the two experimental conditions in the 26.5 h and 29.5 h-old biofilms was that in the latter case, the 24 h LB/10 circulation was closed, and therefore no continuous flow of fresh nutrients was available for the bacteria, leading to the accumulation of bacterial waste products in the growth medium. Indeed, characteristic bands of glycogen started to appear at 1152, 1082, 1049 and 1026cm^{-1} [229] in the 29.5 h-old biofilm (red arrows in figure 4-14a) already in the beginning of the LB/10 closed circulation (6 h of total circulation), while these bands associated to glycogen were not seen in the 26.5 h-old biofilm even after 24 h of LB/10 open circulation. The strong glycogen production was most likely due to the exhaustion of certain nutritive compounds in the medium, such as phosphate and nitrite containing compounds. The same phenomena was seen in the bacterial suspensions. Moreover, the integrated intensities of the major IR bands of the 29.5 h-old biofilm, Amide II, Amide III-NA and PS total, showed a steady growth up to 8 h of total circulation, after which the biofilm had reached a pseudo plateau and the integrated intensities remained stable. Around 13 h of total circulation, the band of Amide III-NA started to decrease and a little later, at 16 h of total circulation, the PS total band started its decline. The Amide II band however stayed at a relatively constant level throughout the experiment. This suggests that the level of polysaccharide and nucleic acid production became less important in

comparison to that of proteins. However, the intensities of the bands assigned for glycogen decreased at a much slower rate, indicating that some glycogen production still remained.

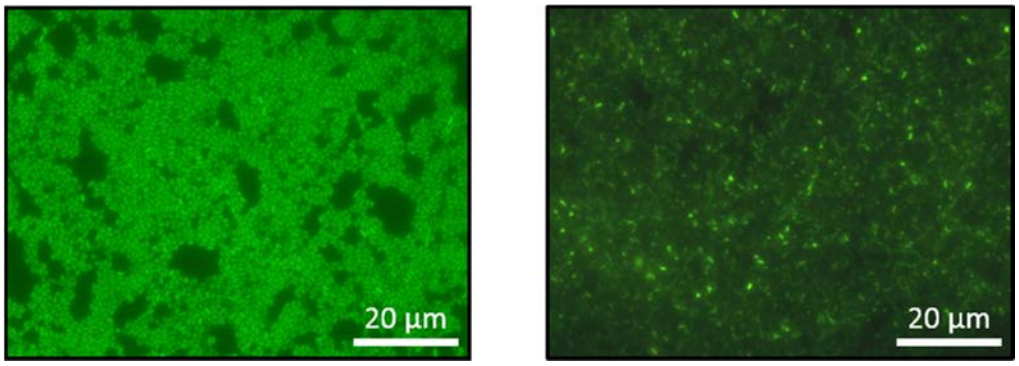


Figure 4-15. Epifluorescence image of a *E2146* control biofilm aged 29.5 h **a)** non-stained (entry) side, OD_{600}=0.45, average coverage ratio of 71.2 ± 19.1 %, exposure time 100 ms **b)** Backlight™ stained (exit) side, average coverage ratio of 49.9 ± 17.3 %, exposure time 100 ms.

After the 29.5 h circulation, epifluorescence images of the biofilm were recorded (figure 4-15) and the average bacterial coverage of the Ge crystal was found to be 71.2 ± 19.1 % for the non-stained side and 49.9 ± 17.3 % for the Backlight™ side. The bacteria fluoresced green throughout the crystal, indicating that the bacterial membranes had not been damaged. The average length of the bacteria were calculated to be 1.8 ± 0.4 µm and 0.7 ± 0.1 µm in width. These bacteria were clearly smaller than those observed in the biofilms aged 2.5 h and 5.5 h (3.2 and 2.8 in length and 1.1 and 0.9 in width, respectively, table 4-3). The bacteria had adapted their morphology with the growth conditions of the biofilm. Yet the coverage was high, suggesting that the bacteria had multiplied on the Ge surface, even though less nutrients were present in the closed circulation environment. Some areas of the crystal were covered by a multilayer of bacteria (data not shown). Table 4-3 recapitulates the average bacteria sizes obtained by epifluorescence microscope in *E2146* biofilms at different times.

Table 4-3. Average sizes of bacteria in biofilms of various ages obtained by epifluorescence microscope. Length and width calculated from 30 randomly taken individual bacteria.

Biofilm age	Bacteria length (μm)	Bacteria width (μm)
2.5 h	3.2 ± 0.6	1.1 ± 0.1
5.5 h	2.9 ± 0.9	0.9 ± 0.1
26.5 h	2.6 ± 0.5	1.0 ± 0.1
29.5 h	1.8 ± 0.4	0.7 ± 0.1

4.3 Cyclic antimicrobial peptide action on a bacterial biofilm

In order to study the effect of a cyclic antimicrobial agent (colistin) on *E2146* biofilms the 5.5 h-old biofilm was subjected to a closed 24 h circulation with LB/10 and colistin (0.87 μM) during which IR spectra was recorded continuously. The biofilm was then either observed with epifluorescence microscopy, AFM imaging or it was again subjected to 17 h fresh LB/10 open circulation, IR spectra was recorded and finally the sample was observed with epifluorescence microcopy. Figure 4-16 illustrates the time evolution (starting from the beginning of the peptide addition) of the IR bands typical to the *E2146* biofilm during the 24 h colistin circulation (figure 4-16a), the *E2146* biofilm spectra during the 17 h LB/10 circulation taking place after the antimicrobial treatment (figure 4-16b) and the time evolution of the integrated intensities of the major IR bands assigned to the *E2146* biofilm (figure 4-16c) during 2.5 h bacterial inoculation (zone 1), 3 h LB/10 open circulation (zone 2), 24 h colistin LB/10 closed circulation (zone 3) and 17 h LB/10 open circulation (zone 4). The spectra recorded during the 24 h colistin circulation show the major peaks assigned to the *E2146* biofilm at the same wavelengths as seen for the control biofilm. An increase of the PS bands of the biofilm during the first 2 h (7.5 h of total circulation) and the Amide I and II bands during the first 9 h of the colistin circulation (14.5 h of total circulation) can be detected. No spectral signature of glycogen was observed.

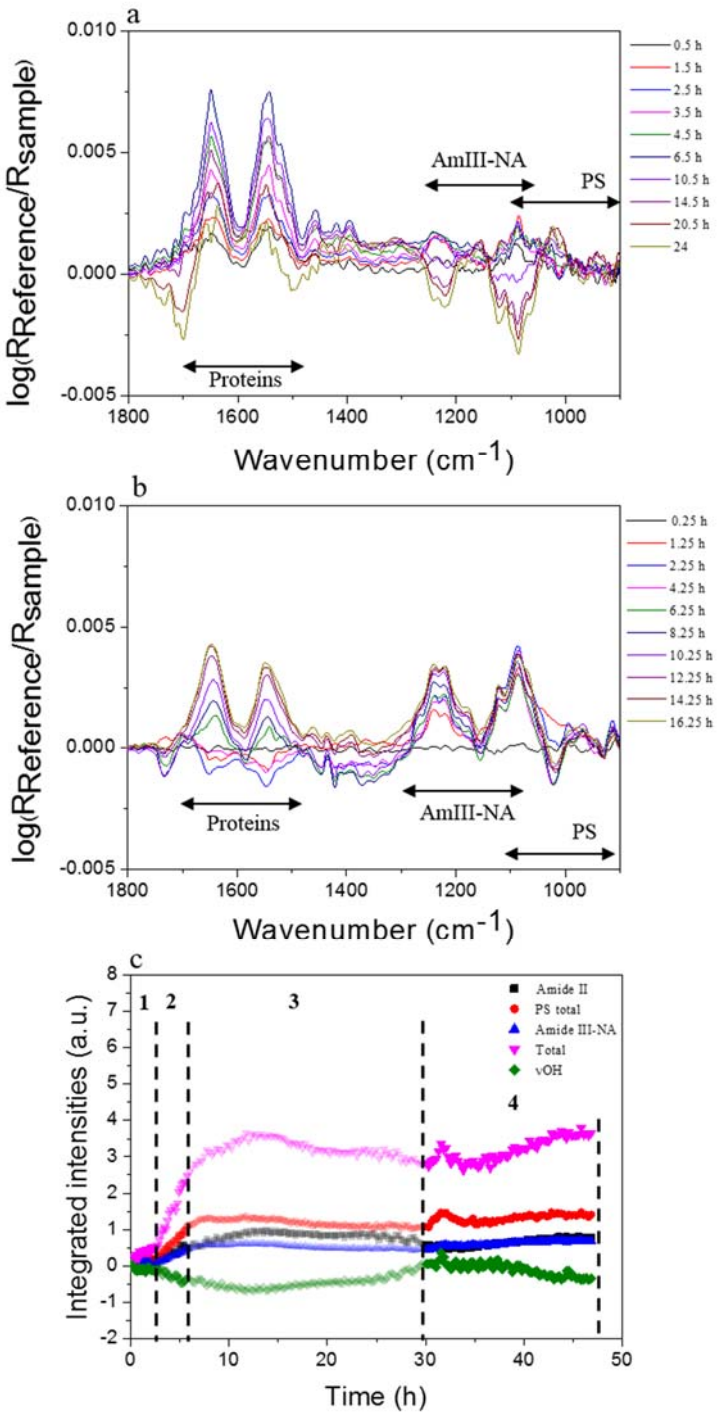


Figure 4-16. a) Evolution of ATR-FTIR spectra of a *E2146* biofilm aged 29.5 h during 24 h closed circulation (50 mL/h) of colistin (0.87 µM) LB/10. Background spectrum recorded immediately after filling the flow cell with fresh colistin (0.87 µM) LB/10 solution. **b)** Evolution of ATR-FTIR spectra of a *E2146* biofilm aged 46.5 h during 17 h open circulation of LB/10. **c)** Evolution of the integrated intensities of the main ATR-FTIR bands of *E2146* biofilm aged 46.5 h as a function of time; **zone 1:** inoculation of 2.5 h (30 min static), **zone 2:** 3 h open circulation of LB/10, **zone 3:** 24 h closed circulation of colistin (0.87 µM) LB/10, **zone 4:** 17 h open circulation of LB/10. Integration limits: νOH: 3580-3400, Amide II: 1591-1484, Amide III-NA: 1279-1182, PS total: 1199-950, total: 1591-950.

At 2 h after the beginning of colistin circulation, the Amide II/PS ratio was calculated to be 0.73 indicating a high nucleic acid and polysaccharide production by the bacteria, compared to protein level. The Amide II/PS ratio at the corresponding stage was calculated to be 0.41 for the control biofilm, suggesting that the nucleic acid and polysaccharide production with respect to proteins was even higher in the control biofilm and therefore inhibited in the biofilm in contact with colistin, already at early stages of the peptide treatment. When looking at the relative intensities of the Amide III-NA band with respect to that of the Amide II band during colistin circulation, a maximal nucleic acid synthesis took place at 2 h after the beginning of colistin circulation, after which a decline of the intensities of the major bands assigned to nucleic acids at 1240, 1222, 1118 and 1064 cm^{-1} was seen. At 9 h after the beginning of colistin circulation, the Amide II/PS ratio was 2.1, suggesting that the polysaccharide production had decreased in comparison to that of proteins. The corresponding rate in the control biofilm was 0.57. This suggests that the LB/10 growth medium containing colistin inhibited the polysaccharide and nucleic acid production with respect to that of proteins and that the inhibition became greater within time. The fact that the PS and Amide III-NA band intensities started to decrease well before the one of the Amide II band intensity, also reflects to a decrease in nucleic acid production and thus to reduction of metabolic activity of the bacteria [230]. Later, as the Amide I and II band intensities also started to decrease along with the two others mentioned, it can be considered that biomass was lost from the immediate proximity of the crystal. This could indicate that the bacteria started to detach from the supporting surface and got carried away by the flux.

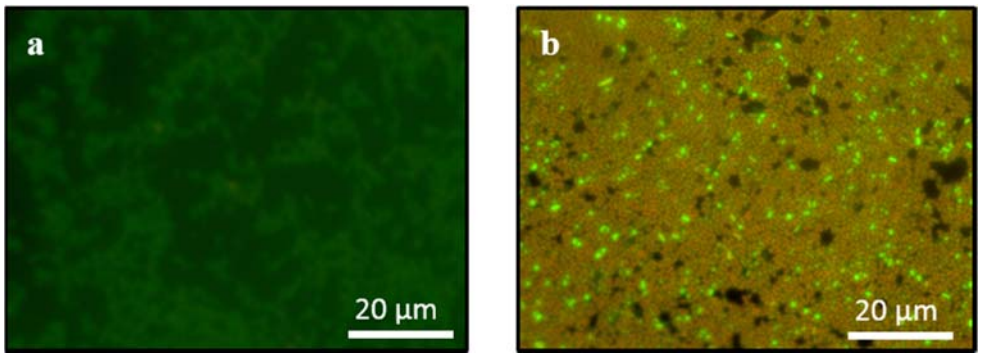


Figure 4-17. Epifluorescence images of a *E2146* biofilm aged 29.5 h with 24 h colistin (0.87 µM) LB/10 closed circulation, initial OD_{600}=0.33 **a)** non-stained side (entry side), average coverage ratio of 48.9 ± 11.9 %, exposure time 7000 ms. **b)** *Bac*Light ™ stained side (exit) side, average coverage ratio of 66.8 ± 16.4 %, exposure time 278 ms.

However, when looking at the epifluorescence images taken immediately after colistin circulation (figure 4-17), the relatively high coverage ratios (48.9 ± 11.9 % and 66.8 ± 16.4 % for entry and exit sides respectively) reveal that the majority of the bacteria remained on the crystal. The coverage ratio of the entry side of the crystal however is smaller than in the case of the non-treated 29.5 h-aged biofilm, which also presented multilayers, with a coverage ratio of 71.2 ± 19.1 %. The non-stained side of the crystal (figure 4-17a) showed highly covered areas with very small (average width 0.6 ± 0.2 µm, average length 0.7 ± 0.1 µm, table 4-6) coccoid shaped bacteria that were weakly fluorescing as the exposure time had to be adjusted up to 7000 ms in order to visualize them. This could support the findings that the metabolic activity of the bacteria was reduced. The *Bac*Light ™ marked side of the crystal (figure 4-17b) showed a similar structure of the bacteria on the surface. On this side however, it was observed that most of the bacteria fluoresced in red, indicating that their cell membranes were damaged. There were still some green (33 %) bacteria among the red (67 %) ones, presenting the bacteria that had not, or to a much lesser extent, been influenced by the colistin treatment.

AFM was also used to examine the effect of colistin on the 5.5 h-old biofilm. The biofilm was formed on a disc shaped Ge crystal as described previously and subjected to 24 h of LB/10 containing 0.87 µM colistin. Figure 4-18 shows AFM images (top panel: height, middle panel: deflection) at different scales and cross sections (bottom panel) obtained from a 5.5 h-old biofilm subjected to colistin at a concentration of 0.87 µM. The images reported in figure 4-18 differ greatly from those reported on the 5.5 h-old biofilm without peptide treatment. Bacterial shape changed and the rod-shaped cells observed before the antimicrobial peptide treatment had become more coccoid or spherical, in accordance with the findings of the epifluorescence images. The bacterial cells in the AFM images exhibited an average length of about 1.6 ± 0.2 µm and a width of 1.1 ± 0.1 µm (table 4-5), representing a 40% loss in terms of length. The bacterial cell wall was less rough after colistin treatment. The analysis of height images revealed a root mean square roughness of 12 ± 3 nm which is 5 times lower than the value measured prior to the antimicrobial peptide treatment. The analysis of the cross sections of the obtained images also revealed the presence of less important depth differences of about 50-150 nm. The average bacterial diameter became 76 ± 18 nm after the slight drying of the colistin-treated biofilm. This value is 4 times lower than the corresponding value measured on dried cells before the peptide treatment (table 4-5). The slight drying reduced the thickness of the bacteria by a factor of 3 for the non-treated and 10 for the colistin treated cells.

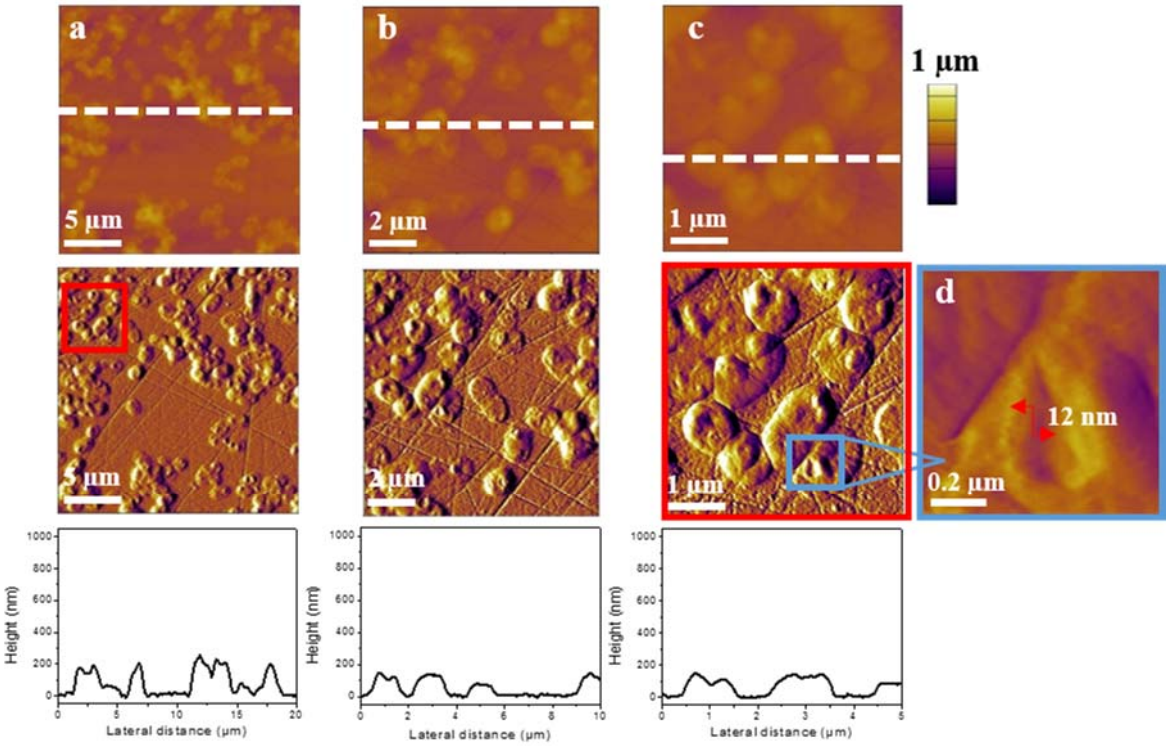


Figure 4-18. A *E2146* biofilm aged 29.5 h after colistin 0.87 µM treatment. AFM images at different lateral sizes (**a**: 20 µm, **b**: 10 µm and **c**: 5 µm, zoom of (a) indicated with the red square, **d**: 1 µm, zoom of (c) indicated with the blue square) showing the morphology of the biofilm; Top panel: height images, middle panel: deflection images and bottom panel: height profiles corresponding to the lateral cross sections indicated by the white dashed lines.

This underlines that the antimicrobial peptide should modify the bacterial membrane permeability. The important morphological differences testified that the biofilm and notably bacterial cell walls were dramatically damaged. This result is in line with literature in which losses of cell wall integrity and mechanical resistance of bacterial cells subjected to colistin has been reported [231]. Figure 4-18d illustrates a zoom into a hole found on the surface of many bacteria in the biofilm subjected to colistin treatment. Although these holes were not seen in the biofilm aged 5.5 h without AMP treatment, it remains unclear whether this phenomenon was caused by the treatment itself or by the drying of the biofilm, or even by the consequence of both.

The analysis of the force-curves recorded on the biofilm after colistin treatment allowed the calculation of the stiffness of the biofilm with the aid of the Sneddon model (equation 8). The statistical distribution of the Young modulus of *E2146* biofilm after colisin treatment as well as a typical force-indentation curve are illustrated in figure 4-19. As described previously, the biofilm aged 5.5 h not subjected to colistin showed a Gaussian behavior of the elastic modulus distribution.

This behavior was lost in the biofilm treated with colistin. Due to the colistin treatment, the elastic distribution became very broad with an average value of 598 ± 277 kPa. The bacterial membranes thus became stiffer due to the action of this cyclic AMP.

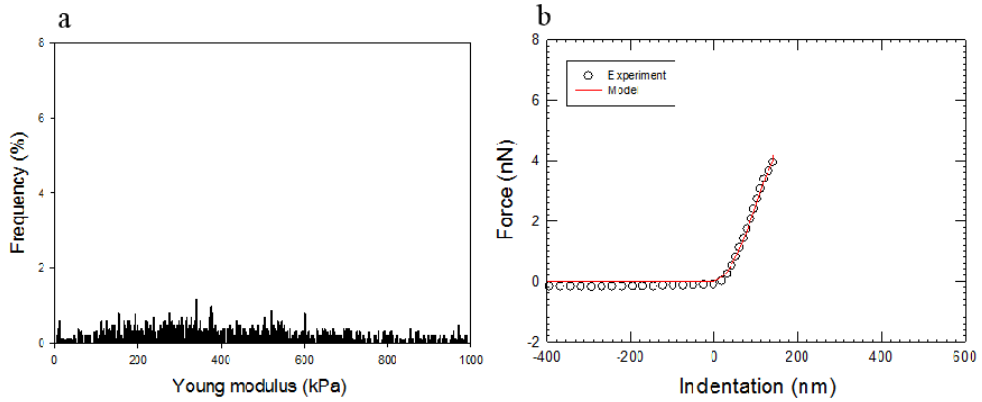


Figure 4-19. *E2146* biofilm aged 29.5 h with 24 h colistin (0.87 µM) treatment. **a)** Statistical distribution of the Young modulus. **b)** Representative force-indentation curve (open circle) with theoretical model (red line).

In addition, the effect of colistin on the biofilm was examined by circulating fresh LB/10 solution for 17 h after the 24 h colistin treatment. Surprisingly, the spectral evolution of the biofilm recovered after the treatment (figure 4-16b) and the major bands assigned to the biofilm were again detected. The Amide I and II band intensities continued their decline until 3.5 h after the beginning of the fresh LB/10 circulation, after which they started to increase, suggesting a slow recovery of the peptide production of the bacteria. The polysaccharide production however was very rapid immediately after the beginning of the new step and continued to increase up to 2 h, after which it found an equilibrium and remained constant. No characteristics of glycogen production was observed, on contrary to what was generally observed in open flow of nutrient medium for this bacteria. This very active production of polysaccharides is seen as a small bump in the figure illustrating the integrated intensities of the major bands (figure 4-16c) around 32 h of total circulation. The Amide III-NA band showed a much slower recovery than that of the polysaccharides, suggesting that the nucleic acid production began moderately.

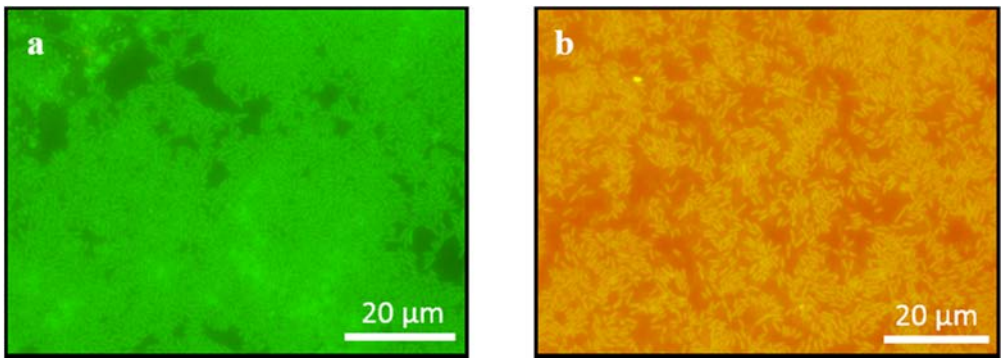


Figure 4-20. Epifluorescence images of a *E2146* biofilm aged 46.5 h with 24 h colistin (0.87 µM) LB/10 closed circulation and 17 h pure LB/10 open circulation, initial OD_{600}=0.41 **a)** non-stained (entry) side, average coverage ratio of 66.7 ± 8.1 %, exposure time 500 ms. **b)** *Bac*Light ™ stained (exit) side, initial OD_{600}=0.41, average coverage ratio of 77.8 ± 10.4 %, exposure time 570 ms.

Figure 4-20 illustrates the epifluorescence images of the 46.5 h-old biofilm subjected to 24 h closed circulation with colistin and finally 17 h circulation of fresh LB/10. The coverage ratios were even higher than in the case of the biofilm immediately imaged after colistin treatment and multilayers of bacteria were observed. This suggests that the bacteria could have started to slowly multiply after the treatment, supported by the slow recovery of the nucleic acid production seen in the IR spectra. Clearly, the recovering metabolic activity of the bacteria was also detected when looking at the non-stained side of the crystal (figure 4-20a) in which the bacteria fluoresce bright green and the exposure time used had dropped to only 500 ms. The bacteria on the *Bac*Light ™ stained side (figure 4-20b) also showed recovery, suggesting that the bacterial membranes had started to recover from the effect of increased permeability induced by colistin. It can therefore be concluded that the effect of colistin on the biofilm was reversible; when the biofilm was no more under the influence of the cyclic AMP, it had the ability to recover itself from the treatment. The bacteria had also started to recover to their original size and form, seen by the increase in the length of the bacteria (1.9 ± 0.3 µm) and the shape that had started to resemble the rod like shape seen in the biofilms not subjected to AMP treatment (figure 4-20b).

It can be drawn as a conclusion, that colistin modified the bacterial metabolism reversibly, influenced the permeability of the bacterial cell membrane, caused a change in the bacterial shape from rod-like to coccoid and increased the bacterial elastic modulus. This antimicrobial agent therefore had a broad influence on the *E2146* biofilm, although once the treatment was over, the biofilm had a strong ability to recover itself.

4.4 Linear antimicrobial peptide action on a bacterial biofilm

In order to study the effect of a linear antimicrobial agent (bCAT) on a *E2146* biofilm, the 5.5 h-old biofilm was subjected to a closed 24 h circulation of bCAT LB/10 in two different bCAT concentrations (30 and 60 µM) during which IR spectra were recorded continuously. The biofilm was then either imaged with epifluorescence microscopy, AFM imaging or it was again subjected to 17 h fresh LB/10 open circulation, IR spectra were recorded and finally the sample was observed with epifluorescence microcopy. Figure 4-21 shows the time evolution (starting from the beginning of the peptide addition) of the IR bands typical to the *E2146* biofilm during the 24 h bCAT (30 µM) circulation (figure 4-21a), the *E2146* biofilm spectra during the 17 h LB/10 circulation taking place after the antimicrobial treatment (figure 4-21b) and the time evolution of the integrated intensities of the major IR bands assigned to the *E2146* biofilm (figure 4-21c) during 2.5 h bacterial inoculation (zone 1), 3 h LB/10 open circulation (zone 2), 24 h bCAT (30 µM) LB/10 closed circulation (zone 3) and 17 h LB/10 open circulation (zone 4). The spectra recorded during the 24 h bCAT (30 µM) circulation showed the major peaks assigned to the *E2146* biofilm at the same wavelengths as seen for the control biofilm. In addition to the Amide I band of the biofilm itself, an Amide I band of bCAT was clearly detectable at 1622 cm^{-1}. This band was not seen in the biofilms without the peptide and can therefore be considered as a characteristic band of bCAT.

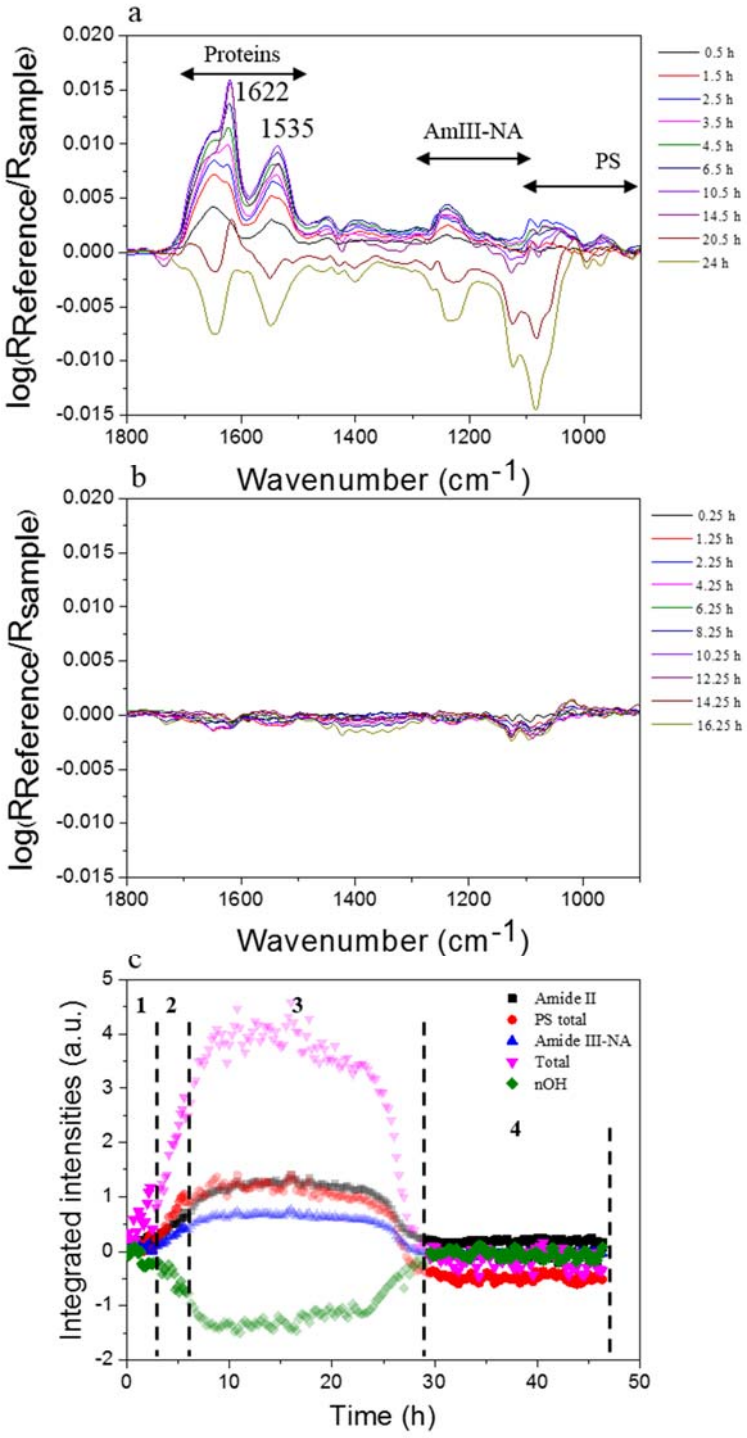


Figure 4-21. a) Evolution of ATR-FTIR spectra of a *E2146* biofilm aged 29.5 h during 24 h closed circulation (50 mL/h) of bCAT (30 µM) LB/10. Background spectrum taken immediately after filling the flow cell with fresh bCAT (30 µM) LB/10 solution. **b)** Evolution of ATR-FTIR spectra of a *E2146* biofilm aged 46.5 h during 17 h open circulation of LB/10. **c)** Evolution of the integrated intensities of the main ATR-FTIR bands of *E2146* biofilm aged 46.5 h as a function of time; **zone 1:** bacterial inoculation of 2.5 h (30 min static), **zone 2:** 3 h open circulation of LB/10, **zone 3:** 24 h closed circulation of bCAT (30 µM) LB/10, **zone 4:** 17 h open circulation of LB/10. Integration limits: νOH: 3580-3400, Amide II: 1591-1484, Amide III-NA: 1279-1182, PS total: 1199-950, total: 1591-950.

This bCAT Amide I band was shifted to a lower wavenumber, 1622 cm^{-1}, with respect to the Amide I band seen for pure bCAT on Ge crystal (at 1642 cm^{-1}), strongly suggesting that the peptide had adopted a β-sheet conformation [215] in the close proximity of the biofilm and the Ge crystal. This is supported by the wavelength of the Amide II band which had shifted to 1535 cm^{-1}, a wavelength typical to β-sheet conformations [232, 233]. The Amide I band of bCAT appeared 30 min after the start of the bCAT (30 μM) treatment and increased its intensity until 10 h after the beginning of the treatment, then slowly and gradually decreased, suggesting either a degradation of the peptide or its displacement beyond the detection limit of the instrument. The Amide I and II bands assigned to the proteins of the bacteria in the biofilm also increased in intensity for the first 6.5 h after the start of the bCAT (30 μM) treatment, but then started to decrease, finally being negative at 24 h after the start of the treatment (figure 4-21a). The spectral profile at the region of the PS massif changed in comparison to that seen in the control biofilm. The intensity if the IR bands assigned to the polysaccharides did not increase remarkably, remaining relatively stable during the first 12 h (17 h of total circulation) of the bCAT (30 μM) treatment, after which they slowly started to decline and finally at the very end of the AMP circulation, were close to zero when referenced with the very beginning of the biofilm inoculation (figure 4-21c). The same phenomena was seen in the other major IR bands assigned to the components of the biofilm. At the maxima of the intensity of Amide II band at 6.5 h, the Amide II/PS ratio was calculated to be 1.98, indicating that the level of peptides were to a much greater extent in comparison to that of polysaccharides. The Amide III-NA IR band intensity however remained stable until 12 h of the start of the treatment, indicating some nucleic acid production in the biofilm. After the 12 h, the integrated intensity of the Amide III-NA band also started to decrease among others and reached close to zero when referenced to the beginning of the biofilm inoculation (figure 4-21c). This being the case also for the peaks assigned to nucleic acids at 1703, 1240, 1222 and 1060 cm^{-1}, further suggesting an inhibition of the nucleic acid production by the peptide. These features suggested a loss of biomass in the biofilm.

The epifluorescence images (figure 4-22) of the biofilm aged 29.5 h subjected to 24 h of bCAT (30 μM) treatment also revealed a decrease in the metabolic activity of the biofilm, firstly as on the non-stained side of the crystal the bacteria fluoresced less intensively than the non-treated bacteria of the control biofilm, with an exposure time of 3000 ms required to detect them. As in the case of colistin, the average coverage ratio had slightly decreased with respect to the non-treated control biofilm, it being 40.4 ± 11.9 for the entry side of the crystal. The *Bac*Light ™ stained side of the crystal showed images of bacteria fluorescing in orange, indicating slight permeability changes in the bacterial membrane. The corresponding average coverage ratio was calculated to be 61.0 ± 8.1

% with an exposure time of 243 ms. In the case of bCAT (30 µM) treatment, the bacteria shape had not changed, but the bacteria had enlarged their size both in length and width, them being 3.8 ± 0.4 and 1.0 ± 0.2 after the bCAT (30 µM) treatment, respectively.

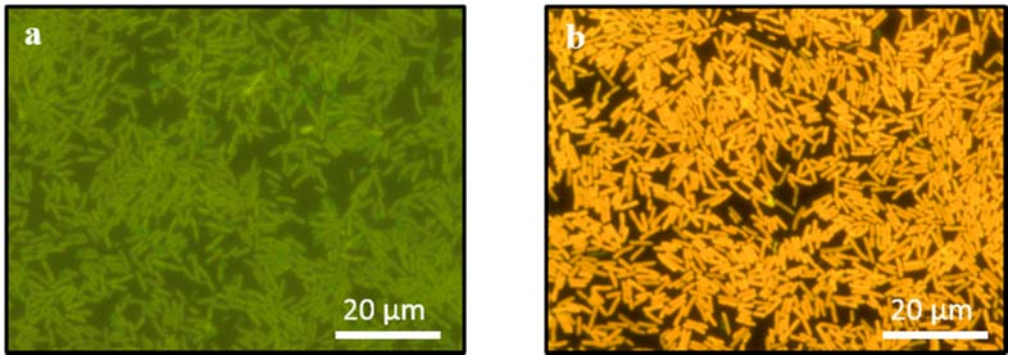


Figure 4-22. Epifluorescence images of a *E2146* biofilm aged 29.5 h with 24 h bCAT (30 µM) LB/10 closed circulation, OD_{600}=0.33 **a)** non-stained (entry) side, average coverage ratio of 40.4 ± 11.9 %, exposure time 3000 ms. **b)** *Bac*Light ™ stained (exit) side, average coverage ratio of 61.0 ± 8.1 %, exposure time 243 ms.

AFM images (top panel: height, middle panel: deflection) at different scales and cross sections (bottom panel) of a *E2146* biofilm after the 24 h bCAT 30 µM treatment are illustrated in figure 4-23. The images reported in figure 4-23 differ from those reported on the biofilm aged 5.5 h without peptide treatment. The bacterial shape had remained rod-like, supporting the shapes seen in the epifluorescence microscopy images. The bacteria morphology was therefore not significantly modified by the bCAT treatment. The bacterial cells in the AFM images exhibited an average length of about 2.1 ± 0.4 µm and a width of 1.2 ± 0.1 µm (Table 4-4), representing a 11 % loss in terms of length.

The analysis of height images revealed a root mean square roughness of 9 ± 2 nm which is 7 times lower than the value measured before the antimicrobial peptide treatment. The average bacterial diameter became 167 ± 23 nm after the slight drying of the biofilm treated with bCAT (30 µM). This is almost twice lower than the corresponding value measured on dried cells before the AMP treatment (Table 4-4). This underlines that the antimicrobial peptide should modify the bacterial membrane permeability, confirming the orange fluorescing images obtained by epifluorescence microscopy.

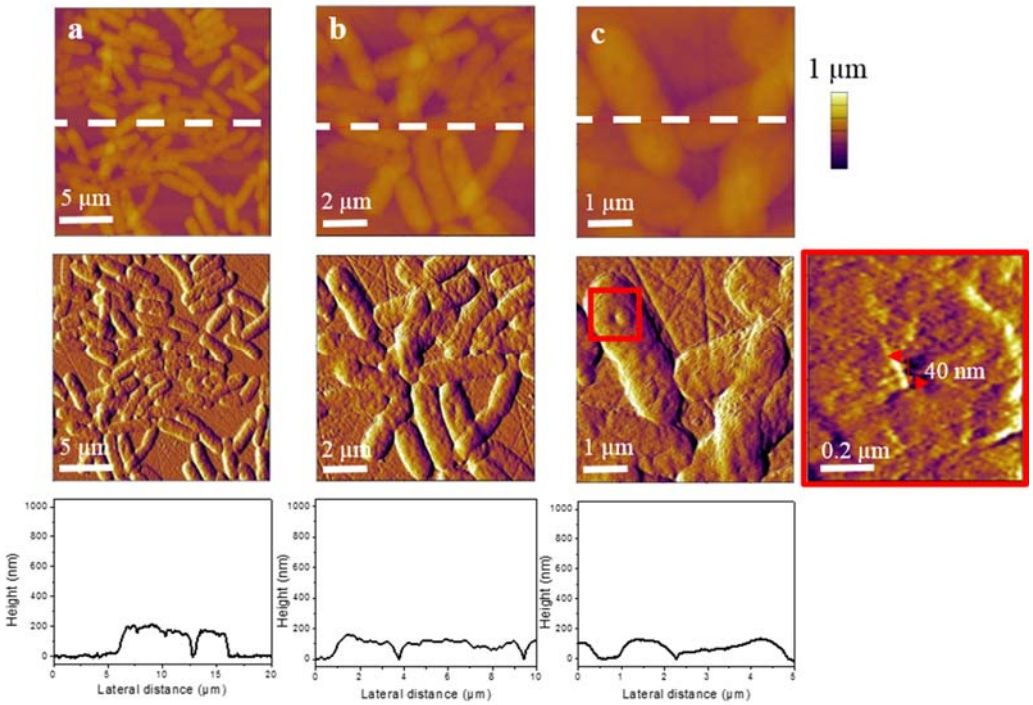


Figure 4-23. A *E2146* biofilm aged 29.5 h with 24h bCAT (30 µM) treatment. AFM images at different lateral sizes (**a**: 20 µm, **b**: 10 µm, **c**: 5 µm and **d**: 1 µm zoom of red square) showing the biofilm morphology. Top panel: height images, middle panel: deflection images and bottom panel: height profiles corresponding to the lateral cross sections indicated by the white dashed lines.

The analysis of the force-curves recorded on the biofilm after bCAT (30 µM) treatment allowed the calculation of the stiffness of the biofilm with the aid of the Sneddon model. The statistical distribution of the Young modulus of *E2146* biofilm after bCAT (30 µM) treatment as well as a typical force-indentation curve are illustrated in figure 4-24. The Gaussian behavior of the statistical distribution was partially maintained even after the bCAT (30 µM) treatment, however the average of the Young modulus was shifted to a lower value of 48 ± 27 kPa. This peptide therefore increased the elasticity of the membrane instead of making the bacterial membranes more rigid as in the case of colistin.

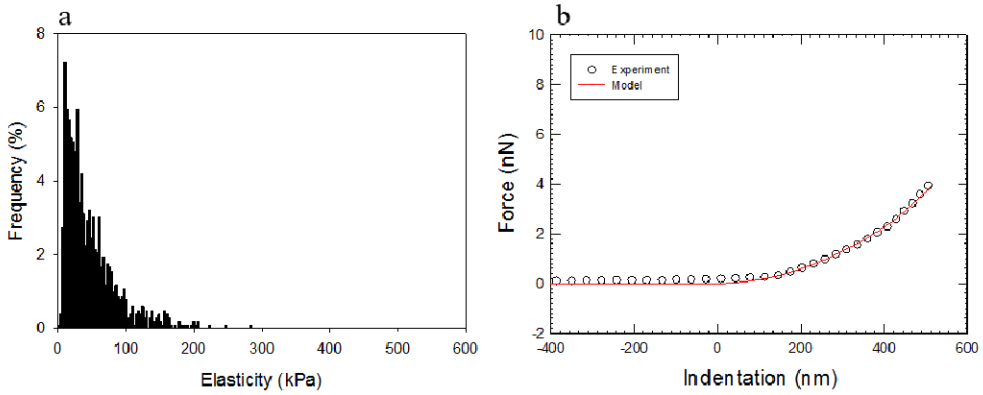


Figure 4-24. A *E2146* biofilm aged 29.5 h with 24h bCAT (30 µM) treatment. **a)** Statistical distribution of the Young modulus **a)** Representative force-indentation curve (open circle) with theoretical model (red line).

After the 24 h bCAT (30 µM) treatment, the *E2146* biofilm was also subjected to fresh LB/10 solution in open circulation for 17 h. The evolution of IR spectra was recorded throughout this time. Surprisingly, the bacterial metabolism did not recover after the treatment, on the contrary, the Amide I and II band intensities continued to very slightly decline and the same was seen for the bands assigned to polysaccharides and nucleic acids. This indicated that the bCAT (30 µM) had a bacteriolytic effect on the biofilm. The biofilm could not recover itself after the treatment. Figure 4-25 illustrates the epifluorescence images after the 17 h open circulation of fresh LB/10. These images show that apart from occasional clusters of bacteria in the biofilm (red circle in figure 4-25), the biofilm was constructed of a single layer of bacteria. The average coverage had declined with respect to seen in the images taken immediately after the AMP treatment, now being 25.6 ± 16.1 % and 34.9 ± 16.9 % for the entry and exit sides of the crystal respectively. The high standard deviation of the coverage ratios suggested a very heterogeneous coverage of the biofilm, with areas of coverage close to 0 % and areas with coverage close to 50 %. Moreover, the bacteria at the *Bac*Light ™ stained side of the crystal (figure 4-25c) fluoresced in red, indicating that the deteriorating effect of bCAT at 30 µM concentration on the bacterial membranes remained even after the treatment had come to an end. The bacteria were also smaller in size than in the epifluorescence images taken immediately after treatment, with a length of 2.2 ± 0.5 µm and a width of 0.8 ± 0.2 µm, confirming that the bacteria had not completely recovered from the effect of the AMP. The epifluorescence images also revealed an important amount of bacterial debris on the Ge surface (red arrows, figure 4-25b), showing that bacteria detached from the surface had left cytoplasmic residues behind. Bacterial filaments were also detected (figure 4-25b). It is known that *E. coli* is able to grow in an anomalous manner and structure itself in filaments in the occasion

when the formation of a bacterial septum in cell division is perturbed [234]. This is usually the case when the bacteria are living in a stressful environment due to lack of nutrients or the presence of antibiotic agents [235]. Therefore these structures seen in the epifluorescence images can be an indication of a stress in the bacteria of the biofilm.

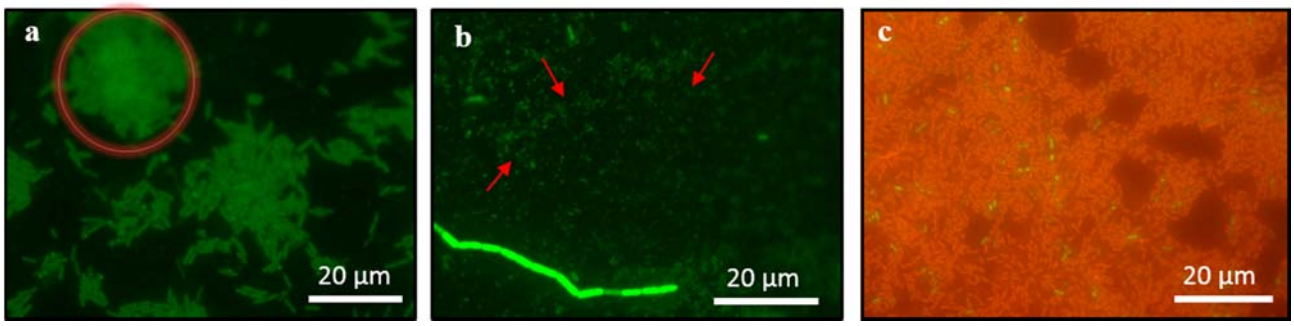


Figure 4-25. Epifluorescence images of a *E2146* biofilm aged 29.5 h with 24 h bCAT (30 µM) LB/10 closed circulation and pure LB/10 open circulation, initial OD_{600} = 0.38 **a-b)** non-stained (entry) side, average coverage ratio of 25.6 ± 16.1 %, exposure time 250 ms. **c)** *Bac*Light ™ stained (exit) side, average coverage ratio of 34.9 ± 16.9 %, exposure time 250 ms.

In addition, the effect of bCAT was studied at the MIC of the peptide, in order to have an overview on the influence of concentration on the action of the AMP. As described, the MIC was calculated to be 60 µM for the bacterial strain in question. Figure 4-26 illustrates the time evolution of the IR bands attributed to the compounds of the *E2146* biofilm during the 24 h bCAT (60 µM) circulation (figure 4-26a), the *E2146* biofilm spectra during the 17 h LB/10 circulation taking place after the antimicrobial treatment (figure 4-26b) and the time evolution of the integrated intensities of the major IR bands assigned to the *E2146* biofilm (figure 4-26c) during 2.5 h bacterial inoculation (zone 1), 3 h LB/10 open circulation (zone 2), 24 h bCAT (30 µM) LB/10 closed circulation (zone 3) and 17 h LB/10 open circulation (zone 4). The spectra recorded during the 24 h bCAT (60 µM) circulation showed the major peaks assigned to the *E2146* biofilm at the same wavelengths as seen for the control biofilm and the overall spectral profile remained similar in comparison to the control biofilm, with the exception of the PS massif area, for the first 8 h of the peptide circulation, during which the intensities of the peaks of the major components gradually increased. Surprisingly, the Amide I band of the bCAT was detected only after 2 h (10.5 h of total circulation) of peptide circulation at a wavelength of 1624 cm^{-1}, again indicating that the peptide adopted a β-sheet conformation when in close contact with the biofilm.

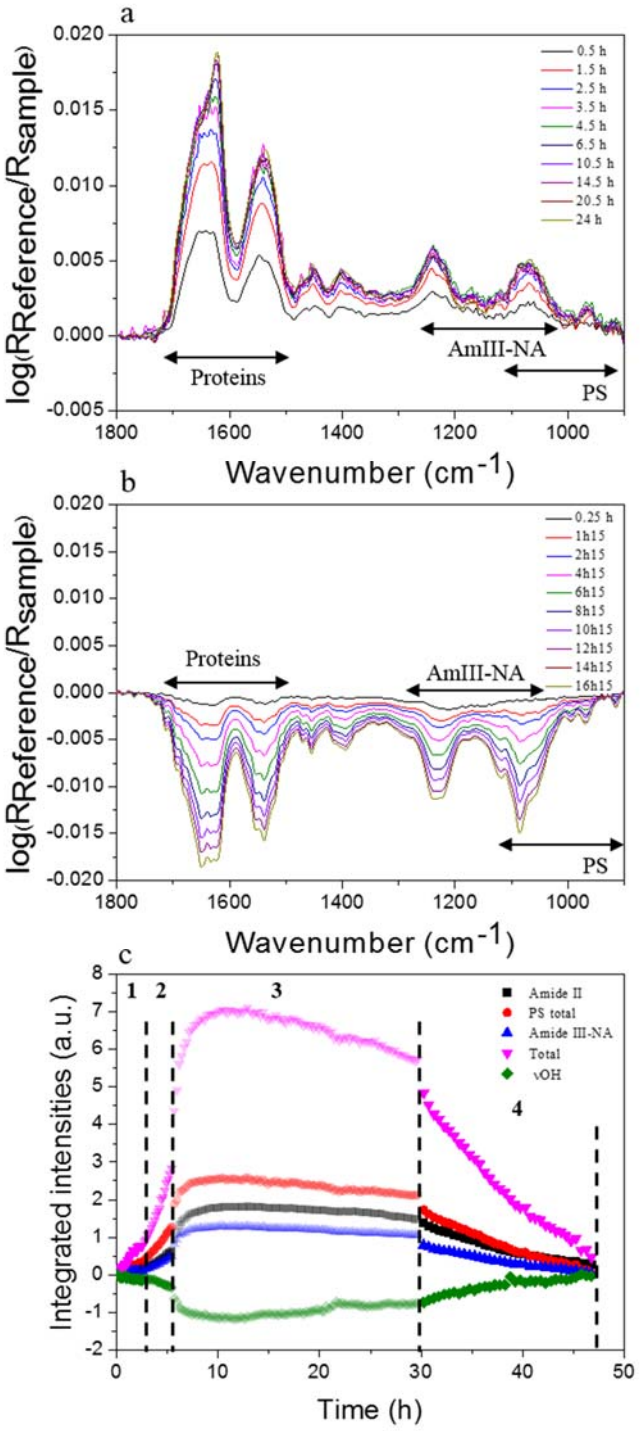


Figure 4-26. a) Evolution of ATR-FTIR spectra of a *E2146* biofilm aged 29.5 h during 24 h closed circulation (50 mL/h) of bCAT (60 µM) LB/10, initial OD_{600} = 0.46. Background spectrum taken immediately after filling the flow cell with fresh bCAT (60 µM) LB/10 solution. **b)** Evolution of ATR-FTIR spectra of a *E2146* biofilm aged 46.5 h during 17 h open circulation of LB/10. **c)** Evolution of the accumulated integrated intensities of the main ATR-FTIR bands of a *E2146* biofilm aged 46.5 h as a function of time; **zone 1:** bacterial inoculation of 2.5 h (30 min static), **zone 2:** 3 h open circulation of LB/10, **zone 3:** 24 h closed circulation of bCAT (60 µM) LB/10, **zone 4:** 17 h open circulation of LB/10. Integration limits: ν*OH*: 3580-3400, Amide II: 1591-1484, Amide III-NA: 1279-1182, PS total: 1199-950, total: 1591-950.

The intensity of the bCAT Amide I band slowly continued to increase throughout the 24 h of the experiment, suggesting a gradual penetration of the AMP into the biofilm. This difference of bCAT penetration into the sample with respect to the two different concentrations could either be related to a concentration dependent action of the AMP, or to possible differences in the biofilm architecture; if more biofilm is present, the penetration time could be expected to be longer. Indeed, when the initial Amide I band in 30 µM bCAT concentration is compared with the initial Amide I band intensity in the case of 60µM bCAT, it can be seen that the band intensity in the case of 30 µM bCAT was slightly less than in the case of 60 µM bCAT, a possible explanation for the differences in the peptide penetration. Nevertheless, the peptide was strongly attracted by the bacteria, since the Amide I band intensity was 7 fold compared to a blank experiment with no biofilm present (data not shown). The overall action of bCAT at 60 µM concentration seemed to differ from the one obtained with the concentration equivalent to half of the MIC (30 µM); instead of the eventual gradual decrease of the major IR band intensities, the intensities remained rather constant throughout the 24 h peptide circulation, although differences in the spectral profile could be seen after 8 h. Around this time, a negative νC=O peak at 1733 cm^{-1} also appeared, suggesting a loss of the membrane phospholipids of the bacteria, indicating a possible penetration of the peptide into the membrane. These changes indicated a change in bacterial metabolism, mainly due to the lack of glycogen and nucleic acid production which was seen in the case of the control biofilm. When looking at the Amide II/PS ratio at 6.5 h after the start of peptide circulation, the calculated ratio was 1.3, suggesting a higher bCAT adsorption and protein production in comparison to that of polysaccharide production as previously also seen for the case of 30 µM bCAT. However, the value of Amide II/PS ratio with 60 µM bCAT concentration remained rather constant throughout the action of the peptide. This kind of action was also seen during the first 6.5 h of the bCAT circulation at 30 µM concentration and is very different of what was seen in the case of colistin, in which the nucleic acid production slowed down already after 2 h of peptide circulation and the production of polysaccharides was greater in comparison to that of proteins.

The epifluorescence images (figure 4-27) of the 29.5 h-old biofilm subjected to 24 h of bCAT (60 µM) treatment however reveal that the biofilm was most likely attempting to maintain its metabolic activity in comparison to the colistin treated biofilm, as at the non-stained side of the crystal (figure 4-27a), the bacteria fluoresced more intensively than in the colistin treated biofilm, with an exposure time of 3000 ms required (7000 ms in the case of colistin). The average coverage had decreased with respect to the non-treated 29.5 h-old control biofilm, it being 36.5 ± 7.3 for the non-stained side of the crystal. The *Bac*Light ™ stained side of the crystal (figure 4-27b) showed images

of bacteria fluorescing in orange, indicating permeability changes in the bacteria membrane. The corresponding coverage ratio was calculated to be 25.5 ± 9.8 % with an exposure time of 50 ms. The bacteria shape had not changed in comparison with the control biofilm, but the bacteria had enlarged their size in length, it being 3.1 ± 0.5 µm with a width of 0.8 ± 0.1 µm after the bCAT (60 µM) treatment.

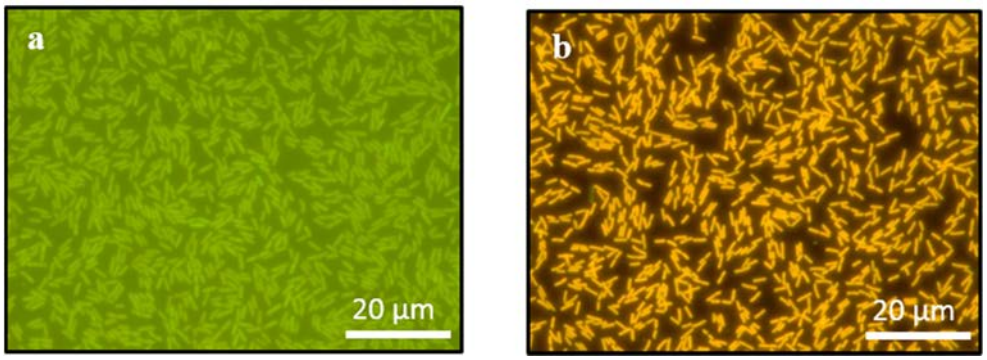


Figure 4-27. Epifluorescence images of a *E2146* biofilm aged 29.5 h with 24 h bCAT (60 µM) LB/10 closed circulation, initial OD_{600}=0.49 **a)** non-stained (entry) side, average coverage ratio of 36.5 ± 7.3 %, exposure time 3000 ms. **b)** *Bac*Light ™ stained (exit) side, average coverage ratio of 25.5 ± 9.8 %, exposure time 50 ms.

AFM images (top panel: height, middle panel: deflection) at different scales and cross sections (bottom panel) of the *E2146* biofilm after the 24 h bCAT 60 µM treatment are illustrated in figure 4-28 and show that the bacterial morphology had remained rod-shaped, again supporting the shapes seen in the epifluorescence images. The bacteria morphology was therefore not significantly modified by the bCAT (60 µM) treatment; however, bacterial debris were also seen in the AFM deflection images. The bacterial cells in the AFM images had an average length of about 2.2 ± 0.3 µm and a width of 0.9 ± 0.1 µm (Table 4-4), representing only a 9 % loss in terms of length in respect to the 5.5 h-old biofilm. The bacterial cell wall roughness of the 60 µM bCAT treated biofilm was very close to the one of the 5.5 h-old biofilm, with root mean square roughness's of 52 ± 12 nm and 60 ± 14 nm respectively. The depth differences seen in the cross sections of the height profile revealed bacterial diameters of around 400 nm, which was greater than those seen for the 5.5 h-old biofilm without AMP treatment and for the biofilm treated with 30 µM bCAT. The diameter of untreated bacteria in hydrated conditions is on average 600-700 nm [229] and the drying has a flattening effect on the bacteria. However, despite the identical drying conditions, the bacteria in the biofilm subjected to 60 µM bCAT concentration only loss around 50 % of their height due to the

effect of drying. This kind of phenomena have also previously been reported for biofilms subjected to high concentrations of AMP [63].

The stiffness of the *E2146* biofilm with 24 h bCAT (60 µM) treatment was calculated from the force-distance curves. The statistical distribution of the Young modulus as well as a typical force-indentation curve are illustrated in figure 4-28d and 4-28e, respectively. As with the bCAT 30 µM treatment, the Gaussian behavior of the statistical distribution was partially maintained after the bCAT 60 µM treatment; however the average of the Young modulus was shifted to even a lower value of 33 ± 26 kPa. This concentration of the peptide therefore even further increased the elasticity of the bacteria, with respect to the increase seen with the concentration equivalent to half of the MIC (30 µM).

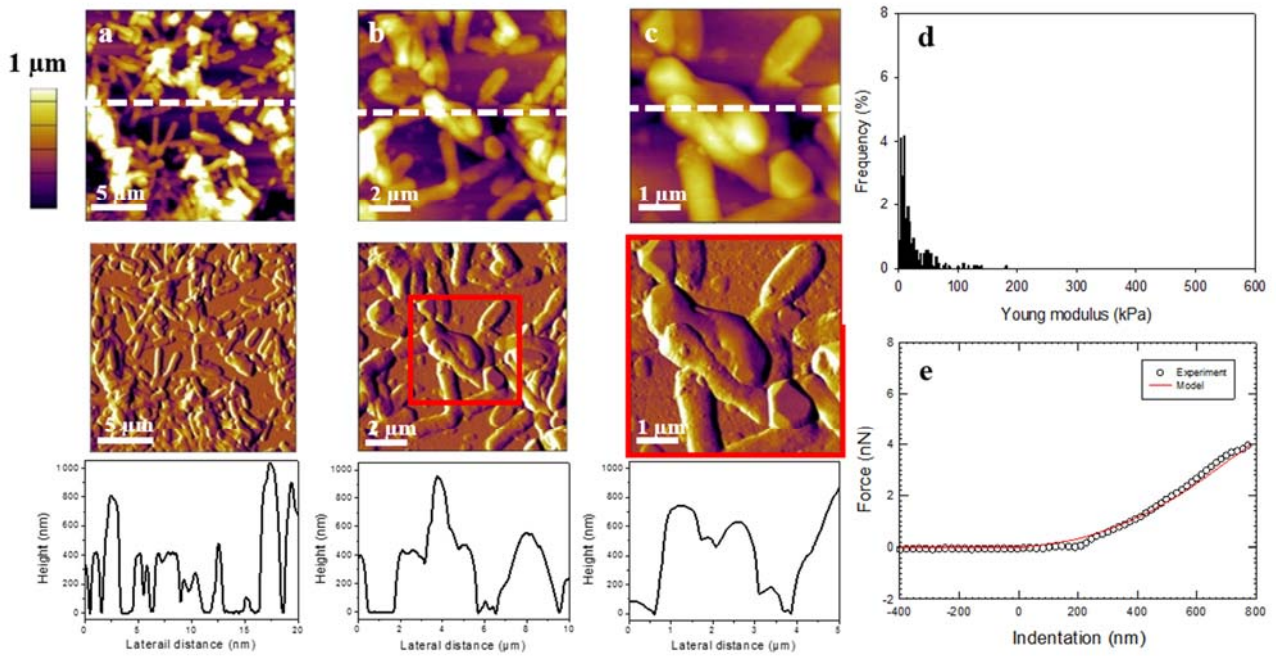


Figure 4-28. A *E2146* biofilm aged 29.5 h with 24h bCAT (60 µM) treatment. AFM images at different lateral sizes (**a**: 20 µm, **b**: 10 µm and **c**: 5 µm, zoom of b indicated with a red square) showing the biofilm morphology. Top panel: height images, middle panel: deflection images and bottom panel: height profiles corresponding to the lateral cross sections indicated by the white dashed lines. **d)** Statistical distribution of the Young modulus **e)** Representative force-indentation curve (open circle) with theoretical model (red line).

After the 24 h bCAT (60 µM) treatment, the *E2146* biofilm was subjected to fresh LB/10 solution in open circulation for 17 h during which the evolution of the IR spectra was recorded every 15 min

(figure 4-26b). The spectral profile corresponded to that of the *E2146* biofilm, however, the main bands of Amide I and II, PS and Amide III-NA assigned to the biofilm were negative and continued to gradually decline over the course of the LB/10 circulation, finally reaching integrated intensities close to zero with respect to those recorded at the very beginning of the biofilm inoculation (figure 4-26c, zone 4). As seen with the bCAT concentration of 30 µM, the effect of bCAT at 60 µM concentration was also bacteriolytic. The peak of Amide II assigned to bCAT at 1622 cm^{-1} was no more present. Neither were peaks characteristic to glycogen production detected, confirming that under the bCAT (60 µM) treatment the bacteria were not likely to produce glycogen supplies. The spectra during the 17 h LB/10 circulation could be due to a loss of bacteria from the Ge crystal. The bacteria detached from the surface and were washed away by the flux of the open circulation.

Indeed, the epifluorescence images recorded after the 17 h LB/10 circulation (figure 4-29) confirmed the loss of bacteria from the surface; with an average coverage ratio of only 1.0 ± 0.8 % (entry side, figure 4-29a), it is clear that only very few bacteria had remained on the crystal. The *Bac*Light ™ stained side (figure 4-29b) revealed great amounts of bacterial debris on the surface, only a few bacteria still remaining. Not only the bacteria were unable to recover from the bCAT (60 µM) treatment, but they also failed to maintain themselves on the support. The average sizes calculated from the remaining bacteria after the 17 h LB/10 circulation were 2.8 ± 0.8 and 0.8 ± 0.1 in length and width respectively.

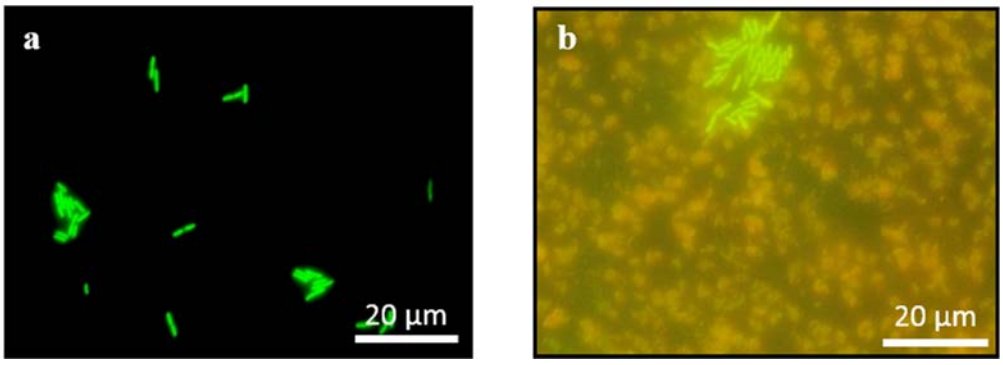


Figure 4-29. Epifluorescence images of a *E2146* biofilm aged 29.5 h with 24 h bCAT (60 µM) LB/10 closed circulation and pure LB/10 open circulation, initial OD_{600} = 0.45 **a)** non-stained (entry) side, average coverage ratio of 1.0 ± 0.8 %, exposure time 500 ms. **b)** *Bac*Light ™ stained (exit) side.

Thus it can be concluded, that according to the spectral fingerprints observed with ATR-FTIR, bCAT changed the metabolism of the *E2146* bacteria in a biofilm. On the contrary to the 29.5 h-old

control biofilm, no glycogen production was detected and the Amide II/PS ratio indicated a higher production of proteins than polysaccharides, also contrary to the control biofilm. The action of bCAT was concentration dependent; at a lower concentration, the changes in the bacterial metabolism were more drastic and changed in the course of the treatment, however the bacterial membrane elasticity was altered more in the case of a higher peptide concentration and according to epifluorescence images, the amount of bacteria detaching from the surface was greater. Also according to epifluorescence images, the average length of the bacteria differed in the case of the two peptide concentrations.

4.5 Comparison of the action of a cyclic and a linear peptide on biofilms

In previous chapters we have shown how a protocol for the formation of a *E2146* biofilm was obtained and how this biofilm was subjected to two distinct antimicrobial peptides in order to study their activity on the biofilms. The activities of the two antibiotic agents in question seem to distinguish from each other and a concentration dependent action of bCAT can be emphasized. The ATR-FTIR spectra recorded in the course of the antimicrobial action revealed differences in the metabolic changes of the biofilm induced by the cyclic and the linear peptide. Where in the presence of colistin, the relative polysaccharide production was to a greater extent at the beginning of the peptide circulation, bCAT altered the polysaccharide production already from the beginning of the 24 h bCAT circulation at both concentrations. On the other hand, colistin seemed to have an inhibitory effect on the nucleic acid production already 2 h after the beginning of the treatment, whereas for the 30 µM bCAT concentration the nucleic acid production started to decline only 12 h after the beginning of the peptide circulation, and it must be mentioned that this happened simultaneously with the decline of other major IR bands, rather suggesting an overall biomass loss than nucleic acid inhibition. An inhibition of the nucleic acid production was also seen with the higher bCAT concentration. The bCAT action on the bacterial metabolism observed by ATR-FTIR was concentration dependent. With both bCAT concentrations studied however, both the IR spectra and the epifluorescence images suggested a bacteriolytic effect of bCAT on the *E2146* biofilm. With colistin on the other hand, the biofilm growth continued after the peptide treatment. Interestingly, the epifluorescence images on the *Bac*Light^{TM} stained side of the crystal of the colistin treated biofilm also suggested a small population of bacteria fluorescing bright green among the other, bigger population emitting red fluorescing light, indicating damaged cell membranes. These intact cells could present a subpopulation of phenotypically differentiated cells that probably

have developed resistance, persisting despite the continued exposure to colistin. Indeed such phenomena is a suggested third mechanism for the increased antimicrobial resistance in biofilms [236, 237].

The sizes and shapes of the *E2146* bacteria in the biofilm varied among the different antimicrobial treatments. The bacteria sizes observed by epifluorescence microcopy after different treatments are listed in table 4-4. Changes in cell morphology is one of the adaptive strategies used by micro-organisms in response to changes in their environment [238]. It must be noted that the greatest difference in terms of size and shape occurred between the two different antimicrobial treatments in question. After colistin treatment, the bacteria adopted cocci shapes suggesting that colistin induced a rod-to-cocci shape transition. During cell division of rod-shaped bacteria such as the *E. coli*, the cell shape is regulated by two reactions of peptidoglycan assembly, one responsible for the lateral wall synthesis and the other responsible for septum formation [239, 240]. It has been reported that certain antimicrobial agents inhibit one or both of these reactions causing a transition in the bacteria morphology, such as the reported rod-to-cocci transition for *E. coli* by amidopenicillanic acid [241, 242]. Based on our results, colistin induced such a rod-to-cocci transition on a biofilm of the *E2146* strain. For the bCAT treated *E2146* biofilms on the other hand, the larger average lengths obtained by epifluorescence microscopy suggested an opposite effect of bCAT on the bacteria cell division, especially at the 30 µM concentration at which bacterial filaments were seen at the very end of the total circulation time, indicating a bacterial stress within the biofilm.

Table 4-4. Sizes of 29.5 h-old *E2146* biofilm bacteria obtained by epifluorescence microscopy with different treatments; directly after 24 h LB/10 or peptide treatment and after 17 h LB/10 open circulation post peptide treatment.

Biofilm	Length (µm) after 24 h	Width (µm) after 24 h	Length (µm) after 17h LB/10	Width (µm) after 17h LB/10
***E2146* 29.5 h control**	1.8 ± 0.4	0.7 ± 0.1	-	-
***E2146* 29.5 h col 0.87 µM**	1.6 ± 0.2	0.7 ± 0.1	1.9 ± 0.23	0.6 ± 0.1
***E2146* 29.5 h bCAT 30 µM**	3.8 ± 0.4	1.0 ± 0.2	2.2 ± 0.5	0.8 ± 0.2
***E2146* 29.5 h bCAT 60 µM**	3.1 ± 0.5	0.8 ± 0.1	2.8 ± 0.8	0.8 ± 0.1

The differences of bacterial morphologies were also detected with AFM imaging and in addition, the AFM force spectra provided information on the changes of the elastic properties of the bacterial

membranes subjected to different antimicrobial treatments. The bacterial sizes and Young modulus values obtained after different antimicrobial treatments by AFM are recapitulated in table 4-5.

Table 4-5. Sizes and Young modulus values of *E2146* biofilm bacteria with different AMP treatments obtained by AFM. *Values calculated on the average of 10 randomly taken individual bacteria. **Young modulus average of three individual force maps.

Biofilm	Height (nm)*	Length (µm)*	Width (µm)*	Young modulus (kPa)**
***E2146* 5.5 h blanc**	303 ± 44	2.3 ± 0.6	0.8 ± 0.1	135 ± 89
***E2146* 29.5 h col 0.87 µM**	76 ± 18	1.6 ±0.2	1.1 ± 0.1	598 ± 277
***E2146* 29.5 h bCAT 30 µM**	167 ± 23	2.1 ± 0.4	1.2 ± 0.1	48 ± 27
***E2146* 29.5 h bCAT 60 µM**	382 ± 44	2.2 ± 0.3	0.8 ± 0.1	33 ± 26

Colistin had a dramatic stiffening impact on the bacteria membranes, contrary to the effect caused by the bCAT treatment obtained for both bCAT concentrations, which lowered the Young modulus of the cells.

The hypothesized mechanisms of action of the two AMPs studied on *E. coli* biofilms are illustrated in figure 4-30. Colistin induced a shape transition of the bacteria within the biofilm. This change transition together with colistin accumulation on the bacteria membranes could possibly be the origins of membrane stiffening. bCAT on the other hand could accumulate on the bacteria membrane as β-sheets, causing pores that could lead to the leak of intracellular material and therefore to a decrease in membrane stiffness observed via force spectroscopy measurements.

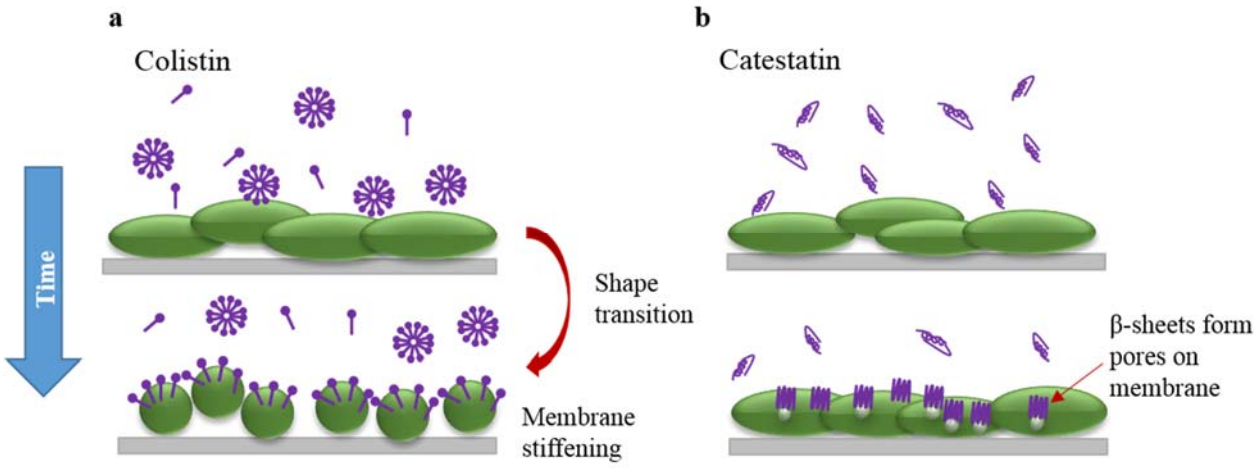


Figure 4-30. Hypothesized mechanism of action of the two AMPs at minimal inhibitory concentration on *E. coli* biofilms. **a)** colistin (0.87 µM) action as a function of time **b)** bCAT (60 µM) action as a function of time).

5. Conclusions

The objective of this work was to study the action of two different antimicrobial agents; 1) colistin, a cyclic polypeptide already being used to treat infections caused by multiresistant bacteria and 2) catestatine bovine, a relatively recently discovered linear peptide that has shown antimicrobial potential. An interdisciplinary and multiscale approach for this study was chosen, starting from the observations of phospholipid and lipopolysaccharide model membranes under the influence of these peptides, continuing to the establishment of a protocol for *E. coli E2146* biofilm formation and finally to the observations of changes caused by the peptides in living sessile bacteria of the biofilm. For these purposes, multiple physico-chemical characterization techniques including Langmuir monolayers of phospholipids, atomic force microscopy (imaging and force spectra) and Fourier transform infrared spectroscopy in attenuated total reflection mode for lipid bilayers and bacterial biofilms were used.

The first step of the study was dedicated to the understanding of interactions of colistin with model phospholipid membranes via Langmuir monolayers. In order to complete the results obtained by monolayers, bilayers of the corresponding phospholipids were studied with AFM and ATR-FTIR. For these purposes, a protocol for bilayer formation on ATR germanium crystal needed to be established, after which the spectral changes of the phospholipid bilayers due to colistin were studied. Complementary results were obtained with these three techniques, suggesting modifications on the elasticity and morphology of the lipid model membranes due to the action of colistin, notably when a mixture of two phospholipids was present. Differences in the spectral characteristics were also observed, especially in the Amide II/C=O integrated intensity ratio that further strengthened the hypothesis that the effects of the peptide were the greatest in mixed phospholipid model membranes.

The work was then continued in order to observe the influence of bCAT on the phospholipid bilayers of DPPC, DOPD and DPPC/DOPC bilayers. AFM images and force spectra evidenced important changes in the structure and elasticity of the bilayers immediately after the addition of bCAT into the system. These changes continued throughout the course of time. According to Amide I bands present in the spectral profile recorded by ATR-FTIR after the addition of bCAT, it was detected that the conformational behavior of bCAT peptide changed with respect to the bilayer content present. Again the Amide II/C=O integrated intensity ratio suggested that the effect of the peptide was greatest in the presence of two different lipid phases and that the peptide action was primarily directed towards the gel phase lipid of the bilayer.

To further develop the understanding of the peptide action on model membranes, bilayers of two lipopolysaccharide compounds with distinct O-antigen chain lengths together with the LPS anchoring lipid A were formed and examined with AFM imaging and force spectra under the influence of colistin and bCAT. It was found that the two antimicrobial agents reorganized the lipid bilayer structure in all of the LPS bilayer compositions, with the exception of bCAT action on a bilayer containing lipid A and total LPS extract, on which the peptide formed pores of various sizes. The influence of the peptides on the elasticities of the bilayers also changed with respect to the lipid composition of the studied samples and a dramatic impact on the stiffness of the bilayer composed of lipid A and total LPS extract was observed due to the influence of bCAT.

In order to be able to move on to the last step of the work which involved bacterial biofilms, the establishment of a protocol for *E. coli E2146* biofilm formation was necessary. For this purpose, growth curves of *E2146* planktonic cells were established together with biofilms of different ages on germanium ATR crystal and the development of the biofilm was monitored with ATR-FTIR in real time. This was important in order to get as homogeneous monolayer of bacterial cells as possible and indeed vast spectral changes were detected among the different biofilm growth times. It was found that a biofilm aged 2.5 h was too young whereas the biofilm aged 26.5 h biofilm was too mature to further be applied to peptide studies. The optimal total biofilm forming time was decided to be 5.5 h, this being a time necessary for the biofilm to develop to a mature state, still at its exponentially growing, yet being developed enough to undergo 24 h antimicrobial treatment. As a consequence, the 5.5 h-old biofilm was chosen as a reference biofilm for the studies conducted with the two different antimicrobial peptides.

Finally, two of the above mentioned techniques, ATR-FTIR and AFM, were used to examine the effect of a 24 h peptide treatment, either colistin or bCAT on the formed *E2146* biofilm. ATR-FTIR enabled the follow up of changes in the spectral fingerprints of the biofilm on the course of the peptide treatment, providing information on the possible changes in bacterial metabolism, whereas AFM was used to visualize the morphological and elastic changes in the biofilm bacteria after a peptide treatment. Both of these techniques provided valuable information on the very different influences of the two peptides on the bacteria in a biofilm; metabolic changes due to colistin were mainly concentrated on nucleic acid production, whereas bCAT seemed to alter the polysaccharide production of the bacteria in the biofilm, showing a concentration dependent mechanism of action. The elastic properties of the bacteria were also altered in different manners with the two different peptides; colistin had a stiffening effect on the bacteria whereas bCAT influenced the bacterial membranes in a fluidizing way. Morphological changes of the bacteria were also seen, colistin

inducing a rod-to-cocci transition of the bacteria and bCAT altering the septum formation process, leading to longer bacterial cells and even filamentous structures seen with epifluorescence microscopy. Furthermore, the continued flow of fresh nutrient media after the peptide treatment evidenced that the influence of colistin treatment was reversible, whereas bCAT induced a bacteriolytic effect on the biofilm and the biofilm could not recover itself from the 24 h peptide treatment.

All the techniques used in this study therefore evidence very different action for the two antimicrobial peptides, colistin and bCAT, at a molecular and nanometer scale as well as on living micro-organisms. It must however be kept in mind that membranes of living organisms are extremely complex systems and that although model membranes can be used to obtain valuable information on specific interactions between membrane compounds and exogenous agents, attention should be paid to the vast simplification of the structure of these membranes and direct comparison between the model membranes and living organisms should be avoided.

Comparative studies of conventional and novel antimicrobial agents involving multiple physico-chemical techniques should be useful when fighting against multiresistant microbes. Novel AMPs could be complementary to conventional antibiotics due to their very different modes of action at various levels of the micro-organism structures, as seen in this study in terms of PL and LPS compositions as well as in bacterial metabolism and morphology. In addition to the possibility of enhanced potential of such antimicrobial “cocktails”, the simultaneous use of AMPs with conventional antibiotics such as colistin could also enable the reduction of the dosage needed, also leading to the reduction of the reported toxicities of colistin. Therefore it should be of great interest to conduct similar studies for instance on mixtures of conventional antibiotics and novel AMPs.

Nevertheless, it should be interesting to further examine the possible effects of mixtures of antimicrobial peptides with such vast differences in their modes of action, especially on the bacterial biofilms, as they are providing an enormous challenge to, for instance, biomaterials used in medical equipment. These kinds of multipotential antimicrobial “cocktails” consisting of conventional antimicrobial agents and novel antimicrobial peptides could be a possible solution in the war against infections caused by multiresistant microbes.

References

1. Campbell, et al., Biology, 8th edition p. 125.
2. Alberts, et al., Molecular Biology of the Cell, 5th edition, p. 617.
3. Danielli and Davson, A contribution to the theory of permeability of thin films. Journal of Cellular and Comparative Physiology, 1935. 5: p. 495.
4. Singer and Nicolson, The fluid mosaic model of the structure of cell membranes. Science, 1972. 175.
5. Nicolson, The Fluid—Mosaic Model of Membrane Structure: Still relevant to understanding the structure, function and dynamics of biological membranes after more than 40 years. Biochimica et Biophysica Acta (BBA) - Biomembranes, 2014. 1838(6): p. 1451-1466.
6. Sourkes, The discovery of lecitin, the first phospholipid. Bull. Hist. Chem, 2004. 29(1).
7. Gorther, On biomolecular Leyers of Lipids on the chromocytes of the blood. Journal of Experimental Medicine, 1925. 41: p. 439-443.
8. Langmuir, The constitution and fundamental properties of solids and liquids. J. Am. Chem., 1917: p. 1848.
9. Alberts et al., Molecular Biology of the Cell. 5th Edition: p. 617-627.
10. Dowhan, Molecular basis for membrane phospholipid diversity: Why Are There So Many Lipids? Annual Review of Biochemistry, 1997. 66(1): p. 199-232.
11. van Meer et al., Membrane lipids: where they are and how they behave. Nat Rev Mol Cell Biol, 2008. 9(2): p. 112-24.
12. Kay and Grinstein, Sensing Phosphatidylserine in Cellular Membranes. Sensors (Basel, Switzerland), 2011. 11(2): p. 1744-1755.
13. van Meer, Cellular lipidomics. The EMBO Journal, 2005. 24(18): p. 3159-3165.
14. Wikipedia, https://en.wikipedia.org/wiki/Cell_membrane#/media/File:Cell_membrane_detailed_diagram_en.svg. 2016.
15. Tripathi et al., Towards a nanoscale view of lactic acid bacteria. Micron, 2012. 43(12): p. 1323-1330.
16. Beveridge, Structures of Gram-negative cell walls and their derived membrane vesicles. Journal of Bacteriology, 1999. 181: p. 4725-4733.
17. Nikaido and Rosenberg, Porin channels in *Escherichia coli*: studies with liposomes reconstituted from purified proteins, Journal of Bacteriology, 1983. 153: p. 241-252.
18. Koebnik and van Gelder, Structure and function of bacterial outer membrane proteins: barrels in a nutshell. Molecular Microbiology, 2000. 37: p. 239-253.

19. Nikaido, Molecular basis of bacterial outer membrane permeability revised. Microbiology and Molecular Biology Reviews, 2003. 67: p. 593-656.
20. Opiyo et al., Evolution of the KDO_2-lipid A biosynthesis in bacteria, BMC Evolutionary Biology, 2010. 10(362): p. 1-13.
21. D'Errico et al., Mesoscopic and microstructural characterization of liposomes formed by the lipooligosaccharide from *Salmonella minnesota* strain 595 (Re mutant). Physical Chemistry Chemical Physics, 2009. 11(13): p. 2314-2322.
22. Nikaido, Molecular basis of bacterial outer membrane permeability. Microbiological Reviews, 1985. 49: p. 1-32.
23. Labischinski et al., High state of order of isolated bacterial lipopolysaccharide and its possible contribution to the permeation barrier property of the outer membrane. Journal of Bacteriology, 1985. 162(1): p. 9-20.
24. Leone et al., Molecular Structure of Endotoxins from Gram-negative Marine Bacteria: An Update. Marine Drugs, 2007. 5(3): p. 85-112.
25. Kučerka et al., Effect of Cations on the Structure of Bilayers Formed by Lipopolysaccharides Isolated from *Pseudomonas aeruginosa* PAO1. The Journal of Physical Chemistry B, 2008. 112(27): p. 8057-8062.
26. Vaara and Nurminen, Outer Membrane Permeability Barrier in *Escherichia coli* Mutants That Are Defective in the Late Acyltransferases of Lipid A Biosynthesis. Antimicrobial Agents and Chemotherapy, 1999. 43(6): p. 1459-1462.
27. van Dalen and de Kruijff, The role of lipids in membrane insertion and translocation of bacterial proteins. Biochimica et Biophysica Acta (BBA) - Molecular Cell Research, 2004. 1694(1–3): p. 97-109.
28. Dowhan, Molecular basis for membrane phospholipid diversity: why are there so many lipids? Annual Review of Biochrmistry, 1997. 66: p. 199-232.
29. Yao et al., Atomic force microscopy and theoretical considerations of surface properties and turgor pressures of bacteria. Colloids and Surfaces B: Biointerfaces, 2002. 23(2): p. 213-230.
30. Burks et al., Macroscopic and nanoscale measurements of the adhesion of bacteria with varying outer layer surface composition. Langmuir, 2003. 19(6): p. 2366-2371.
31. Janmey and Kinnunen, Biophysical properties of lipids and dynamic membranes. Trends Cell Biol, 2006. 16(10): p. 538-46.
32. Vance, Phospholipid synthesis in a membrane fraction associated with mitochondria. J Biol Chem, 1990. 265(13): p. 7248-56.
33. Hadley, The adaptive role of lipids in biological systems. 1985.

34. Akoh and Min., Food Lipids: Chemistry, Nutrition and Biotechnology. 3rd Edition: p. 40.
35. Lodish and Zipursky, Molecular Cell Biology. 4th edition. New York: W. H. Freeman, 2000. Section 5.3, Biomembranes: Structural Organization and Basic Functions.
36. Parsons and Rock, Bacterial lipids: metabolism and membrane homeostasis. Prog Lipid Res, 2013. 52(3): p. 249-76.
37. Glyden et al., Organic Chemistry. 2005: p. 1376.
38. Beauvais, Caracterisation de systemes biologiques a l'echelle nanometrique : etudes des interactions entre des modeles membranaires et des agents exogenes. Universite de Technologie de Compiegne, 2013.
39. Goot and Harder, Raft membrane domains: from a liquid-ordered membrane phase to a site of pathogen attack. Seminars in Immunology, 2001. 13(2): p. 89-97.
40. Cronan et al., Physical properties of membrane lipids: Biological relevance and regulation. Bacteriological Reviews, 1975. 39(3): p. 232-256.
41. Stuart, Infrared spectroscopy: Fundamentals and applications. p. 137-163.
42. Brown and London, Structure and Origin of Ordered Lipid Domains in Biological Membranes. The Journal of Membrane Biology, 1998. 164(2): p. 103-114.
43. Recktenwald and McConnell, Phase equilibriums in binary mixtures of phosphatidylcholine and cholesterol. Biochemistry, 1981. 20(15): p. 4505-4510.
44. Ipsen et al., Relationships between lipid membrane area, hydrophobic thickness, and acyl-chain orientational order. The effects of cholesterol. Biophysical Journal, 1990. 57(3): p. 405-412.
45. Vist and Davis, Phase equilibria of cholesterol/dipalmitoylphosphatidylcholine mixtures: deuterium nuclear magnetic resonance and differential scanning calorimetry. Biochemistry, 1990. 29(2): p. 451-464.
46. Brasseur et al., The Biologically Important Surfactin Lipopeptide Induces Nanoripples in Supported Lipid Bilayers. Langmuir, 2007. 23(19): p. 9769-9772.
47. Kaasgaard et al., Temperature-Controlled Structure and Kinetics of Ripple Phases in One- and Two-Component Supported Lipid Bilayers. Biophysical Journal, 2003. 85(1): p. 350-360.
48. Leidy et al., Ripples and the formation of anisotropic lipid domains: imaging two-component supported double bilayers by atomic force microscopy. Biophys J, 2002. 83(5): p. 2625-33.
49. Chung and Raetz, Interchangeable domains in the Kdo transferases of *Escherichia coli* and Haemophilus influenzae. Biochemistry, 2010. 49(19): p. 4126-37.

50. Clifton et al., Asymmetric phospholipid: lipopolysaccharide bilayers; a Gram-negative bacterial outer membrane mimic. Journal of The Royal Society Interface, 2013. 10(89).
51. Raetz and Whitfield, Lipopolysaccharide Endotoxins. Annual review of biochemistry, 2002. 71: p. 635-700.
52. Reeves et al., Bacterial polysaccharide synthesis and gene nomenclature. Trends in Microbiology, 1996. 4(12): p. 495-503.
53. Kastowsky et al., Comparison of X-ray powder-diffraction data of various bacterial lipopolysaccharide structures with theoretical model conformations. European Journal of Biochemistry, 1993. 217(2): p. 771-779.
54. Leonenko et al., Investigation of Temperature-Induced Phase Transitions in DOPC and DPPC Phospholipid Bilayers Using Temperature-Controlled Scanning Force Microscopy. Biophysical Journal, 2004. 86(6): p. 3783-3793.
55. Kaufmann et al., Supported Lipopolysaccharide Bilayers. Langmuir, 2012. 28(33): p. 12199-12208.
56. Young, The Selective Value of Bacterial Shape. Microbiology and Molecular Biology Reviews, 2006. 70(3): p. 660-703.
57. Wikipedia, https://en.wikipedia.org/wiki/Bacterial_cell_structure#/media/File:Bacterial_morphology_diagram.svg. 2016.
58. Proft and Baker, Pili in Gram-negative and Gram-positive bacteria - structure, assembly and their role in disease. Cell Mol Life Sci, 2009. 66(4): p. 613-35.
59. Campbell et al., Biology. 8th edition: p. 98.
60. Llobet et al., Capsule polysaccharide is a bacterial decoy for antimicrobial peptides. Microbiology, 2008. 154(Pt 12): p. 3877-86.
61. Campos et al., Capsule polysaccharide mediates bacterial resistance to antimicrobial peptides. Infect Immun, 2004. 72(12): p. 7107-14.
62. Watnick and Kolter, Biofilm, city of microbes. J Bacteriol, 2000. 182(10): p. 2675-9.
63. Quilès et al., In situ and real time investigation of the evolution of a *Pseudomonas fluorescens* nascent biofilm in the presence of an antimicrobial peptide. Biochimica et Biophysica Acta (BBA) - Biomembranes, 2016. 1858(1): p. 75-84.
64. Melo and Bott, Heat Exchange Fouling Biofouling in water systems. Experimental Thermal and Fluid Science, 1997. 14(4): p. 375-381.
65. Zobell, The Effect of Solid Surfaces upon Bacterial Activity. Journal of Bacteriology, 1943. 46(1): p. 39-56.
66. Costerton et al., How bacteria stick. Sci Am, 1978. 238(1): p. 86-95.

67. Donlan and Costerton, Biofilms: Survival Mechanisms of Clinically Relevant Microorganisms. Clinical Microbiology Reviews, 2002. 15(2): p. 167-193.
68. Mah and O'Toole, Mechanisms of biofilm resistance to antimicrobial agents. Trends in Microbiology. 9(1): p. 34-39.
69. Stewart and Costerton, Antibiotic resistance of bacteria in biofilms. The lancet, 2001. 358(9276): p. 135-138.
70. Vu et al., Bacterial extracellular polysaccharides involved in biofilm formation. Molecules, 2009. 14(7): p. 2535-54.
71. Chandra et al., Biofilm formation by the fungal pathogen *Candida albicans*: development, architecture, and drug resistance. J Bacteriol, 2001. 183(18): p. 5385-94.
72. Donlan, Biofilm formation: a clinically relevant microbiological process. Clin Infect Dis, 2001. 33(8): p. 1387-92.
73. Lasa, Towards the identification of the common features of bacterial biofilm development. Int Microbiol, 2006. 9(1): p. 21-8.
74. Stoodley et al., Biofilms as complex differentiated communities. Annu Rev Microbiol, 2002. 56: p. 187-209.
75. Gonzales et al., Excessive antibiotic use for acute respiratory infections in the United States. Clinical Infectious Diseases, 2001. 33(6): p. 757-762.
76. Livermore, Minimising antibiotic resistance. Lancet Infectious Diseases, 2005. 5(7): p. 450-459.
77. Wright, Mechanisms of resistance to antibiotics. Current Opinion in Chemical Biology, 2003. 7(5): p. 563-569.
78. Chopra et al., Treatment of health-care-associated infections caused by Gram-negative bacteria: a consensus statement. Lancet Infectious Diseases, 2008. 8(2): p. 133-139.
79. Rice, The clinical consequences of antimicrobial resistance. Current Opinion in Microbiology, 2009. 12(5): p. 476-481.
80. Balhara et al., Membrane selectivity and biophysical studies of the antimicrobial peptide GL13K. Biochimica et Biophysica Acta, 2013. 1828(2193-2203).
81. Park et al., Antibacterial synergism of novel antibiotic peptides with chloramphenicol. Biochemical and Biophysical Research Communications, 2004. 321(1): p. 109-115.
82. Park et al., Mechanism of action of the antimicrobial peptide buforin II: buforin II kills microorganisms by penetrating the cell membrane and inhibiting cellular functions. Biochem Biophys Res Commun, 1998. 244(1): p. 253-7.

83. Park et al., The Role of Antimicrobial Peptides in Preventing Multidrug-Resistant Bacterial Infections and Biofilm Formation. International Journal of Molecular Sciences, 2011. 12(9): p. 5971.
84. Andreu and Rivas, Animal antimicrobial peptides: an overview. Biopolymers, 1998. 47(6): p. 415-33.
85. Epand and Vogel, Diversity of antimicrobial peptides and their mechanisms of action. Biochim Biophys Acta, 1999. 1462(1-2): p. 11-28.
86. Li et al., Atomic force microscopy study of the antimicrobial action of Sushi peptides on Gram negative bacteria. Biochimica et Biophysica Acta (BBA) - Biomembranes, 2007. 1768(3): p. 411-418.
87. Shai, Mechanism of the binding, insertion and destabilization of phospholipid bilayer membranes by α-helical antimicrobial and cell non-selective membrane-lytic peptides. Biochimica et Biophysica Acta (BBA) - Biomembranes, 1999. 1462(1–2): p. 55-70.
88. Matsuzaki, Why and how are peptide-lipid interactions utilized for self-defense? Magainins and tachyplesins as archetypes. Biochim Biophys Acta, 1999. 1462(1-2): p. 1-10.
89. Straus and Hancock, Mode of action of the new antibiotic for Gram-positive pathogens daptomycin: Comparison with cationic antimicrobial peptides and lipopeptides. Biochimica et Biophysica Acta (BBA) - Biomembranes, 2006. 1758(9): p. 1215-1223.
90. Mecke et al., Membrane Thinning Due to Antimicrobial Peptide Binding: An Atomic Force Microscopy Study of MSI-78 in Lipid Bilayers. Biophysical Journal, 2005. 89(6): p. 4043-4050.
91. Yang et al., Barrel-Stave Model or Toroidal Model? A Case Study on Melittin Pores. Biophysical Journal, 2001. 81(3): p. 1475-1485.
92. Henzler Wildman et al., Mechanism of Lipid Bilayer Disruption by the Human Antimicrobial Peptide, LL-37. Biochemistry, 2003. 42(21): p. 6545-6558.
93. Wimley, Describing the Mechanism of Antimicrobial Peptide Action with the Interfacial Activity Model. ACS chemical biology, 2010. 5(10): p. 905-917.
94. Grau-Campistany et al., Membrane interaction of polumyxin B and synthetic analogues studied in biomimetic systems: implications for antibacterial action. Recent Advances in pharmaceutical Sciences III, 2013: p. 61-75.
95. Wolinsky et al., Neurotoxic and nephrotoxic effect of colistin in patients with renal disease. New England Journal of Medicine, 1962. 266(15): p. 759-62.
96. Linden et al., Parenteral and inhaled colistin for treatments of ventilator-associated pneumonia. Clinical Infectious Diseases, 2006. 43: p. 89-94.

97. Falagas and Kasiakou, Colistin: the revival of polymyxins for the management of multidrug-resistant gram-negative bacterial infections. (vol 40, pg 1333, 2005). Clinical Infectious Diseases, 2006. 42(12): p. 1819-1819.
98. Gupta, Colistin and polymyxin B: A re-emergence. Indian Journal of Critical Care Medicine, 2009. 13(2): p. 49-53.
99. Li et al., Evaluation of colistin as an agent against multi-resistant in Gram-negative bacteria. International Journal of Antimicrobial Agents, 2005. 25(1): p. 11-25.
100. Levin et al., Intravenous colistin as therapy for nosocomial infections caused by multidrug-resistant Pseudomonas aeruginosa and *Acinetobacter baumannii*. Clinical Infectious Diseases, 1999. 28(5): p. 1008-1011.
101. Koike, Electron microscopic studies on mode of action of polymyxin. Journal of Bacteriology, 1969. 97(1): p. 448-452.
102. David at al., Antibacterial action of colistin (polymyxin E) againts *Mycobacterium aurum*. Antimicrobial Agents and Chemotherapy, 1985. 27(5): p. 701-707.
103. Mestres et al., Interactions of colistin with lipids in liposomes and monolayers. International Journal of Pharmaceutics, 1998. 160: p. 99-107.
104. Moore et al., Interaction of polycationic antibiotics with *Pseudomonas aerigunosa* lipopolysaccharide and lipid A studies by using dansyl-polymyxin. Antimicrobial Agents and Chemotherapy, 1986. 29(3): p. 496-500.
105. Morrison et al., Binding of polymyxin B to the lipid A position of bacterial lipopolysaccharides. Immunochemistry, 1976. 13: p. 813-818.
106. Schindler et al., Action of polymyxin B on bacterial membranes: morphological changes in the cytoplasm and in the outer membrane of *Salmonella typhimurium* and *Escherichia coli* B. antimicrobial Agents and Chemotherapy, 1975. 8(1): p. 95-104.
107. Teuber et al., Action of polymyxin B on bacterial membranes: phosphatidylglycerol- and cardiolipin-induced susceptibility to polymyxin B in *Acholeplasma laidlawii* B. Antimicrobial Agents and Chemotherapy, 1976. 9(1): p. 26-35.
108. Freudenthal et al., Nanoscale investigation of the interaction of colistin with model phospholipid membranes by Langmuir technique, and combined infrared and force spectroscopies. Biochimica et Biophysica Acta (BBA)-Biomembranes, 2016. 1858(11): p. 2592-2602.
109. Ahn et al., Primary structure of bovine pituitary secretory protein I (chromogranin A) deduced from the cDNA sequence. Proc Natl Acad Sci U S A, 1987. 84(14): p. 5043-7.
110. D'Amico et al., Biological function and clinical relevance of chromogranin A and derived peptides. Endocr Connect, 2014. 3(2): p. R45-54.

111. Akaddar et al., Catestatin, an endogenous chromogranin A-derived peptide, inhibits in vitro growth of *Plasmodium falciparum*. Cell Mol Life Sci, 2010. 67(6): p. 1005-15.
112. Radek et al., The Neuroendocrine Peptide Catestatin Is a Cutaneous Antimicrobial and Induced in the Skin after Injury. Journal of Investigative Dermatology, 2008. 128(6): p. 1525-1534.
113. Jean-Francois et al., Aggregation of cateslytin beta-sheets on negatively charged lipids promotes rigid membrane domains. A new mode of action for antimicrobial peptides? Biochemistry, 2008. 47(24): p. 6394-402.
114. Epand and Epand, Lipid domains in bacterial membranes and the action of antimicrobial agents. Biochimica et Biophysica Acta (BBA) - Biomembranes, 2009. 1788(1): p. 289-294.
115. Maget-Dana, The monolayer technique: a potent tool for studying the interfacial properties of antimicrobial and membrane-lytic peptides and their interactions with lipid membranes. Biochimica et Biophysica Acta (BBA) - Biomembranes, 1999. 1462(1–2): p. 109-140.
116. Barzyk et al., The affinity of two antimicrobial peptides derived from bovine milk proteins for model lipid membranes. Colloids and Surfaces A: Physicochemical and Engineering Aspects, 2009. 343(1–3): p. 104-110.
117. Brezesinski and Möhwald, Langmuir monolayers to study interactions at model membrane surfaces. Advances in Colloid and Interface Science, 2003. 100–102: p. 563-584.
118. Peetla et al., Biophysical interactions with model lipid membranes: applications in drug discovery and drug delivery. Molecular pharmaceutics, 2009. 6(5): p. 1264-1276.
119. Volinsky et al., Investigations of antimicrobial peptides in planar film systems. Biochimica et Biophysica Acta (BBA) - Biomembranes, 2006. 1758(9): p. 1393-1407.
120. Barzyk et al., Penetration of Milk-Derived Antimicrobial Peptides into Phospholipid Monolayers as Model Biomembranes. Biochemistry Research International, 2013. 2013: p. 16.
121. Zhang et al., Interaction of cationic antimicrobial peptides with model membranes. J Biol Chem, 2001. 276(38): p. 35714-22.
122. Volinsky et al., Morphology and Organization of Phospholipid/Diacetylene Langmuir Films Studied by Brewster Angle Microscopy and Fluorescence Microscopy. The Journal of Physical Chemistry B, 2002. 106(36): p. 9231-9236.
123. Vila-Romeu et al., Mixed Langmuir Monolayers of Gramicidin A and Ethyl Palmitate: Pressure−Area Isotherms and Brewster Angle Microscopy. The Journal of Physical Chemistry B, 2002. 106(38): p. 9820-9824.

124. McConnell et al., Periodic structures in lipid monolayer phase transitions. Proceedings of the National Academy of Sciences of the United States of America, 1984. 81(10): p. 3249-3253.
125. Binnig et al., Atomic force microscope. Physical review letters, 1986. 56(9): p. 930.
126. Binnig et al., Surface Studies by Scanning Tunneling Microscopy. Physical Review Letters, 1982. 49(1): p. 57-61.
127. Keller et al., Imaging of single uncoated DNA molecules by scanning tunneling microscopy. Proceedings of the National Academy of Sciences, 1989. 86(14): p. 5356-5360.
128. Rugar and Hansma, Atomic force microscopy. Physics today, 1990. 43(10): p. 23-30.
129. Martin et al., Atomic force microscope–force mapping and profiling on a sub 100-Å scale. Journal of Applied Physics, 1987. 61(10): p. 4723-4729.
130. Lee et al., Direct measurement of the forces between complementary strands of DNA. SCIENCE, 1994: p. 771-771.
131. Ando et al., High-speed AFM and nano-visualization of biomolecular processes. Pflügers Archiv-European Journal of Physiology, 2008. 456(1): p. 211-225.
132. Schitter et al., Design and modeling of a high-speed AFM-scanner. IEEE Transactions on Control Systems Technology, 2007. 15(5): p. 906-915.
133. Attwood et al., Preparation of DOPC and DPPC Supported Planar Lipid Bilayers for Atomic Force Microscopy and Atomic Force Spectroscopy. International Journal of Molecular Sciences, 2013. 14(2): p. 3514.
134. Shaw et al., Memchanisms of antimicrobial peptide action: Studies of indolicidin assembly at model membrane interfaces by in situ atomic force microsopy. Journal of Structural Biology, 2006. 154: p. 42-58.
135. Domenech et al., Interactions of oritavancin, a new lipoglycopeptide derived from vancomycin, with phospholipid bilayers: Effect on membrane permeability and nanoscale lipid membrane organization. Biochimica et Biophysica Acta, 2009. 1788: p. 1832-1840.
136. Francius et al., Nanoscale membrane activity of surfactins: Influence of geometry, charge and hydrophobicity. Biochimica et Biophysica Acta (BBA) - Biomembranes, 2008. 1778(10): p. 2058-2068.
137. Tong and McIntosh, Structure of Supported Bilayers Composed of Lipopolysaccharides and Bacterial Phospholipids: Raft Formation and Implications for Bacterial Resistance. Biophysical Journal, 2004. 86(6): p. 3759-3771.
138. Garcia-Manyes et al., Nanomechanics of lipid bilayers: heads or tails? Journal of the American Chemical Society, 2010. 132(37): p. 12874-12886.

139. Jacquot et al., Morphological and Physical Analysis of Natural Phospholipids-Based Biomembranes. PLoS ONE, 2014. 9(9): p. e107435.
140. Garcia-Manyes and Sanz, Nanomechanics of lipid bilayers by force spectroscopy with AFM: a perspective. Biochimica et Biophysica Acta (BBA)-Biomembranes, 2010. 1798(4): p. 741-749.
141. Meincken et al., Atomic force microscopy study of the effect of antimicrobial peptides on the cell envelope of *Escherichia coli*. Antimicrobial agents and chemotherapy, 2005. 49(10): p. 4085-4092.
142. Mularski et al., Atomic force microscopy reveals the mechanobiology of lytic peptide action on bacteria. Langmuir, 2015. 31(22): p. 6164-6171.
143. Volle et al., Quantitative changes in the elasticity and adhesive properties of Escherichia coli ZK1056 prey cells during predation by Bdellovibrio bacteriovorus 109J. Langmuir, 2008. 24(15): p. 8102-8110.
144. Pembrey et al., Cell surface analysis techniques: what do cell preparation protocols do to cell surface properties? Applied and Environmental Microbiology, 1999. 65(7): p. 2877-2894.
145. Polyakov et al., Automated Force Volume Image Processing for Biological Samples. PLoS ONE, 2011. 6(4): p. e18887.
146. Gaboriaud et al., Surface structure and nanomechanical properties of *Shewanella putrefaciens* bacteria at two pH values (4 and 10) determined by atomic force microscopy. Journal of bacteriology, 2005. 187(11): p. 3864-3868.
147. Touhami et al., Nanoscale mapping of the elasticity of microbial cells by atomic force microscopy. Langmuir, 2003. 19(11): p. 4539-4543.
148. da Silva Jr and Teschke, Effects of the antimicrobial peptide PGLa on live *Escherichia coli*. Biochimica et Biophysica Acta (BBA) - Molecular Cell Research, 2003. 1643(1–3): p. 95-103.
149. Tamm and Tatulian, Infrared spectroscopy of proteins and peptides in lipid bilayers. Quarterly Reviews of Biophysics, 1997. 30(04): p. 365-429.
150. Goormaghtigh et al., Attenuated total reflection infrared spectroscopy of proteins and lipids in biological membranes. Biochimica et Biophysica Acta (BBA) - Reviews on Biomembranes, 1999. 1422(2): p. 105-185.
151. Ter-Minassian-Saraga et al., Fourier transform infrared-attenuated total reflection spectroscopy of hydration of dimyristoylphosphatidylcholine multibilayers. Biochimica et Biophysica Acta (BBA) - Biomembranes, 1988. 946(2): p. 417-423.

152. Picard et al., Quantitative orientation measurements in thin lipid films by attenuated total reflection infrared spectroscopy. Biophys J, 1999. 76(1 Pt 1): p. 539-51.
153. Lewis and McElhaney, The structure and organization of phospholipid bilayers as revealed by infrared spectroscopy. Chemistry and Physics of Lipids, 1998. 96(1–2): p. 9-21.
154. Fringeli, The structure of lipids and proteins studied by attenuated total reflection (ATR) infrared spectroscopy. II. Oriented layers of a homologous series: phosphatidylethanolamine to phosphatidylcholine. Zeitschrift fuer Naturforschung, C: Journal of Biosciences, 1977. 32C(1-2): p. 20-45.
155. Arrondo et al., Infrered studies of protein-induced perturbation of lipids in lipoproteins and membranes. Chemistry and Physics of Lipids, 1998. 96: p. 53-68.
156. Brandenburg and Seydel, Orientation measurements on ordered multibilayers of phospholipids and sphingolipids from synthetic and natural origin by ATR Fourier transform infrared spectroscopy. Zeitschrift für Naturforschung C, 1986. 41(4): p. 453-467.
157. Correa et al., Galleria mellonella native and analogue peptides Gm1 and ΔGm1. I) Biophysical characterization of the interaction mechanisms with bacterial model membranes. Biochimica et Biophysica Acta (BBA) - Biomembranes, 2014. 1838(10): p. 2728-2738.
158. Frey et al., Orientation of mellitin in phospholipid bilayers: A polarized attenuated total reflection infrared study. Biophysical Journal, 1991. 60: p. 922-930.
159. Schmitt and Flemming, FTIR-spectroscopy in microbial and material analysis. International Biodeterioration & Biodegradation, 1998. 41(1): p. 1-11.
160. Quiles et al., Analysis of changes in attenuated total reflection FTIR fingerprints of *Pseudomonas fluorescens* from planktonic state to nascent biofilm state. Spectrochim Acta A Mol Biomol Spectrosc, 2010. 75(2): p. 610-6.
161. Delille et al., In situ monitoring of the nascent *Pseudomonas fluorescens* biofilm response to variations in the dissolved organic carbon level in low-nutrient water by attenuated total reflectance-Fourier transform infrared spectroscopy. Applied and environmental microbiology, 2007. 73(18): p. 5782-5788.
162. Suci et al., Combined light microscopy and attenuated total reflection fourier transform infrared spectroscopy for integration of biofilm structure, distribution, and chemistry at solid-liquid interfaces. Applied and environmental microbiology, 1997. 63(11): p. 4600-4603.
163. Suci et al., Investigation of ciprofloxacin penetration into *Pseudomonas aeruginosa* biofilms. Antimicrobial agents and chemotherapy, 1994. 38(9): p. 2125-2133.

164. Filip and Hermann, An attempt to differentiate *Pseudomonas spp.* and other soil bacteria by FT-IR spectroscopy. European Journal of Soil Biology, 2001. 37(3): p. 137-143.
165. Rinia et al., Blistering of Langmuir-Blodgett bilayers containing anionic phospholipids as observed by atomic force microscopy. Biophysical Journal, 1999. 77: p. 1683-1693.
166. Jass et al., From liposomes to supported, planar bilayer structures on hydrophilic and hydrophobic surfaces: An atomic force microscopy study. Biophysical Journal, 2000. 79: p. 3153-3163.
167. Mainil, *Escherichia coli* virulence factors. Veterinary Immunology and Immunopathology, 2013. 152(1–2): p. 2-12.
168. Microbiology Series, N. and A. Méndez-Vilas, The Battle Against Microbial Pathogens: Basic Science, Technological Advances and Educational Programs.
169. Tenaillon et al., The population genetics of commensal Escherichia coli. Nat Rev Microbiol, 2010. 8(3): p. 207-17.
170. Alberts et al., Molecular Biology of the Cell 5th edition p.25.
171. Riley et al., *Escherichia coli* K-12: a cooperatively developed annotation snapshot--2005. Nucleic Acids Res, 2006. 34(1): p. 1-9.
172. Francius et al., Bacterial Surface Appendages Strongly Impact Nanomechanical and Electrokinetic Properties of *Escherichia coli* Cells Subjected to Osmotic Stress. PLoS ONE, 2011. 6(5): p. e20066.
173. Lambert and Pearson, Susceptibility testing: accurate and reproducible minimum inhibitory concentration (MIC) and non-inhibitory concentration (NIC) values. Journal of applied microbiology, 2000. 88(5): p. 784-790.
174. Jamal, Influence de stress environnementaux sur les propriétés physicochimiques de jeunes biofilms en cours de formation : Etude par spectroscopies vibrationnelles infrarouge-Raman et de force AFM. Université de Lorraine, 2015.
175. Hoppert, Microscopic Techniques in Biology. 2003: p. 86-87.
176. Spector, Basic Methods in Microscopy: Protocols and Concepts from Cells: A Laboratory Manual. 2006: p. 150-151.
177. Toupe, Mécanisme d'action d'un nouveau peptide lantibiotique de *Bacillus clausii* sur des modèles de membranes bactériennes : une approche par résonance magnétique nucléaire et par imageries optiques Université de Bordeau 1, 2012.
178. Cadenhead and Kellner, Some observations on monolayer spreading solvents with special reference to phospholipid monolayers. Journal of Colloid and Interface Science, 1974. 49(1): p. 143-145.

179. Wüstneck et al., The influence of spreading solvent traces in the atmosphere on surface tension measurements by using a micro-film balance and the captive bubble method. Materials Science and Engineering: C, 1999. 8–9: p. 57-64.
180. Barnes, Interfacial Science, An Introduction. 2005: p. 84-88.
181. Eeman and Deleu, From biological membranes to biomimetic model membranes. Biotechnologie, Agronomie, Société et Environnement, 2010. 14(4): p. 719.
182. Corvis, Auto-assemblage d'une protéine fongique, l'hydrophobine SC3, aux interfaces. Applications à l'élaboration de surfaces catalytiques. Université Henri Poincaré, Nancy 1, 2005.
183. Czapla et al., Differentiating oxicam nonsteroidal anti-inflammatory drugs in phosphoglyceride monolayers. Langmuir, 2010. 26(5): p. 3485-92.
184. Korchowiec et al., Glycolipid-cholesterol monolayers: Towards a better understanding of the interaction between the membrane components. Biochimica et Biophysica Acta, Biomembranes, 2011. 1808(10): p. 2466-2476.
185. Wu et al., Domain Structure and Molecular Conformation in Annexin V/1,2-Dimyristoyl-sn-Glycero-3-Phosphate/Ca2+ Aqueous Monolayers: A Brewster Angle Microscopy/Infrared Reflection-Absorption Spectroscopy Study. Biophysical Journal, 1998. 74(6): p. 3273-3281.
186. Shapovalov et al., Effect of Gramicidin A on the Dipole Potential of Phospholipid Membranes. Biophysical Journal, 1999. 77(1): p. 299-305.
187. Davies and Rideal, Interfacial Phenomena, 2nd ed. 1963, New York: Academic Press. 480 pp.
188. Morandat et al., Atomic force microscopy of model lipid membranes. Analytical and Bioanalytical Chemistry. 405(5): p. 1445-1461.
189. Dhahri, Analyse topographique, mecanique et electrochimique a l'echelle sub-micrometrique de processus pilotes par les bacteries. 2013.
190. Gaboriaud and Dufrêne, Atomic force microscopy of microbial cells: Application to nanomechanical properties, surface forces and molecular recognition forces. Colloids and Surfaces B: Biointerfaces, 2007. 54(1): p. 10-19.
191. Santos et al., Filipin-Induced Lesions in Planar Phospholipid Bilayers Imaged by Atomic Force Microscopy. Biophysical Journal, 1998. 75(4): p. 1869-1873.
192. Dufrêne, Recent progress in the application of atomic force microscopy imaging and force spectroscopy to microbiology. Current Opinion in Microbiology, 2003. 6(3): p. 317-323.
193. Beech, The potential use of atomic force microscopy for studying corrosion of metals in the presence of bacterial biofilms — an overview. International Biodeterioration & Biodegradation, 1996. 37(3): p. 141-149.

194. Parot et al., Past, present and future of atomic force microscopy in life sciences and medicine. Journal of Molecular Recognition, 2007. 20(6): p. 418-431.
195. Sneddon, The relation between load and penetration in the axisymmetric boussinesq problem for a punch of arbitrary profile. International Journal of Engineering Science, 1965. 3(1): p. 47-57.
196. Polyakov et al., Automated force volume image processing for biological samples. PLoS One, 2011. 6(4): p. e18887.
197. Reiter et al., Interaction of a bacterial endotoxin with different surfaces investigated by in situ Fourier transform infrared attenuated total reflection spectroscopy. Langmuir, 2002. 18(15): p. 5761-5771.
198. Delille, Etude in situ, par spectroscopie infrarouge en mode ATR, des premières étapes de la formation d'un biofilm de *Pseudomonas fluorescens* et de sa réponse aux variations de la quantité de carbone organique dissous : application à la détection précoce du changement de la qualité microbiologique d'une eau de distribution, Faculté des Sciences et Technologies, Université Henri Poincaré; Nancy, 2007.
199. Oren et al., Structure and organization of the human antimicrobial peptide LL-37 in phospholipid membranes: relevance to the molecular basis for its non-cell-selective activity. Biochemical Journal, 1999. 341(Pt 3): p. 501.
200. Marsh, Dichroic ratios in polarized Fourier transform infrared for nonaxial symmetry of beta-sheet structures. Biophysical journal, 1997. 72(6): p. 2710.
201. Marra, Controlled deposition of lipid monolayers and bilayers onto mica and direct force measurements between galactolipid bilayers in aqueous solutions. Journal of Colloid and Interface Science, 1985. 107(2): p. 446-458.
202. McConlogue and Vanderlick, A Close Look at Domain Formation in DPPC Monolayers. Langmuir, 1997. 13(26): p. 7158-7164.
203. Kim et al., The monolayer behavior and transfer characteristics of phospholipids at the air/water interface. Korean Journal of Chemical Engineering, 1996. 13(1): p. 46-53.
204. Guzmán et al., DPPC–DOPC Langmuir monolayers modified by hydrophilic silica nanoparticles: Phase behaviour, structure and rheology. Colloids and Surfaces A: Physicochemical and Engineering Aspects, 2012. 413: p. 174-183.
205. Sautrey et al., Membrane Activity of Tetra-p-guanidinoethylcalix[4]arene as a Possible Reason for Its Antibacterial Properties. Journal of Physical Chemistry B, 2011. 115(50): p. 15002-15012.

206. Clausell et al., Polymyxin B–lipid interactions in Langmuir–Blodgett monolayers of Escherichia coli lipids: A thermodynamic and atomic force microscopy study. Biopolymers, 2004. 75(6): p. 480-490.
207. Domenech et al., Interactions of oritavancin, a new lipoglycopeptide derived from vancomycin, with phospholipid bilayers: Effect on membrane permeability and nanoscale lipid membrane organization. Biochimica et Biophysica Acta (BBA) - Biomembranes, 2009. 1788(9): p. 1832-1840.
208. El Kirat et al., Nanoscale analysis of supported lipid bilayers using atomic force microscopy. Biochimica et Biophysica Acta (BBA) - Biomembranes, 2010. 1798(4): p. 750-765.
209. Hui et al., The structure and stability of phospholipid bilayers by atomic force microscopy. Biophysical Journal, 1995. 68(1): p. 171-178.
210. Singh and Keller, Atomic force microscopy of supported planar membrane bilayers. Biophysical Journal, 1991. 60(6): p. 1401-1410.
211. Nakanishi et al., On the adsorption of proteins on solid surfaces, a common but very complicated phenomenon. Journal of Bioscience and Bioengineering, 2001. 91(3): p. 233-244.
212. Gremlich et al., FT-infrared and FT-Raman spectroscopy in biological research in Infrared and Raman spectroscopy of biological materials [In: Pract. Spectrosc., 2001; 24]. 2001: Dekker. 581 pp.
213. Grandbois et al., Atomic Force Microscope Imaging of Phospholipid Bilayer Degradation by Phospholipase A2. Biophysical Journal, 1998. 74(5): p. 2398-2404.
214. Berquand et al., Real-time imaging of drug–membrane interactions by atomic force microscopy. Biochimica et Biophysica Acta (BBA) - Biomembranes, 2004. 1664(2): p. 198-205.
215. Kong and Yu, Fourier transform infrared spectroscopic analysis of protein secondary structures. Acta Biochim Biophys Sin (Shanghai), 2007. 39(8): p. 549-59.
216. Jean-François et al., Variability in secondary structure of the antimicrobial peptide Cateslytin in powder, solution, DPC micelles and at the air–water interface. European Biophysics Journal, 2007. 36(8): p. 1019-1027.
217. Tsigelny et al., Mechanism of action of chromogranin A on catecholamine release: molecular modeling of the catestatin region reveals a β-strand/loop/β-strand structure secured by hydrophobic interactions and predictive of activity. Regulatory peptides, 1998. 77(1): p. 43-53.

218. Valenti et al., Infrared study of trifluoroacetic acid unpurified synthetic peptides in aqueous solution: Trifluoroacetic acid removal and band assignment. Analytical Biochemistry, 2011. 410(1): p. 118-123.
219. Handa et al., Immobilization and molecular interactions between bacteriophage and lipopolysaccharide bilayers. Langmuir, 2010. 26(14): p. 12095-103.
220. Papo and Shai, A molecular mechanism for lipopolysaccharide protection of Gram-negative bacteria from antimicrobial peptides. Journal of Biological Chemistry, 2005. 280(11): p. 10378-10387.
221. Delignette-Muller, Relation between the generation time and the lag time of bacterial growth kinetics. International journal of food microbiology, 1998. 43(1): p. 97-104.
222. Al-Qadiri et al., Studying of the bacterial growth phases using fourier transform infrared spectroscopy and multivariate analysis. Journal of Rapid Methods & Automation in Microbiology, 2008. 16(1): p. 73-89.
223. Sezonov et al., *Escherichia coli* physiology in Luria-Bertani broth. Journal of bacteriology, 2007. 189(23): p. 8746-8749.
224. Wilson et al., Regulation of glycogen metabolism in yeast and bacteria. FEMS Microbiology Reviews, 2010. 34(6): p. 952-985.
225. Maquelin et al., Identification of medically relevant microorganisms by vibrational spectroscopy. Journal of Microbiological Methods, 2002. 51(3): p. 255-271.
226. Legal et al., Applications of FTIR spectroscopy in structural studies of cells and bacteria. Journal of Molecular Structure, 1991. 242: p. 397-407.
227. Naumann, Some ultrastructural information on intact, living bacterial cells and related cell-wall fragments as given by FTIR. Infrared Physics, 1984. 24(2): p. 233-238.
228. Boulos et al., LIVE/DEAD® *Bac*Light™: application of a new rapid staining method for direct enumeration of viable and total bacteria in drinking water. Journal of microbiological Methods, 1999. 37(1): p. 77-86.
229. Quiles et al., Production of extracellular glycogen by *Pseudomonas fluorescens*: spectroscopic evidence and conformational analysis by biomolecular recognition. Biomacromolecules, 2012. 13(7): p. 2118-27.
230. Quilès and Humbert, On the production of glycogen by *Pseudomonas fluorescens* during biofilm development: an in situ study by attenuated total reflection-infrared with chemometrics. Biofouling, 2014. 30(6): p. 709-718.
231. Formosa et al., Unravelling of a mechanism of resistance to colistin in *Klebsiella pneumoniae* using atomic force microscopy. Journal of Antimicrobial Chemotherapy, 2015. 70(8): p. 2261-2270.

232. Goormaghtigh et al., Evaluation of the information content in infrared spectra for protein secondary structure determination. Biophysical journal, 2006. 90(8): p. 2946-2957.
233. Nagant et al., Identification of peptides derived from the human antimicrobial peptide LL-37 active against biofilms formed by Pseudomonas aeruginosa using a library of truncated fragments. Antimicrobial agents and chemotherapy, 2012. 56(11): p. 5698-5708.
234. Bi and Lutkenhaus, Cell division inhibitors SulA and MinCD prevent formation of the FtsZ ring. Journal of bacteriology, 1993. 175(4): p. 1118-1125.
235. Jaimes-Lizcano et al., Filamentous *Escherichia coli* cells swimming in tapered microcapillaries. Research in microbiology, 2014. 165(3): p. 166-174.
236. Cochran et al., Reduced susceptibility of thin *Pseudomonas aeruginosa* biofilms to hydrogen peroxide and monochloramine. Journal of applied microbiology, 2000. 88(1): p. 22-30.
237. Das et al., Changes in the biocide susceptibility of *Staphylococcus epidermidis* and *Escherichia coli* cells associated with rapid attachment to plastic surfaces. Journal of applied microbiology, 1998. 84(5): p. 852-858.
238. Pérez-Núñez et al., A new morphogenesis pathway in bacteria: unbalanced activity of cell wall synthesis machineries leads to coccus-to-rod transition and filamentation in *ovococci*. Molecular microbiology, 2011. 79(3): p. 759-771.
239. Satta et al., Control of cell septation by lateral wall extension in a pH-conditional morphology mutant of *Klebsiella pneumoniae*. Journal of bacteriology, 1980. 142(1): p. 43-51.
240. Lleo et al., Bacterial cell shape regulation: testing of additional predictions unique to the two-competing-sites model for peptidoglycan assembly and isolation of conditional rod-shaped mutants from some wild-type *cocci*. Journal of Bacteriology, 1990. 172(7): p. 3758-3771.
241. James et al., Inhibition of an early event in the cell division cycle of *Escherichia coli* by FL1060, an amidinopenicillanic acid. Journal of bacteriology, 1975. 122(3): p. 1283-1292.
242. Satta et al., Early initiation of deoxyribonucleic acid replication and shortening of generation time associated with inhibition of lateral wall formation by mecillinam. Journal of bacteriology, 1981. 148(1): p. 10-19.

Annexes

A-I. Amino acids of bCAT with 1 letter abbreviations, number of corresponding molecules found in the bCAT molecule and the corresponding amino acid pK_a values. $pK_a^{I,II}$: pK_a of the carboxylic acid and amine, pK_a^{lat}: pK_a of the functional group of the lateral chain.

Amino Acid	1 Letter Abbreviation	N° of molecules	$pK_a^{I,II}$	pK_a^{lat}
Alanine	A	1	2.33 9.71	
Arginine	R	5	2.03 9.00	12.10
Glutamine	Q	1	2.17 9.13	
Glycine	G	4	2.4 9.7	
Leucine	L	3	2.36 9.60	
Methionine	M	1	2.28 9.21	
Phenylalanine	F	2	1.83 9.13	
Proline	P	1	1.99 10.96	
Serine	S	2	2.21 9.15	
Tyrosine	Y	1	2.20 9.11	10.07

A-2. Scientific communications

O. Freudenthal, F. Quilès, G. Francius, K. Wojszko, E. Rogalska
Nanoscale investigation of colistin interactions with model phospholipid membranes by combined infrared and force spectroscopies, poster, DocSciLor 2015, June 4th, Nancy, France

O. Freudenthal, F. Quilès, G. Francius, K. Wojszko, E. Rogalska
Nanoscale investigation of colistin interactions with model phospholipid membranes by combined infrared and force spectroscopies, oral communication, Nano in Bio 2016, May 31st - June 5th, Le Gosier, Guadeloupe, France

O. Freudenthal, F. Quilès, G. Francius, K. Wojszko, E. Rogalska
Nanoscale investigation of colistin interactions with model phospholipid membranes by combined infrared and force spectroscopies, oral communication, 16th International Conference on Organized Molecular Films, 2016, Helsinki, Finland

O. Freudenthal, F. Quilès, G. Francius, K. Wojszko, M. Gorczyca, B. Korchowiec, E. Rogalska
Nanoscale investigation of colistin interactions with model phospholipid membranes by Langmuir technique, and combined infrared and force spectroscopies, Biochimica et Biophysica Acta, vol. 1858 (2016), pp. 2592-2602, http://dx.doi.org/10.1016/j.bbamem.2016.07.015